University of Oxford

Department of Chemistry



Synthesis of polymeric materials derived from abundant natural feedstocks using non-toxic heavy metals

Gabija Navickaite

University College

March 2024

This Thesis is submitted in partial fulfilment of the requirement for the degree of Doctor of Philosophy at the University of Oxford

Preface

The work described in this Thesis was carried out in the Chemistry Research Laboratory at the University of Oxford between April 2020 and March 2024 under the supervision of Professor Dermot O'Hare and Doctor Zoë Turner. All work was performed by the author unless otherwise stated, and no part has been previously submitted for another degree at this or any other university.

Gabija Navickaite

University College

March 2024

Abstract

Synthesis of polymeric materials derived from abundant natural feedstocks using non-toxic heavy metals

Gabija Navickaite **D.Phil Thesis**

University College **March 2024**

The aims of this Thesis were: firstly, to develop new di(amido)siloxane complexes using relatively non-toxic bismuth and scandium metals, and secondly, to examine the activity of the bismuth compounds in ring-opening polymerisation (ROP) and small molecule activation reactions.

This Thesis begins with an introduction to bio-derived polylactide (PLA) produced *via* the ROP of lactide. An overview of previously reported main group and rare-earth ROP initiators is provided, presenting challenges in the development of systems that combine high activity, selectivity, robustness, and low toxicity. Bismuth compounds are highlighted as they offer favourable characteristics as heavy metal ROP initiators, while demonstrating remarkably low toxicity.

The synthesis and characterisation of a new family of di(amido)siloxane bismuth complexes, (NON^{R})BiX, is presented. The ligand scaffold was explored through the incorporation of different substitution patterns; the tunable sterics and electronics of the complexes was found to directly influence their ROP initiating capability.

The ROP of lactide was studied using aryloxide/alkoxide initiators, proceeding with induction periods (< 4 hours) and moderate control ($Đ_M$ = 1.33–1.85). A bismuth amide analogue resulted in faster kinetics (four times faster towards *L*-lactide than its aryloxide counterpart), good polymerisation control ($Đ_M$ = 1.36) as well as high heteroselectivity for the ROP of *meso*-lactide (P_m = 0.86).

The amide initiator was shown to readily insert a single cyclic ester unit into the Bi-N bond. The resulting insertion products were proposed to act as propagating species in ROP reactions, representing rare examples of spectroscopically and/or structurally characterised metal complexes with ligands derived from ring-opened cyclic esters.

The reactivity of the bismuth amide was also explored towards small molecules. Facile addition of C-O, C-S, and C-N bonds across the Bi-N bond was observed for electrophilic, unhindered heteroallenes. Conversely, the insertion reaction proved reversible using a less electrophilic, more sterically bulky ketone, 2-benzoylpyridine.

The ligand scaffold was also used to incorporate scandium, affording the first examples of di(amido)siloxane scandium complexes. Their versatile reactivity was studied in salt-metathesis reactions, yielding both “ate” and neutral compounds. The conformational flexibility of the ligand was discussed in relation with varying steric demands, and the bonding environment was contrasted with related bismuth structures, which contain a +3 metal ion with a considerable size difference (r_{Sc3+} = 0.745, r_{Bi3+} = 1.03 Å).

Acknowledgements

Firstly, I would like to thank my supervisors Prof. Dermot O'Hare and Dr Zoë Turner for their guidance and advice throughout my D.Phil. Your constant encouragement has been instrumental in shaping my growth, both as a researcher and as an individual. Additionally, I would like to thank the OxICFM CDT for providing me with the opportunity to carry out research both at Oxford and UCI.

I am grateful for all the technical support I have received during my research. Thank you to Nick for his advice on numerous NMR experiments, to Louis, Zoë, and Clem for single crystal X-ray diffraction, and to Terri for providing me with beautiful amberised NMR tubes. I am also incredibly grateful to Zoë for her diligent proofreading of this Thesis.

I am very fortunate to have worked with fantastic people who have made the past years truly enjoyable. Thank you to everyone in the O'Hare group for not only being supportive colleagues but also wonderful friends. A huge thank you must go to Alex, Justin, Aisling, Rebecca, and Matt – you have been exceptional company during long lab days, pub trips, and on top of the mountains. Rebecca, I cannot thank you enough for everything you have taught me in the lab. I also owe a special thank you to Louis – this Thesis was made possible because of your invaluable insights.

I am grateful for all the friendships I have built in Oxford. Judy and Odysseus, thank you for the past years of laughing with me and at me, and most importantly, for making Oxford feel like a home away from home. Giulia, your unconditional support made challenging times much easier. Linda, Becca, Samvida, Anna, and all the others, I draw inspiration from each and every one of you.

I would not be where I am today without my old friends, both near and far. These friendships have given me confidence to pursue things I once only imagined. Often, you understand me better than I understand myself, and for all your advice, I am immensely grateful.

Finally, thank you to my family. Jūsų besąlygiška meilė ir rūpestis buvo ir visada bus mano gyvenimo varikliai. Ačiū už suteiktą laisvę siekti svajonių, ieškoti ir klysti, žinant, jog visada galiu pasikliauti jumis. Myliu jus be galo.

Abbreviations and Nomenclature

Term	Definition
$\{^1H\}$	Proton decoupled
Å	Ångström, 10^{-10} m
Ad	Adamantyl
Ar	Aryl
bar	bar, 100 kPa
BASH	Band selective decoupling experiment
BDI	β-diketiminato
γ-BL	γ-Butyrolactone
BnOH	Benzyl alcohol, $C_6H_5CH_2OH$
br	Broad
ε-CL	ε-Caprolactone
CN	Coordination number
conv.	Conversion
COSY	Correlation spectroscopy
d	Deuterated
d	Doublet
Da	Dalton, g mol^{-1}
dd	Doublet of Doublets
DFT	Density Functional Theory
Dipp	2,6-di*iso*propylphenyl
$Đ_M$	Molecular weight distribution, M_w/M_n
δ	Chemical shift

eq.	Equivalent(s)
Et	Ethyl
$\Delta G^{\ddagger}$	Gibbs free energy
GPC	Gel permeation chromatography
h	Plank's constant
H	Hertz, s^{-1}
$\Delta H^{\ddagger}$	Enthalpy of activation
HMBC	Heteronuclear multiple bond correlation
HSQC	Heteronuclear single quantum coherence
I	Nuclear spin
I	Initiator
^{i}Pr	*iso*Propyl
IR	Infrared
J	Coupling constant
k_B	Boltzmann's constant
k_i	Initiation rate constant
k_{obs}	Observed rate constant
k_p	Propagation rate constant
k_t	Termination rate constant
k_{tr}	Transesterification rate constant
LA	Lactide
L/L_n	Ligand
Ln	Lanthanide
m	Multiplet
M	Metal
MALDI-ToF	Matrix-assisted laser desorption/ionisation time of flight

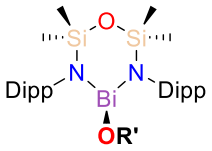
Me	Methyl
M_n	Number average molecular weight
mol%	Percent by mole fraction
MS	Mass spectrometry
M_w	Weight average molecular weight
m/*z*	Mass-to-charge ratio
μ	Bridging
^{n}Bu	*n*-Butyl
NHC	*N*-Heterocyclic carbene
NMR	Nuclear magnetic resonance
OTf	Triflate, -OSO_2CF_3
Ω	Solid angle
PCL	Poly(ε-caprolactone)
PDLA	Poly-*D*-lactide
pent	Pentet
PET	Polyethylene terephthalate
PLA	Polylactide
PLLA	Poly-*L*-lactide
P_m	Probability of forming a *meso* linkage
ppm	Parts per million
P_r	Probability of forming a *racemic* linkage
PTFE	Polytetrafluoroethylene
Py	Pyridine
q	Quartet
r	Radius
R	Gas constant

rac	*Racemic*
ROH	Alcohol
ROP	Ring-opening polymerisation
RT	Room temperature
s	Singlet
$\Delta S^{\ddagger}$	Entropy of activation
sept	Septet
t	Time
T	Temperature
tert	Tertiary
TOF	Turnover frequency
vdW	van der Waals
VT	Variable temperature
t	Triplet
^{t}Bu	*tert*-butyl
T_g	Glass transition temperature
THF	Tetrahydrofuran
T_m	Melting temperature
XRD	X-ray diffraction

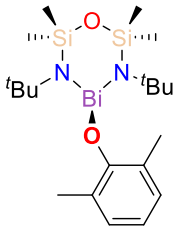
Nomenclature of compounds

Number	Name
1	$(NON^{Dipp})Bi(OC_6H_5)$
2	$(NON^{Dipp})Bi(O\text{-}2,6\text{-}Me\text{-}C_6H_3)$
3	$(NON^{Dipp})Bi(O\text{-}2,6\text{-}^{i}Pr\text{-}C_6H_3)$
4	$(NON^{Dipp})Bi(O^{t}Bu)$
5	$(NON^{tBu})Bi(O\text{-}2,6\text{-}Me\text{-}C_6H_3)$
6	$(NON^{Dipp})Bi(NMe_2)$
7	$(NON^{Dipp})Bi(OCH(Me)C(O)NMe_2)$
8	$(NON^{Dipp})Bi(OC_5H_{10}C(O)NMe_2)$
9	$(NON^{Dipp})Bi(OC_3H_6C(O)NMe_2)$
10	$(NON^{Dipp})Bi(CO_2NMe_2)$
11	$(NON^{Dipp})Bi(CS_2NMe_2)$
12	$(NON^{Dipp})Bi(NPhCONMe_2)$
13	$(NON^{Dipp})Bi(PhCONMe_2Py)$
14	$[(NON^{Dipp})ScCl_2][Li(THF)_4]$
15	$(NON^{tBu})ScCl(THF)_2$
16	$K[(NON^{tBu})Sc(O\text{-}2,6\text{-}^{i}Pr\text{-}C_6H_3)_2]$
17	$[(NON^{Dipp})Sc(CH_2SiMe_3)_2][Li(THF)_4]$
18	$[(NON^{tBu})Sc(CH_2SiMe_3)_2][Li(THF)_4]$
19	$[(NON^{Dipp})Sc(BH_4)_2][Li(THF)_4)]$

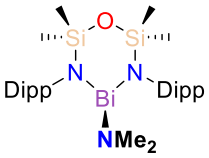
Identification of compounds



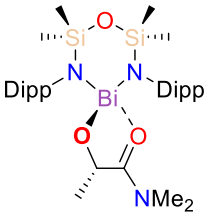
R' = C_6H_5 (**1**)
2,6-Me-C_6H_3 (**2**)
2,6-^{i}Pr-C_6H_3 (**3**)
^{t}Bu (**4**)



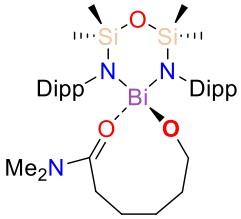
5



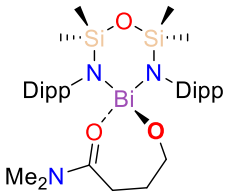
6



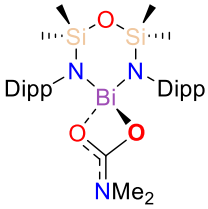
7



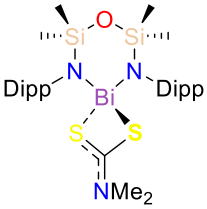
8



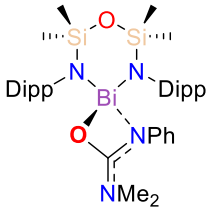
9



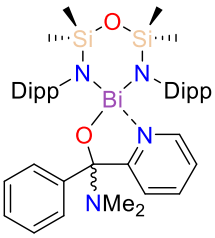
10



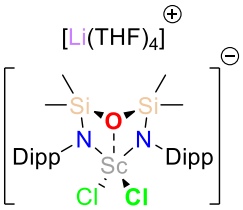
11



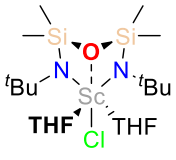
12



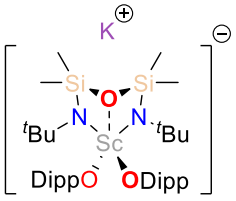
13



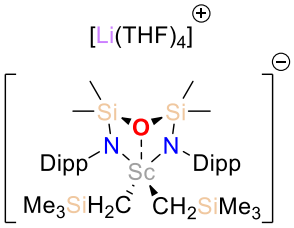
14



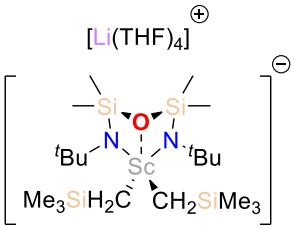
15



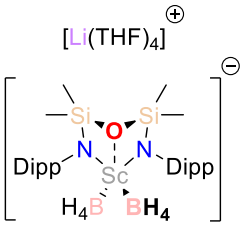
16



17



18



19

Table of Contents

Chapter 1 – Introduction 1
1.1 Polymer industry 1
1.2 Polylactide 3
1.2.1 Life-cycle of PLA 3
1.2.2 Synthetic pathways towards PLA 6
1.3 Ring-opening polymerisation of lactide 6
1.3.1 Polymerisation mechanisms 6
1.3.2 Polymerisation control 9
1.3.3 Polymerisation kinetics 12
1.3.4 Polymerisation stereocontrol 13
1.4 Initiators for the ring-opening polymerisation of lactide 17
1.4.1 Early homoleptic initiators 17
1.4.2 Main group initiators 19
1.4.2.1 Isoselective aluminium initiators 19
1.4.2.2 Indium initiators 21
1.4.2.3 Tin initiators 22
1.4.3 Rare-earth metal initiators 24
1.5 Perspectives of the ring-opening polymerisation of lactide 26
1.6 Scope of the Thesis 28
1.7 References 29
Chapter 2 – Synthesis and characterisation of di(amido)siloxane bismuth complexes 35
2.1 Introduction 35
2.1.1 Bismuth 35
2.1.2 Di(amido)siloxane ligand 36
2.2 Synopsis 38
2.3 Synthesis of pro-ligands 38
2.4 Synthesis and characterisation of di(amido)siloxane bismuth complexes 39
2.4.1 Synthesis of bismuth aryloxide and alkoxide complexes 39
2.4.1.1 NMR spectroscopic analysis 40
2.4.1.2 X-ray crystallographic analysis 42

2.4.1.3 G-Parameter analysis *44*
2.4.2 Synthesis of a bismuth amide complex 46
2.4.2.1 NMR spectroscopic analysis *47*
2.4.2.2 X-ray crystallographic analysis *48*
2.5 Conclusions 49
2.6 References 50
Chapter 3 – Ring-opening polymerisation of cyclic esters using di(amido)siloxane bismuth aryloxide and alkoxide initiators 53
3.1 Introduction 53
3.2 Synopsis 55
3.3 Lactide polymerisation studies using bismuth aryloxide and alkoxide initiators 56
3.3.1 Initiating group variation 56
3.3.2 Ligand framework variation 60
3.3.3 Initiator concentration dependence 63
3.3.4 Monomer stereochemistry variation 67
3.3.5 Temperature variation 70
3.3.6 Polymer end-group analysis 74
3.3.7 Mechanistic analysis 76
3.4 ε-Caprolactone polymerisation studies using a bismuth aryloxide initiator 79
3.4.1 ε-Caprolactone polymerisation 80
3.5 Conclusions 82
3.6 References 83
Chapter 4 – Ring-opening polymerisation of cyclic esters using a di(amido)siloxane bismuth amide initiator 87
4.1 Introduction 87
4.2 Synopsis 91
4.3 Lactide polymerisation studies 91
4.3.1 Monomer stereochemistry variation 92
4.3.2 Initiator concentration dependence 97
4.3.3 Temperature variation 101
4.3.4 Polymer end-group analysis 104
4.3.5 Reactivity of bismuth amide **6** with *L*-lactide 106
4.3.5.1 NMR and IR spectroscopic analyses *108*
4.3.5.2 X-ray crystallographic analysis *110*

4.3.6 Lactide polymerisation studies using bismuth lactate **7** 112
4.3.7 Mechanistic analysis 113
4.4 ε-Caprolactone polymerisation studies 117
4.4.1 ε-Caprolactone polymerisation using bismuth amide **6** 117
4.4.2 Reactivity of bismuth amide **6** with ε-caprolactone 120
4.4.2.1 NMR and IR spectroscopic analyses 122
4.5 γ-Butyrolactone polymerisation studies 124
4.5.1 γ-Butyrolactone polymerisation using bismuth amide **6** 125
4.5.2 Reactivity of bismuth amide **6** with γ-butyrolactone 125
4.5.2.1 NMR and IR spectroscopic analyses 126
4.6 Conclusions 127
4.7 References 129
Chapter 5 – Reactivity towards small molecules using a di(amido)siloxane bismuth amide complex 133
5.1 Introduction 133
5.2 Synopsis 136
5.3 Reactivity studies of di(amido)siloxane bismuth amide (**6**) 136
5.3.1 Reactivity with carbon dioxide 136
5.3.1.1 NMR and IR spectroscopic analyses 138
5.3.1.2 X-ray crystallographic analysis 139
5.3.2 Reactivity with carbon disulfide 141
5.3.2.1 NMR and IR spectroscopic analyses 141
5.3.2.2 X-ray crystallographic analysis 144
5.3.3 Reactivity with phenyl isocyanate 146
5.3.3.1 NMR spectroscopic analysis 147
5.3.3.2 X-ray crystallographic analysis 148
5.3.4 Reactivity with *N,N'*-di*iso*propylcarbodiimide 151
5.3.5 Reactivity with 2-benzoylpyridine 152
5.3.5.1 NMR spectroscopic analysis 152
5.3.5.2 X-ray crystallographic analysis 157
5.4 Conclusions 159
5.5 References 160
Chapter 6 – Synthesis, characterisation, and reactivity of di(amido)siloxane scandium complexes 163
6.1 Introduction 163

6.2 Synopsis 165
6.3 Synthesis, characterisation, and reactivity of di(amido)siloxane scandium complexes 165
6.3.1 Scandium chloride complexes 165
6.3.1.1 Synthesis of scandium chloride complexes 166
6.3.1.2 NMR spectroscopic analysis 167
6.3.1.3 X-ray crystallographic analysis 170
6.3.2 Scandium aryloxide complexes 172
6.3.2.1 Synthesis of a scandium aryloxide complex 172
6.3.2.2 NMR spectroscopic analysis 173
6.3.2.3 X-ray crystallographic analysis 174
6.3.3 Scandium alkyl complexes 176
6.3.3.1 Synthesis of scandium alkyl complexes 176
6.3.3.2 NMR spectroscopic analysis 178
6.3.3.3 Alternative synthesis of a scandium alkyl complex 180
6.3.4 Scandium borohydride complex 181
6.3.4.1 Synthesis of a scandium borohydride complex 182
6.3.4.2 NMR and IR spectroscopic analyses 183
6.3.4.3 X-ray crystallographic analysis 184
6.4 Conclusions 186
6.5 References 187
Chapter 7 – Experimental details 191
7.1 Materials and methods 191
7.1.1 General procedures 191
7.1.2 Commercially supplied materials 191
7.1.3 Solvent preparation 192
7.1.4 Published procedures 193
7.1.5 Solution phase NMR spectroscopy 193
7.1.6 Fourier-transform infrared (FTIR) spectroscopy 193
7.1.7 Elemental analysis 194
7.1.8 Single crystal X-ray crystallography 194
7.1.9 Matrix-assisted laser desorption/ionisation time of flight (MALDI-ToF) mass spectrometry 195
7.1.10 Gel permeation chromatography (GPC) 195
7.2 Experimental details for Chapter Two 196

7.2.1 Dipp-substituted di(amido)siloxane ligand numbering scheme 196
7.2.2 Synthesis of (NON^{Dipp})H_2 196
7.2.3 Synthesis of (NON^{tBu})H_2 196
7.2.4 General synthesis of (NON^{R})Li_2 (R = Dipp, ^{t}Bu) 197
7.2.5 General synthesis of (NON^{R})BiCl (R = Dipp, ^{t}Bu) 197
7.2.6 Synthesis of (NON^{Dipp})Bi(OC_6H_5) (**1**) 198
7.2.7 Synthesis of (NON^{Dipp})Bi(O-2,6-Me-C_6H_3) (**2**) 199
7.2.8 Synthesis of (NON^{Dipp})Bi(O-2,6-^{i}Pr-C_6H_3) (**3**) 200
7.2.9 Synthesis of (NON^{Dipp})Bi(O^{t}Bu) (**4**) 200
7.2.10 Synthesis of (NON^{tBu})Bi(O-2,6-Me-C_6H_3) (**5**) 201
7.2.11 Synthesis of (NON^{Dipp})Bi(NMe_2) (**6**) 202
7.3 Experimental details for Chapters Three and Four 203
7.3.1 General polymerisation procedure 203
7.3.2 Synthesis of (NON^{Dipp})Bi(OCH(Me)C(O)NMe_2) (**7**) 203
7.3.3 Synthesis of (NON^{Dipp})Bi(OC_5H_{10}C(O)NMe_2) (**8**) 204
7.3.4 Synthesis of (NON^{Dipp})Bi(OC_3H_6C(O)NMe_2) (**9**) 205
7.4 Experimental details for Chapter Five 206
7.4.1 Synthesis of (NON^{Dipp})Bi(CO_2NMe_2) (**10**) 206
7.4.2 Synthesis of (NON^{Dipp})Bi(CS_2NMe_2) (**11**) 207
7.4.3 Attempted synthesis of (NON^{Dipp})Bi(^{i}PrNCN^{i}PrNMe_2) 207
7.4.4 Synthesis of (NON^{Dipp})Bi(NPhCONMe_2) (**12**) 208
7.4.5 Synthesis of (NON^{Dipp})Bi(PhCONMe_2Py) (**13**) 208
7.5 Experimental details for Chapter Six 209
7.5.1 Synthesis of [(NON^{Dipp})$ScCl_2$][Li$(THF)_4$] (**14**) 209
7.5.2 Synthesis of (NON^{tBu})ScCl$(THF)_2$ (**15**) 210
7.5.3 Synthesis of K[(NON^{tBu})Sc(O-2,6-^{i}Pr-$C_6H_3)_2$] (**16**) 211
7.5.4 Synthesis of [(NON^{Dipp})Sc$(CH_2SiMe_3)_2$][Li$(THF)_4$] (**17**) 212
7.5.5 Synthesis of [(NON^{tBu})Sc$(CH_2SiMe_3)_2$][Li$(THF)_4$] (**18**) 212
7.5.6 Attempted synthesis of (NON^{Dipp})Sc(CH_2SiMe_3) 213
7.5.7 Synthesis of [(NON^{Dipp})Sc$(BH_4)_2$][Li$(THF)_4$)] (**19**) 213
7.6 References 214
Chapter 8 – Conclusions 216
i) Novel di(amido)siloxane bismuth complexes 216

ii) Di(amido)siloxane bismuth aryloxide and alkoxide complexes as active ROP initiators……217
iii) Di(amido)siloxane bismuth amide as an active ROP initiator.....218
iv) Small molecule activation using a di(amido)siloxane bismuth amide complex219
v) Novel di(amido)siloxane scandium complexes.....220
Appendix.....A-1
A.1 Appendix for Chapter Two A-1
A.2 Appendix for Chapter Three.....A-6
A.3 Appendix for Chapter Four A-8
A.4 Appendix for Chapter Five A-12
A.5 Appendix for Chapter Six A-13
A.6 Appendix for crystallographic data.....A-15

Chapter 1

Introduction

1.1 Polymer industry

Synthetic polymers play a vital role in modern life due to their durability, low cost, and versatile physical properties that can be tailored to a myriad of applications. The majority of these materials are derived from non-renewable fossil fuel resources (e.g. oil, gas, and coal), leading to significant economic and environmental implications.[1] The plastic industry is an important contributor to greenhouse gas emissions, primarily due to the energy consumption during the extraction of raw materials (61% of the plastic industry emissions) and polymer manufacturing process (30%).[2] At the current growth rate of global plastics demand, the plastics-related emissions are predicted to account for 10–15% of the global carbon budget by 2050.[3] In addition, the non-biodegradable nature and durability of commonly used plastics render them extremely persistent in the environment, causing environmental pollution and posing toxicity risks to humans and ecosystems.[4] It is estimated that by the end of 2015, 79% of all plastic waste ever produced was discarded in landfills or natural environment, 12% was incinerated and only 9% was recycled.[5] Increasingly concerning is the proliferation of plastics in the marine environment, with plastic waste constituting up to 80% of the total marine debris.[4]

To address these considerations, an increasing importance is placed on the development of a circular economy approach to sustainable polymers that exhibit closed-loop life-cycles. The main strategies include replacing petrochemical feedstocks with renewable raw materials, the development of new routes for chemical and mechanical recycling, and the design of biodegradable polymers.[6, 7] Recently, a variety of bio-derived degradable plastics have emerged, including polylactide (PLA), polyhydroxyalkonoates (PHA), polybutylene succinate (PBS), and polyglycolide (PGA).[1] All carbon content in these bioplastics is derived from renewable feedstocks, typically high starch content biomass (e.g. corn, potatoes, and sugar beets). Compared to petrochemical-based plastics, bioplastics generally have a lower carbon footprint and can demonstrate advantageous material properties, including biodegradability and/or recyclability.[8]

However, the widespread adoption of bioplastics remains challenging from environmental and economic standpoints. Increased demand for agricultural land not only exacerbates the risk of deforestation, but may also compete with land for food production, ultimately resulting in increased energy and fertiliser usage. Based on projections, the substitution of plastic packaging with bioplastic in the EU would require a minimum of 74 000 km^2 of land, exceeding the total area of Lithuania, and at least 45 billion m^3 of water, equivalent to nearly a fifth of the EU's annual freshwater withdrawal.[9, 10] Consequently, transitioning towards the large-scale production of bioplastics requires a collaborative, multidisciplinary approach to achieve a truly sustainable circular economy.

1.2 Polylactide

1.2.1 Life-cycle of PLA

PLA is one of the leading sustainable alternatives to fossil fuel-based polymers, accounting for almost a third of the global biopolymer market.[11] With high tensile strength, stiffness, and good processability, its performance is comparable to those of polyethylene terephthalate (PET), polystyrene (PS), and polyolefins, such as polypropylene (PP) (**Table 1.1**).[12-14] However, commercial PLA is unsuitable for high temperature applications due to its relatively low glass transition temperature (T_g) and melting temperature (T_m).

Table 1.1 Selected properties for PLA, PP, PET, and PS.[15-17]

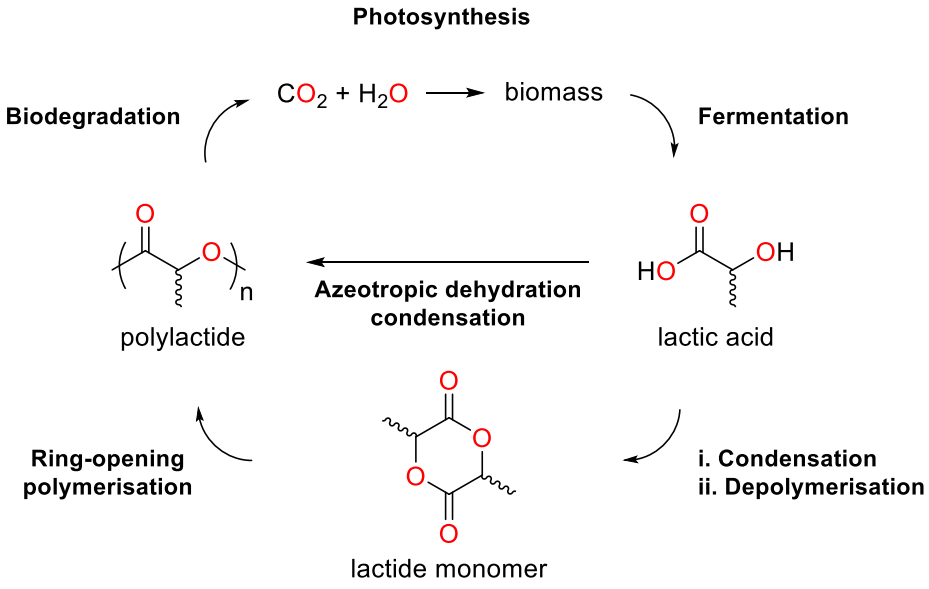
	PLA	**PP**	**PET**	**PS**
Tensile strength (MPa)	59–66	31.0–41.4	58.6–72.4	34.5–68.9
Flexural strength (MPa)	106–119	41.4–48.3	96.5–124.1	68.9–103
Strain (%)[a]	2.0–2.2	100–600	30–80	1.0–2.3
T_g (°C)	55	–7	60–85	not provided
T_m (°C)	155	160–170	250–290	not provided

[a]Elongation at break.

The main applications of PLA include packaging and fibre materials.[18-20] As a biocompatible polymer, it has also found a broad range of biomedical uses (e.g. surgical sutures, fracture fixation, scaffolds for tissue engineering, and drug delivery systems).[21-24] In recent years, the global demand for PLA has surpassed its supply, with projections suggesting that it will double every three to four years.[25]

PLA is a biodegradable aliphatic polyester, which can be produced from renewable resources (**Scheme 1.1**).[26] Its synthesis route starts with bacterial fermentation of

starch-rich biomass to generate lactic acid.[18, 27] The resultant lactic acid contains high levels of impurities, rendering purification crucial to obtain a high-quality final polymer product. One of the most efficient purification methods is based on the esterification of lactic acid, forming alkyl lactate compounds, which are subsequently distilled and hydrolysed back into pure lactic acid.[28, 29] Although lactic acid can also be manufactured synthetically, the fermentation process is generally preferred due to its favourable economics and improved stereochemical control.[30]



Scheme 1.1 The life-cycle of PLA.

Lactic acid can then be converted to lactide (LA) *via* a two-step process, patented by Cargill Dow LLC in 1992.[31] Continuous condensation of lactic acid produces PLA oligomers (2–10 kg mol^{-1}), which are depolymerised into lactide monomers *via* intramolecular transesterification using a tin-based catalyst. The crude *L*-lactide requires purification, typically achieved by distillation, to remove stereoisomeric impurities.[32]

Due to the presence of two stereogenic centres, lactide exists in three stereoisomeric forms: (*S*,*S*)-lactide (*L*-LA), (*R*,*R*)-lactide (*D*-LA), and (*R*,*S*)-lactide (*meso*-LA)

(**Figure 1.1**). In addition, an equimolar mixture of *L*- and *D*-lactide monomers is referred to as *racemic* lactide (*rac*-LA).

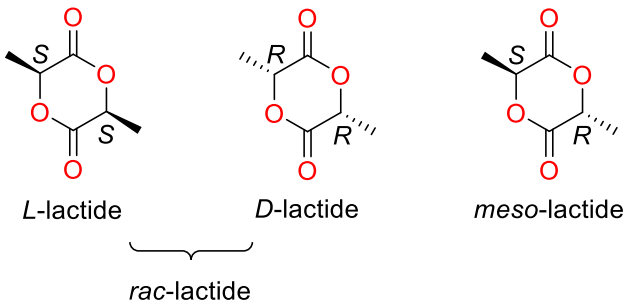


Figure 1.1 Different stereoisomers of lactide.

The majority of commercial production of PLA relies on the ring-opening polymerisation (ROP) of lactide monomers in the presence of an appropriate catalyst system.[30, 33] Alternatively, Mitsui Chemicals manufactures PLA directly from lactic acid *via* azeotropic dehydration condensation.[34]

At the end of its life-cycle, PLA can undergo thermal, photolytic or hydrolytic degradation. Its typical degradation process involves the hydrolysis of polymer ester linkages, resulting in the cleavage of high molecular weight PLA into lower molecular weight oligomers. Subsequently, these oligomers are enzymatically assimilated.[35] Several routes have been explored to promote controlled, accelerated degradation of PLA. For example, block and branched polymer structures have been designed to exhibit reduced crystallinity while preserving favourable polymer properties.[35, 36] With the ultimate formation of H_2O, CO_2, and biomass, PLA is considered to have a sustainable life-cycle.

1.2.2 Synthetic pathways towards PLA

The main methods for producing PLA include the direct polycondensation of lactic acid and the ROP of the lactide monomer. The synthesis of PLA dates back to 1932, when Carothers and co-workers produced a low molecular weight polymer by heating lactic acid under vacuum.[37] Accessing high molecular weight polymers *via* direct polycondensation is challenging due to the reversible nature of this process, with continuous removal of the water by-product required.[38] Chain coupling agents and esterification-promoting adjuvants can be used to facilitate the reaction; however, this typically leads to increased costs and complexity of the process.[39, 40] Alternatively, azeotropic distillation using a high-boiling solvent has been employed as an efficient method for removing water. Nevertheless, the molecular weight of the resultant PLA remained limited, typically below 100 kg mol^{-1}.[41, 42]

Compared to the polycondensation route, the ROP of lactide enables the formation of high molecular weight polymers (> 100 kg mol^{-1}) under relatively mild conditions, while providing a higher degree of control over polymer molecular weight distribution ($Đ_M$), end-group functionality, and microstructure. High molecular weight PLA with tunable properties is of particular importance in commercial applications.[16]

1.3 Ring-opening polymerisation of lactide

1.3.1 Polymerisation mechanisms

The feasibility of the ROP of cyclic esters is largely influenced by thermodynamic parameters.[43] Changes in both enthalpy and entropy of polymerisation are related to the ring size and substitution profile of a monomer. The polymerisation of monomers with lower than eight-membered ring sizes is generally an enthalpy-driven process, enabled

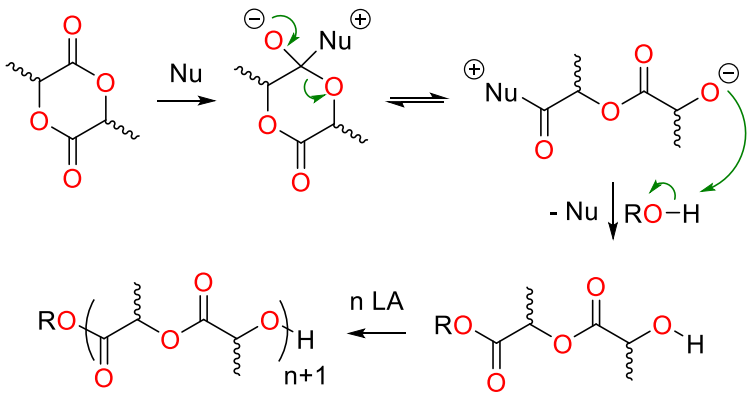
by the relief of ring strain. However, small and medium-sized monomers with low ring strain energies, such five-membered γ-butyrolactone (γ-BL), have often been considered to be impossible to polymerise.[44-46] In the case of larger ring size monomers, their polymerisation is only allowed by a favourable entropy change arising from an increase in conformational freedom in the resultant polymer.

Due to the presence of two ester groups with a nearly planar conformation, lactide exhibits a higher ring strain energy than other six-membered rings. The relief of the lactide ring strain provides the thermodynamic driving force for ROP, with a favourable standard enthalpy of polymerisation (–23 kJ mol^{-1}) offsetting the negative standard entropy (–0.04 kJ K^{-1} mol^{-1}).[47]

Depending on the nature of the initiator and reaction conditions, the ROP of lactide can proceed through different mechanistic pathways. The two predominant mechanisms are coordination-insertion and activated monomer mechanisms, with the latter encompassing cationic, metal-mediated, and organocatalytic routes.[48] An alternative anionic mechanism, typically adopted by nucleophilic initiators, has been less investigated. Due to the formation of highly active anionic polymer chain ends, it is susceptible to side reactions, such as epimerisation, chain termination, and inter-/intramolecular transesterification.[49, 50]

The activated monomer mechanism begins with the activation of lactide towards nucleophilic attack by an exogenous alcohol (**Scheme 1.2**).[51] The resultant ring-opened adduct comprises an ester and an alcohol chain end, with the latter enabling chain propagation. Common initiators that operate *via* the activated monomer mechanism include organocatalytic species (e.g. phosphines and *N*-heterocyclic carbenes) and

Brønsted acids (e.g. HOTf and HCl/Et_2O), often used in tandem with an alcohol (ROH) co-initiator.[52-55]

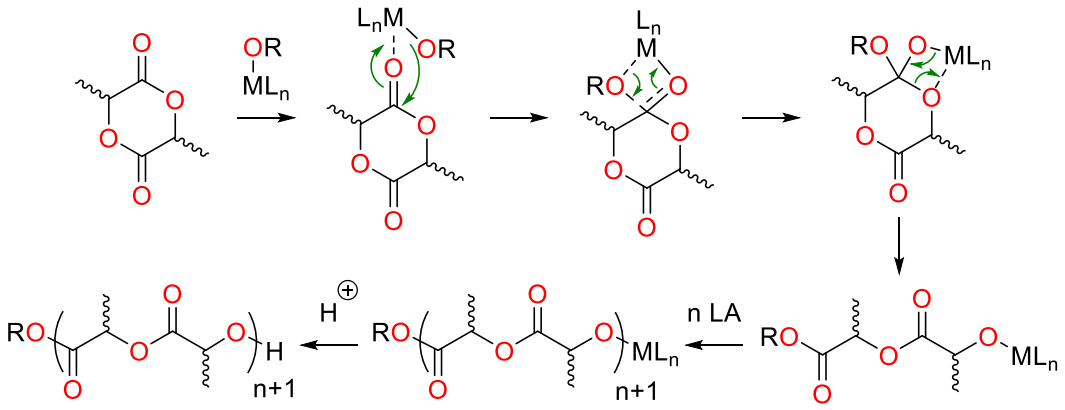


Scheme 1.2 The activated monomer mechanism for the ROP of lactide initiated by a nucleophilic initiator (Nu) and alcohol (ROH).

Neutral and cationic Lewis acidic metal initiators (L_nMX, where X = alkoxide, amide, alkyl, tetrahydroborate) have been shown to initiate the ROP of lactide *via* the coordination-insertion mechanism (**Scheme 1.3**).[43] The initial mechanistic studies investigating an aluminium *iso*propoxide ($Al(O^iPr)_3$) initiator were reported in the late 1980s.[56, 57] Generally, metal alkoxide complexes are considered to be the most efficient ROP initiators in terms of producing PLA with a high molecular weight and a narrow molecular weight distribution.[48] Catalytically active metal alkoxide species can also be formed *in situ* by reacting a metal precursor with an alcohol, such as benzyl alcohol (BnOH).

In the coordination-insertion mechanism, lactide is initially coordinated to the Lewis acidic metal centre, which activates it towards nucleophilic attack of the initiating alkoxide group at the carbonyl carbon.[48] As a result, the metal-alkoxide bond is added across the carbonyl group. Ring-opening of lactide occurs through the cleavage of the acyl-oxygen bond, and the chain is then propagated by subsequent lactide

coordination-insertion steps to produce PLA. During the polymer work-up, the active metal-alkoxide chain end is hydrolysed to form a ω–hydroxyl end group.



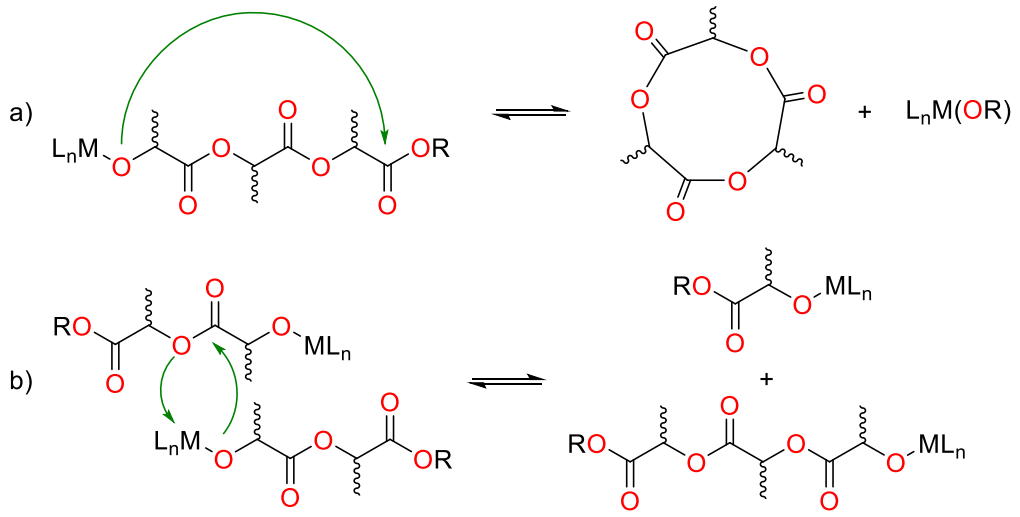
Scheme 1.3 The coordination-insertion mechanism for the ROP of lactide initiated by a metal alkoxide complex ($L_nM(OR)$).

In industry, high molecular weight PLA is typically produced by the ROP of *L*-lactide under melt-conditions (180–210 °C) using a tin(II) 2-ethylhexanoate ($Sn(Oct)_2$) initiator, also referred to as tin(II) octanoate.[16] In the presence of protic reagents, such as alcohol or water, $Sn(Oct)_2$ is proposed to reversibly form Sn-OH/-OR bonds, which act as true initiating species.[58-60] Although approved by the U.S. Food and Drug Administration (FDA), $Sn(Oct)_2$ has been shown to be cytotoxic at 26–125 ppm range (compared to the concentrations of 140–281 ppm used industrially).[61, 62] Current research is therefore focused on utilising more environmentally-benign metal initiators, such zinc, iron, and bismuth, with the aim of preventing traces of toxic residues in polymeric products, particularly for biomedical applications.[63-66]

1.3.2 Polymerisation control

The coordination-insertion polymerisation is not without its challenges as transesterification and chain transfer side reactions can compromise the control over

polymer molecular weights and molecular weight distributions. Transesterification processes can occur both intra- and intermolecularly (**Scheme 1.4**).[50, 62]



Scheme 1.4 a) Intramolecular and b) intermolecular transesterification side reactions in the ROP of lactide.

Intermolecular transesterification involves the exchange of polymer ends between two growing chains, leading to the formation of polymers with varying chain lengths. Alternatively, intramolecular backbiting reaction can produce cyclic oligomers.

In many cases, ROP initiated by Lewis acidic metal initiators exhibits "living" characteristics, defined by the absence of chain transfer and termination reactions.[62] The polymerisation process is deemed truly "living" when several factors are fulfilled, including a linear increase in molecular weight with increasing monomer conversion, a narrow molecular weight distribution, a high rate of initiation *vs.* propagation ($k_i >> k_p$) and a high rate of propagation *vs.* transesterification ($k_p >> k_{tr}$).[67]

In "living" polymerisation, the number of growing polymer chains is determined by the number of active initiator sites. An alternative "immortal" polymerisation process occurs in the presence of protic chain transfer agents, such as alcohol and water, resulting in

rapid and reversible exchange reactions among active sites.[68, 69] The number of polymer chains in "immortal" polymerisation is therefore equal to the number of chain transfer agent and initiator molecules.

The molecular weight distribution is used as a measure of a degree of transesterification during the ROP of lactide. It is defined as the weight average molecular weight divided by the number average molecular weight (M_w/M_n) (**Equation 1.1**).

$$Đ_M = \frac{M_w}{M_n}$$

$$M_n = \frac{\sum N_i M_i}{\sum N_i} \quad M_w = \frac{\sum N_i M_i^2}{\sum N_i M_i}$$

Equation 1.1 Definition of polymer molecular weight distribution, $Đ_M$, where M_w = weight average molecular weight, M_n = number average molecular weight, N_i = number of polymer chains, M_i = molecular weight of a chain.

The most common technique to measure polymer $Đ_M$ values is Gel Permeation Chromatography (GPC).[70] While a perfectly monodisperse polymer yields $Đ_M = 1.0$, deviations from this value are typically observed due to polymerisation side reactions. Generally, well-controlled ROP of cyclic esters is defined by $Đ_M < 1.2$.

Matrix-Assisted Laser Desorption/Ionisation Time of Flight (MALDI-ToF) mass spectrometry is another method employed to evaluate the extent of ROP side reactions. In the absence of transesterification, the mass spectrum of PLA displays a series of peaks with a mass-to-charge ratio (m/z) separation of 144, equivalent to the molecular weight of lactide. Alternatively, peak separation by $m/z = 72$, corresponding to half the molecular weight of a single lactide unit, indicates the presence of transesterification and thus reduced levels of control.[43]

1.3.3 Polymerisation kinetics

The activity of initiators and the nature of the ROP mechanism are both assessed by examining reaction kinetic parameters. As chain-growth polymerisation, the ROP of lactide involves three main steps: initiation, propagation, and termination, each associated with a distinct rate constant (k_i, k_p, and k_t, respectively). Considering the "living" nature of the polymerisation ($k_i >> k_p$ and $k_p >> k_t$), the initiation and termination steps can be omitted, and the rate law is therefore expressed independently of k_i and k_t. The rate law for the ROP of lactide is defined in **Equation 1.2**.[66]

$$-\frac{d[\mathrm{LA}]}{dt} = k_\mathrm{p}[\mathrm{LA}]_0^n[\mathrm{I}]_0^m$$

Equation 1.2 Definition of the rate law for lactide polymerisation, where k_p = propagation rate constant, $[LA]_0$ = initial lactide concentration, $[I]_0$ = initial initiator concentration, n = order in lactide, m = order in initiator.

To determine the propagation rate constant (k_p), *pseudo* first-order experiments are conducted, where a constant lactide concentration is maintained while varying the concentration of initiator (**Equation 1.3**).

$$-\frac{d[\mathrm{LA}]}{dt} = k_\mathrm{obs}[\mathrm{LA}]_0$$

$$k_\mathrm{obs} = k_\mathrm{p}[\mathrm{I}]_0^m$$

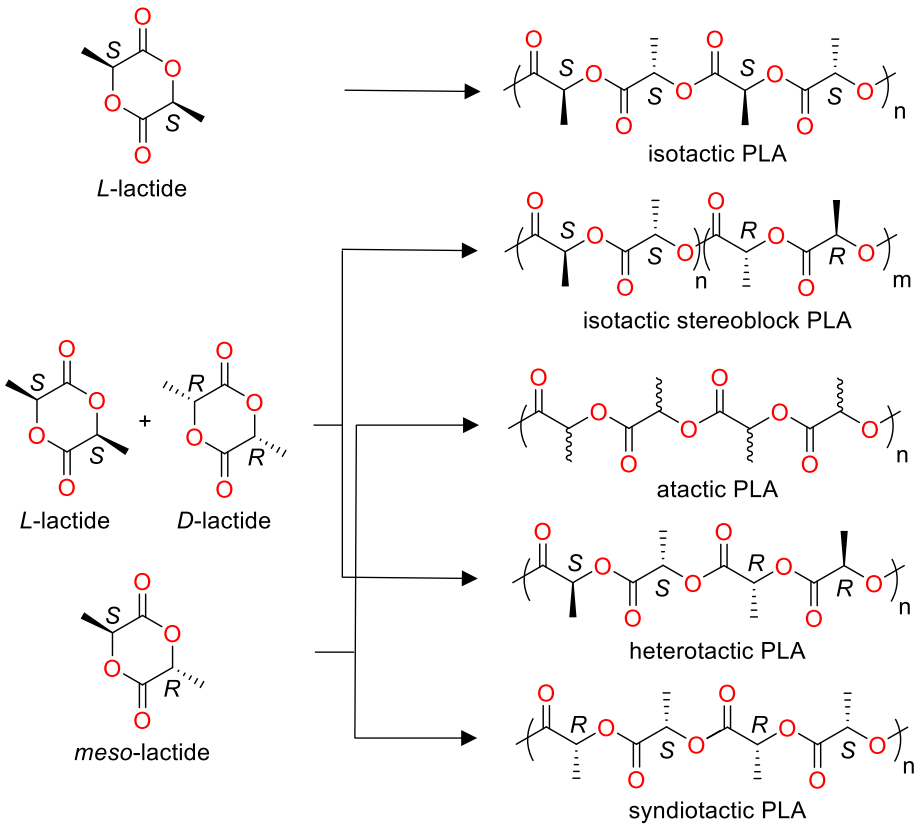
Equation 1.3 Definition of *pseudo* first-order rate law for lactide polymerisation, where k_{obs} = observed rate constant, $[LA]_0$ = initial lactide concentration, $[I]_0$ = initial initiator concentration, m = order in initiator.

The ROP of lactide proceeding by a coordination-insertion mechanism typically obeys a first-order dependence on both lactide and initiator concentrations. Zero, second, and fractional order dependencies are rare but not unprecedented.[71-76]

1.3.4 Polymerisation stereocontrol

Depending on the stereochemistry of the lactide monomer and the type of initiator used, the ROP of lactide results in diverse PLA microstructures (**Scheme 1.5**).[62] Polymer tacticity has a profound influence on its physical, mechanical, and degradation characteristics.[77, 78] Hence, the design of ROP initiators capable of controlling polymer microstructure offers a route to fine-tune the properties of PLA for specific application requirements.

The polymerisation of enantiopure *L*- or *D*-lactide in the absence of epimerisation affords isotactic poly(*L*-LA) (PLLA) or poly(*D*-LA) (PDLA) polymers, respectively. The stereocontrolled ROP of *rac*-lactide produces PLA that is either isotactic stereoblock (sequential blocks of enantiomerically pure *D*- and *L*-lactide units along the polymer backbone) or heterotactic (alternating incorporation of *L*- and *D*-lactide monomers). Furthermore, both syndiotactic (alternating incorporation of stereocentres of opposite relative configuration) and heterotactic PLA polymers can be obtained from the stereocontrolled ROP of *meso*-lactide. In the absence of stereocontrol, the resultant PLA is atactic, characterised by a random arrangement of stereochemical sequences.



Scheme 1.5 Possible microstructures of PLA resulting from the ROP of different lactide stereoisomers.[79]

The stereochemistry of PLA is generally determined by two possible mechanisms: chain-end and enantiomorphic site control.[80] During the chain-end controlled polymerisation, the configuration of the next inserted monomer depends on the stereochemistry of the last monomer unit in the propagating chain. As a result, syndiotactic PLA is produced from the ROP of *meso*-lactide, while the ROP of *rac*-lactide affords heterotactic PLA. In the case of enantiomorphic site control, the chirality of the supporting ligand dictates the configuration of the incoming monomer. The precise mechanism of stereocontrol can be difficult to determine, especially due to possible deviations from classical mechanisms.[81-83]

Due to increased stereoregularity, isotactic and syndiotactic PLA are typically crystalline in nature.[84] Isotactic PLLA exhibits T_m of approximately 170 °C and T_g of 55–65 °C. The

polymer with *L*-lactide levels above 90% is crystalline; however, the introduction of *D*- or *meso*-lactide defects has a detrimental effect on the polymer's crystallinity and thermal properties.[16, 85] For example, with 15% incorporation of stereochemical defects, the T_m of PLLA is reduced to 130 °C, consistent with a decrease in crystallinity. By contrast, both heterotactic and atactic PLA polymers are amorphous, with their T_g of up to 55 °C, rendering them brittle and prone to rapid degradation.[84]

The formation of the stereoblock structure enables access to PLA with significantly improved thermal properties. The stereocomplex PLA with a T_m of 230 °C was first synthesised from an equimolar mixture of PLLA and PDLA polymers by Ikada and co-workers.[86] The notable increase in its T_m relative to isotactic polymers was attributed to the intermolecular co-crystallisation of PLLA and PDLA chains, enforced by van der Waals interactions. While the production of enantiopure homopolymer requires challenging purification, the stereocontrolled ROP of *rac*-lactide provides a facile alternative method to produce stereoblock PLA.[84] The composition of alternating blocks of *L*- and *D*-lactide units results in comparable co-crystallisation stabilising effects and thus improved thermal properties (see **Section 1.4.2.1** for further discussion).

The tacticity of PLA can be assessed by the analysis at the tetrad level using homonuclear decoupled $^{1}H\{^{1}H\}$ and $^{13}C\{^{1}H\}$ NMR spectroscopic experiments.[87] During a typical $^{1}H\{^{1}H\}$ NMR spectroscopic experiment, homonuclear decoupling of the PLA *methyl* proton signal at approximately δ 1.58 ppm is performed to remove the splitting in the *methine* proton region (**Figure 1.2**).[88]

The resultant singlet resonances are assigned in terms of *meso* (–*RR*– and –*SS*–) and *racemic* (–*RS*– and –*SR*–) relationships between stereocentres along the PLA chain, giving rise to *m* and *r* diads, respectively. At the tetrad level, three-letter sequences are

used to describe the polymer tacticity. Isotactic PLLA and PDLA contain repeating tetrads defined by *mmm* (–*RRRR*– or –*SSSS*– linkages), heterotactic PLA is identified by *mrm* and *rmr* tetrads (–*RRSS*– and –*RSSR*– linkages), while *rrr* tetrad (–*SRSR*–) represents syndiotactic PLA.

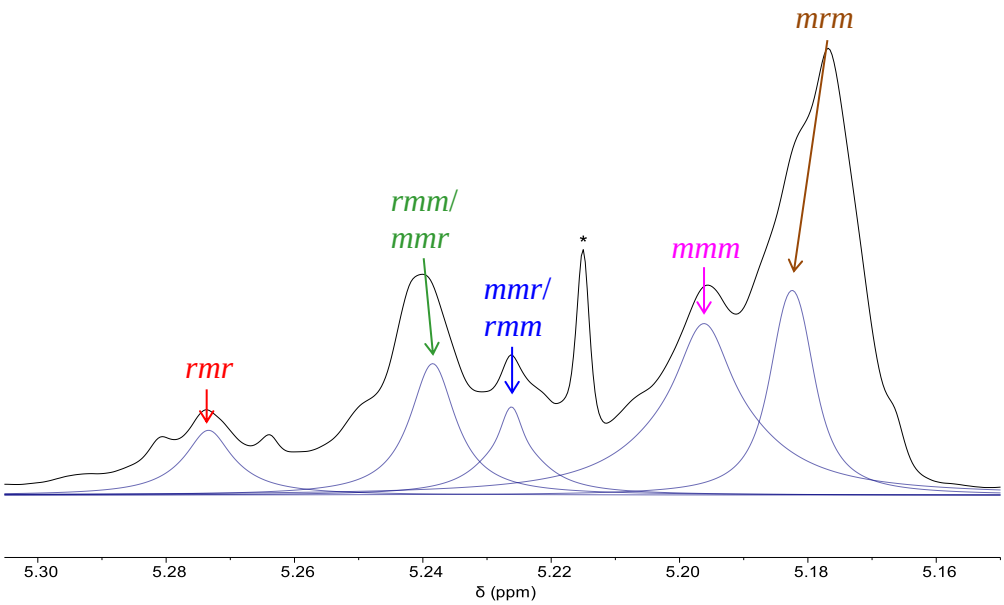


Figure 1.2 *Methine* region of the $^{1}H\{^{1}H\}$ NMR spectrum of heterotactic-enriched PLA (P_m = 0.65). * represents an artefact from BASH processing.

The parameters used to evaluate the degree of polymer stereoregularity are referred to as P_r and P_m – the probability of forming *racemic* (syndiotactic) and *meso* (isotactic) linkages, respectively.[48] In the case of the ROP of *rac*- or *meso*-lactide, the formation of an atactic polymer is described by P_r or $P_m = 0.50$, whereas perfectly heterotactic or syndiotactic polymers are formed when $P_r = 1.00$ or $P_m = 1.00$, respectively. The probability of forming a particular diad can be calculated according to Bernoullian statistics using the P_r and P_m values derived from relative tetrad intensities in $^{1}H\{^{1}H\}$ NMR spectra (**Table 1.2**).[89, 90]

Table 1.2 Tetrad probabilities for *rac*-lactide and *meso*-lactide polymerisation based on Bernoullian statistics.

Tetrad	Probability	
	***rac*-lactide**	***meso*-lactide**
mmm	$P_m{}^2 + \frac{P_r P_m}{2}$	0
mmr	$\frac{P_r P_m}{2}$	0
mrm	$\frac{P_r{}^2 + P_r P_m}{2}$	$\frac{P_m{}^2}{2}$
rmm	$\frac{P_r P_m}{2}$	0
mrr	0	$\frac{P_r P_m}{2}$
rmr	$\frac{P_r{}^2}{2}$	$\frac{P_m{}^2 + P_r P_m}{2}$
rrm	0	$\frac{P_r P_m}{2}$
rrr	0	$P_r{}^2 + \frac{P_r P_m}{2}$

1.4 Initiators for the ring-opening polymerisation of lactide

1.4.1 Early homoleptic initiators

Pioneering research on lactide polymerisation focused on the application of simple homoleptic initiators, such as Al(O^{i}Pr)$_3$, SnCl$_4$, and Sn(Oct)$_2$.[57, 91-93] Using Al(O^{i}Pr)$_3$ as the initiator, the polymerisation of *L*-lactide has been shown to result in notable induction periods and relatively slow kinetics, requiring heating to 125–180 °C for several days.[94] In order to elucidate the observed induction periods, the aggregation of active initiating

species was investigated. In solution, $Al(O^iPr)_3$ was found to exist as a mixture of trimeric and tetrameric clusters, with the trimeric aggregate capable of initiating the ROP of lactide with significantly faster rates.[57, 95] In contrast, $Sn(Oct)_2$ proved to be a more active initiator, rendering polymerisations complete in less than a few hours at 140–180 °C. Despites its lower activity, $Al(O^iPr)_3$ allowed for higher levels of polymerisation control, indicated by predictable molecular weights and narrow molecular weight distributions of polymers ($Đ_M \leq 1.5$ ($Al(O^iPr)_3$) *vs.* $Đ_M \geq 2$ ($Sn(Oct)_2$)).[57] Additionally, research on commercially available or readily synthesised zinc initiators, such as zinc lactate ($Zn(Lact)_2$), provided an alternative of non-toxic initiators, exhibiting comparable activity to $Al(O^iPr)_3$.[96]

To circumvent the need for high reaction temperatures, trivalent rare-earth metal alkoxides have been evaluated as ROP initiators.[91, 97] The *iso*propoxide derivatives proved to be active at room temperature, demonstrating significantly faster rates than those reported for homoleptic aluminium, tin, and zinc compounds. Due to the formation of oxo-*iso*propoxide clusters, described by the general formula $Ln_5(\mu\text{-}O)(O^iPr)_{13}$, a discrepancy in the number of growing PLA chains per active metal site was observed.[98] The average number of reactive sites was found to be 2.6 for yttrium and lanthanum oxo-*iso*propoxides, but appeared closer to 2 in the case of the samarium and ytterbium counterparts. The lanthanum oxo-*iso*propoxide initiator achieved the fastest kinetics in this series, albeit at the expense of reduced control due to transesterification.

The prevalence of complex solution equilibria using homoleptic initiators imposed polymerisation limitations concerning polymer molecular weight, molecular weight distribution, and microstructure. This, in combination with limited scope for ligand optimisation, prompted an investigation of well-defined organometallic initiators. To

date, complexes incorporating metals from across the entire periodic table have been successfully developed as efficient ROP initiators.

1.4.2 *p*-Block initiators

1.4.2.1 Isoselective aluminium initiators

Aluminium complexes supported by a Schiff base (salen) ligand represent some of the most studied heteroleptic initiators capable of achieving stereocontrol in the ROP of *rac*-lactide. Employing an enantiomerically pure, chiral aluminium salen initiator (**Figure 1.3a**), Spassky and co-workers reported the first synthesis of a gradient PDLA-PLLA stereoblock polymer from *rac*-lactide, realised by the preferential consumption of *D*-lactide monomers.[99] Compared to isotactic PLLA, the stereoblock structure resulted in a significantly enhanced T_m of 187 °C. Subsequently, Coates and co-workers demonstrated that isotactic stereoblock PLA with a T_m of 179 °C can also be produced using a *racemic* mixture of a chiral aluminium salen initiator (**Figure 1.3b**).[100] A polymer exchange mechanism was proposed to explain the microstructure, where each enantiomer of the initiator, capable of selectively polymerising monomers with opposite chirality, was rapidly exchanged by propagating polymer chains. In contrast, the lack of stereocontrol in the ROP of *rac*-lactide was observed using the analogous yttrium initiator, attributed to reduced steric shielding of the active site (*vide infra*, **Section 1.4.3**).

Following the development of several stereoselective chiral initiators operating *via* the enantiomorphic site control mechanism, Nomura and co-workers explored the capability of an achiral aluminium salen complex (**Figure 1.3c**), used in the presence of a BnOH co-initiator, to polymerise *rac*-lactide through an alternative chain-end control mechanism.[101] The formation of stereoblock PLA (T_m = 192 °C) was achieved by

incorporating sterically bulky substituents in the *ortho*-phenyl positions of the salen backbone. The resultant sterically congested environment at the aluminium centre was also found to prevent the initiating species from aggregating, leading to well-controlled ROP ($Đ_M$ = 1.06).

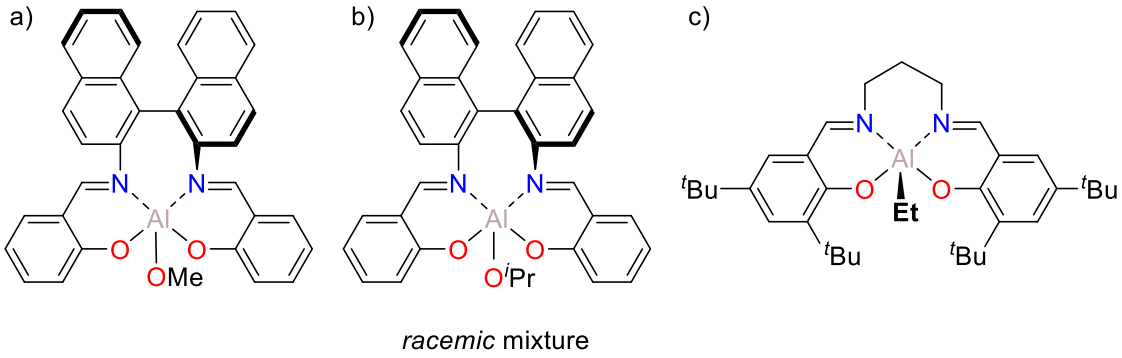


Figure 1.3 Selected examples of isoselective aluminium(III) initiators for the ROP of *rac*-lactide.

To optimise the performance of aluminium-based initiators, salen ligands have been extensively functionalised through modifications of both the flexibility of their diamine bridge and the steric and electronic properties of phenyl substituents. Consequently, a wide variety of aluminium salen complexes have been developed, exhibiting high levels of regio- and stereocontrol in the ROP of *rac*- and *meso*-lactide monomers.[102-105] However, these systems have typically suffered from slow kinetics, with elevated temperatures (70–100 °C), long reaction times (> 24 hours), and high catalyst loadings (~ 1 mol%) required.[106-108] With the aim of improving polymerisation rates while maintaining stereocontrol, there has been a growing research interest in heavier trivalent metal initiators.

1.4.2.2 Indium initiators

Due to the large coordination sphere and tunable Lewis acidity, indium complexes have been employed as ROP initiators, often demonstrating enhanced activity with respect to related aluminium systems.[72] However, very few of them have afforded both high polymerisation rates and high levels of stereocontrol.[109] Generally, the ability of ROP initiators to control the stereochemistry of PLA has been attributed to the formation of a relatively constrained coordination environment, particularly notable for smaller aluminium active sites relative to those of indium.[105] In addition, the substitution of aluminium with the larger indium metal has been shown to alter the underlying ROP mechanism, likely contributing to a loss of stereocontrol.[72]

A series of mononuclear and dinuclear indium initiators bearing a salan ligand have been developed by Mehrkhodavandi and co-workers.[110] These systems demonstrated faster rates in the polymerisation of *rac*-lactide compared to related aluminium initiators. By reducing the steric bulk of the ancillary ligand, enhanced initiator activity was observed yet with lower levels of stereocontrol. The incorporation of even more sterically demanding substituents on the ligand backbone, a strategy commonly employed to enhance stereocontrol using aluminium salen systems, did not yield the anticipated results. Despite achieving the highest level of stereocontrol in the series, the dinuclear ethoxide-bridged initiator produced PLA with only moderate isotacticity (P_m = 0.77) (**Figure 1.4a**), rendering the polymer amorphous in nature. The observed limit on the degree of polymerisation stereocontrol was proposed to result from the relatively large coordination sphere of the indium centre, combined with the flexible ligand structure.

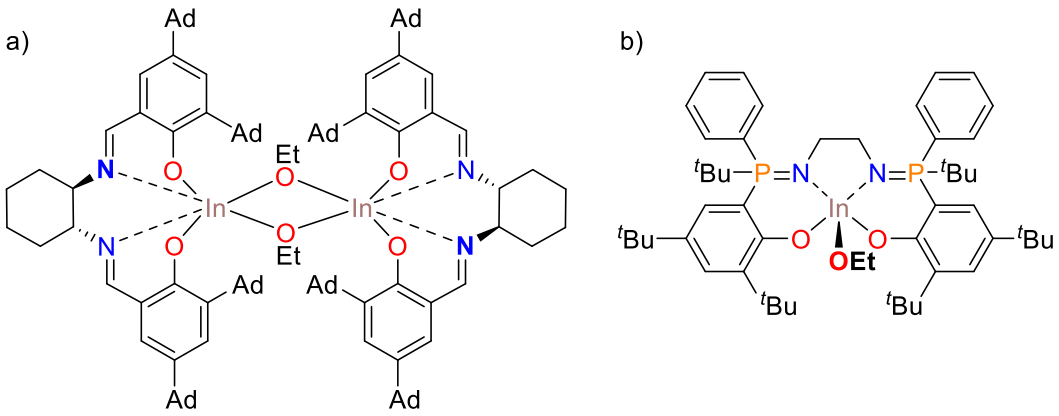


Figure 1.4 Selected examples of indium(III) initiators for the ROP of *rac*-lactide.

Williams and co-workers described the phosphasalen-based indium complex (**Figure 1.4b**), capable of producing highly isotactic PLA from *rac*-lactide (P_m = 0.90–0.91).[111, 112] Consistent with similar trends established using other indium and aluminium Schiff base systems, the reduced steric bulk of *ortho*-phenyl substituents was found to result in poorer stereocontrol.[107, 110] Although the initiator exhibited lower activity than the dimeric indium compound reported by Mehrkhodavandi and co-workers (TOF = 100 h^{-1} *vs.* 196 h^{-1} at 298 K, respectively), the polymerisation rates were still orders of magnitude higher than those of related stereoselective aluminium initiators (TOF = 1–10 h^{-1}).

1.4.2.3 Tin initiators

Since the initial reports of homoleptic tin compounds active in the polymerisation of lactide, most research has focused on $Sn(Oct)_2$ as the preferred industrial initiator.[47, 59, 113] The first well-defined single-site tin(II) initiator, supported by a sterically demanding β-diketiminato (BDI) ligand, was described by Gibson and co-workers (**Figure 1.5a**).[114] In the ROP of *rac*-lactide, the initiator resulted in a slight heterotactic-enriched PLA (P_r = 0.64, 333 K). The polymerisation was found to proceed

with a significant induction period, attributed to the electronic repulsion between the tin-based lone pair and the carbonyl oxygen on the lactide unit.[115] A subsequent study was published to investigate the relationship between the reactivity of these initiators and the steric and electronic profile of the supporting ligand. Two main factors, the reduced steric bulk of aryl groups and the incorporation of electron withdrawing substituents, were shown to lead to enhanced initiator activity alongside shorter induction periods. However, the levels of stereocontrol remained relatively unchanged. The authors suggested that polymer stereochemistry was primarily governed by the geometry constraints imposed by the lone pair of electrons on the tin centre, contrary to the influence of the BDI ligand framework observed using analogous zinc systems.[116]

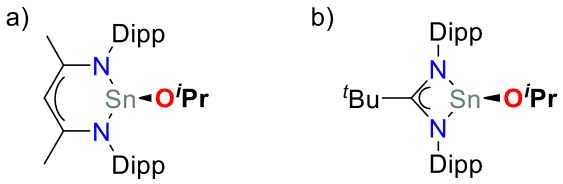


Figure 1.5 Selected examples of tin(II) initiators for the ROP of lactide**.**

Compared to BDI-supported tin complexes, the utilisation of a less sterically demanding amidinato ligand resulted in almost a three-fold increase in polymerisation activity (**Figure 1.5b**), accompanied with relatively narrow polymer molecular weight distributions ($Đ_M \leq 1.27$).[117, 118] Since these reports, a variety of bulky ancillary ligands, such as salicylaldiminato and aminoether-phenolato, have been successfully employed to develop fast tin initiators, displaying high levels of ROP control. Nevertheless, no significant enhancement of stereocontrol has been achieved.[119, 120]

1.4.3 Rare-earth metal initiators

Based on the high activities demonstrated by homoleptic rare-earth initiators, many discrete heteroleptic systems have since been developed for fast and well-controlled ROP.[66] Generally, one of the caveats of rare-earth initiators is their tendency to undergo aggregation and ligand rearrangement reactions, which may compromise polymerisation control and the robustness of initiators.[121-124] The design of bulky and/or multidentate ligands capable of providing control over initiator nuclearity represents an important research goal in the development of new rare-earth initiators.[125]

The synthesis of isotactic PLA from *rac*-lactide using yttrium-based initiators was first described by Arnold and co-workers.[126, 127] Their homochiral yttrium phosphine oxide-alkoxide complex exhibited fast rates and high levels of stereocontrol (P_m = 0.81, 255 K), with relatively narrow polymer molecular weight distributions recorded ($Đ_M \geq 1.23$) (**Figure 1.6a**).

The relationship between the size of an active site in rare-earth metal systems and their activity in ROP has been explored in several studies.[125, 128-130] Williams and co-workers introduced a series of yttrium complexes supported by phosphasalen ligands, the scaffold also utilised in the development of indium initiators (*vide supra*, **Figure 1.4b**).[131, 132] In the presence of the five-coordinate yttrium initiator (**Figure 1.6b**), the polymerisation of *rac*-lactide produced heterotactic PLA (P_r = 0.87, 298 K). The nature of the diimine backbone was found to determine both initiator activity and stereocontrol, with the ethylene linker allowing for the fastest rate and the highest levels of heteroselectivity. By contrast, the six-coordinate yttrium initiator showed high levels of isoselectivity (P_m = 0.77, 298 K or P_m = 0.84, 258 K) (**Figure 1.6c**), attributed to its more sterically constrained environment at the active site.

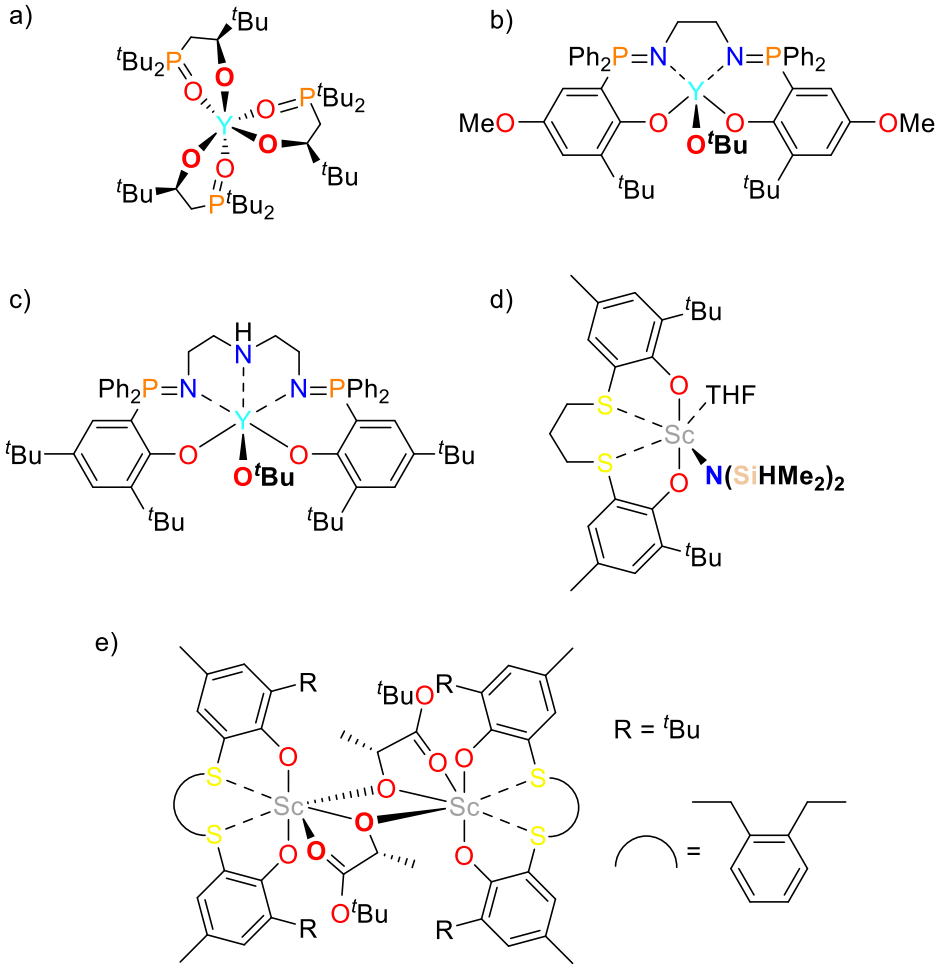


Figure 1.6 Selected examples of rare-earth metal initiators for the ROP of *rac*-lactide.

Following these reports, the phosphasalen ligand was utilised to evaluate the ROP initiating capability across a series of rare-earth metal systems.[133] Their activity in the ROP of *rac*-lactide increased in the order of increasing ionic radius: lutetium (k_{obs} = 6.3 × 10^{-5} s^{-1}) < yttrium (k_{obs} = 6.9 × 10^{-4} s^{-1}) < lanthanum (reaction complete in seconds), consistent with the analogous trend reported for Group 13 initiators. As anticipated, the lutetium initiator demonstrated the highest level of stereocontrol, followed by its yttrium counterpart (P_m = 0.80 and 0.75, respectively). Conversely, the lanthanum initiator polymerised *rac*-lactide with a heterotactic bias (P_r = 0.72), likely due to the relatively more open coordination sphere at the metal centre.

Compared to yttrium, scandium-based initiators have been less widely explored, often demonstrating both diminished activity and control in the ROP of lactide.[130, 134] High levels of heteroselectivity in the ROP of *rac*-lactide have been reported by Okuda and co-workers in their study of scandium *bis*(phenolate) complexes.[82, 135] The authors proposed that enhanced steric bulk of the *ortho*-phenyl substituents and the increased length of the bridging unit were essential for producing highly heterotactic PLA (P_r = 0.95, 298 K) (**Figure 1.6d**). To investigate the mechanism of stereocontrol, a scandium (*R*)-*tert*-butyl lactate derivative was prepared (**Figure 1.6e**), revealing its dimeric structure of a single conformation in the solid state. The observed ROP heteroselectivity was proposed to result from the interconversion of the ligand configuration due to steric repulsion, with each configuration favouring a selective insertion of a lactide stereoisomer of the opposite chirality. Notably, the analogous yttrium initiator demonstrated a slightly reduced level of stereocontrol under the same reaction conditions (P_r = 0.84, 298 K).[82]

1.5 Perspectives of the ring-opening polymerisation of lactide

Significant progress in the development of efficient single-site homogeneous ROP initiators has been made over the past decades. The nature of an initiating system has been demonstrated to significantly impact the economics of PLA production, as well as the properties and applications of the resulting polymers. Most research efforts have focused on improving reaction kinetics, controlling polymer microstructure, molecular weight, and molecular weight distribution, and ensuring that the initiator is robust, cost-effective, and relatively non-toxic.

While the rational selection of an appropriate metal-ligand system has facilitated favourable ROP performance, the optimisation of initiators to simultaneously incorporate all these desired features has proven to be difficult. For example, larger main group and rare-earth metals often exhibit enhanced activity in ROP; however, their ability to achieve high levels of stereocontrol is hindered by their less constrained coordination sphere (**Table 1.3**). The development of robust initiators, such as several indium and tin-based compounds, has allowed for rapid and well-controlled ROP under industrially relevant conditions, yet their applicability can be challenged due to toxicity issues.

Table 1.3 Comparison of selected literature initiators for the ROP of *rac*-lactide.

Initiator [a]	P_m/P_r	**Time (h)**	**Conv. (%)**	***T*** **(°C)**	M_w/M_n	$[LA]_0/[I]_0$
$L_2AlEt/BnOH$[107]	$P_m = 0.97$	19	93	70	1.09	100:1
(*RRR*)-$[(L)In(OEt)]_2$[110]	$P_m = 0.77$	1	98	25	1.42	200:1
(L)In(OEt)[112]	$P_m = 0.90$	4.5	90	25	1.17	500:1
(L)Sn(O^{i}Pr)[115]	$P_r = 0.67$	2	93	60	1.13	100:1
$[(L)Sn(NMe_2)]_2$[119]	$P_r = 0.65$	1	92	60	1.37	100:1
(*RRR*)-(YL_3)[126]	$P_m = 0.81$	0.167	98	–18	1.23	200:1
(L)Y(O^{t}Bu)[132]	$P_r = 0.87$	0.006	86	25	1.50	1000:1
(L)Y(O^{t}Bu)/^{i}PrOH[132]	$P_m = 0.84$	3	77	–15	1.01	1000:1
(L)Sc{$N(SiHMe_2)_2$}(THF)[135]	$P_r = 0.95$	8	81	25	1.85	300:1

[a]Refer to **Figures 1.3**–**1.6** for structural information.

Predicting the performance of initiators is difficult due to the limited understanding of their structure-activity relationship. Even subtle variations in the Lewis acidity and steric environment of the initiator can have a significant influence on polymerisation activity and control. In addition, substituting the metal centre with a heavier analogue may lead

to changes in both the initiation and stereocontrol mechanisms of ROP, as well as affecting aggregation behaviour in solution. As a result, trends established for a specific system are generally not applicable to others. To predict and optimise the selection of initiators, an integrated approach has been pursued, combining experimental structural and mechanistic studies with computational modelling, assisted by machine learning techniques.[136]

1.6 Scope of the Thesis

This Thesis aims to develop a new family of well-defined single-site bismuth initiators for the ROP of lactide and lactone monomers. The utilisation of less commonly studied bismuth offers a pathway for designing ROP initiators that demonstrate relatively low toxicity, possess a large coordination sphere, and offer tunable Lewis acidity. Bismuth-based systems may provide improved ROP performance relative to heavy tin analogues, while also demonstrating potential as non-toxic initiators. In addition, the coordination chemistry of scandium, a lighter and non-toxic metal, is explored, highlighting its diverse reactivity, which presents opportunities for the development of new ROP initiating systems.

Chapter Two describes the synthesis and characterisation of new di(amido)siloxane bismuth complexes. **Chapter Three** focuses on the application of the aryloxide and alkoxide derivatives in the ROP of lactide and ε-caprolactone monomers. Using kinetic and mechanistic studies, the factors governing polymerisation rate, control, and stereocontrol are discussed. **Chapter Four** presents the capability of a di(amido)siloxane bismuth amide complex to polymerise lactide and ε-caprolactone monomers. Its activity towards the insertion of cyclic esters is explored with the goal of understanding the

underlying ROP mechanistic pathways. **Chapter Five** explores the reactivity of this bismuth amide compound towards a range of heteroallenes and 2-benzoylpyridine. **Chapter Six** showcases the development of new di(amido)siloxane scandium complexes, exhibiting versatile reactivity in salt-metathesis reactions.

1.7 References

1. J.-G. Rosenboom, R. Langer and G. Traverso, *Nat. Rev. Mater.*, 2022, **7**, 117-137.
2. J. Zheng and S. Suh, *Nat. Clim. Chang.*, 2019, **9**, 374-378.
3. D. E. MacArthur, D. Waughray and M. R. Stuchtey, The new plastics economy, rethinking the future of plastics, 2016.
4. D. K. A. Barnes, F. Galgani, R. C. Thompson and M. Barlaz, *Philos. Trans. R. Soc. Lond. B Biol. Sci.*, 2009, **364**, 1985-1998.
5. R. Geyer, J. R. Jambeck and K. L. Law, *Sci. Adv.*, 2017, **3**, e1700782.
6. D. K. Schneiderman and M. A. Hillmyer, *Macromolecules*, 2017, **50**, 3733-3749.
7. F. Vidal, E. R. van der Marel, R. W. F. Kerr, C. McElroy, N. Schroeder, C. Mitchell, G. Rosetto, T. T. D. Chen, R. M. Bailey, C. Hepburn, C. Redgwell and C. K. Williams, *Nature*, 2024, **626**, 45-57.
8. E. T. H. Vink and S. Davies, *Ind. Biotechnol.*, 2015, **11**, 167-180.
9. F. Stat, *Rome: FAO*, 2019.
10. J. Brizga, K. Hubacek and K. Feng, *One Earth*, 2020, **3**, 45-53.
11. European Bioplastics, https://www.european-bioplastics.org/, (accessed February 2024).
12. R. A. Auras, S. P. Singh and J. J. Singh, *Packag. Technol. Sci.*, 2005, **18**, 207-216.
13. J. R. Dorgan, H. Lehermeier and M. Mang, *J. Polym. Environ.*, 2000, **8**, 1-9.
14. R. Auras, B. Harte and S. Selke, *J. Sci. Food Agric.*, 2006, **86**, 648-656.
15. R. N. Shreve and J. A. Brink Jr, *Chemical Process Industries*, McGraw-Hill Book Co., 1977.
16. R. E. Drumright, P. R. Gruber and D. E. Henton, *Adv. Mater.*, 2000, **12**, 1841-1846.
17. T. Tábi, T. Ageyeva and J. G. Kovács, *Polym. Test.*, 2021, **101**, 107282.
18. R. Auras, B. Harte and S. Selke, *Macromol. Biosci.*, 2004, **4**, 835-864.
19. W. Hoogsteen, A. R. Postema, A. J. Pennings, G. Ten Brinke and P. Zugenmaier, *Macromolecules*, 1990, **23**, 634-642.
20. K. E. Perepelkin, *Fibre Chem.*, 2002, **34**, 85-100.
21. I. Manavitehrani, A. Fathi, Y. Wang, P. K. Maitz and F. Dehghani, *ACS Appl. Mater. Interfaces*, 2015, **7**, 22421-22430.
22. R. K. Kulkarni, K. C. Pani, C. Neuman and F. Leonard, *Arch. Surg.*, 1966, **93**, 839-843.
23. N. Ashammakhi and P. Rokkanen, *Biomat.*, 1997, **18**, 3-9.

24. Y. Zhang, X. Wu, Y. Han, F. Mo, Y. Duan and S. Li, *Int. J. Pharm.*, 2010, **386**, 15-22.
25. A. Mehmood, N. Raina, V. Phakeenuya, B. Wonganu and K. Cheenkachorn, *Mater. Today Proc.*, 2023, **72**, 3049-3055.
26. A. J. R. Lasprilla, G. A. R. Martinez, B. H. Lunelli, A. L. Jardini and R. M. Filho, *Biotechnol. Adv.*, 2012, **30**, 321-328.
27. R. Datta and M. Henry, *J. Chem. Technol. Biotechnol.*, 2006, **81**, 1119-1129.
28. X. Sun, Q. Wang, W. Zhao, H. Ma and K. Sakata, *Sep. Purif. Technol.*, 2006, **49**, 43-48.
29. P. P. Upare, Y. K. Hwang, J.-S. Chang and D. W. Hwang, *Ind. Eng. Chem. Res.*, 2012, **51**, 4837-4842.
30. J. Lunt, *Polym. Degrad. Stab.*, 1998, **59**, 145-152.
31. *US Pat.*, US5142023, 1992.
32. B. L. C. Cunha, J. O. Bahú, L. F. Xavier, S. Crivellin, S. D. A. de Souza, L. Lodi, A. L. Jardini, R. M. Filho, M. I. R. B. Schiavon, V. O. C. Concha, P. Severino and E. B. Souto, *Bioeng.*, 2022, **9**, 164-185.
33. L. T. Lim, R. Auras and M. Rubino, *Prog. Polym. Sci.*, 2008, **33**, 820-852.
34. *US Pat.*, US5310865A, 1994.
35. H. T. Oyama, Y. Tanaka and A. Kadosaka, *Polym. Degrad. Stab.*, 2009, **94**, 1419-1426.
36. F. Tasaka, H. Miyazaki, Y. Ohya and T. Ouchi, *Macromolecules*, 1999, **32**, 6386-6389.
37. W. H. Carothers, G. L. Dorough and F. J. v. Natta, *J. Am. Chem. Soc.*, 1932, **54**, 761-772.
38. W. H. Carothers, *Trans. Faraday Soc.*, 1936, **32**, 39-49.
39. S. I. Woo, B. O. Kim, H. S. Jun and H. N. Chang, *Polym. Bull.*, 1995, **35**, 415-421.
40. H. Inata and S. Matsumura, *J. Appl. Polym. Sci.*, 1985, **30**, 3325-3337.
41. K. W. Kim and S. I. Woo, *Macromol. Chem. Phys.*, 2002, **203**, 2245-2250.
42. Y. Maryanty, S. Hadiantoro, K. Widjajanti, D. I. K. Putri and L. Nikmah, *IOP Conf. Ser. Mater. Sci. Eng.*, 2021, **1053**, 012043.
43. P. Dubois, O. Coulembier and J.-M. Raquez, *Handbook of ring-opening polymerization*, John Wiley & Sons, 2009.
44. M. Hong and E. Y. X. Chen, *Nat. Chem.*, 2016, **8**, 42-49.
45. R. Bernat, P. Maksym, M. Tarnacka, K. Malarz, A. Mrozek-Wilczkiewicz, T. Biela, S. Golba, E. Kamińska, M. Paluch and K. Kamiński, *RSC Adv.*, 2021, **11**, 34806-34819.
46. A. Falconnet, M. Nicolas, T. Vollgraff, R. Konradi, B. Bruchmann, D. Rodewald, A. S. K. Hashmi and T. Schaub, *Green Chem.*, 2023, **25**, 3624-3632.
47. A. Duda and S. Penczek, *Macromolecules*, 1990, **23**, 1636-1639.
48. M. J. Stanford and A. P. Dove, *Chem. Soc. Rev.*, 2010, **39**, 486-494.
49. A. Bhaw-Luximon, D. Jhurry, N. Spassky, S. Pensec and J. Belleney, *Polymer*, 2001, **42**, 9651-9656.
50. J. Baran, A. Duda, A. Kowalski, R. Szymanski and S. Penczek, *Macromol. Symp.*, 1997, **123**, 93-101.

51. N. E. Kamber, W. Jeong, R. M. Waymouth, R. C. Pratt, B. G. G. Lohmeijer and J. L. Hedrick, *Chem. Rev.*, 2007, **107**, 5813-5840.
52. E. F. Connor, G. W. Nyce, M. Myers, A. Möck and J. L. Hedrick, *J. Am. Chem. Soc.*, 2002, **124**, 914-915.
53. F. Nederberg, E. F. Connor, M. Möller, T. Glauser and J. L. Hedrick, *Angew. Chem. Int. Ed.*, 2001, **40**, 2712-2715.
54. D. Bourissou, B. Martin-Vaca, A. Dumitrescu, M. Graullier and F. Lacombe, *Macromolecules*, 2005, **38**, 9993-9998.
55. X. Lou, C. Detrembleur and R. Jérôme, *Macromolecules*, 2002, **35**, 1190-1195.
56. H. R. Kricheldorf, M. Berl and N. Scharnagl, *Macromolecules*, 1988, **21**, 286-293.
57. P. Dubois, C. Jacobs, R. Jerome and P. Teyssie, *Macromolecules*, 1991, **24**, 2266-2270.
58. H. R. Kricheldorf, I. Kreiser-Saunders and C. Boettcher, *Polymer*, 1995, **36**, 1253-1259.
59. Y. J. Du, P. J. Lemstra, A. J. Nijenhuis, H. A. Van Aert and C. Bastiaansen, *Macromolecules*, 1995, **28**, 2124-2132.
60. A. Kowalski, A. Duda and S. Penczek, *Macromolecules*, 2000, **33**, 7359-7370.
61. M. C. Tanzi, P. Verderio, M. Lampugnani, M. Resnati, E. Dejana and E. Sturani, *J. Mater. Sci.: Mater. Med.*, 1994, **5**, 393-396.
62. O. Dechy-Cabaret, B. Martin-Vaca and D. Bourissou, *Chem. Rev.*, 2004, **104**, 6147-6176.
63. R. D. Rittinghaus, P. M. Schäfer, P. Albrecht, C. Conrads, A. Hoffmann, A. N. Ksiazkiewicz, O. Bienemann, A. Pich and S. Herres-Pawlis, *ChemSusChem*, 2019, **12**, 2161-2165.
64. D. J. Darensbourg and O. Karroonnirun, *Macromolecules*, 2010, **43**, 8880-8886.
65. H. R. Kricheldorf, *Chem. Rev.*, 2009, **109**, 5579-5594.
66. R. H. Platel, L. M. Hodgson and C. K. Williams, *Polym. Rev.*, 2008, **48**, 11-63.
67. C. X. Song and X. D. Feng, *Macromolecules*, 1984, **17**, 2764-2767.
68. S. Inoue, *J. Polym. Sci., Part A: Polym. Chem.*, 2000, **38**, 2861-2871.
69. N. Ajellal, J.-F. Carpentier, C. Guillaume, S. M. Guillaume, M. Helou, V. Poirier, Y. Sarazin and A. Trifonov, *Dalton Trans.*, 2010, **39**, 8363-8376.
70. *CrysAlisPRO*, Oxford Diffraction / Agilent Technologies UK Ltd, 2013.
71. A. Thevenon, C. Romain, M. S. Bennington, A. J. P. White, H. J. Davidson, S. Brooker and C. K. Williams, *Angew. Chem. Int. Ed.*, 2016, **55**, 8680-8685.
72. M. Normand, V. Dorcet, E. Kirillov and J.-F. Carpentier, *Organometallics*, 2013, **32**, 1694-1709.
73. P. I. Binda and E. E. Delbridge, *Dalton Trans.*, 2007, 4685-4692.
74. L. Clark, G. B. Deacon, C. M. Forsyth, P. C. Junk, P. Mountford, J. P. Townley and J. Wang, *Dalton Trans.*, 2013, **42**, 9294-9312.
75. K. B. Aubrecht, M. A. Hillmyer and W. B. Tolman, *Macromolecules*, 2002, **35**, 644-650.
76. N. Ropson, P. Dubois, R. Jérôme and P. Teyssié, *Macromolecules*, 1995, **28**, 7589-7598.
77. G. Perego, G. D. Cella and C. Bastioli, *J. Appl. Polym. Sci.*, 1996, **59**, 37-43.

78. D. E. Henton, P. Gruber, J. Lunt and J. Randall, in *Natural fibers, biopolymers, and biocomposites*, ed. M. M. Amar K. Mohanty, Lawrence T. Drzal, CRC Press, Boca Raton, 2005, vol. 16, pp. 527-577.

79. J. M. Becker, R. J. Pounder and A. P. Dove, *Macromol. Rapid Commun.*, 2010, **31**, 1923-1937.

80. A. Jiménez, M. Peltzer and R. Ruseckaite, *Poly (lactic acid) science and technology: processing, properties, additives and applications*, Royal Society of Chemistry, 2015.

81. R. Hador, A. Botta, V. Venditto, S. Lipstman, I. Goldberg and M. Kol, *Angew. Chem. Int. Ed.*, 2019, **58**, 14679-14685.

82. H. Ma, T. P. Spaniol and J. Okuda, *Inorg. Chem.*, 2008, **47**, 3328-3339.

83. P. McKeown, M. G. Davidson, G. Kociok-Köhn and M. D. Jones, *Chem. Commun.*, 2016, **52**, 10431-10434.

84. A. P. Dove, *Chem. Commun.*, 2008, 6446-6470.

85. D. M. Bigg, *Adv. Polym. Tech.*, 2005, **24**, 69-82.

86. Y. Ikada, K. Jamshidi, H. Tsuji and S. H. Hyon, *Macromolecules*, 1987, **20**, 904-906.

87. M. T. Zell, B. E. Padden, A. J. Paterick, K. A. M. Thakur, R. T. Kean, M. A. Hillmyer and E. J. Munson, *Macromolecules*, 2002, **35**, 7700-7707.

88. H. R. Kricheldorf, I. Kreiser-Saunders, C. Jürgens and D. Wolter, *Macromol. Symp.*, 1996, **103**, 85-102.

89. J. Coudane, C. Ustariz-Peyret, G. Schwach and M. Vert, *J. Polym. Sci., Part A: Polym. Chem.*, 1997, **35**, 1651-1658.

90. M. Chanda, *Introduction to polymer science and chemistry: a problem-solving approach*, CRC press, Boca Raton, 1st edn., 2006.

91. W. M. Stevels, M. J. K. Ankoné, P. J. Dijkstra and J. Feijen, *Macromol. Chem. Phys.*, 1995, **196**, 1153-1161.

92. E. W. Fischer, H. J. Sterzel and G. Wegner, *Kolloid Z. Z. Polym.*, 1973, **251**, 980-990.

93. R. Vasanthakumari and A. J. Pennings, *Polymer*, 1983, **24**, 175-178.

94. P. Degée, P. Dubois, R. Jérôme, S. Jacobsen and H.-G. Fritz, *Macromol. Symp.*, 1999, **144**, 289-302.

95. A. Kowalski, A. Duda and S. Penczek, *Macromolecules*, 1998, **31**, 2114-2122.

96. H. R. Kricheldorf and D.-O. Damrau, *Macromol. Chem. Phys.*, 1997, **198**, 1753-1766.

97. W. M. Stevels, M. J. K. Ankoné, P. J. Dijkstra and J. Feijen, *Macromolecules*, 1996, **29**, 6132-6138.

98. V. Simic, N. Spassky and L. G. Hubert-Pfalzgraf, *Macromolecules*, 1997, **30**, 7338-7340.

99. N. Spassky, M. Wisniewski, C. Pluta and A. Le Borgne, *Macromol. Chem. Phys.*, 1996, **197**, 2627-2637.

100. T. M. Ovitt and G. W. Coates, *J. Am. Chem. Soc.*, 2002, **124**, 1316-1326.

101. N. Nomura, R. Ishii, M. Akakura and K. Aoi, *J. Am. Chem. Soc.*, 2002, **124**, 5938-5939.

102. T. M. Ovitt and G. W. Coates, *J. Am. Chem. Soc.*, 1999, **121**, 4072-4073.

103. H. Du, X. Pang, H. Yu, X. Zhuang, X. Chen, D. Cui, X. Wang and X. Jing, *Macromolecules*, 2007, **40**, 1904-1913.

104. P. Hormnirun, E. L. Marshall, V. C. Gibson, R. I. Pugh and A. J. P. White, *Proc. Nat. Acad. Sci.*, 2006, **103**, 15343-15348.

105. N. Maudoux, T. Roisnel, V. Dorcet, J.-F. Carpentier and Y. Sarazin, *Chem. Eur. J.*, 2014, **20**, 6131-6147.

106. Z. Zhong, P. J. Dijkstra and J. Feijen, *Angew. Chem. Int. Ed.*, 2002, **41**, 4510-4513.

107. N. Nomura, R. Ishii, Y. Yamamoto and T. Kondo, *Chem. Eur. J.*, 2007, **13**, 4433-4451.

108. A. Pilone, K. Press, I. Goldberg, M. Kol, M. Mazzeo and M. Lamberti, *J. Am. Chem. Soc.*, 2014, **136**, 2940-2943.

109. A. Pietrangelo, S. C. Knight, A. K. Gupta, L. J. Yao, M. A. Hillmyer and W. B. Tolman, *J. Am. Chem. Soc.*, 2010, **132**, 11649-11657.

110. D. C. Aluthge, J. M. Ahn and P. Mehrkhodavandi, *Chem. Sci.*, 2015, **6**, 5284-5292.

111. D. Myers, A. J. P. White, C. M. Forsyth, M. Bown and C. K. Williams, *Angew. Chem. Int. Ed.*, 2017, **56**, 5277-5282.

112. N. Yuntawattana, T. M. McGuire, C. B. Durr, A. Buchard and C. K. Williams, *Catal. Sci. Technol.*, 2020, **10**, 7226-7239.

113. V. J. Kleine and H.-H. Kleine, *Makromol. Chem.*, 1959, **30**, 23-38.

114. A. P. Dove, V. C. Gibson, E. L. Marshall, A. J. P. White and D. J. Williams, *Chem. Commun.*, 2001, 283-284.

115. A. P. Dove, V. C. Gibson, E. L. Marshall, H. S. Rzepa, A. J. P. White and D. J. Williams, *J. Am. Chem. Soc.*, 2006, **128**, 9834-9843.

116. B. M. Chamberlain, M. Cheng, D. R. Moore, T. M. Ovitt, E. B. Lobkovsky and G. W. Coates, *J. Am. Chem. Soc.*, 2001, **123**, 3229-3238.

117. N. Nimitsiriwat, V. C. Gibson, E. L. Marshall, A. J. P. White, S. H. Dale and M. R. J. Elsegood, *Dalton Trans.*, 2007, 4464-4471.

118. N. Nimitsiriwat, V. C. Gibson, E. L. Marshall and M. R. J. Elsegood, *Inorg. Chem.*, 2008, **47**, 5417-5424.

119. N. Nimitsiriwat, V. C. Gibson, E. L. Marshall and M. R. J. Elsegood, *Dalton Trans.*, 2009, 3710-3715.

120. V. Poirier, T. Roisnel, S. Sinbandhit, M. Bochmann, J.-F. Carpentier and Y. Sarazin, *Chem. Eur. J.*, 2012, **18**, 2998-3013.

121. H. Ouyang, D. Yuan, K. Nie, Y. Zhang, Y. Yao and D. Cui, *Inorg. Chem.*, 2018, **57**, 9028-9038.

122. E. Grunova, E. Kirillov, T. Roisnel and J.-F. Carpentier, *Organometallics*, 2008, **27**, 5691-5698.

123. R. H. Platel, A. J. P. White and C. K. Williams, *Chem. Commun.*, 2009, 4115-4117.

124. J.-M. E. P. Cols, V. G. Hill, S. K. Williams and R. D. McIntosh, *Dalton Trans.*, 2018, **47**, 10626-10635.

125. Y.-L. Duan, Q. Guo, G.-Y. Liu, Z.-Z. Yi, S.-P. Feng and Y. Huang, *Polym. Chem.*, 2022, **13**, 4249-4259.

126. P. L. Arnold, J.-C. Buffet, R. P. Blaudeck, S. Sujecki, A. J. Blake and C. Wilson, *Angew. Chem. Int. Ed.*, 2008, **47**, 6033-6036.

127. P. L. Arnold, J.-C. Buffet, R. Blaudeck, S. Sujecki and C. Wilson, *Chem. Eur. J.*, 2009, **15**, 8241-8250.

128. K. Nie, L. Fang, Y. Yao, Y. Zhang, Q. Shen and Y. Wang, *Inorg. Chem.*, 2012, **51**, 11133-11143.

129. E. Grunova, E. Kirillov, T. Roisnel and J.-F. Carpentier, *Dalton Trans.*, 2010, **39**, 6739-6752.

130. Y. Chapurina, J. Klitzke, O. d. L. Casagrande Jr, M. Awada, V. Dorcet, E. Kirillov and J.-F. Carpentier, *Dalton Trans.*, 2014, **43**, 14322-14333.

131. C. Bakewell, T.-P.-A. Cao, X. F. Le Goff, N. J. Long, A. Auffrant and C. K. Williams, *Organometallics*, 2013, **32**, 1475-1483.

132. C. Bakewell, T.-P.-A. Cao, N. Long, X. F. Le Goff, A. Auffrant and C. K. Williams, *J. Am. Chem. Soc.*, 2012, **134**, 20577-20580.

133. C. Bakewell, A. J. P. White, N. J. Long and C. K. Williams, *Angew. Chem.*, 2014, **126**, 9380-9384.

134. J. El Haj Hassan, V. Radkov, V. Dorcet, J.-F. Carpentier and E. Kirillov, *J. Organomet. Chem.*, 2016, **823**, 34-39.

135. H. Ma, T. P. Spaniol and J. Okuda, *Angew. Chem. Int. Ed.*, 2006, **45**, 7818-7821.

136. X. Wang, Y. Huang, X. Xie, Y. Liu, Z. Huo, M. Lin, H. Xin and R. Tong, *Nat. Commun.*, 2023, **14**, 3647.

Chapter 2

Synthesis and characterisation of di(amido)siloxane bismuth complexes

2.1 Introduction

2.1.1 Bismuth

Bismuth is the heaviest stable element.[1] Typically found as a by-product from the mining of copper, lead, and tin, it has a relatively low cost.[2] Despite being a heavy metal, bismuth has found applications in cosmetics and pharmaceuticals (e.g. bismuth subsalicylate is used for gastrointestinal disorders, bibrocathol – as an antiseptic for eye infections).[3] In line with the growing incentives to improve sustainability within the chemical industry, bismuth compounds have also attracted attention as environmentally compatible alternatives in electronics and substitutes for lead in alloys.[4, 5]

The electronic configuration of bismuth, $[Xe]4f^{14}5d^{10}6s^{2}6p^{3}$, is strongly influenced by relativistic effects, reducing the energy of its 6s atomic orbital.[6] As a result, bismuth is most commonly found in the +3 oxidation state. While other oxidation states, including +1, +2, and +5, are also accessible, they are less prevalent in the literature due to their relatively low stability.[7-9]

The Lewis acidity of bismuth(III) compounds, associated with the relativistic contraction of the 6s orbital, renders them attractive reagents and catalysts in a variety of chemical transformations, such as arylation, alkynylation, and cross-coupling reactions.[6, 10] Organobismuth(III) species can serve as both σ- and π-acceptors, involving neutral dative ligands, anionic ligands (e.g. halides, alkyls, and aryls) or other metals. In addition to its Lewis acidic character, the large ionic radius of bismuth(III) results in diverse structural chemistry, with coordination numbers ranging from two to ten, allowing for the formation of both covalent and non-covalent interactions to saturate the coordination sphere.[11, 12] Additionally, the coordination geometry of bismuth(III) compounds can be influenced by the presence of the $6s^2$ lone pair, which has been found to exhibit varying degrees of stereochemical activity.[13, 14] However, the organometallic chemistry of well-defined bismuth complexes is relatively underexplored with respect to lighter main group and transition metals.

2.1.2 Di(amido)siloxane ligand

Dianionic *N*,*N*'-chelating di(amido) ligands are widespread in the literature due to their versatility in terms of multiple coordination modes, tunable steric and electronic properties, and varying degrees of backbone flexibility.[15]

The application of di(amido)siloxane ligands ($(O\{SiMe_2NR\}_2)H_2$) dates back to the 1970s, when the groups of Bürger and Rabet reported the ligand coordination chemistry with several main group elements (Ge, Sn, As) and transition metals (Zr, Ti).[16-18] A plethora of complexes have since been isolated and characterised, extended to incorporate a variety of transition (Cr, Mn, Fe), rare-earth (Y), actinide (U, Th), and main group elements (Al, In, Pb, Sb, Bi).[19-29]

Depending on the metal centre and the substituents on nitrogen atoms, di(amido)siloxane metal complexes have been shown to adopt variable bonding modes. For example, both monometallic and bimetallic structures can be accessed *via* *N*,*N*'-bidentate chelation (**Figure 2.1a** and **b**).[30, 31] In the presence of an oxophilic metal centre, such as alkaline earth and rare-earth metals, additional electron density can be provided by coordination of the oxygen atom in the siloxane backbone, giving rise to a *N*,*O*,*N*'-tridentate bonding mode (**Figure 2.1c**).[25, 28, 29] Furthermore, conformations of the resulting six-membered metallacycles have been found to vary from boat to chair, accommodating different degrees of steric demands.[23]

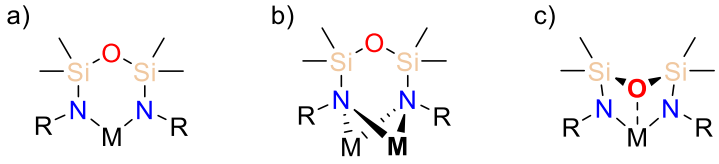


Figure 2.1 Examples of bonding modes in di(amido)siloxane metal complexes (M = metal).

The use of a suitable ligand framework plays a key role in providing sufficient stabilisation for reactive bismuth species, given their susceptibility to structural rearrangements, such as the formation of polymeric aggregates.[32] By varying the steric profile of di(amido) ligands, the extent of such aggregation can be limited.[33, 34] The incorporation of bismuth into the di(amido)siloxane ligand scaffold was pioneered by Coles and co-workers.[25, 35, 36] The ligand has been employed to isolate a series of well-defined low coordinate and/or low-valent compounds, including a stable bismuth(II) radical, demonstrating diverse oxidative reactivity.

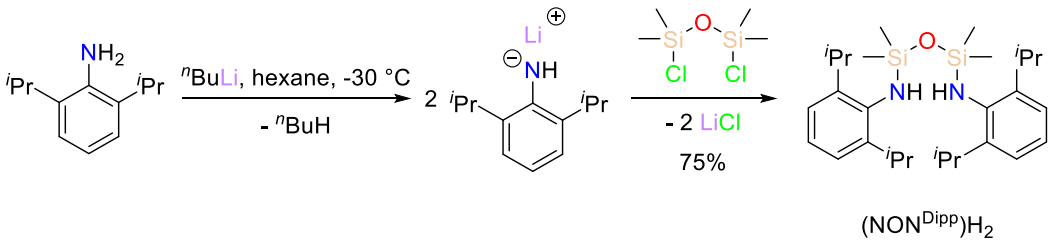
2.2 Synopsis

Chapter Two discusses the synthesis and characterisation of six new di(amido)siloxane bismuth complexes. The di(amido)siloxane ligand environment and the nature of the initiating group at bismuth have been varied to investigate the influence of steric and electronic factors in the development of ROP initiators.

2.3 Synthesis of pro-ligands

The di(amido)siloxane ligand framework was anticipated to be well-suited for the development of a new family of bismuth ROP initiators with readily tunable sterics and electronics. Two different pro-ligands $(NON^{R})H_2$ ($(O\{SiMe_2N(R)\}_2)H_2$; R = Dipp = 2,6-^{i}Pr-C_6H_3, ^{t}Bu) were prepared according to reported procedures.[20, 37]

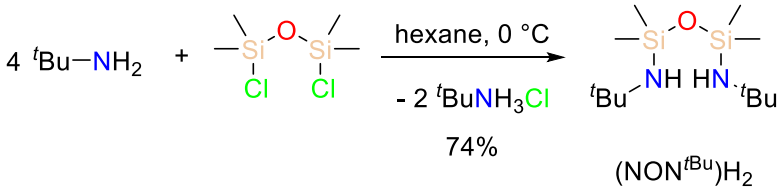
The $(NON^{Dipp})H_2$ pro-ligand was synthesised *via* a one-pot, two-step process (**Scheme 2.1**), where 2,6-di*iso*propylaniline was first lithiated using ^{n}BuLi in hexane, followed by the addition of 1,3-dichloro-1,1,3,3-tetramethyldisiloxane. After stirring the reaction for 16 hours, $(NON^{Dipp})H_2$ was isolated as a colourless oil in 75% overall yield. Its ^{1}H NMR spectrum confirmed the presence of the N*H* protons, represented by a broad singlet at δ 2.67 ppm (**Figure A.1.1** in **Appendix**).



Scheme 2.1 Synthesis of $(NON^{Dipp})H_2$.

To prepare $(NON^{tBu})H_2$, a hexane solution of 1,3-dichloro-1,1,3,3-tetramethyldisiloxane was treated with *tert*-butylamine, and the mixture was stirred for 16 hours (**Scheme 2.2**).

The pro-ligand was isolated as a colourless oil in 74% yield. Analogously to $(NON^{Dipp})H_2$, the ^1H NMR spectrum of $(NON^{tBu})H_2$ displayed a broad singlet at δ 0.88 ppm corresponding to two N*H* protons (**Figure A.1.2** in **Appendix**).

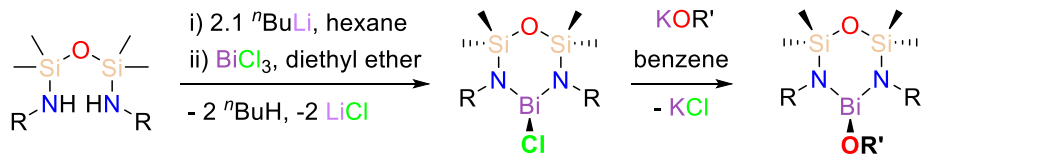


Scheme 2.2 Synthesis of $(NON^{tBu})H_2$.

2.4 Synthesis and characterisation of di(amido)siloxane bismuth complexes

2.4.1 Synthesis of bismuth aryloxide and alkoxide complexes

Di(amido)siloxane bismuth aryloxide and alkoxide complexes $(NON^{R})Bi(OR')$ (R = Dipp, R' = OC_6H_5 (**1**), O-2,6-Me-C_6H_3 (**2**), O-2,6-^{i}Pr-C_6H_3 (**3**), ^{t}Bu (**4**); R = ^{t}Bu, R' = O-2,6-Me-C_6H_3 (**5**)) were prepared *via* salt-metathesis reactions using previously reported $(NON^{R})BiCl$ (R = Dipp, ^{t}Bu) compounds (**Scheme 2.3**).[25]



R = Dipp, ^{t}Bu

R = Dipp, R' = C_6H_5 (**1**), 49%
2,6-Me-C_6H_3 (**2**), 75%
2,6-^{i}Pr-C_6H_3 (**3**), 68%
^{t}Bu (**4**), 61%
R = ^{t}Bu, R' = 2,6-Me-C_6H_3 (**5**), 57%

Scheme 2.3 Salt-metathesis route to $(NON^{R})Bi(OR')$ (R = Dipp, R' = OC_6H_5 (**1**), O-2,6-Me-C_6H_3 (**2**), O-2,6-^{i}Pr-C_6H_3 (**3**) ^{t}Bu, (**4**); R = ^{t}Bu, R' = O-2,6-Me-C_6H_3 (**5**)).

Initially, the pro-ligands were lithiated, and the resulting dilithium salts $(NON^{R})Li_2$ were reacted with anhydrous $BiCl_3$ to produce $(NON^{R})BiCl$ complexes in 55% (R = Dipp) and 52% (R = ^{t}Bu) yields (see **Figures A.1.3**–**A.1.6** in **Appendix** for their ^{1}H NMR spectra). Aryloxide and alkoxide groups were then introduced by treating the $(NON^{R})BiCl$ compounds with an appropriate potassium aryloxide or alkoxide salt in benzene for 16 hours. The $(NON^{R})Bi(OR')$ products were obtained as pale yellow (**1**–**4**) and orange (**5**) powders in 49% (**1**), 75% (**2**), 68% (**3**), 61% (**4**), and 57% (**5**) yields.

2.4.1.1 NMR spectroscopic analysis

All ^{1}H NMR spectra of **1**–**5** are consistent with the chelation of the ligand to the bismuth centre in a C_s-symmetric environment (**Figures 2.2** and **2.3**, and **Figures A.1.7**–**A.1.9** in **Appendix**).

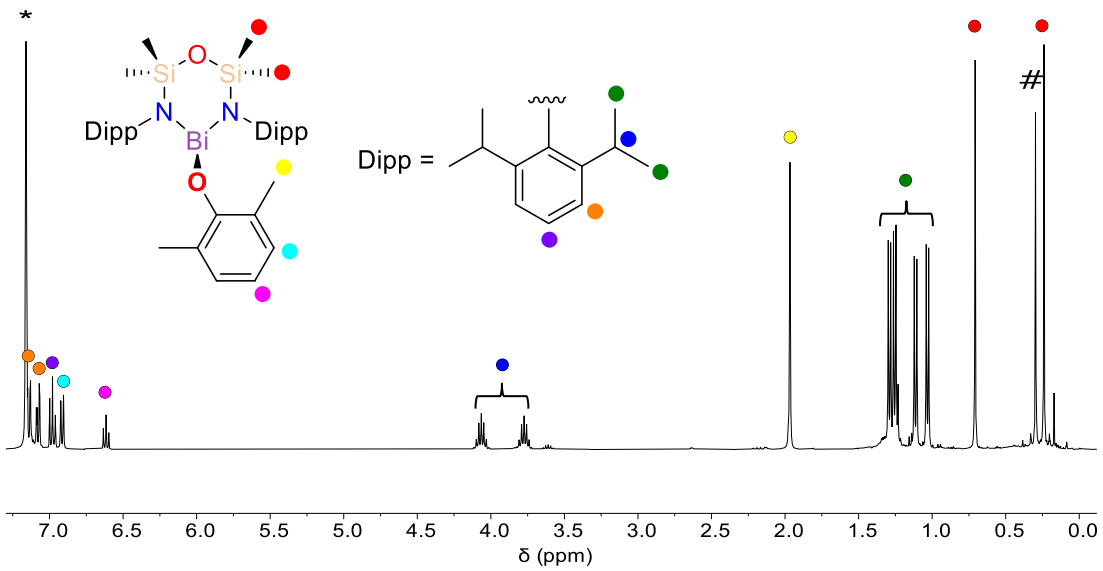


Figure 2.2 ^{1}H NMR spectrum (*benzene-d_6, 600 MHz, 298 K) of $(NON^{Dipp})Bi(O\text{-}2,6\text{-}Me\text{-}C_6H_3)$ (**2**). # represents grease.

Using **2** as a representative example for the solution-state structures of **1**–**4** (**Figure 2.2**), the presence of two low frequency singlets at δ 0.71 and 0.24 ppm, attributed to the Si*Me*$_2$ protons, suggests that the ring flipping of the BiN_2Si_2O metallacycle is restricted,

resulting in the formation of two inequivalent faces of the ligand and hence molecular C_s symmetry (see **Chapter Five** for further discussion on ligand fluxionality). In contrast, the ^{1}H NMR spectrum of pro-ligand (NON^{Dipp})H$_2$ contains a single resonance at δ 0.21 ppm for the Si*Me*$_2$ protons, indicative of C_{2v} molecular symmetry. The C*H*Me$_2$ protons appear as two septets at δ 4.06 and 3.77 ppm, which are mutually coupled to four doublets between δ 1.32–1.03 ppm, assigned to the CH*Me*$_2$ protons. The resonances between δ 7.15–6.98 ppm with a 1:1:1 integral ratio represent two inequivalent *meta*-protons and a *para*-proton of the Dipp substituents. Overall, these observations imply hindered rotation of the amido-*N*-aryl bond.

In the ^{1}H NMR spectrum of the [NON^{tBu}]-chelated complex **5**, the presence of two singlets at δ 0.54 and 0.38 ppm reflects the formation of two inequivalent Si*Me*$_2$ proton environments. The *tert*-butyl proton resonance is located as a singlet at δ 1.15 ppm, suggesting unhindered rotation around the N-^{t}Bu bond. This contrasts with the restricted solution-state rotation observed for more sterically demanding Dipp substituents in **1**–**4**.

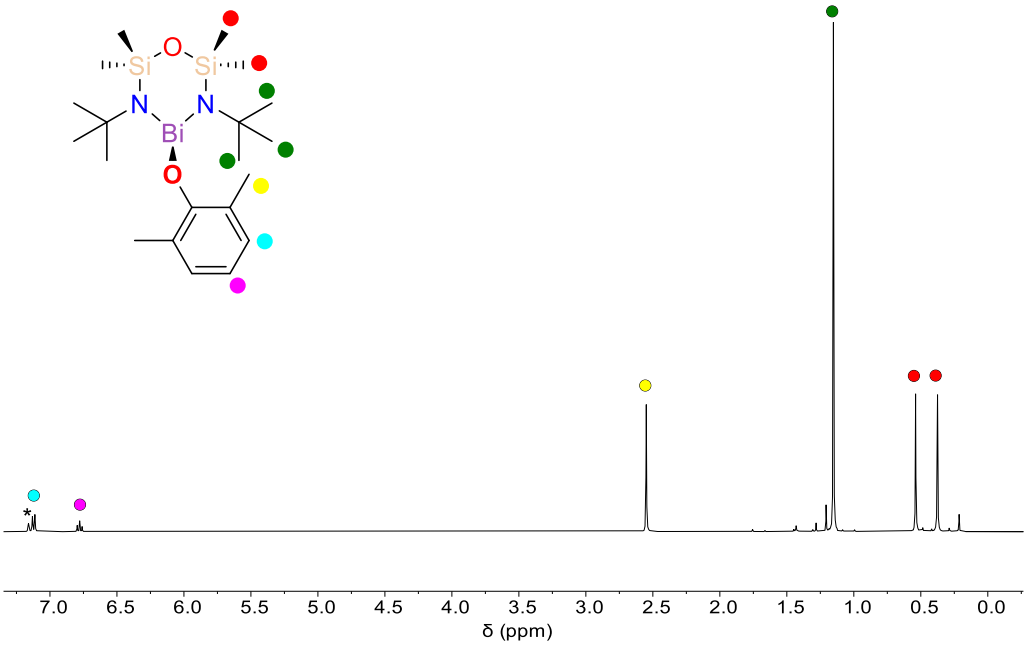


Figure 2.3 ^{1}H NMR spectrum (*benzene-d_6, 400 MHz, 298 K) of (NON^{tBu})Bi(O-2,6-Me-C$_6$H$_3$) (**5**).

2.4.1.2 X-ray crystallographic analysis

Single crystals of compounds **1**–**4**, suitable for X-ray diffraction studies, were grown from slow evaporation of a diethyl ether solution at –30 °C (**2**) and a hexane solution at 23 °C (**1**, **3**, and **4**) (**Figure 2.4**, **Table 2.1**). Complexes **1** and **3** crystallised in the triclinic space group, $P\bar{1}$, while **2** and **4** – in the monoclinic, $P2_1/n$ and $P2_1/c$, respectively.

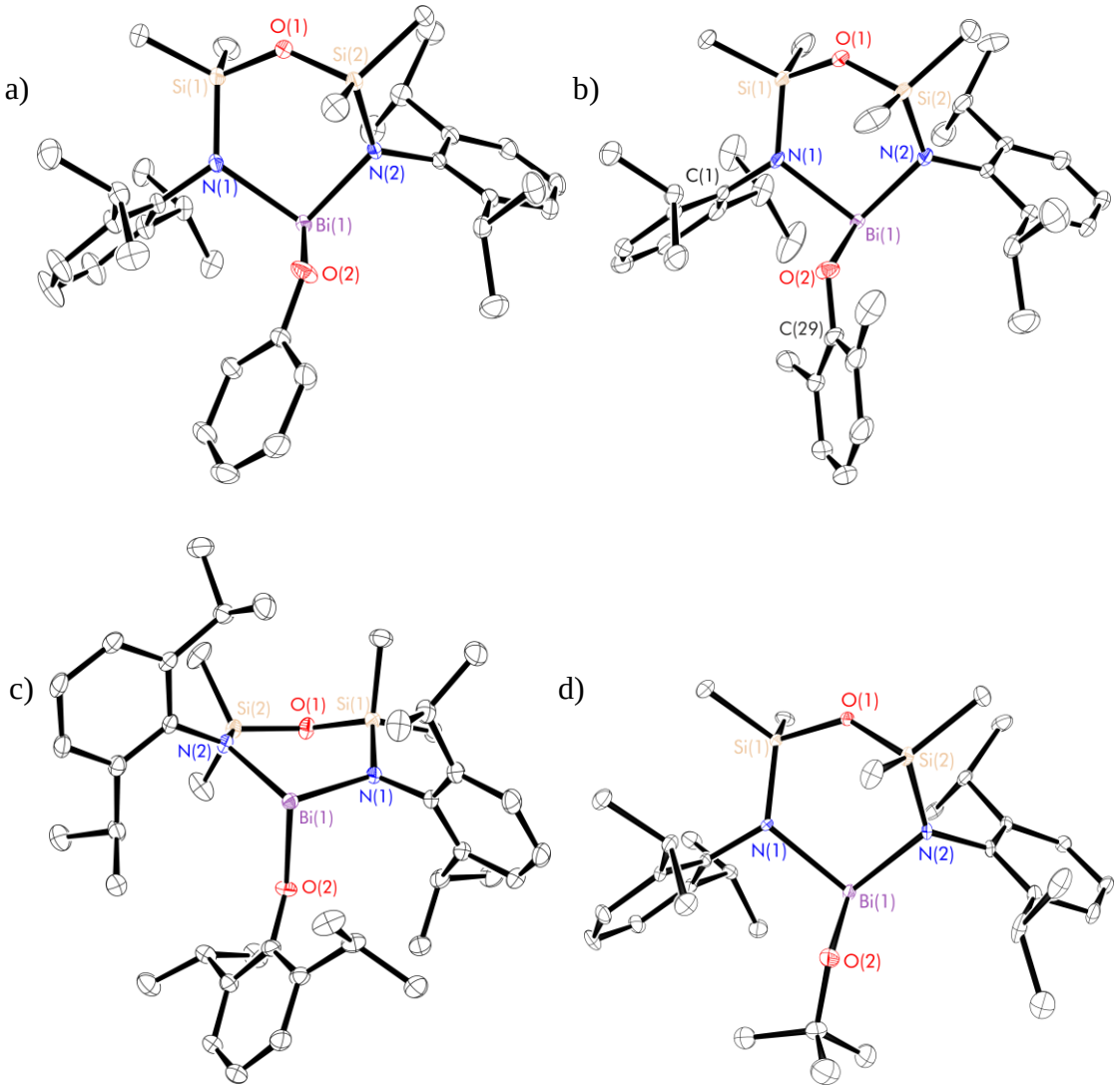


Figure 2.4 Thermal displacement ellipsoid drawings (30%) of asymmetric units of a) (NON^{Dipp})Bi(OC$_6$H$_5$) (**1**), b) (NON^{Dipp})Bi(O-2,6-Me-C$_6$H$_3$) (**2**), c) (NON^{Dipp})Bi(O-2,6-^{i}Pr-C$_6$H$_3$) (**3**), d) (NON^{Dipp})Bi(O^{t}Bu) (**4**). All hydrogen atoms have been omitted for clarity.

In all cases, a three-coordinate pyramidal bismuth centre is chelated by the ancillary [NON^{Dipp}]-ligand in a κ^2-*N*,*N'*-bidentate bonding mode. The degree of pyramidalisation, defined by the sum of angles at bismuth (Σ(∠Bi)), decreases in parallel with an increase in steric hindrance at the metal centre (Σ(∠Bi) = 285.03° (**1**) *vs*. 290.96° (**3**)). This coincides with an increase in N-Bi-N bite angles (94.32(6)° (**1**) *vs*. 97.34(7)° (**3**)).

The Bi-N distances occupy a relatively narrow distribution (Bi(1)-N(1) and Bi(1)-N(2) = 2.1314(15) and 2.1700(14) Å (**1**), 2.1541(1) and 2.1357(1) Å (**2**), 2.1497(17) and 2.1436(17) Å (**3**), 2.181(8) and 2.166(8) Å (**4**)). These distances are relatively short compared to those in the previously reported di(amido)siloxane bismuth TEMPO complex (NON^{Dipp})Bi(OTEMP) (**Table 2.1**).[38] As expected, the Bi-O distances in **1**–**3** increase with increasing steric bulk of the aryloxide substituent (2.1269(14) Å (**1**) ≈ 2.1282(1) Å (**2**) < 2.1358(15) Å (**3**)). These bond lengths are longer than those reported for homoleptic bismuth aryloxides Bi(O-2,6-Me-C_6H_3)$_3$ and Bi(O-2,6-^{i}Pr-C_6H_3)$_3$ (2.090(1)–2.097(9) and 2.069(2)–2.112(2) Å, respectively),[39, 40] yet comparable to the corresponding distance in (NON^{Dipp})Bi(OTEMP) (2.129(3) Å). In comparison to the Bi-O distances of **1**–**3**, the analogous distance in **4** is significantly shorter (Bi(1)-O(2) = 2.096(8) Å), consistent with an increase in the donation of electron density from the *tert*-butoxide substituent. This bond length falls within the range of those reported for other Bi-O^{t}Bu moieties (2.037(6)–2.215 Å).[41, 42] The six-membered BiN_2Si_2O metallacycles adopt a twist-boat conformation, defined by large N(1)-Si(1)-Si(2)-N(2) torsion angles (32.38(9)–43.67(8)°). No significant bonding interaction is observed between the bismuth centre and the oxygen atom in the backbone, as the corresponding distances in complexes **1**–**4** (3.504(1)–3.625(1) Å) lie outside the

sum of covalent radii for Bi and O atoms ($\sum r_{cov}$(Bi,O) = 2.16 Å), albeit within the sum of their van der Waals radii ($\sum r_{vdW}$(Bi,O) = 3.90 Å).[43]

Table 2.1 Selected experimental metrical parameters (bond lengths (Å) and angles (°)) for (NON^{Dipp})Bi(OC$_6$H$_5$) (**1**), (NON^{Dipp})Bi(O-2,6-Me-C$_6$H$_3$) (**2**), (NON^{Dipp})Bi(O-2,6-^{i}Pr-C$_6$H$_3$) (**3**), (NON^{Dipp})Bi(O^{t}Bu) (**4**), and related (NON^{Dipp})Bi(OTEMP) (= (L)BiX).[38] Estimated standard deviations shown in brackets.

	1	**2**	**3**	**4**	(L)BiX[38]
Space group	$P\bar{1}$	$P2_1/n$	$P\bar{1}$	$P2_1/c$	$P\bar{1}$
Bi(1)-N(1)	2.1314(15)	2.1541(1)	2.1497(17)	2.181(8)	2.192(4)
Bi(1)-N(2)	2.1700(14)	2.1357(1)	2.1436(17)	2.166(8)	2.190(4)
Bi(1)-O(2)	2.1269(14)	2.1282(1)	2.1358(15)	2.096(8)	2.129(3)
Bi(1)-O(1)	3.625(1)	3.599(2)	3.504(1)	3.568(7)	3.655(3)
N(1)-Bi(1)-N(2)	94.32(6)	96.79(1)	97.34(7)	96.40(3)	93.83(14)
N(1)-Si(1)-Si(2)-N(2)	43.67(8)	41.4(1)	32.38(9)	41.7(4)	43.0(2)
Σ(∠Bi))	285.03	286.55	290.96	289.8	299.4

2.4.1.3 *G*-Parameter analysis

The *G*-parameter is used as a measure of the encumbrance of the metal centre resulting from steric shielding imparted by ligands. It is derived from the solid angle (Ω), which represents the area of the shadow that each ligand casts on the total sphere around the molecule, assuming a point light source located at the metal centre. The *G*-parameter is calculated as a percentage of the area of this shadow relative to the total coordination

sphere.[44] Analysis of the *G*-parameter is performed using the Cartesian coordinates of a complex, typically with a normalised metal-ligand distance of 2.28 Å. Steric shielding in compounds **1**–**4** was quantified by comparing their *G*-parameter values (**Figure 2.5**).

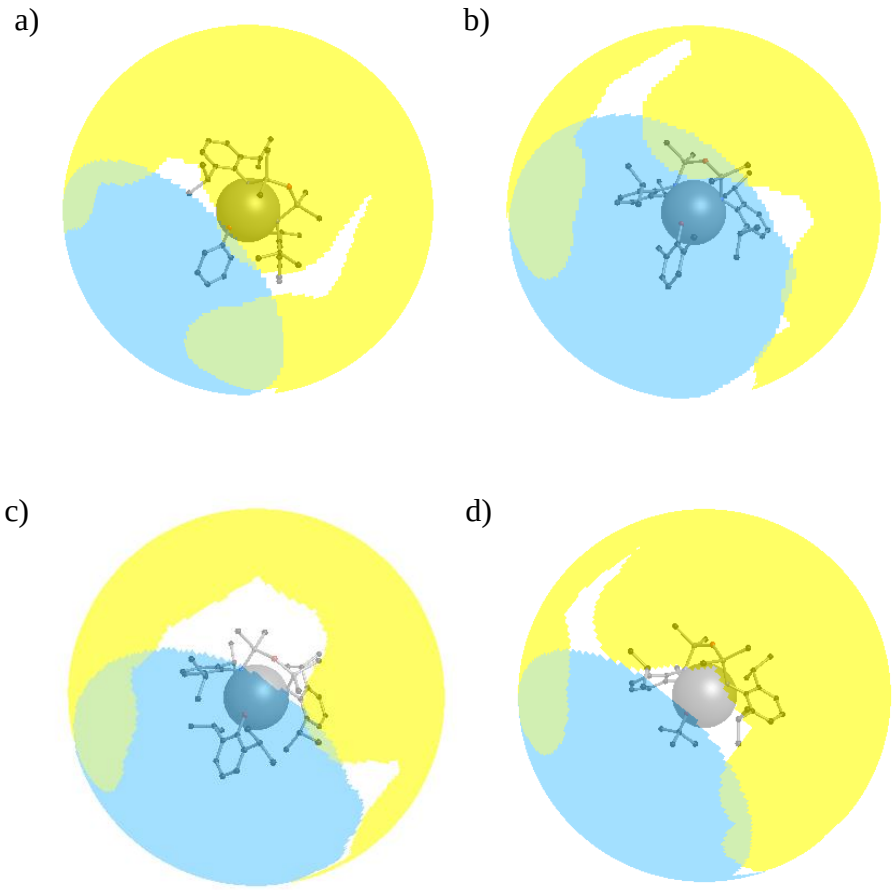


Figure 2.5 Graphical representation of the *G*-parameter in **1**–**4** (a–d), demonstrating the percentage of the complex sphere shielded by ligands [NON^{Dipp}] (yellow) and OR' (blue).

An increase in the steric bulk of the OR' substituents resulted in a modest enhancement of the shielding effect: **1** ($G_{2.28}$ = 73.65%) < **4** ($G_{2.28}$ = 77.92%) ≈ **2** ($G_{2.28}$ = 78.76%) < **3** ($G_{2.28}$ = 80.34%). This trend correlates with decreasing pyramidalisation around the bismuth centre across the series.

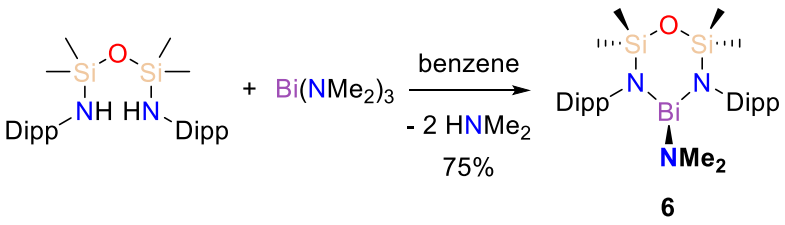
Table 2.2 Selected steric parameters for (NON^{Dipp})Bi(OC$_6$H$_5$) (**1**), (NON^{Dipp})Bi(O-2,6-Me-C$_6$H$_3$) (**2**), (NON^{Dipp})Bi(O-2,6-^{i}Pr-C$_6$H$_3$) (**3**), and (NON^{Dipp})Bi(O^{t}Bu) (**4**).[a]

	1	**2**	**3**	**4**
Ω(NON^{Dipp}) (sr)	7.44	7.53	7.44	7.54
Ω(OR') (sr)	2.21	2.65	2.91	2.62
G(NON^{Dipp}) (%)	59.21	59.89	59.23	59.98
G(OR') (%)	17.60	21.06	23.16	20.84
G(M) (%)	73.65	78.76	80.34	77.92

[a]Ligand solid angle (*Ω*), the percentage of the metal M sphere shielded by the ligand (*G*), and the percentage of the metal M sphere shielded by all ligands (*G*(M)).

2.4.2 Synthesis of a bismuth amide complex

A protonolysis route using (NON^{Dipp})H$_2$ and Bi(NMe$_2$)$_3$ was pursued to synthesise a di(amido)siloxane bismuth amide complex, as the volatile HNMe$_2$ by-product can be readily removed from the benzene solution. The reaction was conducted in the absence of light, utilising freshly sublimed Bi(NMe$_2$)$_3$ due to its sensitivity to both light and temperature. The amide compound (NON^{Dipp})Bi(NMe$_2$) (**6**) was isolated as a moderately light and temperature sensitive yellow powder in 75% yield (**Scheme 2.4**).



Scheme 2.4 Synthesis of (NON^{Dipp})Bi(NMe$_2$) (**6**).

An analogous reaction between the (NON$^{t Bu}$)H$_2$ pro-ligand and Bi(NMe$_2$)$_3$ did not proceed to completion even after heating to 70 °C for 48 hours; instead, slow degradation

of $Bi(NMe_2)_3$ was observed. It is possible that the presence of more electron-donating *tert*-butyl groups reduces the acidity of the N*H* protons, rendering them less reactive towards $Bi(NMe_2)_3$ (pK_a: 10.68 (*tert*-butylamine) *vs*. 4.25 (2,6-di*iso*propylaniline)).[45, 46]

2.4.2.1 NMR spectroscopic analysis

The ^{1}H NMR spectrum of **6** is indicative of a C_s-symmetric species (**Figure 2.6**), consistent with the solution-state structures of bismuth aryloxide and alkoxide compounds **1**–**5**.

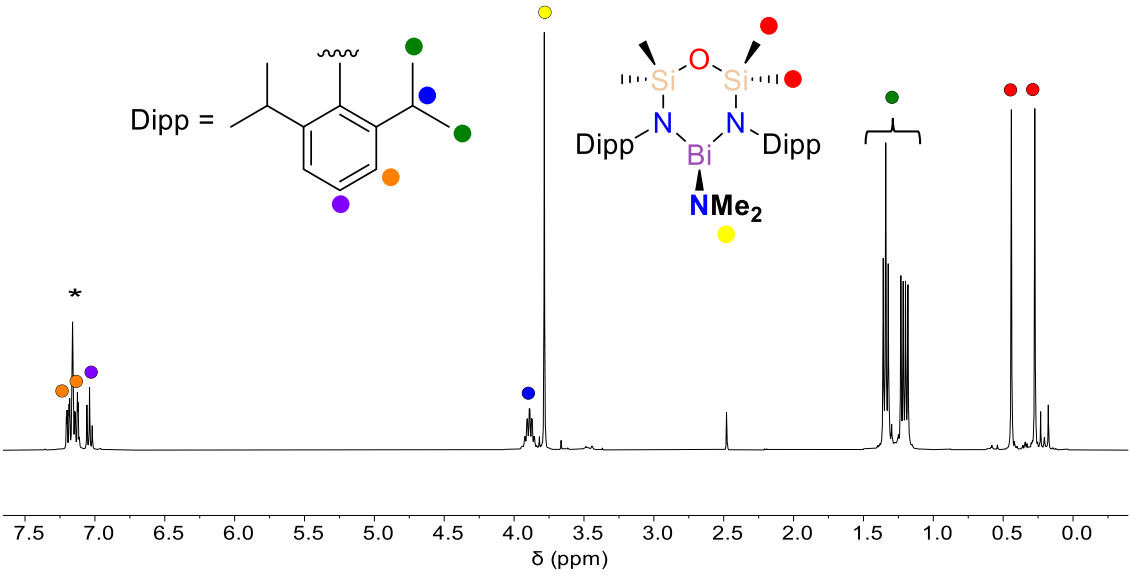


Figure 2.6 ^{1}H NMR spectrum (*benzene-d_6, 400 MHz, 298 K) of (NON^{Dipp})$Bi(NMe_2)$ (**6**).

The chelation of the [NON^{Dipp}]-ligand around the pyramidal bismuth centre is evidenced by the presence of two singlets at δ 0.44 and 0.27 ppm corresponding to two inequivalent Si*Me*$_2$ proton environments. The asymmetry of the two faces of the [NON^{Dipp}]-ligand is also supported by the presence of four doublets between δ 1.35–1.19 ppm assigned to the CH*Me*$_2$ protons. The C*H*Me$_2$ proton resonances are represented by two overlapping septets at δ 3.89 ppm, corresponding to two inequivalent *C*HMe$_2$ carbon atoms, located

at δ 27.7 and 27.5 ppm in the $^{13}C\{^{1}H\}$ NMR spectrum. A singlet at δ 3.78 ppm defines six chemically equivalent N*Me*$_2$ protons.

2.4.2.2 X-ray crystallographic analysis

Slow evaporation of a hexane solution at 23 °C afforded single crystals of complex **6**, solved in the monoclinic space group, *P*2$_1$/*c* (**Figure 2.7**, **Table 2.3**).

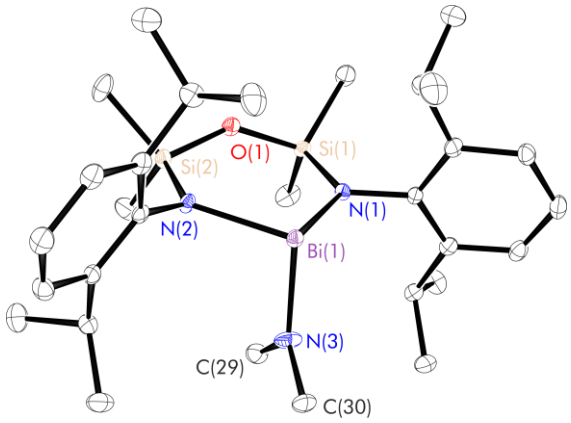


Figure 2.7 Thermal displacement ellipsoid drawing (30%) of the asymmetric unit of (NON^{Dipp})Bi(NMe$_2$) (**6**). All hydrogen atoms have been omitted for clarity.

The solid-state structure of **6** reveals a trigonal pyramidal bismuth centre (Σ(∠Bi) = 297.44°), chelated by the [NON^{Dipp}]-ligand in a κ^2-*N*,*N'*-bidentate bonding mode. In contrast to the solid-state structures of **1**–**4**, the BiN$_2$Si$_2$O metallacycle is in a half-chair conformation, characterised by a small torsion angle (N(1)-Si(1)-Si(2)-N(2) = 0.9(2)°), with the siloxane O(1) atom positioned 0.426 Å outside of the Si$_2$N$_2$Bi mean plane. The Bi-N bond length of the NMe$_2$ moiety (Bi(1)-N(3) = 2.107(4) Å) compares well with the Bi-N distances reported for related bismuth dimethylamide compounds (2.050(14)–2.189(18) Å).[47-49] This bond length is considerably shorter than the Bi-N bond distances associated with the [NON^{Dipp}]-ligand

(2.184(3) and 2.191(3) Å), indicating an increased donation of electron density from the N-centred lone pair into the vacant σ*(Bi-N) orbital.

Table 2.3 Selected experimental metrical parameters (bond lengths (Å) and angles (°)) for (NON^{Dipp})Bi(NMe_2) (**6**). Estimated standard deviations shown in brackets.

Space group	$P2_1/c$
Bi(1)-N(1)	2.184(3)
Bi(1)-N(2)	2.191(3)
Bi(1)-N(3)	2.107(4)
Bi(1)-O(1)	3.516(3)
N(1)-Bi(1)-N(2)	94.32(6)
N(1)-Si(1)-Si(2)-N(2)	0.9(2)
Σ(∠Bi))	297.44

2.5 Conclusions

The di(amido)siloxane ligand (NON^R)H_2 (R = Dipp, ^{t}Bu) was employed as a platform to develop a new family of bismuth complexes. The salt-metathesis route using the dilithium salts of the ligands and $BiCl_3$ resulted in the formation of five different bismuth aryloxide and alkoxide compounds (NON^R)Bi(OR') (R = Dipp, R' = OC_6H_5 (**1**), O-2,6-Me-C_6H_3 (**2**), O-2,6-^{i}Pr-C_6H_3 (**3**), ^{t}Bu (**4**); R = ^{t}Bu, R' = O-2,6-Me-C_6H_3 (**5**)). These complexes were characterised by multinuclear NMR spectroscopy, and in most cases, single-crystal X-ray diffraction and elemental analysis. The solid-state structures of compounds **1**–**4** revealed a three-coordinate pyramidal bismuth centre bound to the [NON^{Dipp}]-ligand in a κ^2-*N*,*N'*-bidentate bonding mode. An increase in the steric bulk of

the OR' substituents led to reduced pyramidalisation at the bismuth centre, alongside enhanced metal surface shielding.

Di(amido)siloxane bismuth amide (NON^{Dipp})Bi(NMe_2) (**6**) was synthesised *via* a protonolysis reaction between the (NON^{Dipp})H_2 pro-ligand and Bi(NMe_2)$_3$. Its solid-state structure was consistent with the chelation of the [NON^{Dipp}]-ligand to the pyramidal bismuth centre in a κ^2-*N*,*N'*-bidentate binding mode.

The catalytic capability of compounds **1**–**6** to act as initiators in the ROP of cyclic esters is discussed in **Chapters Three** and **Four**, while **Chapter Five** explores the reactivity of compound **6** with a range of electrophilic substrates.

2.6 References

1. P. de Marcillac, N. Coron, G. Dambier, J. Leblanc and J.-P. Moalic, *Nature*, 2003, **422**, 876-878.
2. R. Mohan, *Nat. Chem.*, 2010, **2**, 336-336.
3. G. G. Briand and N. Burford, *Chem Rev*, 1999, **99**, 2601-2658.
4. P. Xia, Y. Song, Y.-Z. Liu, M.-X. Long, C. Yang, X.-Y. Zhang and T. Zhang, *J. Mater. Chem. C.*, 2024, **12**, 1609-1624.
5. A. R. Rajamani, S. Jothi, M. Datta and M. Rangarajan, *J. Electrochem. Soc.*, 2018, **165**, D50-D57.
6. P. Pyykko, *Chem. Rev.*, 1988, **88**, 563-594.
7. S. J. Davies, N. A. Compton, G. Huttner, L. Zsolnai and S. E. Garner, *Chem. Ber.*, 1991, **124**, 2731-2738.
8. W. Frank, V. Reiland and G. J. Reiß, *Angew. Chem. Int. Ed.*, 1998, **37**, 2983-2985.
9. S. Wallenhauer and K. Seppelt, *Angew. Chem., Int. Ed. Engl.*, 1994, **33**, 976-978.
10. A. Gagnon, J. Dansereau and A. Le Roch, *Synthesis*, 2017, **49**, 1707-1745.
11. C. Silvestru, H. J. Breunig and H. Althaus, *Chem. Rev.*, 1999, **99**, 3277-3328.
12. K. H. Whitmire, in *Encyclopedia of Inorganic and Bioinorganic Chemistry*, John Wiley & Sons, Ltd, 2013, pp. 1-32.
13. R. A. Wheeler and P. N. V. P. Kumar, *J. Am. Chem. Soc.*, 1992, **114**, 4776-4784.
14. R. Pujales-Paradela, A. Rodríguez-Rodríguez, A. Gayoso-Padula, I. Brandariz, L. Valencia, D. Esteban-Gómez and C. Platas-Iglesias, *Dalton Trans.*, 2018, **47**, 13830-13842.

15. Y. Bai, W. Chen, J. Li and C. Cui, *Coord. Chem. Rev.*, 2019, **383**, 132-154.

16. H. Bürger and K. Wiegel, *Z. Anorg. Allg. Chem.*, 1976, **419**, 157-162.

17. K. Wiegel and H. Bürger, *Z. Anorg. Allg. Chem.*, 1976, **426**, 301-308.

18. U. Wannagat and F. Rabet, *J. Inorg. Nucl. Chem.*, 1970, **6**, 155-162.

19. A. J. Elias, H. W. Roesky, W. T. Robinson and G. M. Sheldrick, *J. Chem. Soc., Dalton Trans.*, 1993, 495-500.

20. N. A. H. Male, M. Thornton-Pett and M. Bochmann, *J. Chem. Soc., Dalton Trans.*, 1997, 2487-2494.

21. R. J. Schwamm, M. D. Anker, M. Lein and M. P. Coles, *Angew. Chem. Int. Ed.*, 2019, **58**, 1489-1493.

22. R. J. Schwamm, M. D. Anker, M. Lein, M. P. Coles and C. M. Fitchett, *Angew. Chem. Int. Ed.*, 2018, **57**, 5885-5887.

23. R. J. Schwamm, C. A. von Randow, A. Mouchfiq, M. J. Evans, M. P. Coles and J. Robin Fulton, *Eur. J. Inorg. Chem.*, 2021, **2021**, 3466-3473.

24. R. J. Schwamm and M. P. Coles, *Chem. Eur. J.*, 2019, **25**, 14183-14191.

25. R. J. Schwamm, J. R. Harmer, M. Lein, C. M. Fitchett, S. Granville and M. P. Coles, *Angew. Chem. Int. Ed.*, 2015, **54**, 10630-10633.

26. M. J. Evans, M. D. Anker, A. Mouchfiq, M. Lein and J. R. Fulton, *Chem. Eur. J.*, 2020, **26**, 2606-2609.

27. E. W. Y. Wong, A. K. Das, M. J. Katz, Y. Nishimura, R. J. Batchelor, M. Onishi and D. B. Leznoff, *Inorg. Chim. Acta*, 2006, **359**, 2826-2834.

28. K. C. Jantunen, F. Haftbaradaran, M. J. Katz, R. J. Batchelor, G. Schatte and D. B. Leznoff, *Dalton Trans.*, 2005, 3083-3091.

29. K. C. Jantunen, R. J. Batchelor and D. B. Leznoff, *Organometallics*, 2004, **23**, 2186-2193.

30. A. K. Das, Z. Moatazedi, G. Mund, A. J. Bennet, R. J. Batchelor and D. B. Leznoff, *Inorg. Chem.*, 2007, **46**, 366-368.

31. G. Mund, D. Vidovic, R. J. Batchelor, J. F. Britten, R. D. Sharma, C. H. W. Jones and D. B. Leznoff, *Chem. Eur. J.*, 2003, **9**, 4757-4763.

32. E. Svensson Grape, V. Rooth, M. Nero, T. Willhammar and A. K. Inge, *Nat. Commun.*, 2022, **13**, 1984.

33. P. Šimon, F. de Proft, R. Jambor, A. Růžička and L. Dostál, *Angew. Chem. Int. Ed.*, 2010, **49**, 5468-5471.

34. M. B. Kindervater, K. M. Marczenko, U. Werner-Zwanziger and S. S. Chitnis, *Angew. Chem. Int. Ed.*, 2019, **58**, 7850-7855.

35. R. J. Schwamm, M. Lein, M. P. Coles and C. M. Fitchett, *Angew. Chem. Int. Ed.*, 2016, **55**, 14798-14801.

36. R. J. Schwamm, M. Lein, M. P. Coles and C. M. Fitchett, *J. Am. Chem. Soc.*, 2017, **139**, 16490-16493.

37. D. B. Leznoff, G. Mund, K. C. Jantunen, P. H. Bhatia, A. J. Gabert and R. J. Batchelor, *J. Nucl. Sci. Technol.*, 2002, **39**, 406-409.

38. R. J. Schwamm, M. Lein, M. P. Coles and C. M. Fitchett, *Chem. Commun.*, 2018, **54**, 916-919.

39. W. J. Evans, J. H. Hain and J. W. Ziller, *J. Chem. Soc., Chem. Commun.*, 1989, 1628-1629.

40. X. Kou, X. Wang, D. Mendoza-Espinosa, L. N. Zakharov, A. L. Rheingold, W. H. Watson, K. A. Brien, L. K. Jayarathna and T. A. Hanna, *Inorg. Chem.*, 2009, **48**, 11002-11016.

41. S. Roggan, C. Limberg, B. Ziemer and M. Brandt, *Angew. Chem. Int. Ed.*, 2004, **43**, 2846-2849.

42. P. C. Andrews, P. C. Junk, I. Nuzhnaya and D. T. Thielemann, *Inorg. Chem.*, 2012, **51**, 751-753.

43. N. H.-W. Wiberg, *Lehrbuch der Anorganischen Chemie*, De Gruyter Berlin, 1985.

44. I. A. Guzei and M. Wendt, *Dalton Trans.*, 2006, 3991-3999.

45. S. Zhang, *J. Comput. Chem.*, 2012, **33**, 2469-2482.

46. R. A. Davies, N. S. Chong and B. G. Ooi, *Opt. Photon. J.*, 2013, **3**, 13-23.

47. H. Dengel and C. Lichtenberg, *Chem. Eur. J.*, 2016, **22**, 18465-18475.

48. B. Nekoueishahraki, S. P. Sarish, H. W. Roesky, D. Stern, C. Schulzke and D. Stalke, *Angew. Chem. Int. Ed.*, 2009, **48**, 4517-4520.

49. W. Clegg, N. A. Compton, R. J. Errington, G. A. Fisher, M. E. Green, D. C. R. Hockless and N. C. Norman, *Inorg. Chem.*, 1991, **30**, 4680-4682.

Chapter 3

Ring-opening polymerisation of cyclic esters using di(amido)siloxane bismuth aryloxide and alkoxide initiators

3.1 Introduction

Bismuth(III) compounds exhibit favourable characteristics as ROP initiators, including a large ionic radius, tunable Lewis acidity of the bismuth centre, and the lability of Bi-X bonds. However, they have been less studied for the polymerisation of cyclic esters compared to lighter transition metal or main group systems.

Inorganic bismuth(III) derivatives, previously employed as initiators in the polymerisation of lactide or the copolymerisation of lactide and lactone monomers, include bismuth alkoxide compounds ($Bi(OR)_3$: 2,3-dimethyl-2-butoxide and *tert*-butoxide) and bismuth alkanoates ($Bi(COOR)_3$: acetate, *n*-hexanoate, and octanoate).[1-4] However, despite their low cost and high robustness, these initiators have typically suffered from the lack of polymerisation stereocontrol and limitations in the molecular weights of the resulting polymers.

Using Pepto-Bismol®, a commercial drug containing bismuth subsalicylate as an active ingredient (**Figure 3.1a**), Chisholm and co-workers reported comparable lactide polymerisation rates to those achieved using the more toxic $Sn(Oct)_2$.[5] However, the poor solubility of the initiator, attributed to its polymeric structure, rendered the ROP activity dependent on surface bismuth active sites.

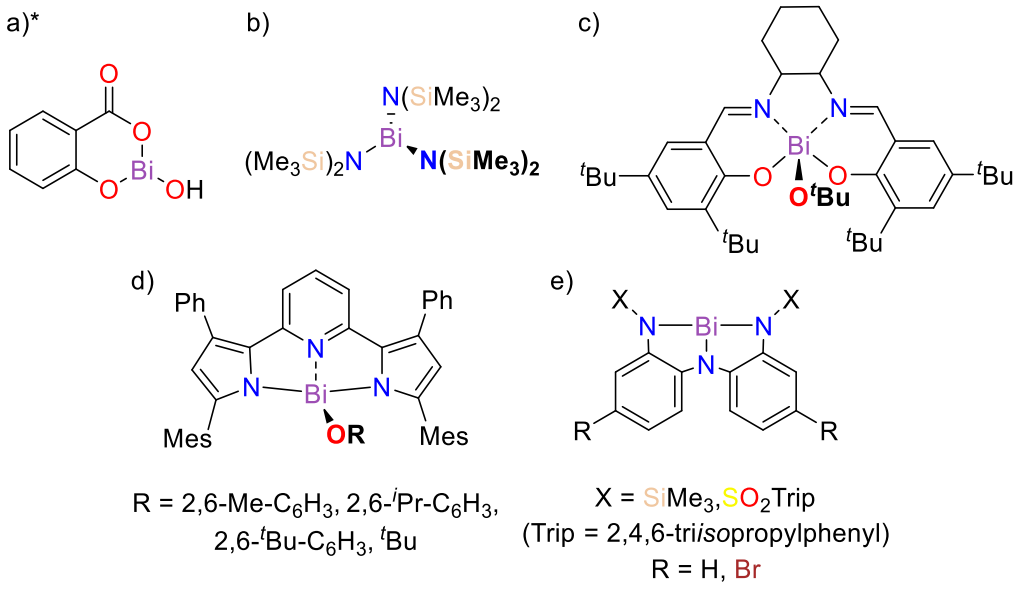


Figure 3.1 Selected examples of bismuth(III) initiators for the ring-opening polymerisation of cyclic esters. * represents an extended polymeric structure.

A limited number of well-defined single-site organobismuth(III) initiators for the polymerisation of lactide have been reported, demonstrating varying degrees of initiator activity and polymerisation control. Bismuth *tris*[*bis*(trimethylsilyl)amide] $Bi\{N(SiMe_3)_2\}_3$ (**Figure 3.1b**), described by Visseaux and co-workers, was found to be a more active initiator for the ROP of *rac*-lactide compared to $Sn(Oct)_2$ under identical reaction conditions.[6] Although the polymerisation proceeded with relatively poor control ($1.85 \leq Đ_M \leq 2.32$), the molecular weight distributions of polymers were significantly improved in the presence of BnOH ($1.28 \leq Đ_M \leq 1.73$), ascribed to the more efficient initiation by the Bi-O *vs*. Bi-N moiety.

Chisholm and co-workers studied a bismuth *tert*-butoxide initiator supported by a salen ligand (**Figure 3.1c**), which combined high activity ($k_p = 9.2 \times 10^{-2}$ M^{-1} s^{-1}, 25 °C) and high levels of heteroselectivity ($P_r = 0.87$) in the ROP of *rac*-lactide.[7] The polymerisation rate proved to be significantly higher with respect to its aluminium counterpart ($k_p = 9.02 \times 10^{-3}$ M^{-1} s^{-1}, 70 °C).

A mechanistic study on bismuth pyridine dipyrrolide pincer initiators ($L^{Mes,Ph}$)BiX was reported by Turner and co-workers (**Figure 3.1d**), with the aim of elucidating the origin of the induction periods observed in *L*-lactide polymerisation.[8] Using a bismuth (*R*)-*tert*-butyl lactate derivative as a model catalytic ROP intermediate, the polymerisation proceeded without an induction period, unlike in the presence of the parent *tert*-butoxide initiator. The authors suggested that the ring-opening of the first lactide unit was rate-limiting and therefore responsible for slow initiation.

Recently, Chitnis and co-workers introduced a new family of planar bismuth triamide complexes (**Figure 3.1e**), exhibiting activity towards the ROP of both *rac*-lactide and ε-caprolactone (ε-CL) monomers.[9] Similarly to the observations made for other main group salen ROP initiators (**Chapter One**, **Section 1.4**), an increase in initiator activity was shown to correlate with the reduced steric bulk of the triamide ligand and the enhanced electrophilicity of the bismuth centre. However, the rates of polymerisation remained relatively low, requiring 16–40 hours at 80 °C to reach near-completion.

3.2 Synopsis

Chapter Three discusses the application of di(amido)siloxane bismuth aryloxide and alkoxide complexes **1**–**5** as initiators for the ROP of lactide and ε-caprolactone monomers (**Figure 3.2**). A new family of compounds extends the range of previously reported

three-coordinate bismuth(III) initiators, offering opportunities for optimised polymerisation performance through facile ligand modifications.

The rates and control of polymerisation have been studied with respect to the initiator type, initiator concentration, monomer stereochemistry, and reaction temperature. The isolated polymers have been characterised by NMR spectroscopy, mass spectrometry, and GPC analysis.

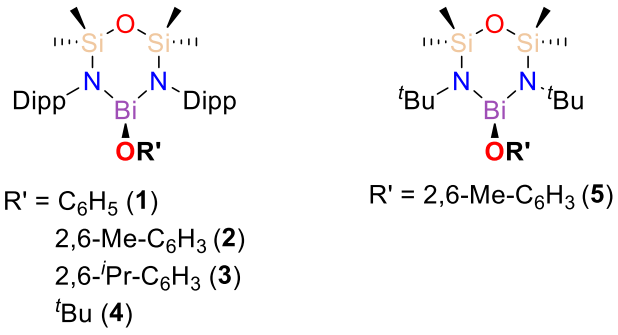


Figure 3.2 Di(amido)siloxane bismuth compounds **1**–**5** investigated as ROP initiators in **Chapter Three**.

3.3 Lactide polymerisation studies using bismuth aryloxide and alkoxide initiators

Polymerisations were conducted in J. Young's tap NMR spectroscopy tubes with an initial lactide monomer concentration ($[LA]_0$) of 0.5 M in 0.6 mL of benzene-d_6. The reactions were monitored by ^{1}H NMR spectroscopy and halted by cooling in an ice bath, followed by quenching with wet pentane.

3.3.1 Initiating group variation

Bismuth complexes supported by the [NON^{Dipp}]-ligand framework, (NON^{Dipp})Bi(OR') with R' = OC_6H_5 (**1**), O-2,6-Me-C_6H_3 (**2**), O-2,6-^{i}Pr-C_6H_3 (**3**), ^{t}Bu (**4**), were initally tested as initiators in the ROP of *L*-lactide (**Figure 3.3, Table 3.1**).

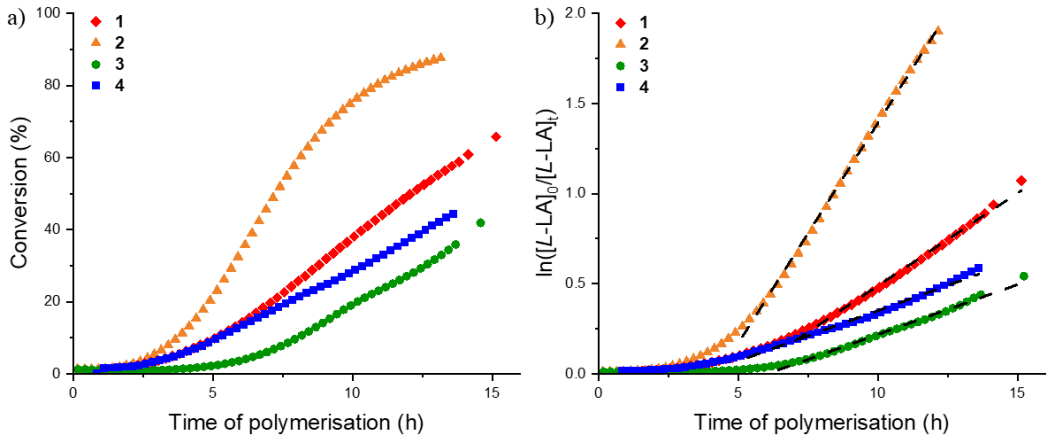


Figure 3.3 a) Plots of percentage conversion *vs*. polymerisation time for *L*-lactide polymerisation. b) Plots of ln([*L*-LA]$_0$/[*L*-LA]$_t$) *vs*. polymerisation time for *L*-lactide polymerisation. Red rhombi: (NON^{Dipp})Bi(OC$_6$H$_5$) (**1**), k_{obs} = 0.100 ± 0.002 h^{-1}, R^2 = 0.993; orange triangles: (NON^{Dipp})Bi(O-2,6-Me-C$_6$H$_3$) (**2**), k_{obs} = 0.246 ± 0.011 h^{-1}, R^2 = 0.998; green circles: (NON^{Dipp})Bi(O-2,6-^{i}Pr-C$_6$H$_3$) (**3**), k_{obs} = 0.055 ± 0.001 h^{-1}, R^2 = 0.992; blue squares: (NON^{Dipp})Bi(O^{t}Bu) (**4**), k_{obs} = 0.056 ± 0.001 h^{-1}, R^2 = 0.990. Polymerisation conditions: benzene-d_6, 70 °C, [*L*-LA]$_0$/[Bi]$_0$ = 50:1, and [*L*-LA]$_0$ = 0.5 M.

All polymerisations displayed induction periods for up to approximately 4 hours. The longest induction period observed using **3** correlates with its largest steric shielding effect ($G_{2.28}$ = 80.34%) relative to the other compounds in the series ($G_{2.28}$ = 73.65–78.76%) (**Chapter Two**, **Section 2.4.1.3**). This suggests that the increased steric congestion at the active site may supress its accessibility to the incoming lactide monomer as well as hinder monomer ring-opening. The steric influence of the initiating group on ROP initiation efficiency has also been demonstrated in other main group alkoxide initiators, with a decrease in steric bulk shown to result in lower energy pathways for initiation in terms of both lactide coordination and its acyl-oxygen bond cleavage steps (see **Section 3.3.7** for further discussion).[10]

The presence of an induction period in the polymerisation of lactide has been commonly observed using initiators with main group, transition, and rare-earth metals. A

combination of factors is known to determine initiation efficiency, including the steric, electronic, and chelating effects of the initiating system. For example, slow initiation observed for several homoleptic aluminium and yttrium alkoxide initiators has been attributed to the aggregation of active species.[11-13] The degree of association has been shown to depend on both the steric and electronic profile of the initiator as well as polymerisation conditions, including temperature and solvent polarity. Alternatively, the induction period in the presence of a dinuclear copper diiminopyrrole system, described by Schaper and co-workers, was found to correlate with the strength of the coordination of the pyridine functionality on the ligand backbone to the copper centre.[14] As a result, ligand rearrangement was required prior to monomer binding. Turner and co-workers suggested that the induction period observed for their bismuth pincer initiators was due to the slow insertion of the first lactide monomer into the Bi-O bond (i.e. $k_{LA_1} << k_{LA_2} < k_p$; **Section 3.1**).[8] Additionally, Gibson and co-workers discussed the implications of the tin(II)-centred lone pair of electrons on the induction period displayed in the ROP of *rac*-lactide using tin BDI initiators.[15] The energy profile of the insertion process using (BDI)Sn(OMe) was proposed to depend on the repulsive interactions between the tin-based lone pair and the carbonyl oxygen on either the incoming lactide monomer or the ring-opened monomer unit in the growing polymer chain. Following a rapid insertion of the first monomer, the second insertion step was found to be less favourable, thus responsible for the observed induction periods. Subsequently, these interactions became less significant in the growing polymer chain.

In the case of **1**–**4**, after the observed induction period, all polymerisations followed a first-order dependence on *L*-lactide concentration, as evidenced by the linear plots of $\ln([L\text{-LA}]_0/[L\text{-LA}]_t)$ *vs*. polymerisation time (**Figure 3.3b**). These results are consistent

with the presence of one propagating polymer chain per active site.[16] To determine the observed *pseudo* first-order rate constant (k_{obs}) for each initiator, the gradients of the corresponding plots were measured in the propagation regime (see **Figure 3.3b** as a representative example). Compound **2** displayed the highest activity, followed by **1**, whereas the polymerisation rates for **3** and **4** were two-fold lower (0.246 ± 0.011 h^{-1} (**2**) > 0.100 ± 0.002 h^{-1} (**1**) > 0.056 ± 0.001 h^{-1} (**4**) ≈ 0.055 ± 0.001 h^{-1} (**3**)). Evidently, the polymerisation activity was not solely determined by the steric bulk of the OR' group alone, suggesting a contribution from both steric and electronic effects.

Table 3.1 ROP of *L*-lactide using (NON^{Dipp})Bi(OR') (R' = OC_6H_5 (**1**), O-2,6-Me-C_6H_3 (**2**), O-2,6-^{i}Pr-C_6H_3 (**3**), ^{t}Bu (**4**)).[a]

Initiator	Conv.[b] (%)	k_{obs}[c] (h^{-1})	R^{2}[c]	$M_{n,GPC}$[d] (g mol^{-1})	$M_{n,theo}$[e] (g mol^{-1})	M_w/M_n[d]
1	76	0.100 ± 0.002	0.993	5 564	5 543	1.85
2	88	0.246 ± 0.011	0.998	5 346	6 458	1.33
3	82	0.055 ± 0.001	0.992	5 335	6 082	1.51
4	91	0.056 ± 0.001	0.990	7 705	6 626	1.33

[a]Polymerisation conditions: benzene-d_6, 70 °C, [*L*-LA]$_0$/[Bi]$_0$ = 50:1, [*L*-LA]$_0$ = 0.5 M. [b]Measured by ^{1}H NMR spectroscopy; averaged over two repeats. [c]Obtained from plots of ln([*L*-LA]$_0$/[*L*-LA]$_t$) *vs.* polymerisation time. [d]Determined by GPC analysis calibrated with PS standards in THF with the appropriate Mark-Houwink corrections.[17] [e]Theoretical M_n for PLA = (conv.(%) × [*L*-LA]$_0$/[Bi]$_0$) × 144.13 + (M_w of end groups).

Initiators **1**–**4** demonstrated varying degrees of polymerisation control (**Table 3.1**). When **2**–**4** were used, the experimental molecular weights ($M_{n,GPC}$) of the isolated PLLAs were in a relatively good agreement with the theoretical values ($M_{n,theo}$), and intermediate molecular weight distributions ($Đ_M$ = 1.33–1.51) were recorded (**Figure 3.4**). In contrast, compound **1** resulted in the broadest molecular weight distribution in the series

($Đ_M$ = 1.85), implying a relatively high degree of inter- and/or intramolecular transesterification occurring. In addition, ^{1}H NMR spectroscopic analysis of the polymerisation in the presence of **1** revealed increasing relative amounts of the (NON^{Dipp})H$_2$ pro-ligand during the course of the reaction. The observed partial deactivation of the initiator is a likely contributing factor to poor polymerisation control.

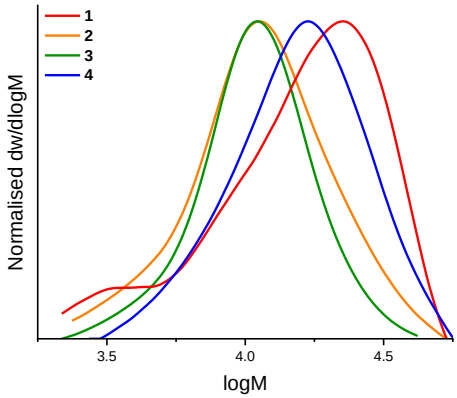


Figure 3.4 GPC plots of the PLLAs produced using **1** (red, M_n = 5 564 g mol^{-1}, $Đ_M$ = 1.85); **2** (orange, M_n = 5 346 g mol^{-1}, $Đ_M$ = 1.33); **3** (green, M_n = 5 335 g mol^{-1}, $Đ_M$ = 1.51); **4** (blue, M_n = 7 705 g mol^{-1}, $Đ_M$ = 1.33). Polymerisation conditions: benzene-d_6, 70 °C, [*L*-LA]$_0$/[Bi]$_0$ = 50:1, and [*L*-LA]$_0$ = 0.5 M.

Overall, the intermediate $Đ_M$ recorded using initiators **1**–**4** are all within the range of those reported for other bismuth aryloxide and alkoxide ROP initiators.[7, 8] Although BnOH is often employed as a chain-transfer agent to improve control over polymer molecular weights and their dispersity,[18] compounds **1**–**4** were incompatible with an exogeneous alcohol reagent due to their susceptibility to protonation.

3.3.2 Ligand framework variation

The effect of variations in the supporting ligand structure on ROP rates and control was examined. [NON^{tBu}]-ligand-supported bismuth aryloxide **5** was studied as a ROP initiator using reaction conditions identical to those described for **1**–**4** (**Figure 3.5**, **Table 3.2**).

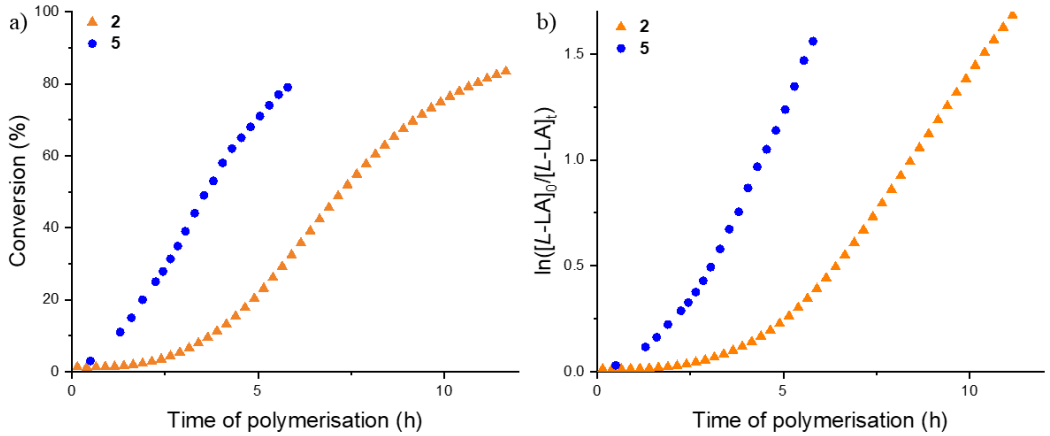


Figure 3.5 a) Plots of percentage conversion *vs*. polymerisation time for *L*-lactide polymerisation. b) Plots of ln([*L*-LA]$_0$/[*L*-LA]$_t$) *vs*. polymerisation time for *L*-lactide polymerisation. Orange triangles: (NON^{Dipp})Bi(O-2,6-Me-C$_6$H$_3$) (**2**), k_{obs} = 0.246 ± 0.011 h^{-1}, R^2 = 0.998; blue circles: (NON^{tBu})Bi(O-2,6-Me-C$_6$H$_3$) (**5**), k_{obs} = 0.356 ± 0.008 h^{-1}, R^2 = 0.991. Polymerisation conditions: benzene-d_6, 70 °C, [*L* LA]$_0$/[Bi]$_0$ = 50:1, and [*L*-LA]$_0$ = 0.5 M.

The plots of ln([*L*-LA]$_0$/[*L*-LA]$_t$) *vs*. polymerisation time were established to compare the performance of initiators **5** and **2**, based on a different di(amido)siloxane ligand yet the same initiating group (**Figure 3.5b**). A significantly shorter induction period was observed using **5**, accompanied by its enhanced activity (k_{obs} = 0.356 ± 0.008 h^{-1} (**5**) *vs*. 0.246 ± 0.011 h^{-1} (**2**)). These findings can be attributed to the reduced steric shielding of the active site imparted by the [NON^{tBu}]-ligand ((NON^{R})BiCl: $G_{2.28}$ = 49.5% (R = ^{t}Bu); 57.9% (R = Dipp)) (**Figure 3.6**).[19, 20] An increase in ROP activity due to the reduced ligand steric bulk has been well-documented for other main group initators.[21-23]

In addition to steric effects, the increased electron donation from *tert*-butyl substituents may render the bismuth centre in **5** less Lewis acidic, which is likely to inhibit coordination yet accelerate lactide ring-opening due to a weakened Bi-O bond. A similar observation has been made in the study of the ROP of *rac*-lactide using gallium systems supported by 8-quinolinolato ligands.[24] A three-fold increase in activity for the gallium

initiator $(L)_2Ga(O^tBu)$ relative to its aluminium counterpart was attributed to the Ga-O bond lability. By contrast, an increase in the Lewis acidity of the active site has been found to enhance ROP rates in some other cases.[25-27] However, structure-activity relationships established through ligand substitution generally cannot be directly extended to heavier metal analogues.[28]

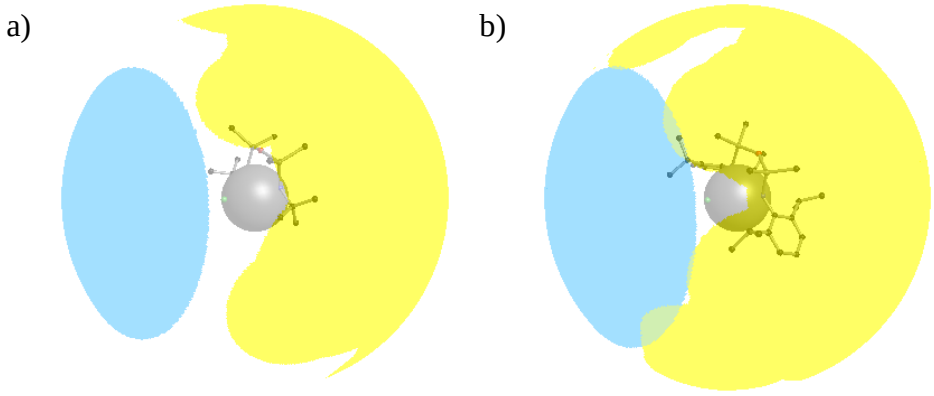


Figure 3.6 Graphical representation of the *G*-parameter in a) $(NON^{tBu})BiCl$ and b) $(NON^{Dipp})BiCl$, demonstrating the percentage of the complex sphere shielded by ligands $[NON^R]$ (yellow) and Cl (blue).

Table 3.2 ROP of *L*-lactide using $(NON^{tBu})Bi(O\text{-}2,6\text{-}Me\text{-}C_6H_3)$ (**5**).[a]

Conv.[b] **(%)**	k_{obs}[c] **(h^{-1})**	R^2[c]	$M_{n,GPC}$[d] **(g mol^{-1})**	$M_{n,theo}$[e] **(g mol^{-1})**	M_w/M_n[d]
79	0.356 ± 0.008	0.991	5 424	5 767	1.56

[a]Polymerisation conditions: benzene-d_6, 70 °C, $[L\text{-LA}]_0/[Bi]_0$ = 50:1, $[L\text{-LA}]_0$ = 0.5 M. [b]Measured by ^1H NMR spectroscopy; averaged over two repeats. [c]Obtained from plots of $\ln([L\text{-LA}]_0/[L\text{-LA}]_t)$ *vs.* polymerisation time. [d]Determined by GPC analysis calibrated with PS standards in THF with the appropriate Mark-Houwink corrections.[17] [e]Theoretical M_n for PLA = (conv.(%) × $[L\text{-LA}]_0/[Bi]_0$) × 144.13 + (M_w of end groups).

The polymerisation in the presence of **5** proceeded with moderate control, resulting in a relatively predictable polymer molecular weight, albeit with a broadened molecular weight distribution (**Table 3.2**). A higher activity of **5** may explain the resulting slightly

higher $Đ_M$ compared to that recorded for the polymerisation initiated by **2** ($Đ_M$ = 1.56 *vs.* 1.33, respectively).

3.3.3 Initiator concentration dependence

Initiator concentration studies were conducted using **2** as a model substrate. Polymerisations were carried out at various concentrations ([*L*-LA]$_0$:[Bi]$_0$ = 50:1, 100:1, 200:1, 300:1) in benzene-d_6 at 70 °C (**Figure 3.7**, **Table 3.3**).

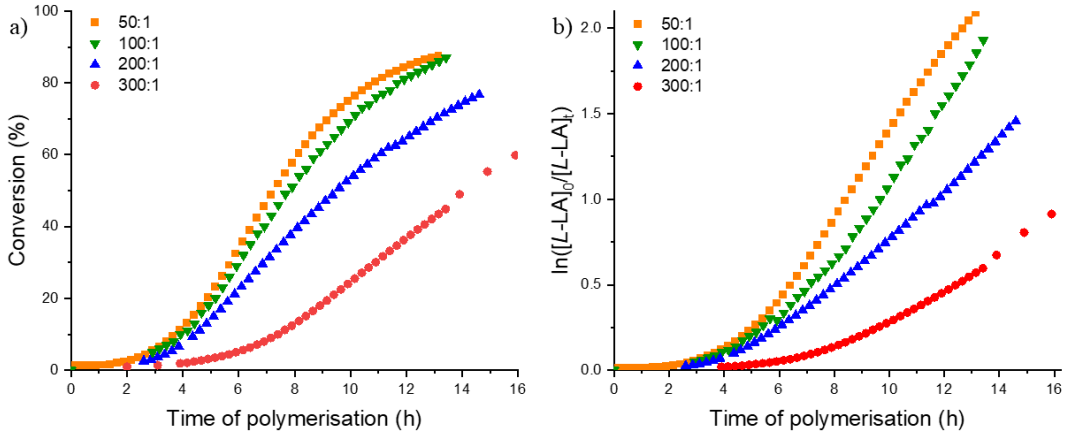


Figure 3.7 a) Plots of percentage conversion *vs.* polymerisation time for *L*-lactide polymerisation. b) Plots of ln([*L*-LA]$_0$/[*L*-LA]$_t$) *vs.* polymerisation time for *L*-lactide polymerisation. Orange squares: [*L*-LA]$_0$:[**2**]$_0$ = 50:1, k_{obs} = 0.246 ± 0.011 h^{-1}, R^2 = 0.998; green down triangles: [*L*-LA]$_0$:[**2**]$_0$ = 100:1, k_{obs} = 0.209 ± 0.003 h^{-1}, R^2 = 0.990; blue up triangles: [*L*-LA]$_0$:[**2**]$_0$ = 200:1, k_{obs} = 0.121 ± 0.002 h^{-1}, R^2 = 0.996; red circles: [*L*-LA]$_0$:[**2**]$_0$ = 300:1, k_{obs} = 0.098 ± 0.002 h^{-1}, R^2 = 0.985. Polymerisation conditions: benzene-d_6, 70 °C, [*L*-LA]$_0$ = 0.5 M.

The linear plots of ln([*L*-LA]$_0$/[*L*-LA]$_t$) *vs.* polymerisation time confirmed a first-order dependence on monomer concentration at all initiator loadings (**Figure 3.7b**). A decrease in the concentration of **2** resulted in longer induction periods, combined with reduced polymerisation rates (k_{obs} = 0.246 ± 0.011 h^{-1} ([LA]$_0$/[Bi]$_0$ = 50:1) > 0.121 ± 0.002 h^{-1} ([LA]$_0$/[Bi]$_0$ = 200:1)). This is expected since reducing the initiator concentration leads to a smaller number of active sites involved in the polymerisation process.[29]

The $M_{n,GPC}$ values of the produced PLLAs increased with decreasing initiator concentration ($M_{n,GPC}$ = 15 342 g mol^{-1} ([LA]$_0$/[Bi]$_0$ = 200:1) > 5 346 g mol^{-1} ([LA]$_0$/[Bi]$_0$ = 50:1)) (**Table 3.3**), attributed to the enhanced probability of monomer enchainment due to the reduction of bismuth active sites. In all cases, these values appeared to be lower than expected, suggesting the occurrence of transesterification side reactions.[30] Based on the narrow-to-intermediate $Đ_M$ recorded ($Đ_M$ = 1.02–1.33), the polymerisations proved to be relatively well-controlled at all initiator concentrations (**Figure 3.8**). At the lowest initiator loading, $Đ_M$ was notably narrower ($Đ_M$ = 1.02 with [LA]$_0$/[Bi]$_0$ = 300:1). It has been previously suggested that a decrease in the initiator concentration could mitigate the possible aggregation of active species, consequently enhancing control over the polymerisation process.[31, 32] Alternatively, extended reaction times at lower initiator loadings can also lead to increased levels of transesterification, resulting in broader $Đ_M$ values.[6]

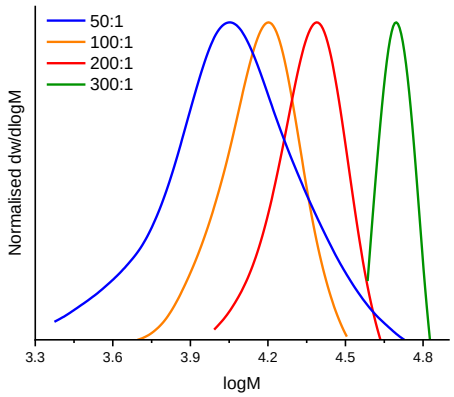


Figure 3.8 GPC plots of the PLLAs produced with [*L*-LA]$_0$:[**2**]$_0$ = 50:1 (blue, M_n = 5 346 g mol^{-1}, $Đ_M$ = 1.33); [*L*-LA]$_0$:[**2**]$_0$ = 100:1 (orange, M_n = 11 871 g mol^{-1}, $Đ_M$ = 1.22); [*L*-LA]$_0$:[**2**]$_0$ = 200:1 (red, M_n = 15 342 g mol^{-1}, $Đ_M$ = 1.13); [*L*-LA]$_0$:[**2**]$_0$ = 300:1 (green, M_n = 28 827 g mol^{-1}, $Đ_M$ = 1.02)*. Polymerisation conditions: benzene-d_6, 70 °C, [*L*-LA]$_0$ = 0.5 M. * GPC polymer trace was analysed up to the THF solvent trace.

A plot of $-\ln(k_{obs})$ *vs.* $-\ln([Bi]_0)$ revealed a linear relationship with a gradient of 0.54 ± 0.08 (R^2 = 0.954) (**Figure 3.9a**), suggesting a first-order dependence on initiator concentration, consistent with the typical coordination-insertion mechanism.[16] Similar first-order dependency values have been previously reported for bismuth, scandium, and zirconium initiating systems.[8, 33, 34] A fractional dependence may also indicate the aggregation of active species.[35, 36]

To determine the propagation rate constant (k_p), a plot of k_{obs} *vs.* $[Bi]_0$ was constructed, with the k_p value calculated to be 17.56 ± 4.68 $M^{-1}\,h^{-1}$ (R^2 = 0.876) (**Figure 3.9b**). The idealised overall rate law for the ROP of *L*-lactide using **2** is defined by **Equation 3.1** as follows:

$$-\frac{d[\mathrm{LA}]}{dt} = k_p[\mathrm{LA}]_0[\mathbf{2}]_0$$

Where k_p = 17.56 ± 4.68 $M^{-1}\,h^{-1}$.

Equation 3.1 Definition of the rate law for the ROP of *L*-lactide using **2**, where k_p = propagation rate constant, $[LA]_0$ = initial lactide concentration, $[\mathbf{2}]_0$ = initial initiator concentration.

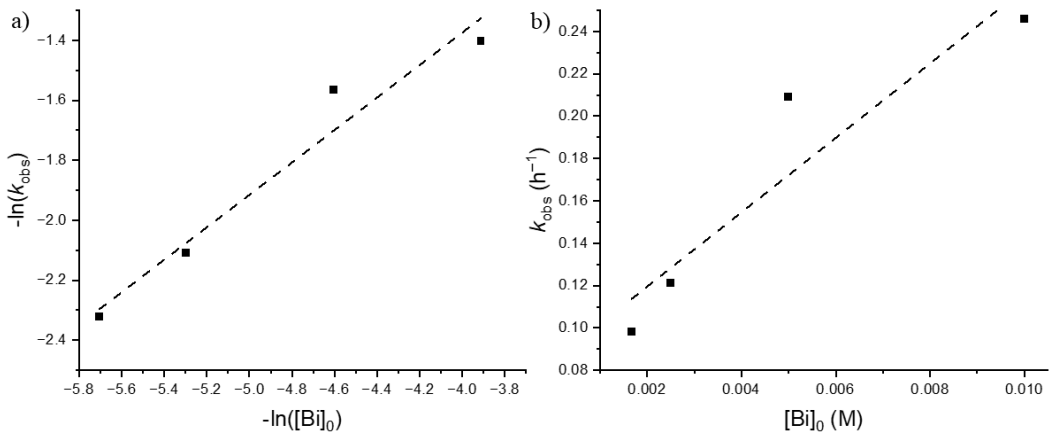


Figure 3.9 a) Plot of $-\ln(k_{obs})$ *vs.* $-\ln([Bi]_0)$ for *L*-lactide polymerisation using **2**; slope = 0.54 ± 0.08 (R^2 = 0.954). b) Plot of k_{obs} *vs.* $[Bi]_0$ for *L*-lactide polymerisation using **2**; slope = 17.56 ± 4.68 $M^{-1}\,h^{-1}$ (R^2 = 0.876). Polymerisation conditions: benzene-d_6, 70 °C, $[L\text{-LA}]_0$ = 0.5 M.

Table 3.3 ROP of *L*-lactide at different $[L\text{-LA}]_0/[\text{Bi}]_0$ ratios using $(\text{NON}^{\text{Dipp}})\text{Bi}(\text{O-2,6-Me-C}_6\text{H}_3)$ (**2**).[a]

$[L\text{-LA}]_0/[\text{Bi}]_0$	Conv.[b] (%)	k_{obs}[c] (h^{-1})	R^{2c}	$M_{n,GPC}$[d] (g mol^{-1})	$M_{n,theo}$[e] (g mol^{-1})	M_w/M_n[d]
50:1	88	0.246 ± 0.011	0.998	5 346	6 458	1.33
100:1	87	0.209 ± 0.003	0.990	11 871	12 661	1.13
200:1	88	0.121 ± 0.002	0.996	15 342	25 662	1.22
300:1	73	0.098 ± 0.002	0.985	28 827	31 470	1.02

[a]Polymerisation conditions: benzene-d_6, 70 °C, $[L\text{-LA}]_0$ = 0.5 M. [b]Measured by ^{1}H NMR spectroscopy; averaged over two repeats. [c]Obtained from plots of $\ln([L\text{-LA}]_0/[L\text{-LA}]_t)$ *vs.* polymerisation time. [d]Determined by GPC analysis calibrated with PS standards in THF with the appropriate Mark-Houwink corrections.[17] [e]Theoretical M_n for PLA = (conv.(%) × $[L\text{-LA}]_0/[\text{Bi}]_0$) × 144.13 + ($M_w$ of end groups).

In a wider context, the activity of **2** appears to be moderate relative to other well-defined bismuth initiators previously discussed in **Section 3.1**. While the pyridine dipyrrolide bismuth lactate initiator demonstrated a lower activity (k_p = 8.6 ± 1.2 M^{-1} h^{-1} at 80 °C), a higher polymerisation rate was recorded in the presence of the bismuth *tert*-butoxide complex bearing a salen ligand (k_p = 180 M^{-1} h^{-1} at 25 °C).[7, 8] Furthermore, the activity of **2** is relatively low compared to other main group metal systems despite their smaller ionic radii, including amidinato tin(II) alkoxide (L)Sn($OCPh_3$) (k_p = 1 548 M^{-1} h^{-1} at 80 °C) and a *bis*(pyrrolidene) Schiff base aluminium ethyl complex (L)AlEt (k_p = 289.8 M^{-1} h^{-1} at 70 °C), though both used in conjunction with an alcohol co-initiator.[35, 37]

These differences are likely to result from the less Lewis acidic nature of bismuth, leading to more covalent bonding interactions. The enhanced electrophilicity of the initiator active site has been shown to accelerate lactide coordination-insertion steps.[38] The activity of **2** is also likely influenced by steric constraints imposed by both the $[\text{NON}^{\text{Dipp}}]$-ligand framework and the $6s^2$ lone pair on bismuth(III). In comparison to

lighter main group elements, bismuth systems generally exhibit pronounced relativistic effects, with consequences on their Lewis acidity and coordination chemistry.[39, 40] In addition, the potential aggregation of active bismuth sites may hinder the ROP initiating capability.[41] Finally, the relatively high activities of the latter main group systems may also be linked to the utilisation of a co-initiator/chain transfer agent.[42-44] However, making a direct comparison with literature data is confounded by the varying experimental conditions employed.

3.3.4 Monomer stereochemistry variation

The catalytic capability of **2** was also evaluated for the polymerisation of different lactide stereoisomers: *L*-, *D*-, *rac*-, and *meso*-lactide (**Figure 3.10**, **Table 3.4**).

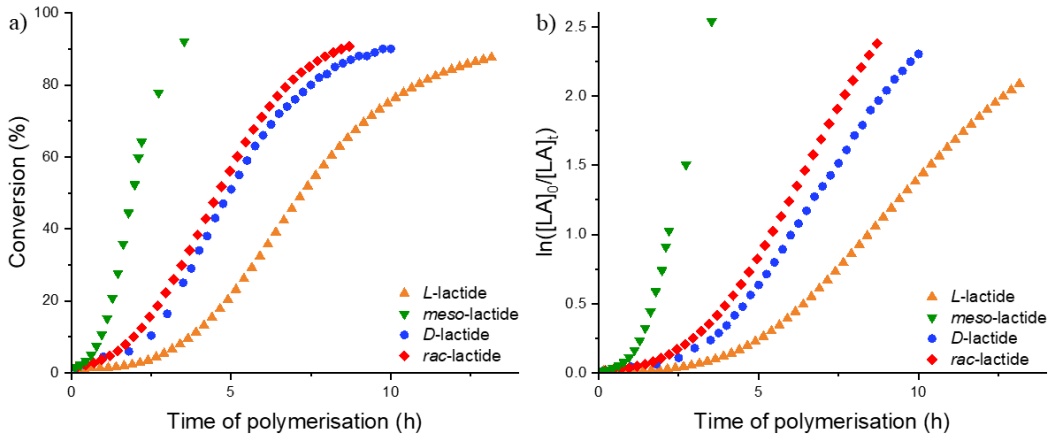


Figure 3.10 a) Plots of percentage conversion *vs*. polymerisation time for lactide polymerisation. b) Plots of $\ln([LA]_0/[LA]_t)$ *vs*. polymerisation time for lactide polymerisation. Orange up triangles: *L*-LA, $k_{obs} = 0.246 \pm 0.011$ h^{-1}, $R^2 = 0.998$; green down triangles: *meso*-LA, $k_{obs} = 0.935 \pm 0.026$ h^{-1}, $R^2 = 0.981$; blue circles: *D*-LA, $k_{obs} = 0.342 \pm 0.003$ h^{-1}, $R^2 = 0.998$; red rhombi: *rac*-LA, $k_{obs} = 0.398 \pm 0.007$ h^{-1}, $R^2 = 0.995$. Polymerisation conditions: benzene-d_6, 70 °C, $[LA]_0/[Bi]_0 = 50{:}1$, and $[LA]_0 = 0.5$ M.

The polymerisation of *meso*-lactide proceeded at the fastest rate ($k_{obs} = 0.935 \pm 0.026$ h^{-1}) with a negligible induction period (**Figure 3.10b**). Relatively fast rates in the ROP of *meso*-lactide are typically attributed to the inherent ring strain of the monomer, providing

a driving force for the ROP process.[45] The polymerisation of *rac*- and *D*-lactide exhibited comparable rates (k_{obs} = 0.398 ± 0.007 and 0.342 ± 0.003 h^{-1}, respectively), both of which were higher than that for *L*-lactide (k_{obs} = 0.246 ± 0.011 h^{-1}).

Table 3.4 ROP of *L*-, *D*-, *rac*-, and *meso*-lactide monomers using (NON^{Dipp})Bi(O-2,6-Me-C_6H_3) (**2**).[a]

Monomer	**Conv.[b] (%)**	**k_{obs}[c] (h^{-1})**	**R^{2c}**	**$M_{n,GPC}$[d] (g mol^{-1})**	**$M_{n,theo}$[e] (g mol^{-1})**	**M_w/M_n[d]**
L-LA	88	0.246 ± 0.011	0.998	5 346	6 458	1.33
D-LA	91	0.342 ± 0.003	0.998	5 208	6 680	1.89
meso-LA	92	0.935 ± 0.026	0.981	5 712	6 752	1.38
rac-LA	96	0.398 ± 0.007	0.995	3 217	7 012	2.14

[a]Polymerisation conditions: benzene-d_6, 70 °C, $[LA]_0/[Bi]_0$ = 50:1, $[LA]_0$ = 0.5 M. [b]Measured by ^{1}H NMR spectroscopy; averaged over two repeats. [c]Obtained from plots of $\ln([LA]_0/[LA]_t)$ *vs.* polymerisation time. [d]Determined by GPC analysis calibrated with PS standards in THF with the appropriate Mark-Houwink corrections.[17] [e]Theoretical M_n for PLA = (conv.(%) × $[LA]_0/[Bi]_0$) × 144.13 + (M_w of end groups).

The polymerisation of all four stereoisomers resulted in lower than expected $M_{n,GPC}$ values, ascribed to transesterification side reactions (**Table 3.4**). Intermediate $Đ_M$ values were recorded for the polymers produced from *L*-, *D*-, and *meso*-lactide ($Đ_M$ = 1.33–1.89). In contrast, the polymerisation of *rac*-lactide showed the poorest control, as defined by a broad $Đ_M$ of 2.14 and the largest discrepancy between the $M_{n,GPC}$ and $M_{n,theo}$ values of the polymer product (**Figure 3.11**). These results imply that polymerisation control is diminished upon the formation of *racemic* linkages in the polymer chain.[46]

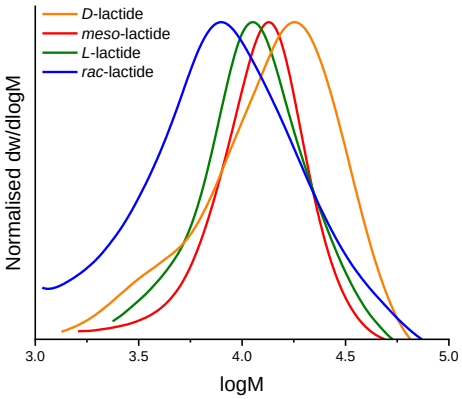


Figure 3.11 GPC plots of the PLAs produced from *D*-LA (orange, M_n = 5 208 g mol^{-1}, $Đ_M$ = 1.89); *meso*-LA (red, M_n = 5 712 g mol^{-1}, $Đ_M$ = 1.38); *L*-LA (green, M_n = 5 346 g mol^{-1}, $Đ_M$ = 1.33); *rac*-LA (blue, M_n = 3 217 g mol^{-1}, $Đ_M$ = 2.14)*. Polymerisation conditions: benzene-d_6, 70 °C, $[LA]_0/[Bi]_0$ = 50:1 and $[LA]_0$ = 0.5 M. * GPC polymer trace was analysed up to the THF solvent trace.

The stereoselectivity of **2** was determined by $^1H\{^1H\}$ NMR spectroscopic analyses of the isolated polymers based on Bernoullian probabilities.[47] Isotactic PLA was formed during the polymerisation of *L*- and *D*-lactide (P_m = 1.00) (**Figure 3.12a**). The absence of epimerisation (i.e. random inversion of stereochemistry at a stereogenic centre) was confirmed by a single resonance observed in the polymer *methine* region (δ 5.04 ppm). These findings are consistent with previous reports of bismuth ROP initiators, capable of polymerising *L*- and *D*-lactide without epimerisation.[5] A relatively low degree of stereocontrol was observed in the case of *rac*- and *meso*-lactide: the ROP of *meso*-lactide displayed a slight heterotactic bias (P_m = 0.65), whereas the ROP of *rac*-lactide afforded atactic PLA (P_r = 0.59) (**Figure 3.12b** and **c**, respectively).

Due to the absence of chirality in **2**, the ROP of *meso*-lactide is most likely to proceed *via* a chain-end control mechanism.[48] The observed low stereoregularity of the polymer products is not surprising, since the large ionic radius of bismuth may account for a more open coordination environment and, consequently, a less effective mechanism of

stereocontrol.[49] In the case of related bismuth pyridine dipyrrolide initiators ($L^{Mes,Ph}$)BiX, the relatively poor stereoselectivity was also ascribed to the prevalence of transesterification side reactions.[8] In addition, the presence of the metal-centred lone pair of electrons has been proposed to impose a limit on the stereocontrol achieved by BDI-supported tin(II) ROP initiators.[15] Hence, the influence of the bismuth-based $6s^2$ lone pair on both polymerisation kinetics and stereocontrol cannot be ruled out.

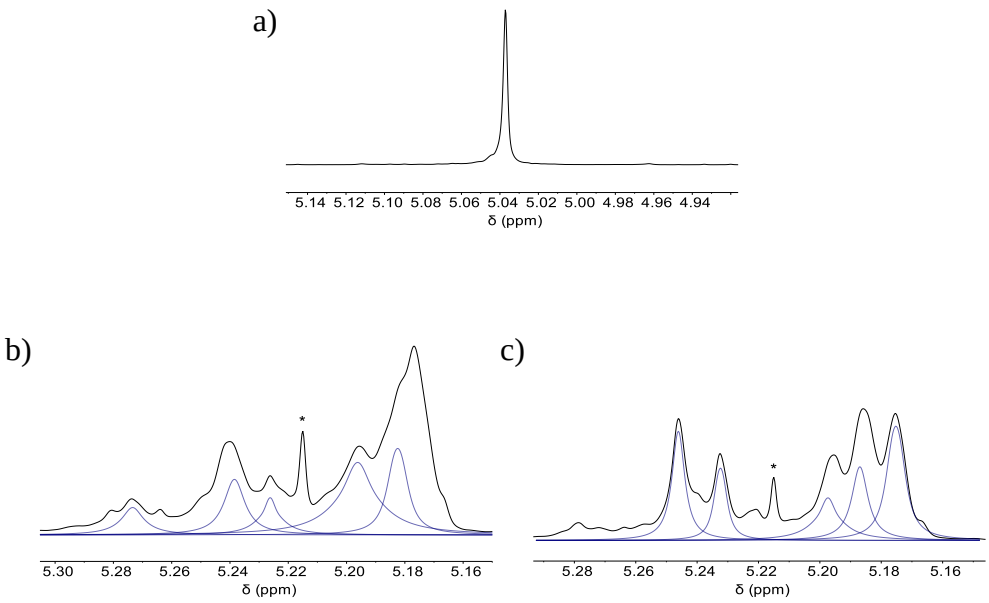


Figure 3.12 $^1H\{^1H\}$ NMR spectra (chloroform-d_1, 500 MHz, 298 K) of the *methine* protons in the PLAs produced by **2** from a) *L*- and *D*-LA (P_m = 1.00), b) *meso*-LA (P_m = 0.65), c) *rac*-LA (P_r = 0.59). Polymerisation conditions: benzene-d_6, 70 °C, $[LA]_0/[Bi]_0$ = 50:1 and $[LA]_0$ = 0.5 M. * represents an artefact from BASH processing.

3.3.5 Temperature variation

The effect of polymerisation temperature on the catalytic capability of **2** was investigated. Polymerisations were conducted in the range of 50−80 °C in benzene-d_6 (**Figure 3.13**, **Table 3.5**).

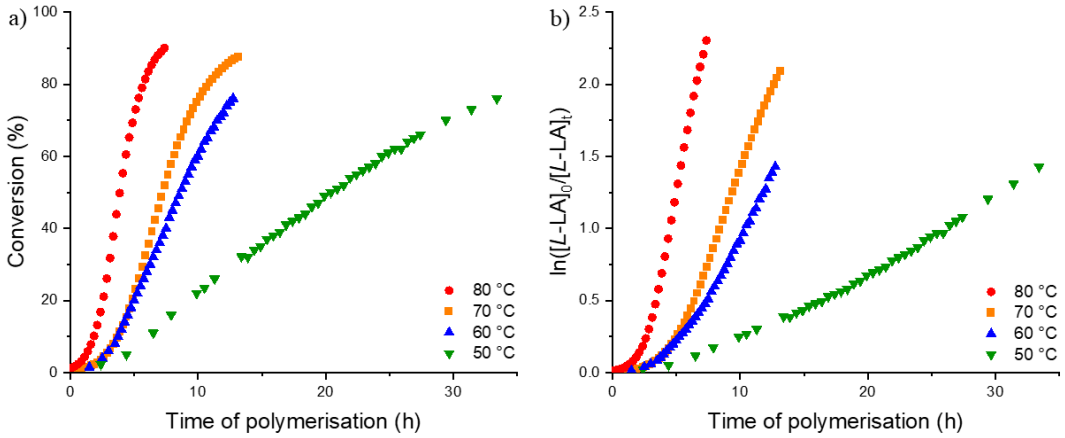


Figure 3.13 a) Plots of percentage conversion *vs*. polymerisation time for *L*-lactide polymerisation. b) Plots of ln([*L*-LA]$_0$/[*L*-LA]$_t$) *vs*. polymerisation time for *L*-lactide polymerisation. Red circles: 80 °C, k_{obs} = 0.453 ± 0.007 h^{-1}, R^2 = 0.993; orange squares: 70 °C, k_{obs} = 0.246 ± 0.011 h^{-1}, R^2 = 0.998; blue up triangles: 60 °C, k_{obs} = 0.149 ± 0.003 h^{-1}, R^2 = 0.988; green down triangles: 50 °C, k_{obs} = 0.051 ± 0.004 h^{-1}, R^2 = 0.992. Polymerisation conditions: benzene-d_6, [*L*-LA]$_0$/[Bi]$_0$ = 50:1, and [*L*-LA]$_0$ = 0.5 M.

As expected, an increase in polymerisation temperature led to shorter induction periods and higher observed rates (k_{obs} = 0.453 ± 0.007 h^{-1} (80 °C) > 0.051 ± 0.004 h^{-1} (50 °C)) (**Figure 3.13b**). The $M_{n,GPC}$ values of the polymers produced at 50 and 60 °C were found to be slightly higher than expected (**Table 3.5**). This suggests that not all of the bismuth centres were active during the polymerisation, presumably due to less efficient initiation at lower reaction temperatures. The $Đ_M$ of PLLAs increased in parallel with increasing temperature ($Đ_M$ = 1.68 (80 °C) > 1.17 (50 °C)) (**Figure 3.14**), indicating a higher prevalence of transesterification at higher temperatures.[46, 50]

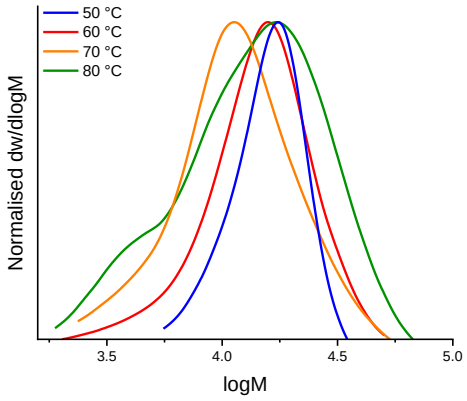


Figure 3.14 GPC plots of the PLLAs produced at 50 °C (blue, M_n = 8 152 g mol^{-1}, $Đ_M$ = 1.17); 60 °C (red, M_n = 6 810 g mol^{-1}, $Đ_M$ = 1.38); 70 °C (orange, M_n = 5 346 g mol^{-1}, $Đ_M$ = 1.33); 80 °C (green, M_n = 5 768 g mol^{-1}, $Đ_M$ = 1.68). Polymerisation conditions: benzene-d_6, [*L*-LA]$_0$/[Bi]$_0$ = 50:1, and [*L*-LA]$_0$ = 0.5 M.

Table 3.5 ROP of *L*-lactide at different temperatures using (NON^{Dipp})Bi(O-2,6-Me-C$_6$H$_3$) (**2**).[a]

T **(°C)**	**Conv.**[b] **(%)**	k_{obs}[c] **(h^{-1})**	R^{2}[c]	$M_{n,GPC}$[d] **(g mol^{-1})**	$M_{n,theo}$[e] **(g mol^{-1})**	M_w/M_n[d]
50	88	0.051 ± 0.004	0.992	8 152	6 752	1.17
60	76	0.149 ± 0.003	0.988	6 810	5 599	1.38
70	88	0.246 ± 0.011	0.998	5 346	6 458	1.33
80	90	0.453 ± 0.007	0.993	5 768	6 608	1.68

[a]Polymerisation conditions: benzene-d_6, [*L*-LA]$_0$/[Bi]$_0$ = 50:1, [*L*-LA]$_0$ = 0.5 M. [b]Measured by ^{1}H NMR spectroscopy; averaged over two repeats. [c]Obtained from plots of ln([*L*-LA]$_0$/[*L*-LA]$_t$) *vs.* polymerisation time. [d]Determined by GPC analysis calibrated with PS standards in THF with the appropriate Mark-Houwink corrections.[17] [e]Theoretical M_n for PLA = (conv.(%) × [*L*-LA]$_0$/[Bi]$_0$) × 144.13 + (M_w of end groups).

In order to determine the thermodynamic parameters of the ROP of *L*-lactide initiated by **2**, the Eyring plot of ln(k_{obs}/T) *vs.* 1/*T* was established according to the Eyring equation (**Equation 3.2**, **Figure 3.15**).

$$\ln\left(\frac{k_{\text{obs}}}{T}\right) = -\left(\frac{\Delta H^{\ddagger}}{R}\right)\left(\frac{1}{T}\right) + \ln\left(\frac{k_B}{h}\right) + \left(\frac{\Delta S^{\ddagger}}{R}\right)$$

Equation 3.2 Definition of the Eyring equation, where $\Delta H^{\ddagger}$ = enthalpy of activation, $\Delta S^{\ddagger}$ = entropy of activation, T = temperature, R = gas constant, k_B = Boltzmann's constant, h = Planck's constant.

Based on the gradient and intercept values derived from the Eyring plot, the enthalpy ($\Delta H^{\ddagger}$) and entropy ($\Delta S^{\ddagger}$) of activation were determined to be 68 ± 0.1 kJ mol^{-1} and −139 ± 23 J K^{-1} mol^{-1}, respectively. Such relatively large negative entropy indicates a highly ordered transition state formed upon lactide binding, characteristic of ROP proceeding *via* a coordination-insertion mechanism.[51]

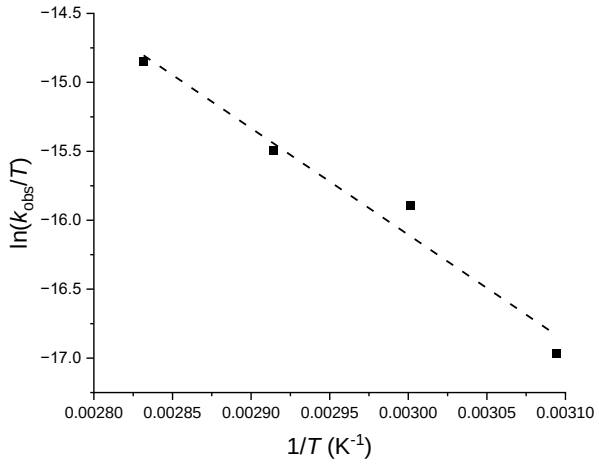


Figure 3.15 Eyring plot of ln(k_{obs}/T) *vs.* 1/T using **2** ($\Delta H^{\ddagger}$ = 68 ± 0.1 kJ mol^{-1}; $\Delta S^{\ddagger}$ = −139 ± 23 J K^{-1} mol^{-1}; slope = −7 729 ± 9, R^2 = 0.876; intercept = 7.1 ± 2.8). Polymerisation conditions: benzene-d_6, [*L*-LA]$_0$/[Bi]$_0$ = 50:1, and [*L*-LA]$_0$ = 0.5 M.

The Gibbs free energy ($\Delta G^{\ddagger}$) of activation was calculated according to **Equation 3.3**:

$$\Delta G^{\ddagger} = \Delta H^{\ddagger} - T\Delta S^{\ddagger}$$

Equation 3.3 Definition of the Gibbs free energy, where $\Delta G^{\ddagger}$ = Gibbs free energy, $\Delta H^{\ddagger}$ = enthalpy of activation, $\Delta S^{\ddagger}$ = entropy of activation, T = temperature.

For the temperature range of 50−80 °C, the $\Delta G^{\ddagger}$ values were found to be 113−117 kJ mol^{-1}. In comparison, a lower $\Delta G^{\ddagger}$ value has been reported for a bismuth pyridine dipyrrolide complex with a *tert*-butoxide initiating group ($L^{Mes,Ph}$)Bi(O^{t}Bu) ($\Delta G^{\ddagger}$ = 93 kJ mol^{-1} at 70 °C).[8, 52] A combination of factors may account for the relatively high $\Delta G^{\ddagger}$ parameter associated with **2**, including steric crowding at the active site imposed by the ligand framework and the modest Lewis acidity of the bismuth centre.

3.3.6 Polymer end-group analysis

Polymer end groups were analysed by MALDI-ToF mass spectrometry using the PLLA polymers/oligomers produced by ROP in the presence of initiators **1**–**4** (**Figures 3.16** and **3.17**; **Figures A.2.2** and **A.2.3** in **Appendix**). All four mass spectra displayed peaks separated by m/z = 72, corresponding to half of the lactide monomer unit. These observations confirm the occurrence of intermolecular transesterification side reactions, consistent with the intermediate $Đ_M$ values recorded for this series of initiators (*vide supra*, **Table 3.1**).[53] Using compound **2**, the series of peaks in the mass spectrum was assigned to the PLLA chain comprising lactide repeat units with α–O-2,6-Me-C_6H_3 and ω–OH terminal groups (**Figure 3.16**). For example, the peak at 1 889.8 g mol^{-1} represents α–O-2,6-Me-C_6H_3/ω–OH end-capped polymer chain containing 12 lactide units alongside K^+ (M_n = (144.1 × 12 + 39.1 + 122.2) g mol^{-1}). Analogously, the anticipated end groups corresponding to α–OC_6H_5, α–O-2,6-^{i}Pr-C_6H_3, and α–O^{t}Bu were detected by the analysis of PLLAs afforded by **1**, **3**, and **4**, respectively.

In addition to linear PLLA chains, the MALDI-ToF mass spectra recorded for the use of **1**, **3**, and **4** revealed the presence of side products: cyclic PLLA, indicated by the absence of polymer end groups, and α–OH/ω–OH terminated PLLA, likely formed due to hydrolysis of the initiator (**Figure 3.17**).[53] Both of these are common side products that

have previously been observed using main group initiators, including bismuth compounds.[54, 55]

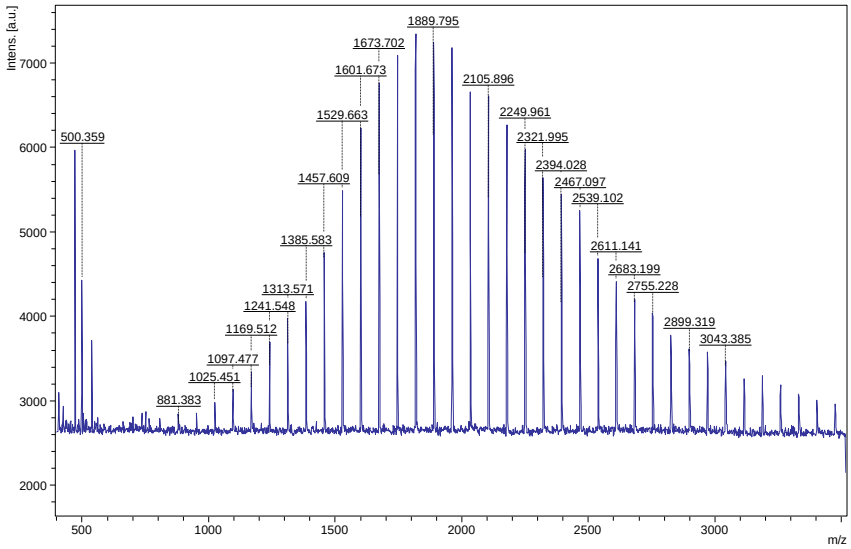


Figure 3.16 MALDI-ToF mass spectrum of the PLLA produced using **2**. Polymerisation conditions: benzene-d_6, 70 °C, [*L*-LA]$_0$/[Bi]$_0$ = 25:1, [*L*-LA]$_0$ = 0.5 M.

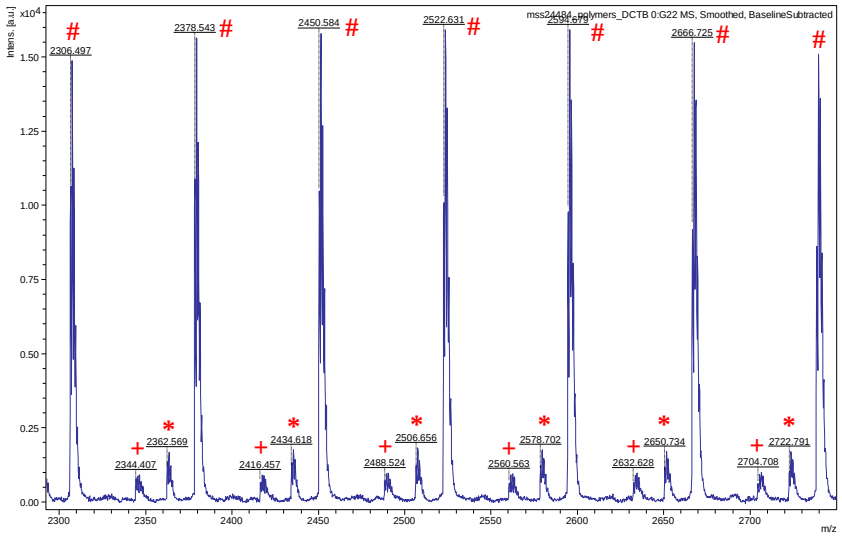


Figure 3.17 MALDI-ToF mass spectrum of the PLLA produced using **3**. Polymerisation conditions: benzene-d_6, 70 °C, [*L*-LA]$_0$/[Bi]$_0$ = 50:1, [*L*-LA]$_0$ = 0.5 M. # represents linear α–O-2,6-^{i}Pr-C_6H_3/ω–OH terminated PLLA. * cyclic PLLA. + α–OH/ω–OH terminated PLLA.

3.3.7 Mechanistic analysis

To determine the nature of the propagating species in the ROP of *L*-lactide, an equimolar reaction between **2** and *L*-lactide was probed by ^{1}H NMR spectroscopy. No reactivity was initially observed after 16 hours at 50 °C, whereas prolonged heating resulted in the formation of PLLA together with an intractable mixture of other species, such as the $(NON^{Dipp})H_2$ pro-ligand. Conversely, compound **2** alone remained stable in the benzene-d_6 solution even when heated to 50 °C for 48 hours. These observations suggest that the initiation rate is slower than propagation and that the putative ring-opened intermediate is not sufficiently stabilised by chelate effects. Similar results have been described in the studies of tin aryloxide compounds Ph_3SnX (X = $OCH(CF_3)_2$ and OPh) and *O*,*S*,*S*,*O*-ligand supported yttrium silylamide (OSSO)Y{$N(SiHMe_2)_2$}(THF).[56, 57]

Metal lactate complexes, usually prepared by reacting an organometallic initiator with a potassium lactate reagent, can be employed as model compounds for the propagating species formed during the insertion of the first lactide monomer (see **Chapter Four** for detailed discussion).[8, 41, 58] However, an attempted reaction between **2** and potassium (*R*)-*tert*-butyl lactate resulted in the protonolysis of **2**.

The progress of the polymerisation of *L*-lactide using **2** with $[L\text{-LA}]_0/[Bi]_0 = 50:1$ at 70 °C was monitored by ^{1}H NMR spectroscopy. Initially (*L*-lactide conversion < 3%, 15 minutes after mixing), the ^{1}H NMR spectrum displayed characteristic resonances for **2** and *L*-lactide (**Figure 3.18a**).

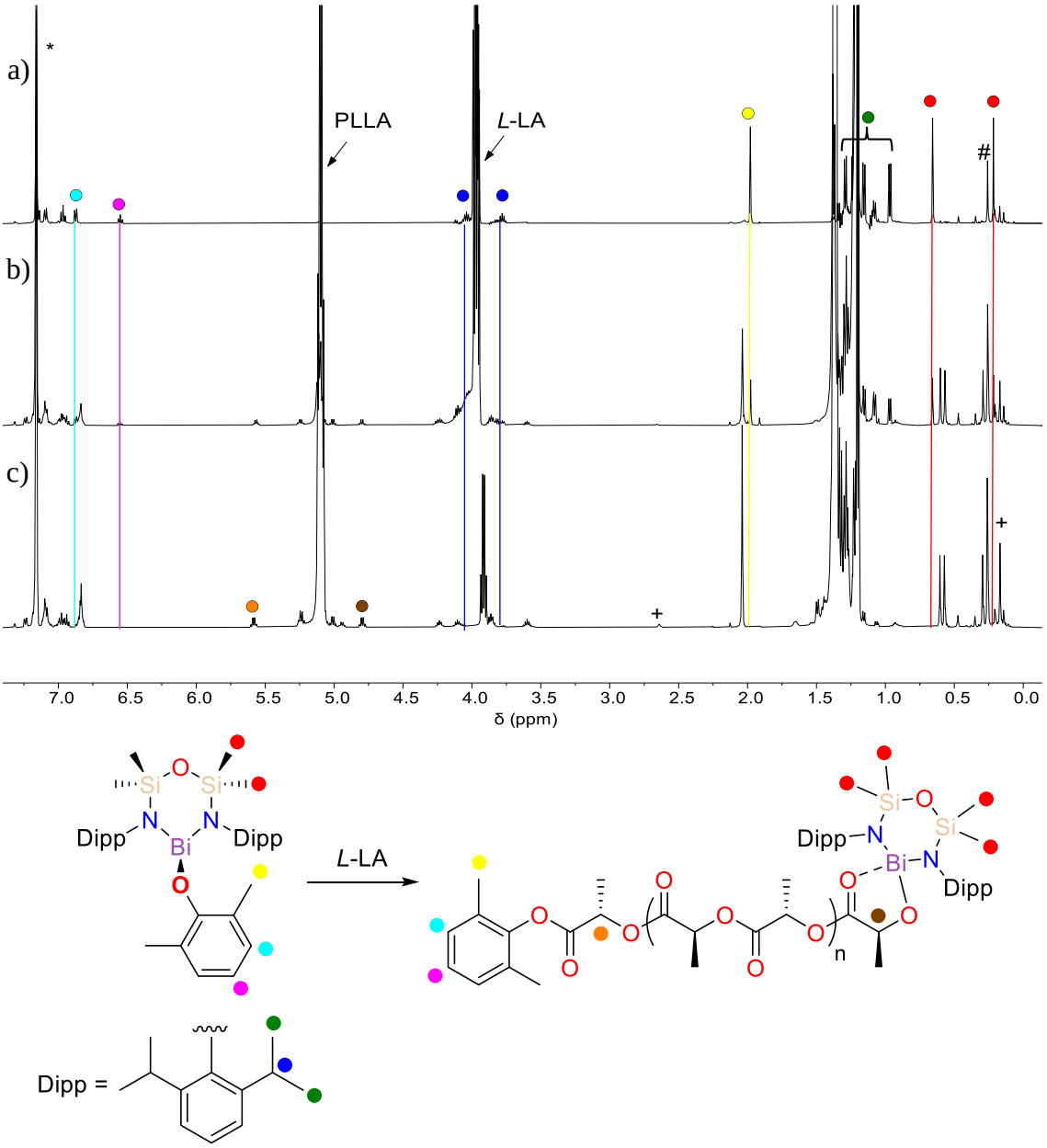


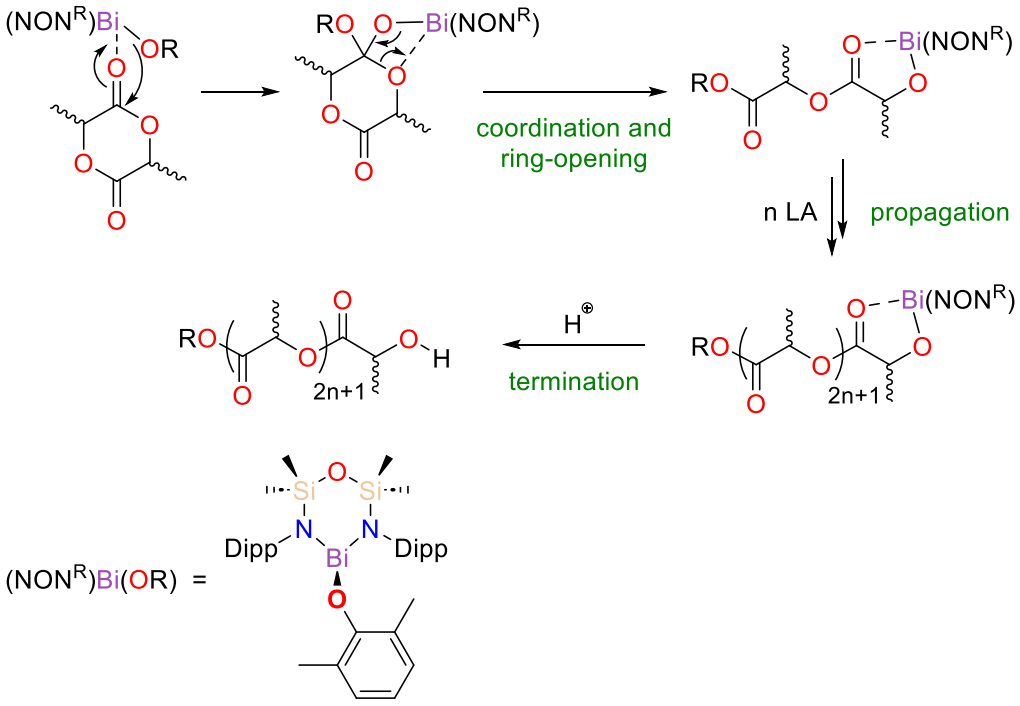
Figure 3.18 ^{1}H NMR spectra (*benzene-d_6, 400 MHz, 298 K) of *L*-lactide polymerisation using **2** at t = a) 0.25 hours, b) 4.5 hours, c) 13 hours. Polymerisation conditions: benzene-d_6, 70 °C, $[L\text{-LA}]_0/[\text{Bi}]_0$ = 50:1, and $[L\text{-LA}]_0$ = 0.5 M. # and + represent grease and the $(\text{NON}^{\text{Dipp}})\text{H}_2$ pro-ligand, respectively.

As the polymerisation proceeded with the conversion of *L*-lactide (*methine* protons at δ 3.93 ppm) to PLLA (*methine* protons at δ 5.09 ppm) (**Figure 3.18b** and **c**), **2** was fully consumed and replaced by a propagating intermediate, represented by a new set of resonances consistent with C_1 molecular symmetry. These include a higher frequency

singlet at δ 1.98 ppm corresponding to the O-2,6-*Me*-C_6H_3 protons and four new singlets between δ 0.60–0.26 ppm assigned to the Si*Me*$_2$ protons. The reduced symmetry of this species relative to **2** may arise from the interactions between the bismuth centre and the carbonyl oxygen in the propagating chain.[15] In addition, two new quartets at δ 4.79 and 5.60 ppm were assigned to the *methine* proton of the lactide unit nearest to the bismuth centre and the *methine* proton close to the α–O-2,6-Me-C_6H_3 end group, respectively. Over the course of the polymerisation, the formation of a relatively small amount of pro-ligand (NON^{Dipp})H_2 was identified (Si*Me*$_2$ at δ 0.17 ppm), suggesting a partial deactivation of the initiator.

The absence of a distinguishable set of resonances to define the insertion of a single lactide monomer into **2** provides further evidence that the first monomer insertion is significantly slower than subsequent insertion steps. In contrast, several lactate compounds formed during the ring-opening of a single lactide unit by main group initiators have been successfully characterised by ^{1}H NMR spectroscopy.[56, 59, 60] The corresponding ROP processes were proposed to involve a rapid first monomer insertion step, followed by significantly slower propagation.

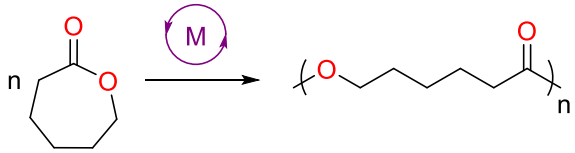
Based on these results, the ROP of lactide using initiator **2** proceeds *via* a coordination-insertion mechanism, which is first-order with respect to both monomer and initiator (**Scheme 3.1**). The first monomer ring-opening is proposed to be rate-limiting, thus accounting for a significant induction period. Following this, the polymer chain propagates through consecutive lactide coordination-insertion steps until terminated by hydrolysis, which generates the ω–OH polymer end group. A similar mechanistic pathway has been proposed for other bismuth aryloxide and alkoxide ROP initiators.[1, 8]



Scheme 3.1 Proposed coordination-insertion mechanism for the ROP of lactide using **2** ((NON^{R})Bi(OR)).

3.4 ε-Caprolactone polymerisation studies using a bismuth aryloxide initiator

Poly(ε-caprolactone) (PCL) is a biodegradable and biocompatible polyester. Analogous to lactide, the seven-membered ε-caprolactone monomer can be polymerised in a controlled manner *via* coordination-insertion ROP (**Scheme 3.2**).[61]



Scheme 3.2 Ring-opening polymerisation of ε-caprolactone initiated by a metal-based initiator.

Following the observed activity of **2** in the ROP of lactide, the ability of the complex to initiate the ROP of ε-caprolactone was examined. Polymerisation studies were conducted using J. Young's tap NMR spectroscopy tubes with an initial ε-caprolactone to catalyst

ratio ($[\varepsilon\text{-CL}]_0/[\text{Bi}]_0$) of 50:1 and an initial monomer concentration ($[\varepsilon\text{-CL}]_0$) of 0.5 M in 0.6 mL of benzene-d_6 at 70 °C. The reactions were monitored by ^{1}H NMR spectroscopy and halted by cooling in an ice bath, followed by quenching with wet pentane.

3.4.1 ε-Caprolactone polymerisation

The polymerisation rates and control imparted by **2** were compared for both *L*-lactide and ε-caprolactone monomers (**Figure 3.19**, **Table 3.6**). In contrast to *L*-lactide, ε-caprolactone was polymerised without a significant induction period. The enhanced reactivity of **2** towards the ring-opening of ε-caprolactone can be explained by the relatively lesser steric demand of the monomer, coupled with its high Lewis basicity.[11]

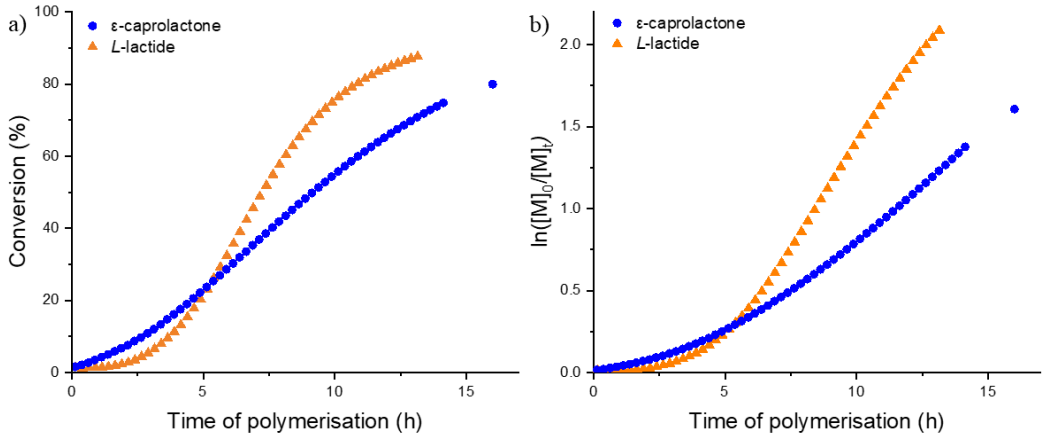


Figure 3.19 a) Plots of percentage conversion *vs*. polymerisation time. b) Plots of $\ln([\text{M}]_0/[\text{M}]_t)$ *vs*. polymerisation time (where M = monomer). Blue circles: ε-CL, k_{obs} = 0.123 ± 0.001 h^{-1}, R^2 = 0.996; orange triangles: *L*-LA, k_{obs} = 0.246 ± 0.011 h^{-1}, R^2 = 0.998. Polymerisation conditions: benzene-d_6, 70 °C, $[\text{M}]_0/[\text{Bi}]_0$ = 50:1, and $[\text{M}]_0$ = 0.5 M.

A linear plot of $\ln([\varepsilon\text{-CL}]_0/[\varepsilon\text{-CL}]_t)$ *vs*. polymerisation time revealed a first-order dependence on monomer concentration (**Figure 3.19b**), in agreement with a coordination-insertion mechanism (see **Chapter Four**, **Section 4.4.2** for a mechanistic discussion).[62] Unexpectedly, the ROP activity of **2** towards ε-caprolactone was found to

be two times lower than that observed for *L*-lactide (k_{obs} = 0.123 ± 0.001 *vs.* 0.246 ± 0.011 h^{-1}, respectively). Despite proceeding without an induction period, the ROP of ε-caprolactone required 16 hours to reach 80% conversion, compared to less than 11 hours for *L*-lactide. Typically, faster polymerisation rates are anticipated when using ε-caprolactone compared to lactide, owing to its inherently high ring strain and improved solubility.[63, 64] However, the difference in propagation rates may also arise from the relative stability of propagating species formed during monomer insertion, as well as the reactivity of the M-OR bond.[65] Enhanced initiator activity towards lactide has previously been attributed to the presence of two ester groups in lactide contrary to one in ε-caprolactone, providing a greater number of potential sites for monomer coordination and ring-opening.[66]

The polymerisation of ε-caprolactone proceeded with moderate control, as evidenced by a broadened polymer $Đ_M$ of 1.89 and a disparity between its $M_{n,GPC}$ and $M_{n,theo}$ values. Among a limited number of organobismuth initiators studied for ε-caprolactone, superior control has been achieved using the previously discussed planar bismuth triamide complexes ($Đ_M$ = 1.09–1.37), whereas the Ph_2BiOEt initiator, described by Kricheldorf and co-workers, has also suffered from limited control ($Đ_M \geq 1.76$).[9, 67]

Table 3.6 ROP of ε-caprolactone using (NON^{Dipp})Bi(O-2,6-Me-C_6H_3) (**2**).[a]

Conv.[b] **(%)**	k_{obs}[c] **(h^{-1})**	R^2[c]	$M_{n,GPC}$[d] **(g mol^{-1})**	$M_{n,theo}$[e] **(g mol^{-1})**	M_w/M_n[d]
80	0.123 ± 0.001	0.996	5 874	4 688	1.89

[a]Polymerisation conditions: benzene-d_6, 70 °C, $[\varepsilon\text{-CL}]_0/[Bi]_0$ = 50:1, $[\varepsilon\text{-CL}]_0$ = 0.5 M. [b]Measured by ^{1}H NMR spectroscopy; averaged over two repeats. [c]Obtained from plots of $\ln([\varepsilon\text{-CL}]_0/[\varepsilon\text{-CL}]_t)$ *vs.* polymerisation time. [d]Determined by GPC analysis calibrated with PS standards in THF with the appropriate Mark-Houwink corrections.[17] [e]Theoretical M_n for PCL = (conv.(%) × $[\varepsilon\text{-CL}]_0/[Bi]_0$) × 114.14 + ($M_w$ of end groups).

3.5 Conclusions

A series of new di(amido)siloxane bismuth aryloxide and alkoxide complexes proved to be active initiators for the ROP of lactide monomers. The polymerisations displayed significant induction periods, attributed to the first insertion of lactide as the rate-limiting step. The longest induction period observed for **3** was likely due to its most sterically demanding initiating group in the series, hindering monomer binding and/or ring-opening. The k_{obs} values increased in the order of **2** > **1** > **3** ≈ **4**, suggesting that both steric and electronic influences contribute to the polymerisation kinetics. This was further evidenced by comparing the ROP activities of **2** and **5**, as the incorporation of a less sterically demanding and more electron-donating *tert*-butyl substituent on the ligand backbone resulted in a shorter induction period, alongside an increased k_{obs} value.

Moderate polymerisation control, defined by intermediate $Đ_M$ values, was recorded, consistent with previous reports of ROP initiators comprising metals with large ionic radii. The GPC and MALDI-ToF analyses of the isolated PLLAs indicated varying degrees of intra- and intermolecular transesterification processes occurring. From these results, it is evident that subtle variations in the steric profile of both the supporting ligand and the initiating group, as well as the Lewis acidity of the active site, may influence the performance of the initiator regarding the induction period, rate, and control exerted on polymerisation. Compared to more extensively studied complexes based on lighter main group and transition metals, the development of bismuth initiators presents challenges due to their larger coordination spheres and the presence of the $6s^2$ lone pair.

A more in-depth polymerisation study using initiator **2** suggested that the ROP of lactide proceeds *via* a typical coordination-insertion mechanism, which is first-order with respect to monomer and initiator. The relatively high Gibbs free energy of activation, determined

from variable temperature experiments, was ascribed to the sterically congested environment and modest Lewis acidity of the system. Isotactic PLA was obtained from the ROP of *L*- and *D*-lactide, whereas *rac*- and *meso*-lactide polymerisations afforded atactic and slight heterotactic-enriched ($P_m = 0.65$) polymers, respectively. Such relatively low degree of stereocontrol is not unprecedent when large ionic radii metals are employed for ROP initiators.

Finally, **2** polymerised ε-caprolactone with lower activity and reduced polymerisation control relative to *L*-lactide. This disparity may result from differences in the reactivity of **2** in both the initial ring-opening step and chain propagation. Further optimisation of the steric and electronic profile of the di(amido)siloxane ligand framework can be pursued to improve polymerisation rates and control.

Chapter Four explores the influence of introducing the amide initiating group on the initiator activity for the ROP of various cyclic ester monomers.

3.6 References

1. S. Vuorinen, M. Lahcini, T. Hatanpää, M. Sundberg, M. Leskelä and T. Repo, *Macromol. Chem. Phys.*, 2013, **214**, 707-715.
2. H. R. Kricheldorf, H. Hachmann-Thiessen and G. Schwarz, *Biomacromolecules*, 2004, **5**, 492-496.
3. H. R. Kricheldorf and A. Serra, *Polym. Bull.*, 1985, **14**, 497-502.
4. H. R. Kricheldorf, K. Bornhorst and H. Hachmann-Thiessen, *Macromolecules*, 2005, **38**, 5017-5024.
5. V. Balasanthiran, T. L. Beilke and M. H. Chisholm, *Dalton Trans.*, 2013, **42**, 9274-9278.
6. C. Bonné, A. Pahwa, C. Picard and M. Visseaux, *Inorg. Chim. Acta*, 2017, **455**, 521-527.
7. V. Balasanthiran, M. H. Chisholm, C. B. Durr and J. C. Gallucci, *Dalton Trans.*, 2013, **42**, 11234-11241.
8. Z. R. Turner, J. T. Wilmore, N. H. Rees and J.-C. Buffet, *Dalton Trans.*, 2022, **51**, 3060-3074.
9. T. J. Hannah, W. M. McCarvell, T. Kirsch, J. Bedard, T. Hynes, J. Mayho, K. L. Bamford, C. W. Vos, C. M. Kozak, T. George, J. D. Masuda and S. S. Chitnis, *Chem. Sci.*, 2023, **14**, 4549-4563.

10. D. Cheshmedzhieva, I. Angelova, S. Ilieva, G. S. Georgiev and B. Galabov, *Comput. Theor. Chem.*, 2012, **995**, 8-16.

11. P. Dubois, C. Jacobs, R. Jerome and P. Teyssie, *Macromolecules*, 1991, **24**, 2266-2270.

12. W. M. Stevels, M. J. K. Ankoné, P. J. Dijkstra and J. Feijen, *Macromolecules*, 1996, **29**, 6132-6138.

13. T. Ouhadi, C. Stevens and P. Teyssié, *Makromol. Chem.*, 1975, **1**, 191-201.

14. S. Fortun, P. Daneshmand and F. Schaper, *Angew. Chem. Int. Ed.*, 2015, **54**, 13669-13672.

15. A. P. Dove, V. C. Gibson, E. L. Marshall, H. S. Rzepa, A. J. P. White and D. J. Williams, *J. Am. Chem. Soc.*, 2006, **128**, 9834-9843.

16. R. H. Platel, L. M. Hodgson and C. K. Williams, *Polym. Rev.*, 2008, **48**, 11-63.

17. J. R. Dorgan, J. Janzen, D. M. Knauss, S. B. Hait, B. R. Limoges and M. H. Hutchinson, *J. Polym. Sci., Part B: Polym. Phys.*, 2005, **43**, 3100-3111.

18. X. Tang, M. Hong, L. Falivene, L. Caporaso, L. Cavallo and E. Y. X. Chen, *J. Am. Chem. Soc.*, 2016, **138**, 14326-14337.

19. R. J. Schwamm, J. R. Harmer, M. Lein, C. M. Fitchett, S. Granville and M. P. Coles, *Angew. Chem. Int. Ed.*, 2015, **54**, 10630-10633.

20. R. J. Schwamm, M. Lein, M. P. Coles and C. M. Fitchett, *Angew. Chem. Int. Ed.*, 2016, **55**, 14798-14801.

21. C. Nakonkhet, T. Nanok, W. Wattanathana, P. Chuawong and P. Hormnirun, *Dalton Trans.*, 2017, **46**, 11013-11030.

22. Z. Tang and V. C. Gibson, *Eur. Polym. J.*, 2007, **43**, 150-155.

23. H. Du, X. Pang, H. Yu, X. Zhuang, X. Chen, D. Cui, X. Wang and X. Jing, *Macromolecules*, 2007, **40**, 1904-1913.

24. C. Bakewell, A. J. P. White, N. J. Long and C. K. Williams, *Inorg. Chem.*, 2013, **52**, 12561-12567.

25. H. von Schenck, M. Ryner, A.-C. Albertsson and M. Svensson, *Macromolecules*, 2002, **35**, 1556-1562.

26. C. K. Williams, L. E. Breyfogle, S. K. Choi, W. Nam, V. G. Young, M. A. Hillmyer and W. B. Tolman, *J. Am. Chem. Soc.*, 2003, **125**, 11350-11359.

27. P. Hormnirun, E. L. Marshall, V. C. Gibson, R. I. Pugh and A. J. P. White, *Proc. Nat. Acad. Sci.*, 2006, **103**, 15343-15348.

28. A. J. Chmura, M. G. Davidson, M. D. Jones, M. D. Lunn, M. F. Mahon, A. F. Johnson, P. Khunkamchoo, S. L. Roberts and S. S. F. Wong, *Macromolecules*, 2006, **39**, 7250-7257.

29. Z. R. Turner, J.-C. Buffet and D. O'Hare, *Organometallics*, 2014, **33**, 3891-3903.

30. W. Punyodom, P. Meepowpan, S. Girdthep and W. Limwanich, *Polym. Bull.*, 2022, **79**, 11409-11429.

31. B. J. O'Keefe, L. E. Breyfogle, M. A. Hillmyer and W. B. Tolman, *J. Am. Chem. Soc.*, 2002, **124**, 4384-4393.

32. M. G. Ortiz-Aldaco, J. E. Báez and J. O. C. Jiménez-Halla, *RSC Adv.*, 2020, **10**, 30815-30824.

33. N. Diteepeng, J.-C. Buffet, Z. R. Turner and D. O'Hare, *Dalton Trans.*, 2019, **48**, 16099-16107.
34. Z. R. Turner, J. V. Lamb, T. P. Robinson, D. Mandal, J.-C. Buffet and D. O'Hare, *Dalton Trans.*, 2021, **50**, 4805-4818.
35. K. B. Aubrecht, M. A. Hillmyer and W. B. Tolman, *Macromolecules*, 2002, **35**, 644-650.
36. N. Ropson, P. Dubois, R. Jérôme and P. Teyssié, *Macromolecules*, 1995, **28**, 7589-7598.
37. H. Du, A. H. Velders, P. J. Dijkstra, Z. Zhong, X. Chen and J. Feijen, *Macromolecules*, 2009, **42**, 1058-1066.
38. M. H. Chisholm, N. W. Eilerts, J. C. Huffman, S. S. Iyer, M. Pacold and K. Phomphrai, *J. Am. Chem. Soc.*, 2000, **122**, 11845-11854.
39. J. S. Thayer, *J. Chem. Educ.*, 2005, **82**, 1721.
40. J. M. Lipshultz, G. Li and A. T. Radosevich, *J. Am. Chem. Soc.*, 2021, **143**, 1699-1721.
41. B. M. Chamberlain, M. Cheng, D. R. Moore, T. M. Ovitt, E. B. Lobkovsky and G. W. Coates, *J. Am. Chem. Soc.*, 2001, **123**, 3229-3238.
42. L. Wang, V. Poirier, F. Ghiotto, M. Bochmann, R. D. Cannon, J.-F. Carpentier and Y. Sarazin, *Macromolecules*, 2014, **47**, 2574-2584.
43. E. Grunova, E. Kirillov, T. Roisnel and J.-F. Carpentier, *Dalton Trans.*, 2010, **39**, 6739-6752.
44. C. Wei, B. Han, D. Zheng, Q. Zheng, S. Liu and Z. Li, *Organometallics*, 2019, **38**, 3816-3823.
45. J.-C. Buffet and J. Okuda, *Polym. Chem.*, 2011, **2**, 2758-2763.
46. J. V. Lamb, J.-C. Buffet, J. E. Matley, C. M. R. Wright, Z. R. Turner and D. O'Hare, *Dalton Trans.*, 2019, **48**, 2510-2520.
47. J. Coudane, C. Ustariz-Peyret, G. Schwach and M. Vert, *J. Polym. Sci., Part A: Polym. Chem.*, 1997, **35**, 1651-1658.
48. M. J. Stanford and A. P. Dove, *Chem. Soc. Rev.*, 2010, **39**, 486.
49. N. Maudoux, T. Roisnel, V. Dorcet, J.-F. Carpentier and Y. Sarazin, *Chem. Eur. J.*, 2014, **20**, 6131-6147.
50. C. Robert, T. E. Schmid, V. Richard, P. Haquette, S. K. Raman, M.-N. Rager, R. M. Gauvin, Y. Morin, X. Trivelli, V. Guérineau, I. del Rosal, L. Maron and C. M. Thomas, *J. Am. Chem. Soc.*, 2017, **139**, 6217-6225.
51. A. F. Douglas, B. O. Patrick and P. Mehrkhodavandi, *Angew. Chem. Int. Ed.*, 2008, **47**, 2290-2293.
52. D. R. Witzke, R. Narayan and J. J. Kolstad, *Macromolecules*, 1997, **30**, 7075-7085.
53. M. H. Chisholm and E. E. Delbridge, *New J. Chem.*, 2003, **27**, 1177-1183.
54. W. Gruszka and J. A. Garden, *Chem. Commun.*, 2022, **58**, 1609-1612.
55. H. R. Kricheldorf, G. Behnken and G. Schwarz, *J. Polym. Sci., Part A: Polym. Chem.*, 2008, **46**, 851-859.
56. M. H. Chisholm and E. E. Delbridge, *New J. Chem.*, 2003, **27**, 1167-1176.
57. H. Ma and J. Okuda, *Macromolecules*, 2005, **38**, 2665-2673.
58. H. Ma, T. P. Spaniol and J. Okuda, *Angew. Chem. Int. Ed.*, 2006, **45**, 7818-7821.

59. M. H. Chisholm, J. C. Gallucci, K. T. Quisenberry and Z. Zhou, *Inorg. Chem.*, 2008, **47**, 2613-2624.

60. V. Poirier, T. Roisnel, S. Sinbandhit, M. Bochmann, J.-F. Carpentier and Y. Sarazin, *Chem. Eur. J.*, 2012, **18**, 2998-3013.

61. M. Labet and W. Thielemans, *Chem. Soc. Rev.*, 2009, **38**, 3484-3504.

62. P. Dubois, N. Ropson, R. Jérôme and P. Teyssié, *Macromolecules*, 1996, **29**, 1965-1975.

63. W. Gruszka, L. C. Walker, M. P. Shaver and J. A. Garden, *Macromolecules*, 2020, **53**, 4294-4302.

64. W. Gruszka, A. Lykkeberg, G. S. Nichol, M. P. Shaver, A. Buchard and J. A. Garden, *Chem. Sci.*, 2020, **11**, 11785-11790.

65. C. Diaz, J. Fu, S. Soobrattee, L. Cao, K. Nyamayaro, C. Goonesinghe, B. O. Patrick and P. Mehrkhodavandi, *Inorg. Chem.*, 2022, **61**, 3763-3773.

66. D. J. Darensbourg and O. Karroonnirun, *Macromolecules*, 2010, **43**, 8880-8886.

67. M. Lahcini, G. Schwarz and H. R. Kricheldorf, *J. Polym. Sci., Part A: Polym. Chem.*, 2008, **46**, 7483-7490.

Chapter 4

Ring-opening polymerisation of cyclic esters using a di(amido)siloxane bismuth amide initiator

4.1 Introduction

Extensive research has been undertaken to elucidate the underlying mechanisms for the ROP of cyclic esters by probing the reactivity of initiators towards a single monomer unit. Several studies have demonstrated that compounds formed during the first monomer ring-opening event are representative of propagating species, thus providing deeper insights into polymerisation rates and stereocontrol.[1-7]

The ring-opening step of a lactide or lactone molecule is key in the ROP initiation process, generally determined by the properties of both the monomer and the initiator. Enhanced nucleophilicity of an initiating group, combined with the reduced steric bulk of coordinated ligands, is proposed to accelerate the monomer insertion step.[8] In terms of the monomer, factors such as its substitution pattern, which is in turn correlated with the electrophilicity of the carbonyl group and the overall steric demand, can also influence its susceptibility to ring-opening.[9] Following initiation, the relative stability of the

resulting ring-opened intermediate is crucial in determining the propagation activity.[4] For example, the introduction of sterically bulky substituents on the ligand backbone has been shown to enhance the activity of the ROP intermediates comprising ring-opened lactide units by reducing the chelate effect.[4]

Lactate (OCH(Me)C(O)R) and lactyl lactate (OCH(Me)C(O)OCH(Me)C(O)R) ligands act as models of the propagating intermediates of lactide polymerisation. A variety of the corresponding complexes spanning transition, main group, and rare-earth metals have been characterised crystallographically.[2, 5, 10-20] However, only four of the structurally authenticated complexes have been formed *via* the ring-opening of lactide, thus providing a more accurate representation of the active species involved in the polymerisation. Aside from these compounds, examples of ROP intermediates resulting from the coordination of lactide preceding the ring-opening step have not been yet isolated.

The insertion of a *rac*-lactide molecule into an M-O bond was first reported by Lewinski and co-workers using a dimeric dialkyl aluminium compound with bridging alkoxide groups $[Me_2Al(\mu\text{-}OCH_2CH_2OMe)]_2$.[4] Despite its relatively low reactivity and poor selectivity (96 hours, 40 °C), the reaction using two equivalents of *rac*-lactide resulted in the formation of $[Me_2Al(\mu\text{-}OCH(Me)C(O))_2O(CH_2)_2OMe]_2$ as an isolable *rac*-lactate dimer (**Figure 4.1a**). The enhanced stability of the lactate chelate was found to supress its polymerisation activity at ambient temperatures. As a result, the ROP of *rac*-lactide proceeded with slow kinetics (24 hours, 70 °C).

A cationic amino-phenolato aluminium complex $[(L)Al(O^iPr)(THF)][B(C_6F_5)_4]$, described by Dagorne and co-workers, was shown to insert *L*-lactide to form a chiral aluminium lactate cation (**Figure 4.1b**).[21] This compound proved to be inactive in the

polymerisation of lactide even at 100 °C, attributed to a strong chelate effect, reinforced by the high electrophilicity of the metal centre.

Williams and co-workers demonstrated that their phosphasalen indium *tert*-butoxide initiator readily inserts *D*-lactide into the In-O bond, forming a transesterified five-membered chelate (**Figure 4.1c**).[5] The reaction, however, was not selective, resulting in the concomitant formation of oligomeric species, ascribed to transesterification processes. This compound was proposed to act as the propagating intermediate in the polymerisation of *rac*-lactide, affording highly isotactic PLA (P_m of up to 0.92) *via* a chain-end control mechanism.

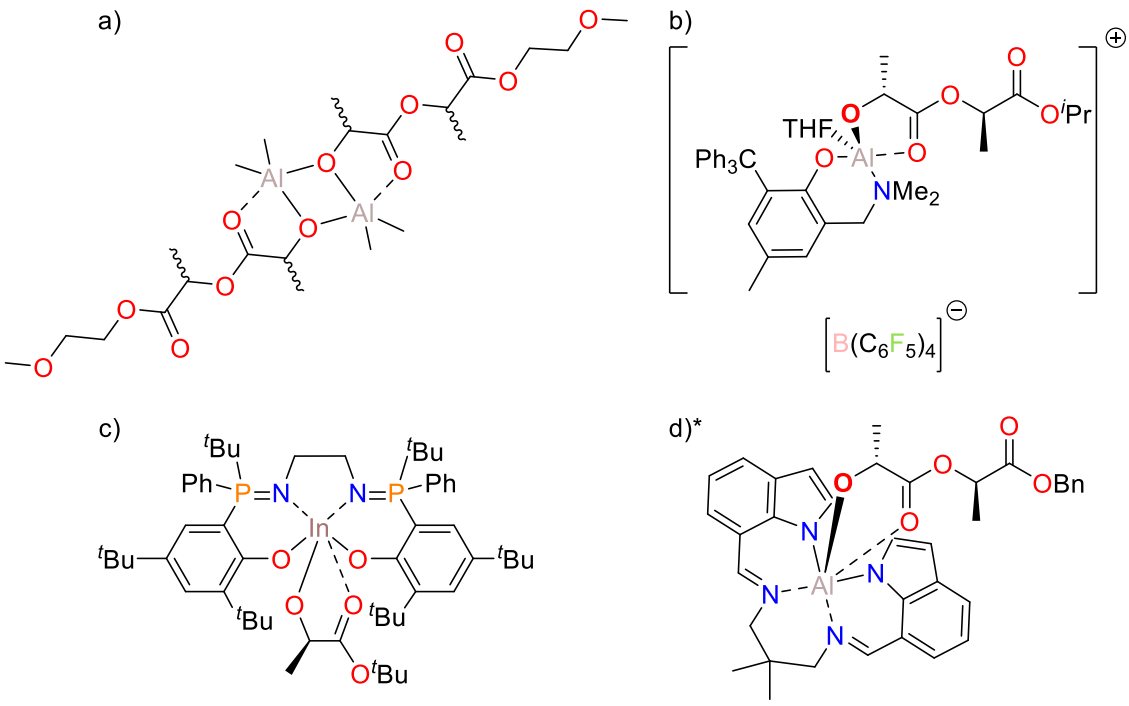


Figure 4.1 Examples of structurally characterised metal lactyl lactate and lactate compounds formed during the ring-opening of a lactide monomer. * represents a single enantiomer.

Tolman and co-workers studied a ring-opening reaction of *rac*-lactide using two different aluminium alkoxides, (L)Al(OBn), bearing an indoline-imine ligand, connected at either the 7-position (**Figure 4.1d**) or the 2-position.[22] Their mechanistic analysis suggested

that the relative thermodynamic stability of rapidly interconverting diastereomeric ring-opened products was responsible for the isoselectivity of the initiator observed in the ROP of *rac*-lactide (P_m of up to 0.92).

Studies of model compounds mimicking propagating intermediates involved in the ROP of lactones are rare. These examples include a family of aluminium and yttrium complexes supported by a tridentate pyridine *bis*(phenolato) ligand, (ONO)M((*R*)-OCH(Me)CH_2C(O)OMe), prepared as catalytic intermediates for the ROP of *rac*-β-butyrolactone using methyl (*R*)-3-hydroxybutyrate as a precursor.[12] The molecular structures of the resultant six-membered metallacycles confirmed the coordination of the ester carbonyl group to the metal centre, consistent with the bonding environment observed for κ^2-*O,O'*-chelating lactate ligands.

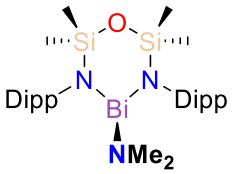
Additionally, the capability of a Lewis acidic metal complex to form a Lewis acid-base adduct with a lactone molecule has been demonstrated on several occasions. Such species featuring various coordinated lactones: ε-caprolactone, γ-butyrolactone, γ-valerolactone, and β-propiolactone, have been prepared using rare-earth, rhenium, aluminium, and lithium compounds.[21, 23-28] A series of recently reported structures of lactone adducts, based on amine *tris*(phenolate) ligand-supported niobium(V) and tantalum(V) ethoxide complexes (L)M(OEt)Cl, represent unprecedented model compounds for catalytic ROP intermediates.[1, 29] At ambient temperatures, these initiators reacted with ε-caprolactone and δ-valerolactone substrates without monomer ring-opening, resulting in the formation of new adduct compounds, with both the lactone molecule and the ethoxide initiating group coordinated to the metal centre. The analogous reaction to prepare a lactide adduct proved to be unfeasible due to the increased steric bulk of the monomer. At temperatures above 60 °C, both niobium(V) and tantalum(V) systems were found to be active for the

ROP of ε-caprolactone, *rac*-β-butyrolactone, and δ-valerolactone, demonstrating moderate polymerisation control ($Đ_M$ = 1.24–1.90).[29]

4.2 Synopsis

Chapter Four explores the capability of the di(amido)siloxane bismuth amide complex **6** ((NON^{Dipp})Bi(NMe$_2$); **Figure 4.2**) to initiate the ROP of various cyclic ester monomers, including lactide, ε-caprolactone, and γ-butyrolactone. Differences in the observed ROP activity have been discussed by examining the reactivity of **6** towards the insertion of a single monomer molecule.

As the main focus of this Chapter, the ROP of lactide has been studied with respect to monomer stereochemistry, initiator concentration, and reaction temperature to assess the rates and control of polymerisation. The characterisation of the produced polymers has been conducted using NMR spectroscopy, mass spectrometry, and GPC analyses.



6

Figure 4.2 Di(amido)siloxane bismuth amide **6** investigated as a ROP initiator in **Chapter Four**.

4.3 Lactide polymerisation studies

Polymerisations were conducted in J. Young's tap NMR spectroscopy tubes with an initial lactide monomer concentration ([*L*-LA]$_0$) of 0.5 M in 0.6 mL of benzene-d_6. The reactions were monitored by ^{1}H NMR spectroscopy and halted by cooling in an ice bath, followed by quenching with wet pentane.

4.3.1 Monomer stereochemistry variation

The ROP activity of (NON^{Dipp})Bi(NMe$_2$) (**6**) towards *L*-, *D*-, *rac*-, and *meso*-lactide stereoisomers was investigated (**Figure 4.3**, **Table 4.1**).

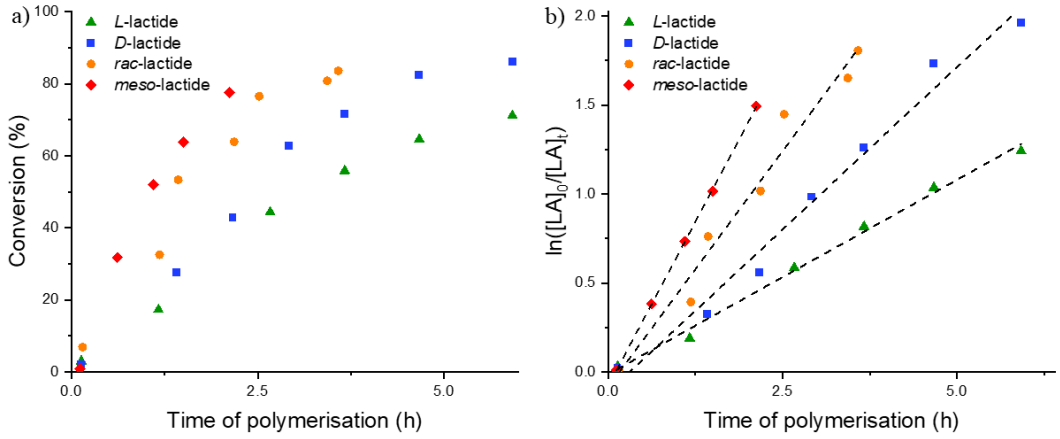


Figure 4.3 a) Plots of percentage conversion *vs*. polymerisation time for lactide polymerisation. b) Plots of $\ln([LA]_0/[LA]_t)$ *vs*. polymerisation time for lactide polymerisation. Green up triangles: *L*-LA, k_{obs} = 0.219 ± 0.008 h^{-1}, R^2 = 0.994; blue squares: *D*-LA, k_{obs} = 0.365 ± 0.022 h^{-1}, R^2 = 0.982; orange circles: *rac*-LA, k_{obs} = 0.531 ± 0.041 h^{-1}, R^2 = 0.971; red rhombi: *meso*-LA, k_{obs} = 0.738 ± 0.005 h^{-1}, R^2 = 0.999. Polymerisation conditions: benzene-d_6, 50 °C, $[LA]_0/[Bi]_0$ = 50:1, and $[LA]_0$ = 0.5 M.

Generally, monomer percentage conversion can be determined by quantifying the relative ratio of monomer to polymer based on the integration of their *methine* proton regions in ^{1}H NMR spectra. Using **6** as an initiator, direct interpretation of these resonance integrations was not feasible due to signal broadening, and deconvoluted *methine* proton regions were analysed instead (see **Figure A.3.1** in **Appendix** for a representative ^{1}H NMR spectrum). The observed broadening of the signals corresponding to lactide is tentatively attributed to the aggregation and/or dynamic coordination behaviour of propagating species. The tendency of bismuth amide compounds to form aggregates in solution has been well-documented.[30-33] For example, Lichtenberg and co-workers

proposed that dinuclear cationic bismuth amide complexes $[(L)Bi(OTf)(THF)_x]_2$ and their related derivatives, formed upon insertion of an unsaturated molecule into the Bi-N bond, were prone to aggregation in solution, indicated by comparable signal broadening in their room-temperature ^{1}H NMR spectra.[31-33] Although aggregation of active species has been typically found to supress initiator catalytic performance, ROP initiated by **6** proceeded with relatively good control (*vide infra*).[34, 35]

A linear relationship in the plots of $\ln([LA]_0/[LA]_t)$ *vs*. polymerisation time was confirmed for all four monomers (**Figure 4.3b**), indicating a first-order dependence on monomer concentration. The polymerisations proceeded without an induction period, contrary to the observations made using bismuth aryloxide and alkoxide initiators **1**–**5**, as discussed in **Chapter Three**. This suggests that the ring-opening of lactide using **6** is relatively facile, likely due to the enhanced lability of the Bi-N bond relative to the Bi-O bond (see **Section 4.3.6** for further discussion). Furthermore, **6** demonstrated a four-fold increase in the polymerisation rate for *L*-lactide with respect to initiator **2**. The ROP initiation capability of **6** is also superior to that of a series of previously reported tin(II) amide initiators (BDI)Sn(NMe_2), which exhibited induction periods of more than 2 hours at 60 °C.[16] Interestingly, these tin amide complexes resulted in longer induction periods and slower polymerisation rates than their *iso*propoxide counterparts. The authors attributed the less efficient initiation by the amide compounds to their relatively greater steric demands.

The polymerisation of *meso*-lactide displayed the fastest rate (k_{obs} = 0.738 ± 0.005 h^{-1}), consistent with the high ground-state energy of the monomer.[36] *rac*-Lactide was polymerised faster than *D*-lactide, followed by *L*-lactide polymerisation (k_{obs} = 0.531 ± 0.041 h^{-1} (*rac*-LA) > 0.365 ± 0.022 h^{-1} (*D*-LA) > 0.219 ± 0.008 h^{-1}

(*L*-LA)). A comparable trend in polymerisation activity was also seen in the study of **2** (**Chapter Three**, **Section 3.3.4**).

The polymerisation of *meso*-, *D*-, and *L*-lactide resulted in monomodal, intermediate polymer molecular weight distributions ($Đ_M$ = 1.22–1.36) (**Figure 4.4**). In contrast, poorer polymerisation control was observed for *rac*-lactide, indicated by its broadened, bimodal molecular weight distribution ($Đ_M$ = 2.07).

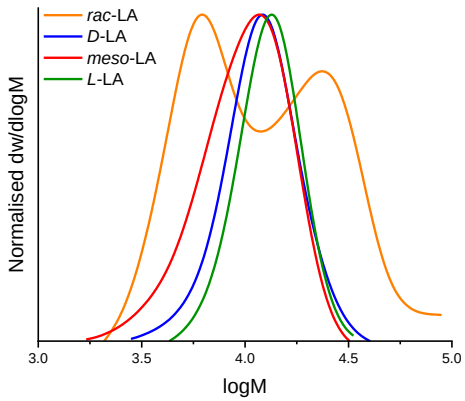


Figure 4.4 GPC plots of the PLAs produced from *rac*-LA (orange, M_n = 5 063 g mol^{-1}, $Đ_M$ = 2.07); *D*-LA (blue, M_n = 6 167 g mol^{-1}, $Đ_M$ = 1.22); *meso*-LA (red, M_n = 4 768 g mol^{-1}, $Đ_M$ = 1.33); *L*-LA (green, M_n = 5 207 g mol^{-1}, $Đ_M$ = 1.36). Polymerisation conditions: benzene-d_6, 50 °C, $[LA]_0/[Bi]_0$ = 50:1, and $[LA]_0$ = 0.5 M.

The presence of bimodal polymer GPC traces is commonly associated for rapid, poorly controlled ROP.[37, 38] The bimodality has been proposed to result from the formation of two distinct PLA structures, cyclic and linear, with the former eluting at longer retention times due to its smaller hydrodynamic radius.[39, 40] While the possibility of cyclic PLA formation cannot be ruled out in this case, analysis of the isolated polymer sample by MALDI-ToF mass spectrometry provided no evidence for cyclic products (**Figure A.3.2** in **Appendix**). Alternatively, the bimodal nature of the GPC trace may be indicative of

different types of active species present in solution; this is plausible for the use of **6**, given its susceptibility to transesterification and aggregation.[41, 42]

Polymers produced from *L*- and *D*-lactide were defined by a relatively good agreement between their $M_{n,GPC}$ and $M_{n,theo}$ values, whereas lower than expected polymer molecular weights were recorded for both *rac*- and *meso*-lactide. These results suggest that the formation of *racemic* and *meso* linkages in the polymer chain was susceptible to transesterification side reactions.

Table 4.1 ROP of *L*-, *D*-, *rac*-, and *meso*-lactide monomers using (NON^{Dipp})Bi(NMe$_2$) (**6**).[a]

Monomer	**Conv.**[b] **(%)**	k_{obs}[c] **(h^{-1})**	R^{2}[c]	$M_{n,GPC}$[d] **(g mol^{-1})**	$M_{n,theo}$[e] **(g mol^{-1})**	M_w/M_n[d]
L-LA	78	0.219 ± 0.008	0.994	5 207	5 743	1.36
D-LA	96	0.365 ± 0.022	0.982	6 167	6 963	1.22
meso-LA	84	0.738 ± 0.005	0.999	4 768	6 099	1.33
rac-LA	83	0.531 ± 0.041	0.971	5 063	6 026	2.07

[a]Polymerisation conditions: benzene-d_6, 50 °C, $[LA]_0/[Bi]_0$ = 50:1, $[LA]_0$ = 0.5 M. [b]Measured by ^{1}H NMR spectroscopy. [c]Obtained from plots of $\ln([LA]_0/[LA]_t)$ *vs.* polymerisation time. [d]Determined by GPC analysis calibrated with PS standards in THF with the appropriate Mark-Houwink corrections.[43] [e]Theoretical M_n for PLA = (conv.(%) × $[LA]_0/[Bi]_0$) × 144.13 + (M_w of end groups).

To assess the stereoselectivity of **6**, the isolated polymers were analysed by ^{1}H{^{1}H} NMR spectroscopy using the Bernoulli model.[44] The polymerisation of *L*- and *D*-lactide revealed the absence of epimerisation, with isotactic polymers formed (P_m = 1.00) (**Figure 4.5a**). The polymerisation of *meso*-lactide produced heterotactic-enriched PLA (P_m = 0.86) (**Figure 4.5b**), likely proceeding *via* a chain-end control mechanism, where *meso*-enchainment is favoured by the last monomer unit inserted in the propagating chain. The relatively high degree of stereoselectivity imparted by **6** compared to that of aryloxide initiator **2** (P_m = 0.65) can be attributed to improved polymerisation control and

more efficient initiation in the presence of **6**. To date, there are very few reported examples of bismuth initiators active for the ROP of *meso*-lactide.[2, 45] While operating *via* an analogous chain end mechanism, a series of pyridine dipyrrolide bismuth aryloxide initiators, ($L^{Mes,Ph}$)Bi(OR), exhibited a significantly lower heterotactic bias (P_m = 0.54–0.56).[2]

In contrast, atactic PLA (P_r = 0.50) was formed during the polymerisation of *rac*-lactide (**Figure 4.5c**). This is surprising considering previous studies, which associated the enhanced polymerisation rate for *rac*-lactide relative to *L*- and *D*-lactide, as seen in the case of **6**, with stereocontrol mechanisms leading to the preferential formation of either *meso* or *racemic* linkages.[13, 46] However, poor polymerisation control is likely to account for the lack of stereoselectivity of **6** in the ROP of *rac*-lactide.

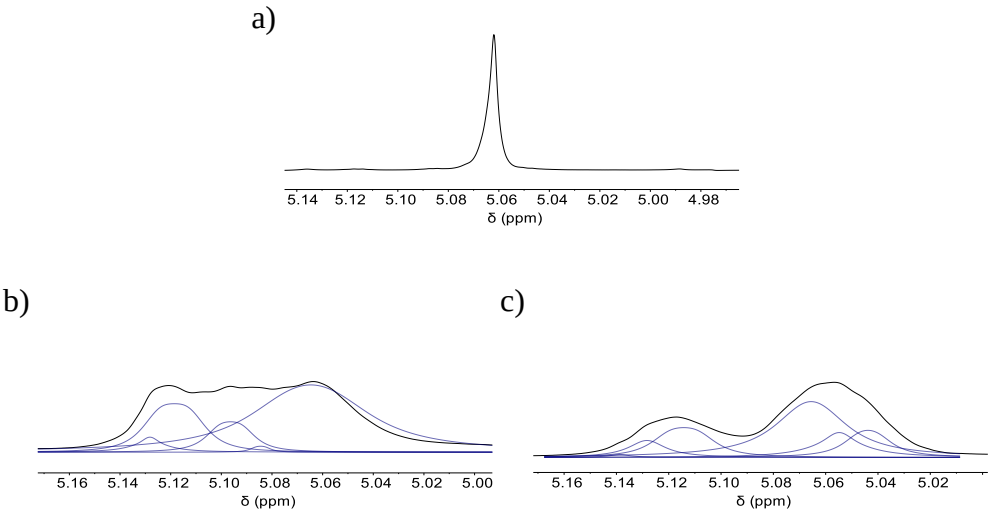


Figure 4.5 $^{1}H\{^{1}H\}$ NMR spectra (chloroform-d_1, 500 MHz, 298 K) of the *methine* protons in the PLAs produced by **6** from a) *L*- and *D*-LA (P_m = 1.00), b) *meso*-LA (P_m = 0.85), c) *rac*-LA (P_r = 0.50). Polymerisation conditions: benzene-d_6, 50 °C, $[LA]_0/[Bi]_0$ = 50:1, and $[LA]_0$ = 0.5 M.

4.3.2 Initiator concentration dependence

The rates and control of the polymerisation of *L*-lactide were examined at various initiator loadings ([*L*-LA]$_0$:[Bi]$_0$ = 50:1, 100:1, 200:1, 300:1) in benzene-d_6 at 50 °C (**Figure 4.6**, **Table 4.2**).

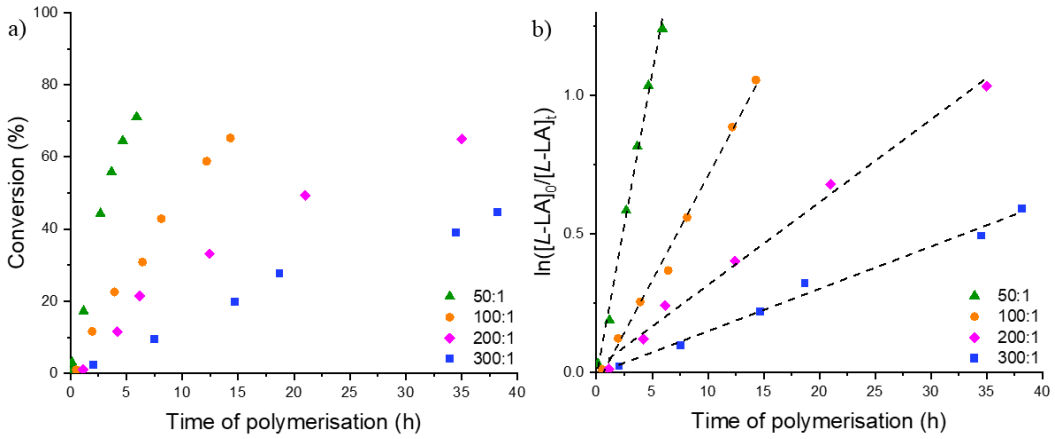


Figure 4.6 a) Plots of percentage conversion *vs*. polymerisation time for *L*-lactide polymerisation. b) Plots of ln([*L*-LA]$_0$/[*L*-LA]$_t$) *vs*. polymerisation time for *L*-lactide polymerisation. Green up triangles: [*L*-LA]$_0$:[**6**]$_0$ = 50:1, k_{obs} = 0.219 ± 0.008 h^{-1}, R^2 = 0.994; orange circles: [*L*-LA]$_0$:[**6**]$_0$ = 100:1, k_{obs} = 0.076 ± 0.003 h^{-1}, R^2 = 0.993; pink rhombi: [*L*-LA]$_0$:[**6**]$_0$ = 200:1, k_{obs} = 0.030 ± 0.001 h^{-1}, R^2 = 0.992; blue squares: [*L*-LA]$_0$:[**6**]$_0$ = 300:1, k_{obs} = 0.015 ± 0.001 h^{-1}, R^2 = 0.988. Polymerisation conditions: benzene-d_6, 50 °C, [*L*-LA]$_0$ = 0.5 M.

All polymerisations followed a first-order dependence on monomer concentration, as evidenced by the linear fits to plots of ln([*L*-LA]$_0$/[*L*-LA]$_t$) *vs.* polymerisation time (**Figure 4.6b**). As expected, polymerisation rates increased in parallel with the reduced concentration of **6** (k_{obs} = 0.219 ± 0.008 h^{-1} ([LA]$_0$/[Bi]$_0$ = 50:1) > 0.030 ± 0.001 h^{-1} ([LA]$_0$/[Bi]$_0$ = 200:1)). A decrease in initiator concentration, accompanied by a reduction of active bismuth sites, also resulted in an increase in polymer $M_{n,GPC}$ values ($M_{n,GPC}$ = 26 848 g mol^{-1} ([LA]$_0$/[Bi]$_0$ = 200:1) > 5 207 g mol^{-1} ([LA]$_0$/[Bi]$_0$ = 50:1)).

At lower initiator loadings, $M_{n,GPC}$ was found to be slightly higher than expected (e.g. $M_{n,GPC}$ = 26 848 *vs.* $M_{n,theo}$ = 23 106 g mol^{-1} ([LA]$_0$/[Bi]$_0$ = 200:1)) (**Table 4.2**). These observations imply that not all of the bismuth centres were active during the corresponding polymerisations, presumably due to extended reaction times.[47] Overall, relatively good polymerisation control was maintained at all initiator loadings ($Đ_M$ = 1.15–1.36) (**Figure 4.7**).

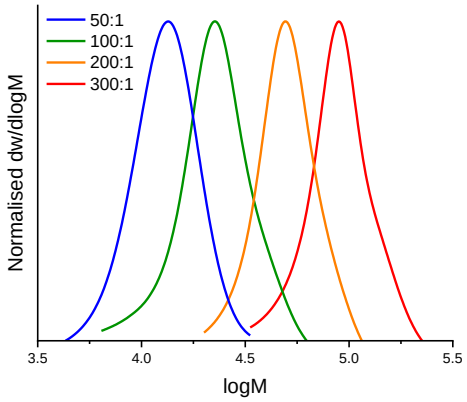


Figure 4.7 GPC plots of the PLLAs produced with [*L*-LA]$_0$:[**6**]$_0$ = 50:1 (blue, M_n = 5 207 g mol^{-1}, $Đ_M$ = 1.36); [*L*-LA]$_0$:[**6**]$_0$ = 100:1 (green, M_n = 11 522 g mol^{-1}, $Đ_M$ = 1.22); [*L*-LA]$_0$:[**6**]$_0$ = 200:1 (orange, M_n = 26 848 g mol^{-1}, $Đ_M$ = 1.14); [*L*-LA]$_0$:[**6**]$_0$ = 300:1 (red, M_n = 35 462 g mol^{-1}, $Đ_M$ = 1.15). Polymerisation conditions: benzene-d_6, 50 °C, [*L*-LA]$_0$ = 0.5 M.

A linear relationship of $-\ln(k_{obs})$ *vs.* $-\ln([Bi]_0)$ displayed a gradient of 1.45 ± 0.21 (R^2 = 0.961) (**Figure 4.8a**), indicative of a first-order dependence on initiator within the associated error. A non-integer dependence of up to 1.56 has been previously attributed to the aggregation of catalytically active species resulting in different levels of ROP activity, although its mechanistic interpretation is not well-understood.[13, 48-50] In the case of **6**, these results may suggest the occurrence of complex equilibria involving transesterified and/or aggregated polymerisation intermediates (see **Section 4.3.4** for further discussion).

Table 4.2 ROP of *L*-lactide at different $[L\text{-LA}]_0/[\text{Bi}]_0$ ratios using $(\text{NON}^{\text{Dipp}})\text{Bi}(\text{NMe}_2)$ (**6**).[a]

$[L\text{-LA}]_0/[\text{Bi}]_0$	Conv.[b] (%)	k_{obs}[c] (h^{-1})	R^2[c]	$M_{n,GPC}$[d] (g mol^{-1})	$M_{n,theo}$[e] (g mol^{-1})	M_w/M_n[d]
50:1	78	0.219 ± 0.008	0.994	5 207	5 378	1.36
100:1	84	0.076 ± 0.003	0.993	11 522	12 152	1.22
200:1	80	0.030 ± 0.001	0.992	26 848	23 106	1.14
300:1	77	0.015 ± 0.001	0.988	35 462	33 339	1.15

[a]Polymerisation conditions: benzene-d_6, 50 °C, $[L\text{-LA}]_0$ = 0.5 M. [b]Measured by ^{1}H NMR spectroscopy. [c]Obtained from plots of $\ln([L\text{-LA}]_0/[L\text{-LA}]_t)$ *vs.* polymerisation time. [d]Determined by GPC analysis calibrated with PS standards in THF with the appropriate Mark-Houwink corrections.[43] [e]Theoretical M_n for PLA = (conv.(%) × $[L\text{-LA}]_0/[\text{Bi}]_0$) × 144.13 + ($M_w$ of end groups).

A plot of k_{obs} *vs.* $[\text{Bi}]_0$ was constructed, and the k_p value for **6** was determined to be 24.68 ± 1.82 M^{-1} h^{-1} (R^2 = 0.988) (**Figure 4.8b**). The idealised overall rate law for the ROP of *L*-lactide is therefore described by **Equation 4.1**.

$$-\frac{d[\text{LA}]}{dt} = k_p[\text{LA}]_0[\mathbf{6}]_0$$

Where k_p = 24.68 ± 1.82 M^{-1} h^{-1}.

Equation 4.1 Definition of the rate law for the ROP of *L*-lactide using **6**, where k_p = propagation rate constant, $[\text{LA}]_0$ = initial lactide concentration, $[\mathbf{6}]_0$ = initial initiator concentration.

The amide initiator **6** appeared to be significantly more active towards *L*-lactide than its aryloxide counterpart **2** (k_p = 17.56 ± 4.68 M^{-1} h^{-1} at 70 °C), while maintaining comparable levels of polymerisation control. The relative lability of the Bi-N bond is likely to contribute to the enhanced ROP capability of **6**. Its versatile reactivity is further explored in **Chapter Five**.

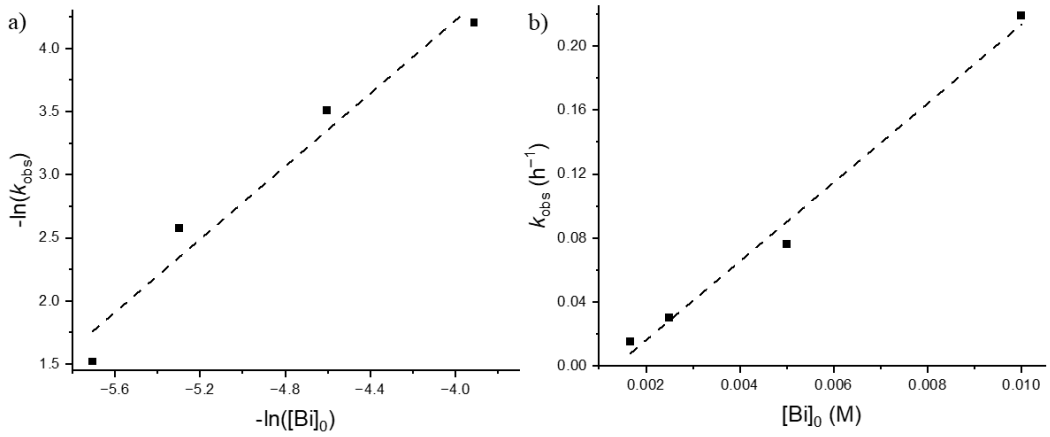


Figure 4.8 a) Plot of $-\ln(k_{obs})$ *vs.* $-\ln([Bi]_0)$ for *L*-lactide polymerisation using **6**; slope = 1.45 ± 0.21 (R^2 = 0.961). b) Plot of k_{obs} *vs.* $[Bi]_0$ for *L*-lactide polymerisation using **6**; slope = 24.68 ± 1.82 M^{-1} h^{-1} (R^2 = 0.988). Polymerisation conditions: benzene-d_6, 50 °C, $[L\text{-LA}]_0$ = 0.5 M.

Generally, metal alkoxide and aryloxide initiators have been shown to afford fast, well-controlled ROP due their relatively high nucleophilicity.[16, 51, 52] While the opposite trend is rare, similar observations have nevertheless been reported using several rare-earth systems, exhibiting enhanced activities with respect to their alkoxide/aryloxide counterparts. For example, ytterbium *bis*(trimethylsilyl)amide, supported by a five-coordinate Schiff base ligand, resulted in 90% conversion of *rac*-lactide within 5 minutes with good polymerisation control ($Đ_M$ = 1.19), compared to 70% conversion observed for its aryloxide analogue ($Đ_M$ = 1.21) (25 °C with $[rac\text{-LA}]_0/[Yb]_0$ = 500:1).[53] In the study of salalen lanthanide complexes, relatively slow ROP rates seen using alkoxide compounds relative to the *bis*(trimethylsilyl)amide derivatives were rationalised by the tendency of the former compounds to form alkoxo-bridged clusters in solution.[54]

In a wider context, the activity of **6** is modest compared to other Lewis acidic metal amide and silylamide initiators. Despite trivalent lanthanum and bismuth metals having similar ionic radii (1.032 and 1.030 Å, respectively),[55] a significantly higher activity has been

reported for a lanthanum phenolate complex $(L)_2La\{N(SiMe_3)_2\}$ ($k_p = 2.9 \times 10^4$ M^{-2} h^{-1} at 25 °C).[56] Similarly, a faster polymerisation rate has been achieved using *bis*(phenolato)-ligand-supported yttrium silylamide $(OSSO)Y\{N(SiHMe_2)_2\}(THF)$ ($k_p = 2.87 \times 10^2$ M^{-1} h^{-1} at 25 °C) and a series of BDI tin(II) amide complexes, $(BDI)Sn(NMe_2)$ ($k_{obs} = 0.703 \pm 0.043$−$1.884 \pm 0.177$ h^{-1} at 60 °C with $[rac\text{-LA}]_0/[Sn]_0 = 100:1$ *vs*. **6**: $k_{obs} = 0.531 \pm 0.041$ h^{-1} at 50 °C with $[rac\text{-LA}]_0/[Bi]_0 = 50:1$).[16, 57] Consistent with previous findings for initiator **2** (**Chapter Three**, **Section 3.3.3**), the activity of **6** is likely to be determined by a combination of factors: the modest Lewis acidity of bismuth, the steric constraints imposed by the [NON^{Dipp}]-ligand framework, the implication of the bismuth-centred $6s^2$ lone pair, and the possible aggregation of active species.

4.3.3 Temperature variation

The effect of temperature was studied for *L*-lactide polymerisation carried out at 35−70 °C in benzene-d_6 (**Figure 4.9**, **Table 4.3**).

As expected, the activity of **6** increased with increasing temperature ($k_{obs} = 0.466 \pm 0.053$ h^{-1} (70 °C) > 0.055 ± 0.003 h^{-1} (35 °C)) (**Figure 4.9b**). Moderate polymerisation control was observed across the entire temperature range, as indicated by narrow-to-intermediate $Đ_M$ values (1.16−1.36) (**Figure 4.10**). In addition, the $M_{n,GPC}$ and $M_{n,theo}$ of the polymers produced were in a good agreement.

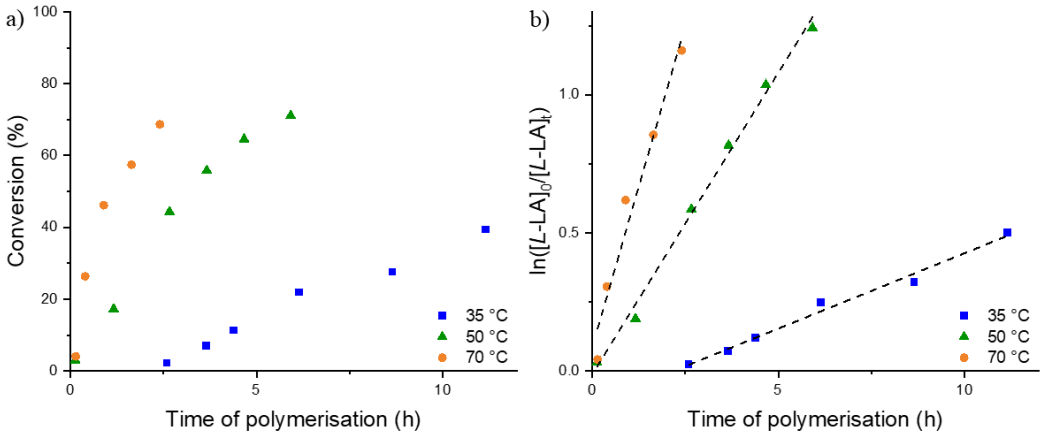


Figure 4.9 a) Plots of percentage conversion *vs*. polymerisation time for *L*-lactide polymerisation. b) Plots of $\ln([L\text{-LA}]_0/[L\text{-LA}]_t)$ *vs*. polymerisation time for *L*-lactide polymerisation. Blue squares: 35 °C, k_{obs} = 0.055 ± 0.003 h^{-1}, R^2 = 0.987; green up triangles: 50 °C, k_{obs} = 0.219 ± 0.008 h^{-1}, R^2 = 0.994; orange circles: 70 °C, k_{obs} = 0.466 ± 0.053 h^{-1}, R^2 = 0.962. Polymerisation conditions: benzene-d_6, $[L\text{-LA}]_0/[Bi]_0$ = 50:1, and $[L\text{-LA}]_0$ = 0.5 M.

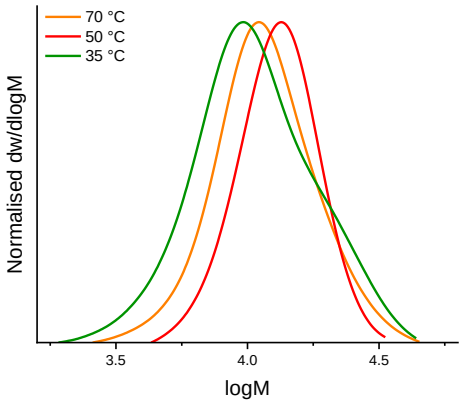


Figure 4.10 GPC plots of the PLLAs produced at 70 °C (orange, M_n = 5 964 g mol^{-1}, $Đ_M$ = 1.26); 50 °C (red, M_n = 5 207 g mol^{-1}, $Đ_M$ = 1.36); 35 °C (green, M_n = 6 911g mol^{-1}, $Đ_M$ = 1.16). Polymerisation conditions: benzene-d_6, $[L\text{-LA}]_0/[Bi]_0$ = 50:1, and $[L\text{-LA}]_0$ = 0.5 M.

The Eyring plot of $\ln(k_{obs}/T)$ *vs.* $1/T$ was constructed to deduce the thermodynamic parameters for the ROP of *L*-lactide initiated by **6** (**Figure 4.11**). The corresponding $\Delta H^‡$, $\Delta S^‡$, and $\Delta G^‡$ values were calculated to be 50 ± 12 kJ mol^{-1}, −173 ± 36 J K^{-1} mol^{-1}, and

103−109 kJ mol^{-1} at 35−70 °C, respectively. These data are characteristic of a high-order transition state inherent in the coordination-insertion mechanism.[58]

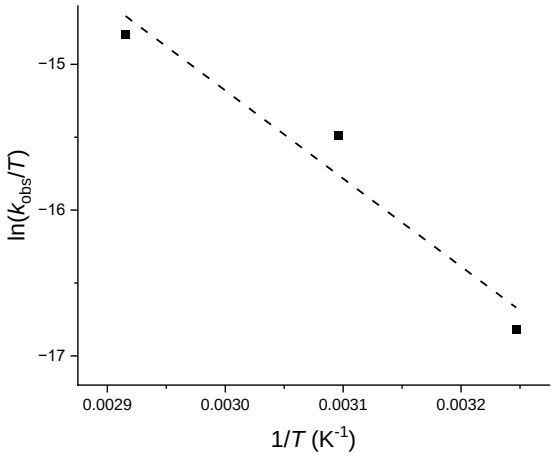


Figure 4.11 Eyring plot of ln(k_{obs}/T) *vs.* 1/T using **6** ($\Delta H^{‡}$ = 50 ± 12 kJ mol^{-1}; $\Delta S^{‡}$ = −173 ± 36 J K^{-1} mol^{-1}; slope = −6 036 ± 1 428, R^2 = 0.947; intercept = 2.9 ± 4.4). Polymerisation conditions: benzene-d_6, [*L*-LA]$_0$/[Bi]$_0$ = 50:1, and [*L*-LA]$_0$ = 0.5 M.

The Gibbs free energy associated with **6** is slightly lower than that for **2** (113−117 kJ mol^{-1} at 50−80 °C). Comparable yet slightly lower thermodynamic parameters have been reported using other sterically constrained Lewis acidic metal systems: pyridine dipyrrolide bismuth *tert*-butoxide ((L^{Mes,Ph})Bi(O^{t}Bu): $\Delta H^{‡}$ = 37 ± 1 kJ mol^{-1}; $\Delta S^{‡}$ = –162 ± 10 J K^{-1} mol^{-1}), an alkoxy-bridged dinuclear indium initiator ([(NNO)InCl$_2$(μ-OEt)(μ-Cl)]$_2$: $\Delta H^{‡}$ = 49 ± 2 kJ mol^{-1}; $\Delta S^{‡}$ = –140 ± 12 J K^{-1} mol^{-1}), and amine-bridged *bis*(phenolato) neodymium alkoxide ((L)Nd(OCH$_2$CF$_3$)(THF)$_2$: $\Delta H^{‡}$ = 40 kJ mol^{-1}; $\Delta S^{‡}$ = –120 J K^{-1} mol^{-1}).[2, 59, 60]

Table 4.3 ROP of *L*-lactide at different temperatures using (NON^{Dipp})Bi(NMe$_2$) (**6**).[a]

T **(°C)**	**Conv.[b] (%)**	k_{obs}[c] **(h^{-1})**	R^{2}[c]	$M_{n,GPC}$[d] **(g mol^{-1})**	$M_{n,theo}$[e] **(g mol^{-1})**	M_w/M_n[d]
35	94	0.055 ± 0.003	0.987	6 911	6 819	1.16
50	78	0.219 ± 0.008	0.994	5 207	5 378	1.36
70	90	0.466 ± 0.053	0.962	5 964	6 531	1.26

[a]Polymerisation conditions: benzene-d_6, [*L*-LA]$_0$/[Bi]$_0$ = 50:1, [*L*-LA]$_0$ = 0.5 M. [b]Measured by ^{1}H NMR spectroscopy. [c]Obtained from plots of ln([*L*-LA]$_0$/[*L*-LA]$_t$) *vs.* polymerisation time. [d]Determined by GPC analysis calibrated with PS standards in THF with the appropriate Mark-Houwink corrections.[43] [e]Theoretical M_n for PLA = (conv.(%) × [*L*-LA]$_0$/[Bi]$_0$) × 144.13 + (M_w of end groups).

4.3.4 Polymer end-group analysis

A PLLA polymer sample afforded by **6** was analysed by MALDI-ToF mass spectrometry to determine the nature of polymer end groups (**Figure 4.12**).

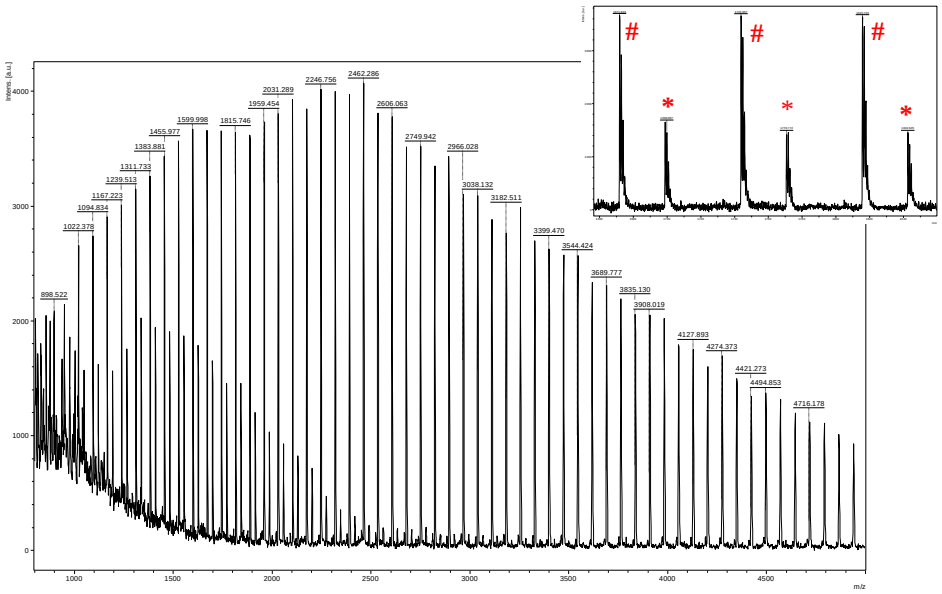


Figure 4.12 MALDI-ToF mass spectrum of the PLLA produced using **6**. Polymerisation conditions: benzene-d_6, 50 °C, [*L*-LA]$_0$/[Bi]$_0$ = 50:1, [*L*-LA]$_0$ = 0.5 M. # represents linear α–NMe$_2$/ω–OH terminated PLLA. * represents cyclic PLLA.

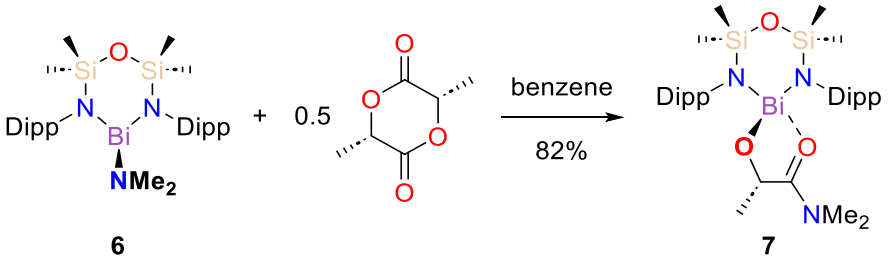
The mass spectrum displayed a series of peaks separated by $m/z = 72$, indicative of intermolecular transesterification taking place during the polymerisation. The major series of peaks was assigned to the PLLA chain terminated by α–NMe_2 and ω–OH end groups, consistent with ROP proceeding *via* a coordination-insertion mechanism. This can be illustrated by the peak at 2 966.1 g mol^{-1} corresponding to the α–NMe_2/ω–OH end-capped polymer chain comprising 20 lactide units together with K^+ (M_n = (144.1 × 20 + 39.1 + 45.1) g mol^{-1}). The presence of the α–NMe_2 end group was also observed in the ^{1}H NMR spectrum of the isolated PLLA, with two characteristic proton singlets located at δ 2.45 and 2.09 ppm (**Figure A.3.3** in **Appendix**).

An additional series of peaks at the lower molecular weight range was attributed to the polymer chain without end groups, indicating the formation of macrocyclic PLLA *via* intramolecular transesterification. The tandem formation of both linear and cyclic PLLA was also evidenced by ^{1}H NMR spectroscopic analysis (**Figure A.3.1** in **Appendix**). The observed relative broadening of the PLLA *methine* proton resonance is typically attributed to the overlapping signals arising from monomer repeating units with different stereochemistry. Further characterisation of these cyclic structures could be performed by intrinsic viscosity measurements, as cyclic polymers are characterised by lower intrinsic viscosities than their linear counterparts due to their smaller hydrodynamic radii.[61] Generally, the formation of low molecular weight cyclic PLA is a common ROP side reaction for the application of main group initiators.[62] Procedures for the selective synthesis of high molecular weight cyclic PLA have also been described.[8, 63] Overall, these analyses provide evidence for the occurrence of both intra- and intermolecular transesterification processes during the ROP of lactide in the presence of **6**, consistent

with the associated moderate polymerisation control as well as the postulated aggregation of propagating intermediates.

4.3.5 Reactivity of bismuth amide 6 with *L*-lactide

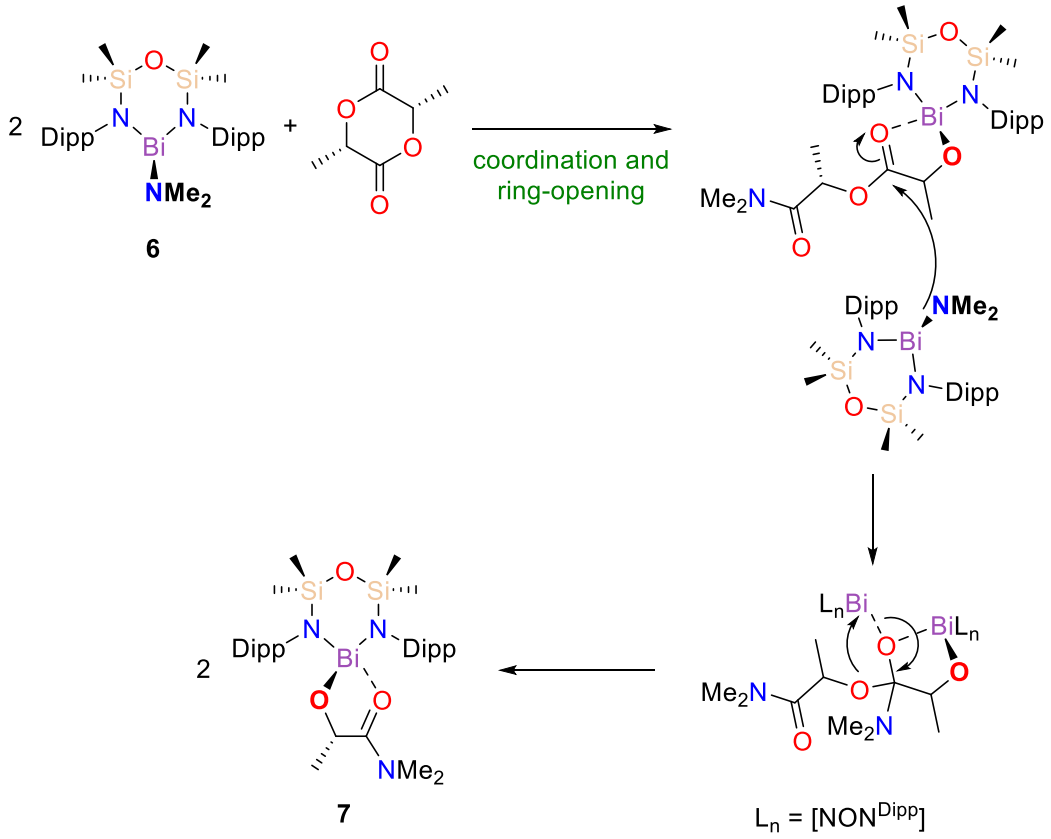
An equimolar reaction between **6** and *L*-lactide was probed to determine the nature of the propagating species in the ROP of *L*-lactide. The addition of a stoichiometric amount of *L*-lactide into a benzene-d_6 solution of **6** resulted in immediate monomer insertion into the Bi-N bond, forming a new bismuth lactate compound, alongside half an equivalent of the monomer remaining, as indicated by ^{1}H NMR spectroscopy. The reaction stoichiometry was subsequently adjusted to 1:2 ratio of *L*-lactide:**6**, resulting in the quantitative formation of (NON^{Dipp})Bi(OCH(Me)C(O)NMe$_2$) (**7**) (**Scheme 4.1**). The compound was isolated as a white powder in 82% yield.



Scheme 4.1 Synthesis of (NON^{Dipp})Bi(OCH(Me)C(O)NMe$_2$) (**7**).

The formation of **7** is proposed to proceed *via* the ring-opening of *L*-lactide by the nucleophilic attack of the NMe$_2$ group (**Scheme 4.2**). The putative lactyl lactate intermediate may undergo rapid bimolecular transesterification to generate a five-membered metallacycle. The implication of intermolecular transesterification during the formation metal lactate compounds has been previously suggested in the studies of tin and bismuth initiators.[2, 39] For example, Chisholm and co-workers used ^{1}H NMR spectroscopic analysis to demonstrate that the reaction between their tin(IV) initiator Ph$_2$Sn(NMe$_2$)$_2$ with 2−5 equivalents of *L*-lactide led to the predominant formation of the

ring-opened lactide intermediate $Ph_2Sn[OCH(Me)C(O)OCH(Me)C(O)NMe_2]_2$ and its transesterified derivative $Ph_2Sn[OCH(Me)C(O)NMe_2]_2$.[8] As *L*-lactide conversion progressed, the authors observed increasing amounts of the transesterified species relative to the lactyl lactate complex, suggesting the occurrence of inter-/intramolecular transesterification, presumably taking place at the α-ketonic ester carbon.



Scheme 4.2 Proposed reaction pathway to form $(NON^{Dipp})Bi(OCH(Me)C(O)NMe_2)$ (**7**).

The formation of the stable and isolable bismuth lactate compound **7** using initiator **6** is in stark contrast to complex **2**. The relatively enhanced stability of **7** can be attributed to the stronger chelating capability of the carbamate group ($RCONMe_2$) relative to the carboxylate moiety (RCOOR'), allowing for increased electron donation from the carbonyl oxygen to the bismuth centre. Similar observations based on ^{1}H NMR spectroscopic analysis have been reported by Chisholm and co-workers in their *L*-lactide

polymerisation study using triphenyl tin(IV) initiators (Ph_3SnX).[8] In the case of the amido ligand (X = NMe_2), the resulting ring-opened tin lactate intermediate exhibited greater stability and proved to be less prone to further chain propagation in comparison to its alkoxide analogue (X = OMe).

4.3.5.1 NMR and IR spectroscopic analyses

The ^{1}H NMR spectrum of **7** reveals the loss of C_s molecular symmetry observed for **6**, consistent with the formation of a chiral C_1-symmetric compound (**Figure 4.13**).

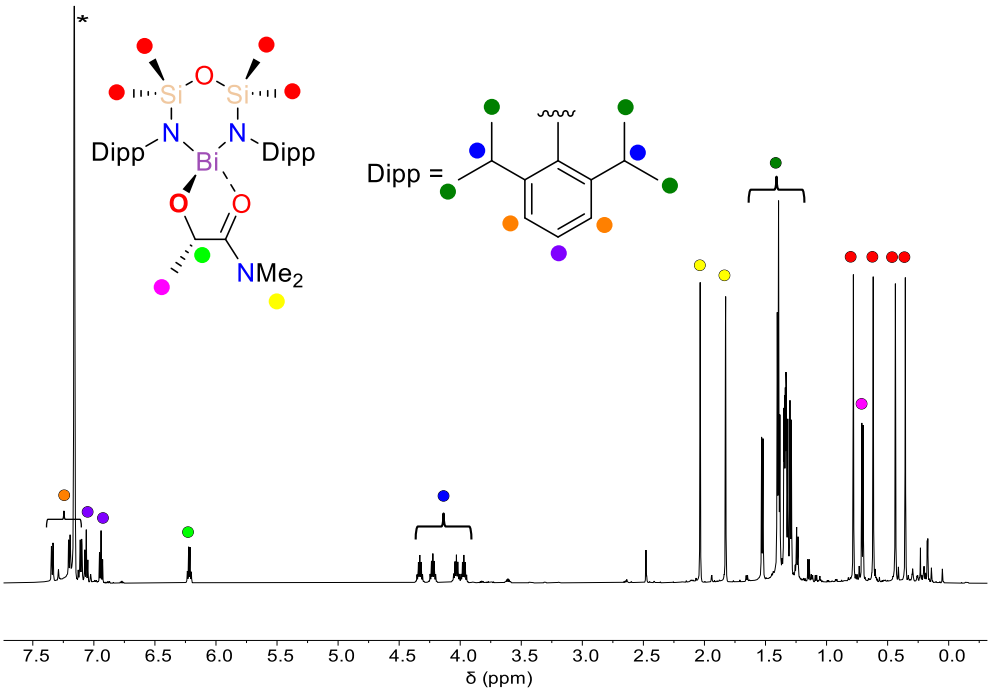


Figure 4.13 ^{1}H NMR spectrum (*benzene-d_6, 600 MHz, 298 K) of (NON^{Dipp})Bi(OCH(Me)C(O)NMe_2) (**7**).

The asymmetric nature of the [NON^{Dipp}]-ligand is defined by the presence of four singlets at δ 0.78, 0.62, 0.44, 0.36 ppm corresponding to the Si*Me*$_2$ protons and four septets at δ 4.33, 4.22, 4.03, 3.97 ppm assigned to the C*H*Me_2 protons. In addition, there are eight distinct CH*Me*$_2$ proton environments between δ 1.53–1.28 ppm and six separate signals between δ 7.34–6.94 ppm corresponding to the aromatic Dipp protons. Unrestricted

rotation of the methyl group of the lactate unit is deduced from two mutually coupled resonances ($^{3}J_{H\text{-}H}$ = 6.6 Hz): a doublet at δ 0.71 ppm corresponding to the CH*Me* protons and a quartet at δ 6.22 ppm assigned to the C*H*Me proton. Due to coordination to the Lewis acidic bismuth centre, the latter signal is significantly shifted with respect to that for *L*-lactide (δ 3.76 ppm). Hindered rotation of the conjugated NMe_2 group results in the inequivalence of the two NMe_2 protons, located as two singlets of equal integration at δ 2.04 and 1.83 ppm.

The $^{13}C\{^{1}H\}$ NMR spectrum reveals a high frequency signal at δ 182.6 ppm corresponding to the carbonyl carbon. This signal is shifted to a higher frequency compared to that for *L*-lactide (δ 167.0 ppm), indicating the formation of a relatively strong bismuth-carbonyl intramolecular interaction. Comparable $^{13}C\{^{1}H\}$ NMR spectroscopic shifts for the carbonyl group have been observed for related metal lactate and lactyl lactate compounds: the pyridine dipyrrolide-supported bismuth compound (L)Bi((*R*)-OCH(Me)C(O)O^{t}Bu) (δ 185.0 ppm), the pyridine *bis*(phenolate) complex (L)Al((*R*)-OCH(Me)C(O)O^{i}Pr) (δ 189.5 ppm), and diastereomeric amino-phenolate supported (L)Sn((*R*)-OCH(Me)C(O)O^{t}Bu) compounds (δ 187.85 and 187.26 ppm).[2, 12, 15]

The IR spectrum of **7** displays a strong absorption at 1613 cm^{-1} corresponding to ν(CO) stretching vibration (**Figure A.3.4** in **Appendix**), providing further evidence for the coordination of the carbonyl moiety to the bismuth centre. In comparison, the IR spectrum of the aluminium lactyl lactate cationic species, discussed previously in **Section 4.1**, contains two absorptions at 1779 and 1685 cm^{-1}, indicating one non-coordinated and one chelating carbonyl group of the ring-opened lactide unit.[21]

4.3.5.2 X-ray crystallographic analysis

Single crystals of **7**, suitable for an X-ray diffraction study, were grown from slow evaporation of a hexane solution at 23 °C. Compound **7** crystallised in the orthorhombic space group, $P2_12_12_1$ (**Figure 4.14**, **Table 4.4**).

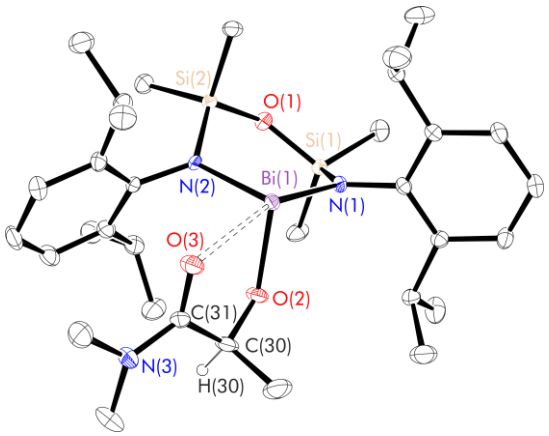


Figure 4.14 Thermal displacement ellipsoid drawing (30%) of the asymmetric unit of (NON^{Dipp})Bi(OCH(Me)C(O)NMe_2) (**7**). All hydrogen atoms apart from that on C(30) have been omitted for clarity.

The solid-state structure of **7** confirms the formation of an enantiopure compound, implying that the insertion of *L*-lactide into the Bi-N bond proceeds without racemisation. The coordination geometry at the bismuth centre is distorted disphenoidal, with axial sites occupied by atoms O(3) and N(1) (O(3)-Bi(1)-N(1) = 161.3(1)°), while O(2) and N(2) sit in equatorial positions (O(2)-Bi(1)-N(2) = 94.7(1)°). The lactate ligand is bound to the bismuth centre in a κ^2-*O,O'*-bidentate chelating mode, consistent with the solid-state structures of previously described metal lactate compounds (**Section 4.1**).[4, 5, 21, 22] Apart from these, a rare example of the absence of carbonyl-metal interaction has been reported for a salen aluminium lactate complex, attributed to the steric shielding imparted by the ligand.[6]

The formation of the chelating lactate structure results in two different Bi-O bond lengths: a single covalent bond (Bi(1)-O(2) = 2.111(3) Å) and a longer non-covalent interaction (Bi(1)-O(3) = 2.590(3) Å). The extent of bond asymmetry is comparable to the environment in the pyridine dipyrrolide bismuth lactate complex (2.063(13) and 2.660(15) Å, respectively, **Table 4.4**).[2] The asymmetric bonding environment within the lactate ligand is also evidenced by the formation of a single C-O bond (C(30)-O(2) = 1.401(6) Å) and a double C=O bond (C(31)-O(3) = 1.240(6) Å), both relatively long compared to the range of the corresponding bond lengths for previously reported metal lactate compounds (M = Zn, Al, In, Sn, and Bi) (C-O = 1.35(2)−1.41(2) Å and C=O = 1.20(2)−1.24(3) Å).[2, 5, 7, 13, 15, 64]

Table 4.4 Selected experimental metrical parameters (bond lengths (Å) and angles (°)) for (NON^{Dipp})Bi(OCH(Me)C(O)NMe_2) (**7**) and a related bismuth lactate complex ($L^{Mes,Ph}$)BiX.[2] Estimated standard deviations shown in brackets.

	7	($L^{Mes,Ph}$)BiX[2] X = (*R*)-OC(H)(Me)C(O)O^{t}Bu
Space group	$P2_12_12_1$	$P1$
Bi(1)-N(1)	2.193(3)	-
Bi(1)-N(2)	2.184(3)	-
Bi(1)-O(2)	2.111(3)	2.063(13)
Bi(1)-O(3)	2.590(3)	2.660(15)
C(30)-O(2)	1.401(6)	1.35(2)
C(31)-O(3)	1.240(6)	1.24(3)
N(1)-Bi(1)-N(2)	94.12(14)	-

4.3.6 Lactide polymerisation studies using bismuth lactate 7

Bismuth lactate **7** was studied as a model substrate for the propagating intermediate formed during the ROP of *L*-lactide. The polymerisation reactions were carried out under the same conditions as previously defined for the use of **6** (**Figure 4.15**, **Table 4.5**).

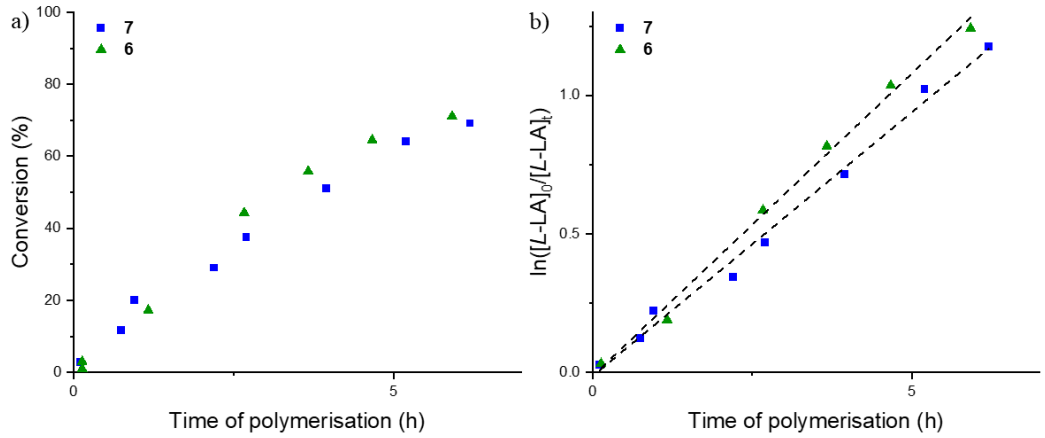


Figure 4.15 a) Plots of percentage conversion *vs.* polymerisation time for *L*-lactide polymerisation. b) Plots of $\ln([L\text{-LA}]_0/[L\text{-LA}]_t)$ *vs.* polymerisation time for *L*-lactide polymerisation. Blue squares: **7**, k_{obs} = 0.191 ± 0.007 h^{-1}, R^2 = 0.991; green up triangles: **6**, k_{obs} = 0.219 ± 0.008 h^{-1}, R^2 = 0.994. Polymerisation conditions: benzene-d_6, 50 °C, $[L\text{-LA}]_0/[Bi]_0$ = 50:1, and $[L\text{-LA}]_0$ = 0.5 M.

A linear plot of $\ln([L\text{-LA}]_0/[L\text{-LA}]_t)$ *vs.* polymerisation time confirmed the expected first-order dependence on monomer concentration (**Figure 4.15b**). Both **6** and **7** exhibited similar activities (k_{obs} = 0.219 ± 0.008 and 0.191 ± 0.007 h^{-1}, respectively). Furthermore, the polymer afforded by **7** showed a good agreement between its $M_{n,GPC}$ and $M_{n,theo}$, in conjunction with a relatively narrow $Đ_M$ of 1.20, hence implying good polymerisation control. A close alignment of the polymerisation data recorded for both **6** and **7** infers that the lactate compound **7** serves as the propagating species in the polymerisation of lactide. This finding is consistent with previous literature studies of metal lactate species that have been shown to mimic catalytically active ROP intermediates.[2, 3, 5, 13]

Additionally, this hypothesis was supported by ^{1}H NMR spectroscopic studies. Using either **6** or **7** as the initiator in the ROP of *L*-lactide, the initial ^{1}H NMR spectra (*L*-lactide conversion < 3%) were essentially identical.

Table 4.5 ROP of *L*-lactide using (NON^{Dipp})Bi(O(CMeH)C(NMe$_2$)O) (**7**).[a]

Conv.[b] **(%)**	k_{obs}[c] **(h^{-1})**	R^{2}[c]	$M_{n,GPC}$[d] **(g mol^{-1})**	$M_{n,theo}$[e] **(g mol^{-1})**	M_w/M_n[d]
92	0.191 ± 0.007	0.991	6 914	6 752	1.20

[a]Polymerisation conditions: benzene-d_6, 50 °C, [*L*-LA]$_0$/[Bi]$_0$ = 50:1, [*L*-LA]$_0$ = 0.5 M. [b]Measured by ^{1}H NMR spectroscopy. [c]Obtained from plots of ln([*L*-LA]$_0$/[*L*-LA]$_t$) *vs.* polymerisation time. [d]Determined by GPC analysis calibrated with PS standards in THF with the appropriate Mark-Houwink corrections.[43] [e]Theoretical M_n for PLA = (conv.(%) × [*L*-LA]$_0$/[Bi]$_0$) × 144.13 + (M_w of end groups).

4.3.7 Mechanistic analysis

A room-temperature reaction between **7** and a further equivalent of *L*-lactide in benzene-d_6 showed no reactivity by ^{1}H NMR spectroscopy after 24 hours. Heating the reaction mixture to 50 °C for an additional 2 hours led to the formation of a small amount of PLLA oligomer, with unreacted **7** still present in solution. The lack of the observable insertion of the second lactide monomer into **6** confirms that the initiation step is relatively fast compared to propagation (i.e. $k_{LA_1} > k_p$). Similar observations have been made for aluminium, gallium, and tin initiators.[52, 65-68]

Overall, these reactivity studies highlight the significance of the chelation effect in determining the activity of ROP initiators. Generally, the catalytic capability of metal lactate or lactyl lactate complexes in ROP is known to depend on the strength of the interaction between the metal centre and the carbonyl group of the κ^2-chelated ligand (**Section 4.1**). The enhanced stability of the bismuth lactate chelate of **7** relative to initiator **6** is likely to account for the reduced rate of the ring-opening of the second lactide

molecule. Following this, the insertion of additional monomer units is expected to weaken the chelate effect, rendering the resulting insertion products indistinguishable.[16]

For comparison, a phosphasalen scandium alkoxide initiator, reported by Williams and co-workers, was found to form a ring-opened lactate complex, exhibiting no activity towards further lactide insertion steps.[69] Conversely, the initiator proved to be active for the ROP of ε-caprolactone, likely due to the reduced stability of its putative lactone insertion product. Similarly, a strong chelate effect was proposed to result in the lack of ROP activity observed for the cationic aluminium lactate compound, discussed in **Section 4.1**.[21] In contrast to these examples, several other metal lactate compounds, including pyridine dipyrrolide bismuth lactate ($L^{Mes,Ph}$)Bi((*R*)-OCH(Me)C(O)O^{t}Bu) and BDI-supported zinc lactate *rac*-(BDI)Zn(OCH(Me)C(O)OMe), have demonstrated high activities in lactide polymerisation.[2, 13]

To gain a better understanding of the ROP mechanism adopted by **6**, the polymerisation of *L*-lactide with $[L\text{-LA}]_0/[Bi]_0 = 50$ at 50 °C was probed by ^{1}H NMR spectroscopy. The polymerisation proceeded with rapid lactide ring-opening to cleanly yield bismuth lactate **7**. This was evidenced by the ^{1}H NMR spectrum of the reaction mixture (*L*-lactide conversion < 3%, 10 minutes after mixing) (**Figure 4.16a**), primarily comprising **7** and *L*-lactide, along with a negligible amount of PLLA. Over the course of the polymerisation, **7** was completely consumed, forming an active propagating PLLA chain, defined by the appearance of a new set of resonances (**Figure 4.16b**). Accordingly, two N*Me*$_2$ proton signals of **7** at δ 2.04 and 1.83 ppm were replaced by two higher frequency resonances at δ 2.48 and 2.16 ppm corresponding to the polymer α−NMe$_2$ end group. The resonances for the [NON^{Dipp}]-ligand-coordinated propagating polymer chain were identified as four new singlets due to the Si*Me*$_2$ protons and two new septets assigned to

the two of the C*H*Me$_2$ protons (the remaining two septets were overlapped with *L*-LA *methine* proton peak). Additionally, two new quartets were present at δ 4.76 and 5.70 ppm, consistent with a *methine* proton of the lactide unit nearest to the bismuth centre and the *methine* proton adjacent to the terminal α−NMe$_2$ group, respectively. This pattern closely resembles the proton environment of the [NON^{Dipp}]-ligand-bound propagating PLLA chain using initiator **2**.

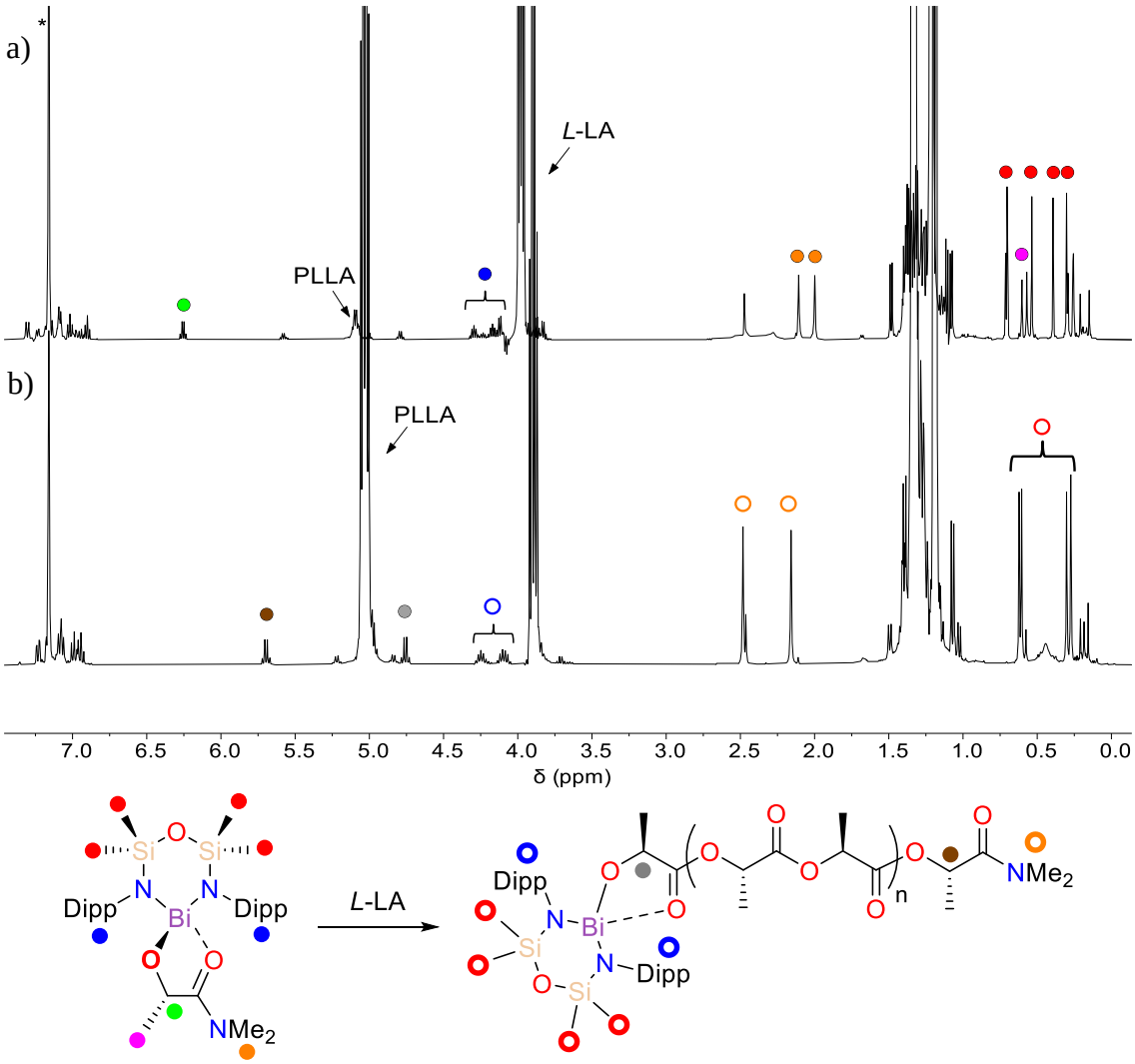
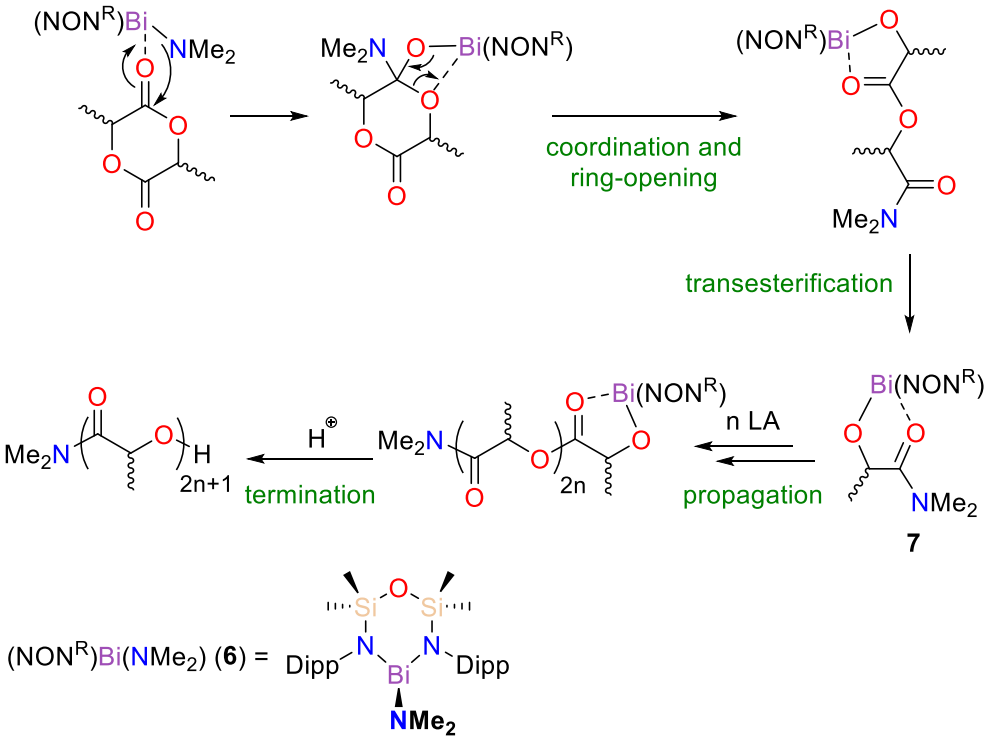


Figure 4.16 ^{1}H NMR spectra (*benzene-d_6, 400 MHz, 298 K) of *L*-lactide polymerisation using **6** at t = a) 10 minutes and b) 4.7 hours. Polymerisation conditions: benzene-d_6, 50 °C, [*L*-LA]$_0$/[Bi]$_0$ = 50, and [*L*-LA]$_0$ = 0.5 M.

These results suggest that the polymerisation of lactide in the presence of **6** follows the common coordination-insertion mechanism (**Scheme 4.3**),[70] analogous to the mechanistic pathway proposed for **2** (**Chapter Three**, **Section 3.3.7**). The coordination of the lactide monomer to the bismuth centre precedes the intramolecular nucleophilic attack at the carbonyl group by the $-NMe_2$ initiating group. The resulting ring-opened intermediate is likely susceptible to intermolecular transesterification, leading to the formation of the more stable bismuth lactate compound **7**. Subsequent coordination-insertion steps of additional monomer units occur at the new Bi-O bond, thereby facilitating chain propagation. After hydrolysis, the bismuth-coordinated chain end becomes capped with a secondary alcohol group, with the other end comprising the $-NMe_2$ group.



Scheme 4.3 Proposed coordination-insertion mechanism for the ROP of lactide using **6** ($(NON^R)Bi(NMe_2)$).

4.4 ε-Caprolactone polymerisation studies

Polymerisations were conducted in J. Young's tap NMR spectroscopy tubes with an initial ε-caprolactone to catalyst ratio ($[\varepsilon\text{-CL}]_0/[\text{Bi}]_0$) of 50:1 and an initial monomer concentration ($[\varepsilon\text{-CL}]_0$) of 0.5 M in 0.6 mL of benzene-d_6 at 50 °C. The reactions were monitored by ^{1}H NMR spectroscopy and halted by cooling in an ice bath, followed by quenching with wet pentane.

4.4.1 ε-Caprolactone polymerisation using bismuth amide 6

The ROP initiation capability of **6** was studied towards ε-caprolactone. Polymerisation results were directly compared to those obtained using *L*-lactide as the monomer, under the same reaction conditions (**Figure 4.17**, **Table 4.6**).

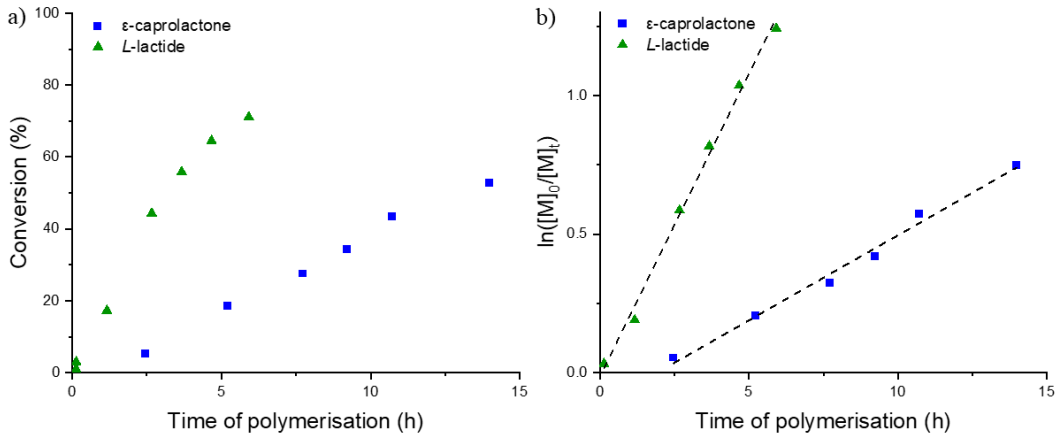


Figure 4.17 a) Plots of percentage conversion *vs*. polymerisation time. b) Plots of $\ln([\text{M}]_0/[\text{M}]_t)$ *vs*. polymerisation time (where M = monomer). Blue squares: ε-CL, k_{obs} = 0.061 ± 0.003 h^{-1}, R^2 = 0.989; green up triangles: *L*-LA, k_{obs} = 0.219 ± 0.008 h^{-1}, R^2 = 0.994. Polymerisation conditions: benzene-d_6, 50 °C, $[\text{M}]_0/[\text{Bi}]_0$ = 50:1, and $[\text{M}]_0$ = 0.5 M.

Unlike the ROP of *L*-lactide, ε-caprolactone was polymerised with an induction period of approximately 2 hours. The reduced initiation efficiency towards ε-caprolactone is

likely influenced by the reactivity of the polymerisation intermediate formed upon insertion of the first ε-caprolactone unit into **6** (*vide infra*).

A plot of $\ln([\varepsilon\text{-CL}]_0/[\varepsilon\text{-CL}]_t)$ *vs*. polymerisation time indicated a first-order dependence on monomer concentration after an induction period (**Figure 4.17b**), consistent with ROP proceeding *via* a typical coordination-insertion mechanism.[71] The activity of **6** in the polymerisation of ε-caprolactone was found to be more than three-fold lower than that for *L*-lactide (k_{obs} = 0.061 ± 0.003 and 0.219 ± 0.008 h^{-1}, respectively). Although it is difficult to directly compare the ROP activity towards ε-caprolactone of the initiators **2** and **6** due to the different reaction temperature used (**Chapter Three**, **Section 3.4.1**), both complexes proved to be less active in the ROP of ε-caprolactone with respect to *L*-lactide. Possible reasons include the presence of two ester groups on lactide, differences in the strength of the initiating Bi-O group of the propagating intermediate, as well as the varied initiator susceptibility to aggregation, potentially leading to the formation of species with different reactivities.[72, 73]

Conversely, superior rates in the polymerisation of ε-caprolactone with respect to *L*-lactide have been reported for several organometallic initiators.[74-78] The relatively high monomer ring strain and the diminished chelate effect in the propagating intermediate have been discussed as some of the factors contributing to rapid kinetics in the ROP of ε-caprolactone. In the case of **6**, the lactide insertion product **7** is expected to exhibit lower chelate ring strain compared to the nine-membered metallacycle formed during the insertion of ε-caprolactone (*vide infra*, **Section 4.4.2**).[79] However, a subtle balance between steric, electronic, and chelation effects can have a significant impact on the activity of the initiator.

Table 4.6 ROP of ε-caprolactone using (NON^{Dipp})Bi(NMe_2) (**6**).[a]

Conv.[b] **(%)**	k_{obs}[c] **(h^{-1})**	R^{2}[c]	$M_{n,GPC}$[d] **(g mol^{-1})**	$M_{n,theo}$[e] **(g mol^{-1})**	M_w/M_n[d]
66	0.061 ± 0.003	0.989	2 928	3 812	1.32

[a]Polymerisation conditions: benzene-d_6, 50 °C, $[\varepsilon\text{-CL}]_0/[Bi]_0$ = 50:1, $[\varepsilon\text{-CL}]_0$ = 0.5 M. [b]Measured by ^{1}H NMR spectroscopy. [c]Obtained from plots of $\ln([\varepsilon\text{-CL}]_0/[\varepsilon\text{-CL}]_t)$ *vs.* polymerisation time. [d]Determined by GPC analysis calibrated with PS standards in THF with the appropriate Mark-Houwink corrections.[43] [e]Theoretical M_n for PCL = (conv.(%) × $[\varepsilon\text{-CL}]_0/[Bi]_0$) × 114.14 + ($M_w$ of end groups).

The relatively modest activity of **6** in the ROP of ε-caprolactone is not surprising, given similar observations made in the study of *L*-lactide polymerisation. In comparison, higher activities have been documented for several other Lewis acidic metal initiators. For example, an ytterbium amide initiator bearing a BDI ligand ((BDI)Yb(NPh_2)Cl(THF)) polymerised ε-caprolactone within 1 minute (25 °C with $[\varepsilon\text{-CL}]_0/[Yb]_0$ = 200:1).[80] Furthermore, quantitative formation of PCL was observed within 15 minutes using a bimetallic aluminium(II) complex supported by an imino-acenaphthene-type ligand, used in the presence of an excess of BnOH (25 °C with $[\varepsilon\text{-CL}]_0/[I]_0$ = 1000:1).[23] However, its monomeric aluminium(III) analogue, stabilised by the amino-alkoxide $OCH_2CH_2NMe_2$ group, resulted in only 15% conversion after 24 hours under comparable reaction conditions. Hence, bimetallic cooperativity was deemed to be responsible to the observed ROP activity.

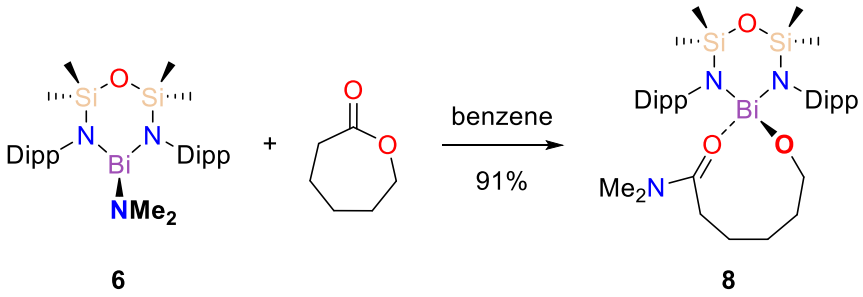
Contrary to these initiators, relatively low polymerisation rates have been typically recorded using tin and bismuth compounds. A tin triflate initiator $Sn(OTf)_2$ produced PCL within 3 hours (110 °C with $[\varepsilon\text{-CL}]_0/[Sn]_0$ = 30:1), whereas the industrial $Sn(Oct)_2$ initiator required 24 hours under the same reaction conditions.[81] Similarly, the polymerisation was complete only within 24 hours using a benzyl-*bis*(phenyl) tin(IV) complex with a methoxide initiating group (75 °C with $[\varepsilon\text{-CL}]_0/[Sn]_0$ = 120:1).[82] The

Ph_2BiOEt initiator polymerised ε-caprolactone in bulk within less than 3 hours (60 °C with $[\varepsilon\text{-CL}]_0/[Bi]_0 = 50:1$), hence demonstrating somewhat higher activity than **6**.[83]

The polymerisation initiated by **6** proved to be moderately controlled ($Đ_M = 1.32$), affording a slightly lower than expected polymer molecular weight ($M_{n,GPC} = 2\ 928$ g mol^{-1} *vs.* $M_{n,theo} = 3\ 812$ g mol^{-1}). These results compare well with those observed in the presence of *L*-lactide, suggesting the occurrence of transesterification side reactions when **6** is employed as a ROP initiator.

4.4.2 Reactivity of bismuth amide 6 with ε-caprolactone

Examination of an equimolar reaction between ε-caprolactone and **6** in benzene indicated rapid ε-caprolactone ring-opening, followed by its insertion into the Bi-N bond. The reaction product (NON^{Dipp})Bi($OC_5H_{10}C(O)NMe_2$) (**8**) was isolated as a yellow oil in 91% yield (**Scheme 4.4**), with residual monomer present. Attempts to crystallise the compound were unsuccessful due to the persistent formation of an amorphous powder.



Scheme 4.4 Synthesis of (NON^{Dipp})Bi($OC_5H_{10}C(O)NMe_2$) (**8**).

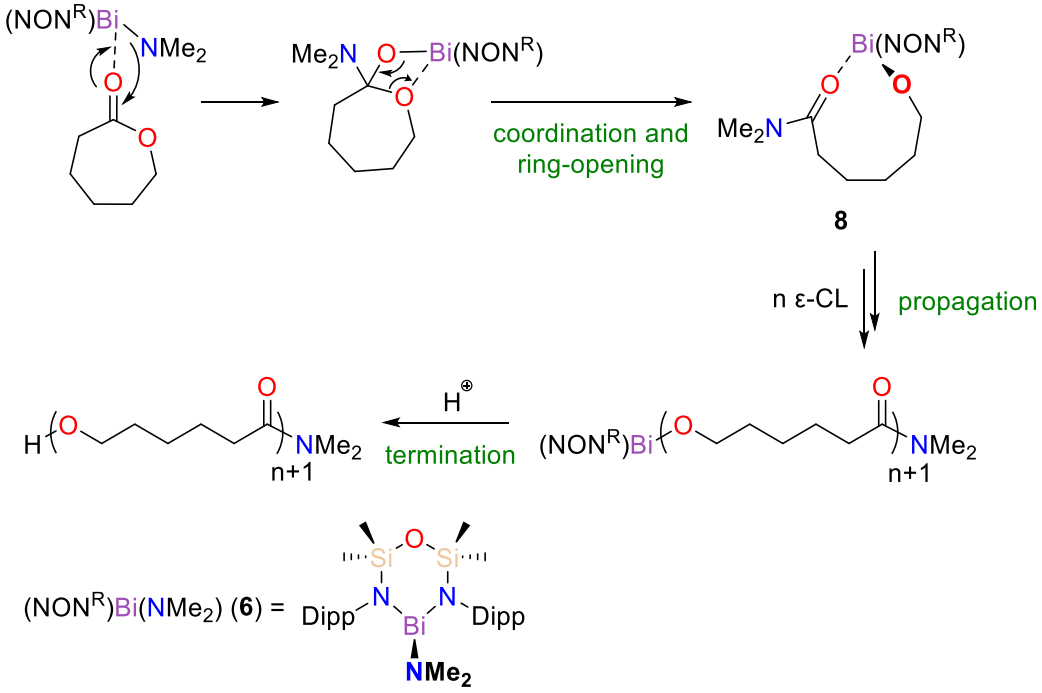
Despite several examples of the structurally characterised addition products formed *via* coordination of an ε-caprolactone molecule to the Lewis acidic metal centre (e.g. [(dpp-bian)Al(ε-CL)]$_2$ and $YCl_3(\varepsilon\text{-CL})_3$),[23, 24] a ring-opened insertion product has not yet been isolated. The formation of an organometallic compound comprising a κ^2-*O,O'*-chelated ring-opened ε-caprolactone moiety has been predicted by DFT

modelling of lactone ring-opening pathways in the presence of metal alkoxide initiators.[20, 84]

Compound **8** demonstrated no room-temperature reactivity with an additional equivalent of ε-caprolactone, as indicated by the *in situ* ^{1}H NMR spectrum after 48 hours. The resistance of **8** towards the ROP of ε-caprolactone may explain the induction period observed in the polymerisation, with elevated temperatures required for chain propagation. Compared to the parent bismuth amide initiator **6**, the enhanced strength of the Bi-O bond in **8** is likely to contribute to the reduced polymerisation activity. Similar findings have been reported for a bimetallic *tris*(amide) aluminium methyl system, (L)Al_2Me_3.[85] ^{1}H NMR spectroscopic analysis indicated the insertion of the first monomer unit into the Al-N bond proceeding rapidly at room temperature; however no reactivity with a second monomer equivalent was detected. Even after 17 hours at 60 °C, the ring-opened compound remained observable in the reaction mixture, along with an increasing amount of PCL formed.

Based on these findings, the coordination-insertion pathway for the ROP of ε-caprolactone is proposed to begin with monomer coordination to the bismuth centre of **6** (**Scheme 4.5**). This activates the monomer towards ring-opening and insertion into the Bi-N bond, readily forming a ring-opened intermediate **8**. Subsequent monomer coordination-insertion steps proceed at a slower rate, thus leading to an induction period. The propagating polymer chain is terminated by hydrolysis, which ultimately forms α–NMe_2/ω–OH capped PCL.[86] The presence of the α–NMe_2 end group was also observed in the ^{1}H NMR spectrum of the isolated PCL sample, with its two proton signals found at δ 2.67 and 2.20 ppm (**Figure A.3.7** in **Appendix**). Comparable NMR spectroscopic

data were recorded in the case of α–NMe_2/ω–OH terminated PLLA (N*Me*$_2$ at δ 2.45 and 2.09 ppm).



Scheme 4.5 Proposed coordination-insertion mechanism for the ROP of ε-caprolactone using **6** ((NON^R)Bi(NMe$_2$)).

4.4.2.1 NMR and IR spectroscopic analyses

The ^{1}H NMR spectrum of **8** confirms the formation of a C_s-symmetric complex, with two singlets at δ 0.60 and 0.28 ppm assigned to the Si*Me*$_2$ protons in the [NON^{Dipp}]-ligand backbone (**Figure 4.18**). The presence of two septets at δ 4.15 and 3.81 ppm assigned to the C*H*Me$_2$ protons and four doublets between δ 1.46–1.21 ppm corresponding to the CH*Me*$_2$ protons suggests that rotation around the amido-*N*-aryl bond is restricted. The ring-opened lactone unit features five distinct C*H*$_2$ proton environments. These signals include three apparent pentets (δ 1.61, 1.28–1.22, 1.17–1.07 ppm) and two triplets (δ 4.08, 1.91 ppm), with the highest frequency signal assigned to the C*H*$_2$ protons adjacent to the Bi-O bond. The presence of two N*Me*$_2$ proton resonances at δ 2.65 and

2.24 ppm is analogous to the proton environment in **7**, consistent with conjugation in the carbamate functionality.

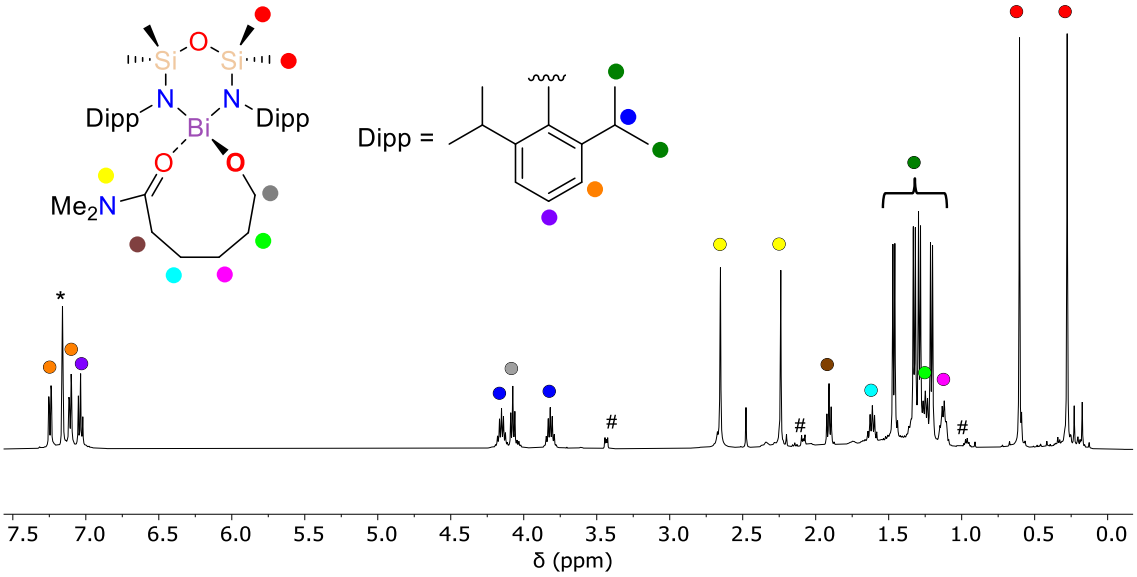


Figure 4.18 ^{1}H NMR spectrum (*benzene-d_6, 600 MHz, 298 K) of (NON^{Dipp})Bi($OC_5H_{10}C(O)NMe_2$) (**8**). # represents residual ε-caprolactone.

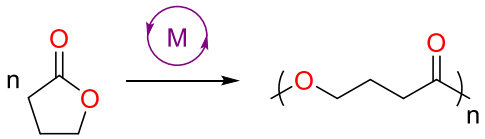
In the $^{13}C\{^{1}H\}$ NMR spectrum of **8**, the carbonyl carbon is observed as the highest frequency resonance at δ 171.8 ppm, revealing a slight shift with respect to ε-caprolactone (δ 174.9 ppm). This aligns with the NMR spectroscopic data reported for a cyclopentadienyl titanium complex (η^6-C_6H_5)Ti($OC_5H_{10}C(O)OMe$) (*C*O at δ 173.9 ppm) prepared as a model compound for the ε-caprolactone insertion product using (η^6-C_6H_5)$TiCl_3$ and a methyl 6-hydroxyhexanoate precursor.[87] In comparison to these values, the corresponding signal is at a higher frequency in **7** (δ 182.6 ppm), suggesting a stronger carbonyl coordination to the bismuth centre, likely reinforced by its relatively smaller chelate ring size.

The chelation of the ring-opened ε-caprolactone moiety was also indicated by IR spectroscopic analysis (**Figure A.3.8** in **Appendix**). A strong absorption at 1650 cm^{-1} corresponding to *ν*(CO) stretching vibration is at a considerably lower frequency

compared to the monomer (ν(CO) = 1720 cm^{-1}). This value is consistent with that recorded for the addition product (L)AlMe(ε-CL), formed between ε-caprolactone and methylaluminium *bis*(phenoxide) (ν(CO) = 1640 cm^{-1}).[26]

4.5 γ-Butyrolactone polymerisation studies

The polymerisation of γ-butyrolactone (γ-BL), a biomass-derived monomer, offers a route to produce poly-4-hydroxybutyrate P(γ-BL) as an alternative biopolymer (**Scheme 4.6**). In addition to fast degradation rates, P(γ-BL) displays comparable physical properties to those of PCL.[88]



Scheme 4.6 Ring-opening polymerisation of γ-butyrolactone initiated by a metal-based initiator.

However, the γ-butyrolactone monomer is typically considered as non-polymerisable due to the lack of ring strain.[89] Most reports on the ROP of γ-butyrolactone are limited to the synthesis of oligomers using high-temperature and high-pressure reaction conditions. Examples of ROP procedures for high molecular weight P(γ-BL) are extremely rare, with metal-free initiators employed predominantly.[90-93]

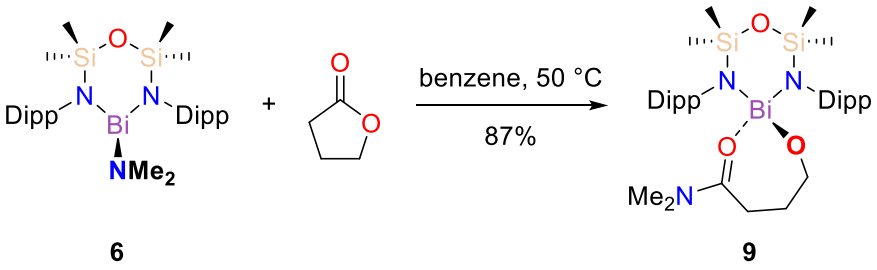
In light of the activity of **6** observed in the ROP of lactide and ε-caprolactone, its initiating capability was also tested for the ROP of γ-butyrolactone. The polymerisation reaction was conducted in a J. Young's tap NMR spectroscopy tube with an initial γ-butyrolactone to catalyst ratio ([γ-BL]$_0$/[Bi]$_0$) of 50:1 and an initial monomer concentration ([γ-BL]$_0$) of 0.5 M in 0.6 mL of benzene-d_6 at 50 °C.

4.5.1 γ-Butyrolactone polymerisation using bismuth amide 6

Compound **6** was found to be inactive for the ROP of γ-butyrolactone under the given reaction conditions. ^{1}H NMR spectroscopic analysis revealed a gradual conversion of **6** into a new [NON^{Dipp}]-ligand-supported compound; however, no formation of P(γ-BL) was observed even when the polymerisation reaction was heated to 50 °C for 48 hours.

4.5.2 Reactivity of bismuth amide 6 with γ-butyrolactone

The complete consumption of **6** seen during the attempted polymerisation reaction using γ-butyrolactone prompted an investigation into its activity towards monomer ring-opening. Upon adding an equivalent of γ-butyrolactone to a benzene-d_6 solution of **6**, no reaction initially occurred at room temperature. Instead, heating to 50 °C for 16 hours was required for the insertion reaction to proceed, resulting in the formation of the ring-opened product (NON^{Dipp})Bi(OC$_3$H$_6$C(O)NMe$_2$) (**9**) (**Scheme 4.7**). The compound was subsequently isolated as a pale yellow powder in 87% yield.



6 **9**

Scheme 4.7 Synthesis of (NON^{Dipp})Bi(OC$_3$H$_6$C(O)NMe$_2$) (**9**).

According to ^{1}H NMR spectroscopic analysis (*vide infra*), the solution-state structure of **9** is consistent with the intermediate species detected during the polymerisation of γ-butyrolactone. Compound **9** is therefore proposed to form as the first monomer insertion product. Its lack of ROP activity can be rationalised by stabilising chelate interactions as well as the reduced lability of the Bi-O bond relative to the Bi-N bond of

6. Notably, well-defined metal complexes prepared *via* the ring-opening and insertion of a single γ-butyrolactone molecule are not known.

4.5.2.1 NMR and IR spectroscopic analyses

The ^{1}H NMR spectrum of **9** indicates C_s molecular symmetry on the NMR spectroscopic timescale (**Figure 4.19**).

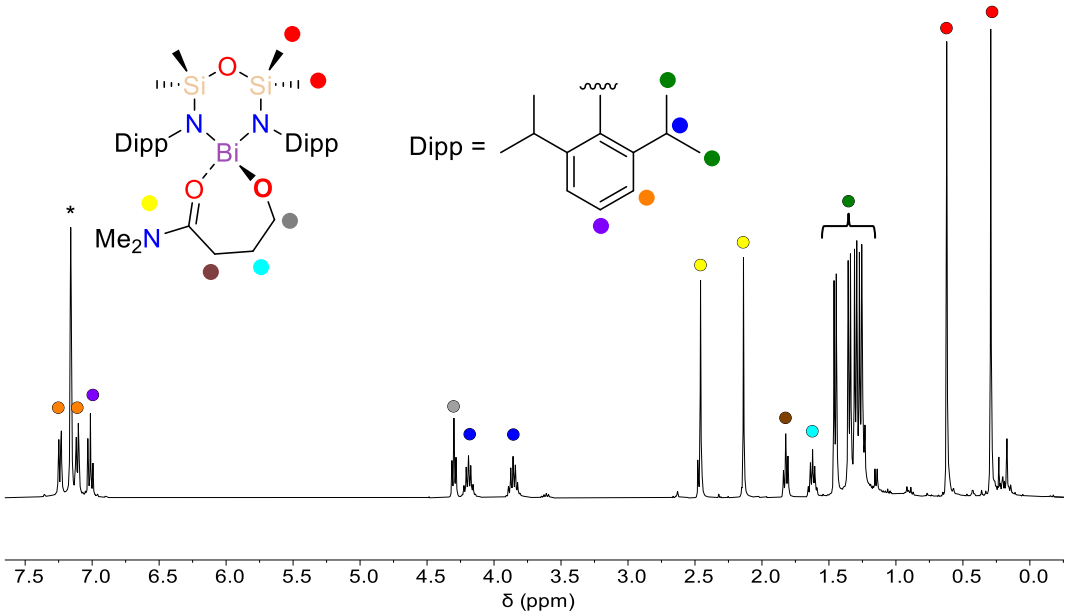


Figure 4.19 ^{1}H NMR spectrum (*benzene-d_6, 400 MHz, 298 K) of (NON^{Dipp})Bi(OC$_3$H$_6$C(O)NMe$_2$) (**9**).

This mirrors the solution-state structure of **8**, with comparable chemical shifts recorded for both [NON^{Dipp}]-ligand proton environments. Two singlets at δ 0.62 and 0.29 ppm are representative of the Si*Me*$_2$ protons, while two septets at δ 4.19 and 3.86 ppm correspond to the C*H*Me$_2$ protons. As anticipated, the N*Me*$_2$ protons of the carbamate functionality appear as two singlets at δ 2.47 and 2.15 ppm. The C*H*$_2$ protons of the ring-opened γ-butyrolactone moiety are located as two triplets at δ 4.30 and 1.82 ppm and a mutually coupled apparent pentet at δ 1.62 ppm. These signals are at a higher frequency relative to the corresponding resonances for the monomer, consistent with the formation of the

κ^2-*O,O'*-chelated ligand. Coordination between the carbonyl group and the bismuth centre is also supported by the presence of a high frequency carbonyl signal at δ 171.9 ppm in the $^{13}C\{^1H\}$ NMR spectrum, in agreement with those observed for the other two bismuth chelate compounds **7** and **8** (δ 182.6 and 171.8 ppm, respectively).

The IR spectrum of **9** contains a strong absorption at 1630 cm^{-1} assigned to ν(CO) stretching vibration (**Figure A.3.9** in **Appendix**), which is shifted to a lower frequency relative to the monomer (1770 cm^{-1}).[94] This value appears to be intermediate compared to the corresponding absorption bands for **7** and **8** (1613 and 1650 cm^{-1}, respectively).

4.6 Conclusions

Di(amido)siloxane bismuth amide **6** was found to be an active initiator for the ROP of lactide and ε-caprolactone. The polymerisation of lactide exhibited faster rates and proceeded without an induction period compared to the observations made using bismuth aryloxide and alkoxide analogues **1**–**5**. The enhanced ROP initiation capability of **6** is likely due to the lability of the Bi-N bond. In comparison to other main group and rare-earth amide initiators, the activity of **6** is moderate, attributed to the modest Lewis acidity and steric demands of the system.

The initiator was proposed to operate *via* a typical coordination-insertion mechanism, exhibiting a first-order dependence on both monomer and initiator concentrations. The polymerisations were well-controlled, resulting in predictable molecular weights and narrow-to-intermediate molecular weight distributions of polymers. MALDI-ToF, GPC, and ^1H NMR spectroscopic analyses of the isolated polymers suggested that intra- and intermolecular transesterification reactions using initiator **6** could not be supressed.

Based on polymer tacticity analysis, the ROP of *L*- and *D*-lactide produced isotactic PLA, whereas heterotactic-enriched PLA ($P_m = 0.86$) was obtained from the ROP of *meso*-lactide, demonstrating superior levels of stereocontrol relative to the ROP initiated by the aryloxide counterpart **2**. However, the ROP of *rac*-lactide afforded atactic PLA, correlating with poor reaction control.

Furthermore, compound **6** was shown to readily react with an equivalent of *L*-lactide, forming a bismuth chelate compound **7** featuring a κ^2-*O*,*O'*-bound lactate ligand. This represents a rare example of a structurally characterised ring-opened product of a single lactide unit. Further kinetic and mechanistic analyses suggested that **7** acts as the propagating species in the polymerisation of *L*-lactide.

Reactivity studies using ε-caprolactone and γ-butyrolactone highlighted the capability of **6** to form stable chelate compounds of various ring-opened polar monomers. While the ring-opening of ε-caprolactone proceeded rapidly at room temperature, the reaction with γ-butyrolactone required heating to 50 °C for 16 hours due to the relatively low strain energy of its five-membered ring. The insertion of a single ε-caprolactone molecule into the Bi-N bond of **6** led to a reduction in its activity towards subsequent monomer insertion steps. Consequently, the ROP of ε-caprolactone displayed an induction period and proceeded at a rate more than three times lower than that for *L*-lactide. In contrast, initiator **6** was inactive towards the ROP for γ-butyrolactone, attributed to both the high thermodynamic stability of the monomer and the reduced reactivity of the ring-opened intermediate. These compounds demonstrate unprecedented examples of well-defined, spectroscopically characterised metal complexes resulting from ε-caprolactone and γ-butyrolactone coordination and insertion chemistry.

4.7 References

1. A. Buchard, M. G. Davidson, G. Gobius du Sart, M. D. Jones, G. Kociok-Köhn, S. N. McCormick and P. McKeown, *Inorg. Chem.*, 2023, **62**, 15688-15699.
2. Z. R. Turner, J. T. Wilmore, N. H. Rees and J.-C. Buffet, *Dalton Trans.*, 2022, **51**, 3060-3074.
3. T. M. Ovitt and G. W. Coates, *J. Am. Chem. Soc.*, 2002, **124**, 1316-1326.
4. J. Lewiński, P. Horeglad, K. Wójcik and I. Justyniak, *Organometallics*, 2005, **24**, 4588-4593.
5. N. Yuntawattana, T. M. McGuire, C. B. Durr, A. Buchard and C. K. Williams, *Catal. Sci. Technol.*, 2020, **10**, 7226-7239.
6. Z. Tang, X. Pang, J. Sun, H. Du, X. Chen, X. Wang and X. Jing, *J. Polym. Sci., Part A: Polym. Chem.*, 2006, **44**, 4932-4938.
7. N. Nomura, R. Ishii, Y. Yamamoto and T. Kondo, *Chem. Eur. J.*, 2007, **13**, 4433-4451.
8. M. H. Chisholm and E. E. Delbridge, *New J. Chem.*, 2003, **27**, 1177-1183.
9. A. Duda and A. Kowalski, in *Handbook of Ring-Opening Polymerization*, 2009, pp. 1-51.
10. B.-T. Ko, F.-C. Wang, Y.-L. Sun, C.-H. Lin, C.-C. Lin and C.-Y. Kuo, *Polyhedron*, 1998, **17**, 4257-4264.
11. N. Nomura, R. Ishii, M. Akakura and K. Aoi, *J. Am. Chem. Soc.*, 2002, **124**, 5938-5939.
12. J. S. Klitzke, T. Roisnel, E. Kirillov, O. d. L. Casagrande, Jr. and J.-F. Carpentier, *Organometallics*, 2014, **33**, 309-321.
13. B. M. Chamberlain, M. Cheng, D. R. Moore, T. M. Ovitt, E. B. Lobkovsky and G. W. Coates, *J. Am. Chem. Soc.*, 2001, **123**, 3229-3238.
14. P. Horeglad, P. Kruk and J. Pécaut, *Organometallics*, 2010, **29**, 3729-3734.
15. L. Wang, C. E. Kefalidis, S. Sinbandhit, V. Dorcet, J.-F. Carpentier, L. Maron and Y. Sarazin, *Chem. Eur. J.*, 2013, **19**, 13463-13478.
16. A. P. Dove, V. C. Gibson, E. L. Marshall, H. S. Rzepa, A. J. P. White and D. J. Williams, *J. Am. Chem. Soc.*, 2006, **128**, 9834-9843.
17. A. Steudel, J. Stehr, E. Siebel and R. D. Fischer, *J. Organomet. Chem.*, 1998, **570**, 89-96.
18. M.-W. Hsiao and C.-C. Lin, *Dalton Trans.*, 2013, **42**, 2041-2051.
19. P. Horeglad, M. Cybularczyk, A. Litwińska, A. M. Dąbrowska, M. Dranka, G. Z. Żukowska, M. Urbańczyk and M. Michalak, *Polym. Chem.*, 2016, **7**, 2022-2036.
20. I. E. Nifant'ev, A. V. Shlyakhtin, V. V. Bagrov, M. E. Minyaev, A. V. Churakov, S. G. Karchevsky, K. P. Birin and P. V. Ivchenko, *Dalton Trans.*, 2017, **46**, 12132-12146.
21. S. Dagorne, F. Le Bideau, R. Welter, S. Bellemin-Laponnaz and A. Maisse-François, *Chem. Eur. J.*, 2007, **13**, 3202-3217.
22. A. M. Luke, A. Peterson, S. Chiniforoush, M. Mandal, Y. Popowski, H. Sajjad, C. J. Bouchey, D. Y. Shopov, B. J. Graziano, L. J. Yao, C. J. Cramer, T. M. Reineke and W. B. Tolman, *Macromolecules*, 2020, **53**, 1809-1818.

23. O. V. Kazarina, C. Gourlaouen, L. Karmazin, A. G. Morozov, I. L. Fedushkin and S. Dagorne, *Dalton Trans.*, 2018, **47**, 13800-13808.
24. W. J. Evans, J. L. Shreeve and R. J. Doedens, *Inorg. Chem.*, 1993, **32**, 245-246.
25. W. J. Evans, J. L. Shreeve, J. W. Ziller and R. J. Doedens, *Inorg. Chem.*, 1995, **34**, 576-585.
26. J. Lewiński, P. Horeglad, E. Tratkiewicz, W. Grzenda, J. Lipkowski and E. Kolodziejczyk, *Macromol. Rapid Commun.*, 2004, **25**, 1939-1942.
27. T. Afroz, D. M. Seo, S.-D. Han, P. D. Boyle and W. A. Henderson, *J. Phys. Chem. C*, 2015, **119**, 7022-7027.
28. I. Saura-Llamas, D. M. Dalton, A. M. Arif and J. A. Gladysz, *Organometallics*, 1992, **11**, 683-693.
29. A. Buchard, M. G. Davidson, G. Gobius du Sart, M. D. Jones, G. Kociok-Köhn, S. N. McCormick and P. McKeown, *Inorg. Chem.*, 2024, **63**, 27-38.
30. H. Dengel and C. Lichtenberg, *Chem. Eur. J.*, 2016, **22**, 18465-18475.
31. K. Oberdorf, P. Grenzer, P. Pfister, A. Hanft, A. Rempel and C. Lichtenberg, *ChemPlusChem*, 2023, **88**, e202200455.
32. K. Oberdorf, P. Grenzer, N. Wieprecht, J. Ramler, A. Hanft, A. Rempel, A. Stoy, K. Radacki and C. Lichtenberg, *Inorg. Chem.*, 2021, **60**, 19086-19097.
33. K. Oberdorf, P. Pfister, P. Grenzer, J. Ramler, A. Hanft, A. Stoy, X. Xie and C. Lichtenberg, *Organometallics*, 2023, **42**, 885-895.
34. K. B. Aubrecht, M. A. Hillmyer and W. B. Tolman, *Macromolecules*, 2002, **35**, 644-650.
35. A. Kowalski, A. Duda and S. Penczek, *Macromolecules*, 1998, **31**, 2114-2122.
36. J.-C. Buffet and J. Okuda, *Polym. Chem.*, 2011, **2**, 2758-2763.
37. K. R. Delle Chiaie, A. B. Biernesser, M. A. Ortuño, B. Dereli, D. A. Iovan, M. J. T. Wilding, B. Li, C. J. Cramer and J. A. Byers, *Dalton Trans.*, 2017, **46**, 12971-12980.
38. Y. Zhou, G. S. Nichol and J. A. Garden, *Eur. J. Inorg. Chem.*, 2022, **2022**, e202200134.
39. M. H. Chisholm and E. E. Delbridge, *New J. Chem.*, 2003, **27**, 1167-1176.
40. P. Wongmahasirikun, P. Prom-on, P. Sangtrirutnugul, P. Kongsaeree and K. Phomphrai, *Dalton Trans.*, 2015, **44**, 12357-12364.
41. K. Yu and C. W. Jones, *J. Catal.*, 2004, **222**, 558-564.
42. L. Clark, G. B. Deacon, C. M. Forsyth, P. C. Junk, P. Mountford, J. P. Townley and J. Wang, *Dalton Trans.*, 2013, **42**, 9294-9312.
43. J. R. Dorgan, J. Janzen, D. M. Knauss, S. B. Hait, B. R. Limoges and M. H. Hutchinson, *J. Polym. Sci., Part B: Polym. Phys.*, 2005, **43**, 3100-3111.
44. J. Coudane, C. Ustariz-Peyret, G. Schwach and M. Vert, *J. Polym. Sci., Part A: Polym. Chem.*, 1997, **35**, 1651-1658.
45. H. R. Kricheldorf and C. Boettcher, *J. Macromol. Sci. A*, 1993, **30**, 441-448.
46. M. H. Chisholm, N. W. Eilerts, J. C. Huffman, S. S. Iyer, M. Pacold and K. Phomphrai, *J. Am. Chem. Soc.*, 2000, **122**, 11845-11854.
47. C. Bonné, A. Pahwa, C. Picard and M. Visseaux, *Inorg. Chim. Acta*, 2017, **455**, 521-527.

48. H.-Y. Chen, J. Zhang, C.-C. Lin, J. H. Reibenspies and S. A. Miller, *Green Chem.*, 2007, **9**, 1038-1040.

49. C. K. Williams, L. E. Breyfogle, S. K. Choi, W. Nam, V. G. Young, M. A. Hillmyer and W. B. Tolman, *J. Am. Chem. Soc.*, 2003, **125**, 11350-11359.

50. A. Kowalski, J. Libiszowski, A. Duda and S. Penczek, *Macromolecules*, 2000, **33**, 1964-1971.

51. H. Wang, Y. Yang and H. Ma, *Inorg. Chem.*, 2016, **55**, 7356-7372.

52. N. Nimitsiriwat, V. C. Gibson, E. L. Marshall, A. J. P. White, S. H. Dale and M. R. J. Elsegood, *Dalton Trans.*, 2007, 4464-4471.

53. Y. Cui, W. Gu, Y. Wang, B. Zhao, Y. Yao and Q. Shen, *Catal. Sci. Technol.*, 2015, **5**, 3302-3312.

54. K. Nie, W. Gu, Y. Yao, Y. Zhang and Q. Shen, *Organometallics*, 2013, **32**, 2608-2617.

55. R. D. Shannon, *Acta Crystallogr. A*, 1976, **32**, 751-767.

56. P. I. Binda and E. E. Delbridge, *Dalton Trans.*, 2007, 4685-4692.

57. H. Ma and J. Okuda, *Macromolecules*, 2005, **38**, 2665-2673.

58. N. Diteepeng, J.-C. Buffet, Z. R. Turner and D. O'Hare, *Dalton Trans.*, 2019, **48**, 16099-16107.

59. A. F. Douglas, B. O. Patrick and P. Mehrkhodavandi, *Angew. Chem. Int. Ed.*, 2008, **47**, 2290-2293.

60. G. Hu, Z. Deng, Y. Wang, D. Yuan, Y. Zhang and Y. Yao, *J. Organomet. Chem.*, 2024, **1003**, 122941.

61. P. Piromjitpong, P. Ratanapanee, W. Thumrongpatanaraks, P. Kongsaeree and K. Phomphrai, *Dalton Trans.*, 2012, **41**, 12704-12710.

62. M. D. Jones, L. Brady, P. McKeown, A. Buchard, P. M. Schäfer, L. H. Thomas, M. F. Mahon, T. J. Woodman and J. P. Lowe, *Chem. Sci.*, 2015, **6**, 5034-5039.

63. C. Goonesinghe, H.-J. Jung, H. Roshandel, C. Diaz, H. A. Baalbaki, K. Nyamayaro, M. Ezhova, K. Hosseini and P. Mehrkhodavandi, *ACS Catal.*, 2022, **12**, 7677-7686.

64. J. S. Klitzke, T. Roisnel, E. Kirillov, O. d. L. Casagrande, Jr. and J.-F. Carpentier, *Organometallics*, 2014, **33**, 5693-5707.

65. K. Phomphrai, P. Chumsaeng, P. Sangtrirutnugul, P. Kongsaeree and M. Pohmakotr, *Dalton Trans.*, 2010, **39**, 1865-1871.

66. A. B. Kremer, R. J. Andrews, M. J. Milner, X. R. Zhang, T. Ebrahimi, B. O. Patrick, P. L. Diaconescu and P. Mehrkhodavandi, *Inorg. Chem.*, 2017, **56**, 1375-1385.

67. M. H. Chisholm, J. C. Gallucci, K. T. Quisenberry and Z. Zhou, *Inorg. Chem.*, 2008, **47**, 2613-2624.

68. P. Horeglad, M. Cybularczyk, B. Trzaskowski, G. Z. Żukowska, M. Dranka and J. Zachara, *Organometallics*, 2015, **34**, 3480-3496.

69. C. Bakewell, A. J. P. White, N. J. Long and C. K. Williams, *Inorg. Chem.*, 2015, **54**, 2204-2212.

70. R. H. Platel, L. M. Hodgson and C. K. Williams, *Polym. Rev.*, 2008, **48**, 11-63.

71. P. Dubois, N. Ropson, R. Jérôme and P. Teyssié, *Macromolecules*, 1996, **29**, 1965-1975.

72. D. J. Darensbourg and O. Karroonnirun, *Macromolecules*, 2010, **43**, 8880-8886.

73. A. Duda and S. Penczek, *Macromolecules*, 1995, **28**, 5981-5992.
74. C. Diaz, J. Fu, S. Soobrattee, L. Cao, K. Nyamayaro, C. Goonesinghe, B. O. Patrick and P. Mehrkhodavandi, *Inorg. Chem.*, 2022, **61**, 3763-3773.
75. W. Gruszka, A. Lykkeberg, G. S. Nichol, M. P. Shaver, A. Buchard and J. A. Garden, *Chem. Sci.*, 2020, **11**, 11785-11790.
76. W. Gruszka and J. A. Garden, *Chem. Commun.*, 2022, **58**, 1609-1612.
77. P. Dubois, C. Jacobs, R. Jerome and P. Teyssie, *Macromolecules*, 1991, **24**, 2266-2270.
78. W. Saiyasombat, R. Molloy, T. M. Nicholson, A. F. Johnson, I. M. Ward and S. Poshyachinda, *Polymer*, 1998, **39**, 5581-5585.
79. M. Sugimoto, J. Fujita, H. Ito, K. Toriumi and T. Ito, *Inorg. Chem.*, 1983, **22**, 955-960.
80. Y. Yao, Z. Zhang, H. Peng, Y. Zhang, Q. Shen and J. Lin, *Inorg. Chem.*, 2006, **45**, 2175-2183.
81. M. Möller, R. Kånge and J. L. Hedrick, *J. Polym. Sci., Part A: Polym. Chem.*, 2000, **38**, 2067-2074.
82. D. Pappalardo, L. Annunziata, C. Pellecchia, M. Biesemans and R. Willem, *Macromolecules*, 2007, **40**, 1886-1890.
83. H. R. Kricheldorf, G. Behnken, G. Schwarz and J. Kopf, *Macromolecules*, 2008, **41**, 4102-4107.
84. M. O. Miranda, Y. DePorre, H. Vazquez-Lima, M. A. Johnson, D. J. Marell, C. J. Cramer and W. B. Tolman, *Inorg. Chem.*, 2013, **52**, 13692-13701.
85. M.-H. Thibault and F.-G. Fontaine, *Dalton Trans.*, 2010, **39**, 5688-5697.
86. M. Labet and W. Thielemans, *Chem. Soc. Rev.*, 2009, **38**, 3484-3504.
87. J. Okuda and I. L. Rushkin, *Macromolecules*, 1993, **26**, 5530-5532.
88. D. P. Martin and S. F. Williams, *Biochem. Eng. J.*, 2003, **16**, 97-105.
89. K. N. Houk, A. Jabbari, H. K. Hall and C. Alemán, *J. Org. Chem.*, 2008, **73**, 2674-2678.
90. M. Hong and E. Y.-X. Chen, *Angew. Chem. Int. Ed.*, 2016, **55**, 4188-4193.
91. M. Hong and E. Y. X. Chen, *Nat. Chem.*, 2016, **8**, 42-49.
92. N. Zhao, C. Ren, H. Li, Y. Li, S. Liu and Z. Li, *Angew. Chem. Int. Ed.*, 2017, **56**, 12987-12990.
93. J.-B. Zhu, E. M. Watson, J. Tang and E. Y.-X. Chen, *Science*, 2018, **360**, 398-403.
94. D. P. McDermott, *J. Phys. Chem.*, 1986, **90**, 2569-2574.

Chapter 5

Reactivity towards small molecules using a di(amido)siloxane bismuth amide complex

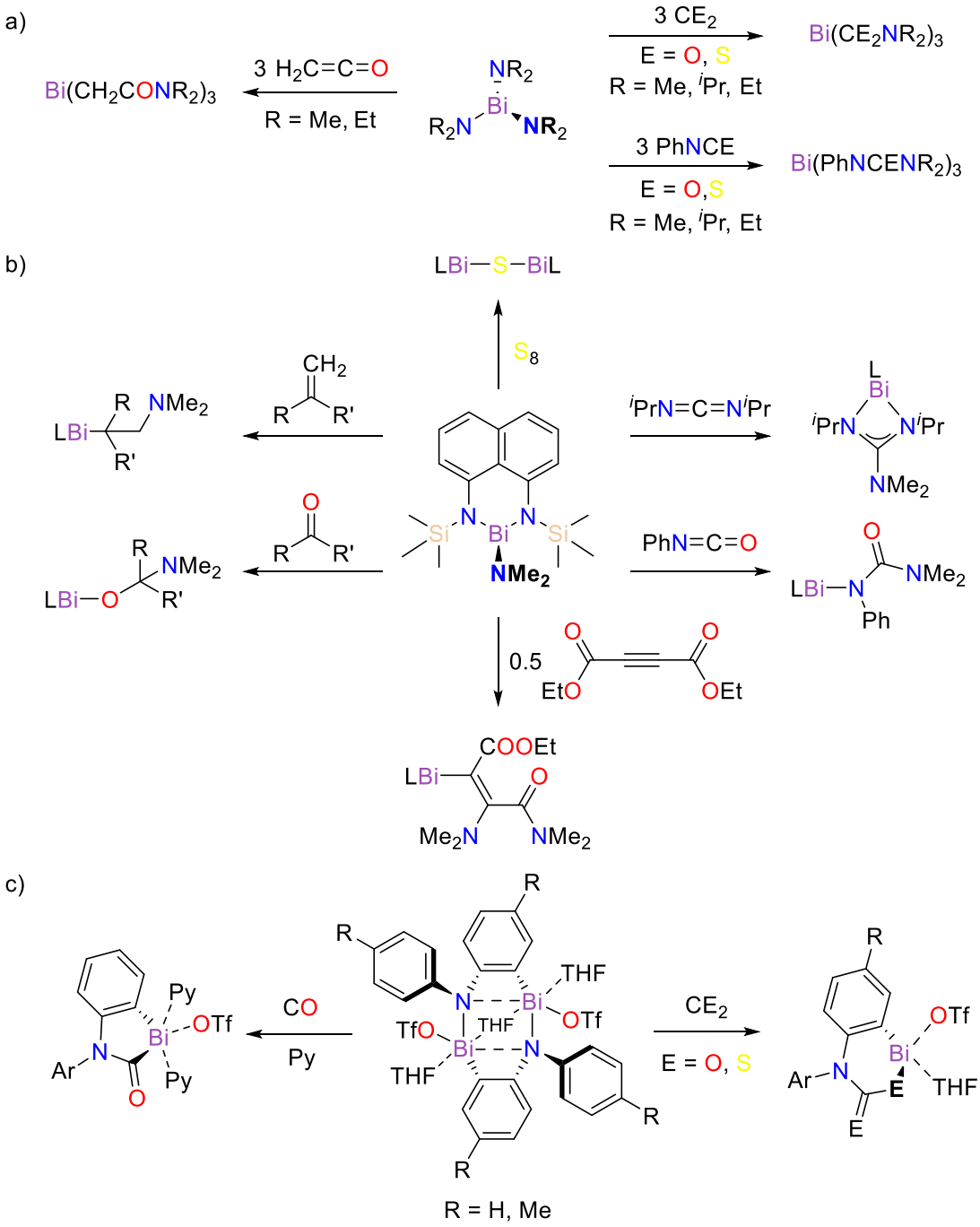
5.1 Introduction

The presence of large, diffuse, and polarisable atomic valence orbitals of bismuth results in the inefficient orbital overlap of Bi-X bonds (X = H, C, N, O), rendering them weaker compared to those of other *p*-block elements.[1] For example, this is reflected in the E-H bond dissociation enthalpies when E = P (81.4 kcal mol^{-1}) > As (74.6 kcal mol^{-1}) > Sb (63.3 kcal mol^{-1}) > Bi (51.8 kcal mol^{-1}).[2, 3] Due to the low bond dissociation energy, both Bi-N and Bi-O bonds can be cleaved *via* either the heterolytic or homolytic pathway, thus offering potential for diverse reactivity in synthetic chemistry.[1, 4, 5] The facile homolysis of Bi-O bonds has been investigated in catalysis, with applications such as the use of a heterogeneous Bi-Mo catalyst in the Standard Oil of Ohio (SOHIO) process for the selective oxidation and ammoxidation of propene.[6] Additionally, bismuth amide compounds with reactive Bi-N bonds have been employed as precursors for thin films and nanoparticles.[7, 8]

The activation of unsaturated substrates provides important building blocks for numerous chemical reactions. While transition metals have been extensively studied for C-C, C-O,

and C-N multiple bond transformations, cheaper and more widely abundant main group compounds have emerged as attractive alternatives.[9] The reactivity of homoleptic $Bi(NR_2)_3$ compounds (R = Me, ^{i}Pr, Et) towards heteroallenes (CO_2, CS_2, phenyl isocyanate, and phenyl isothiocyanate) was first discussed by Ando and co-workers in 1975 (**Scheme 5.1a**).[10] The insertion of CO_2 and CS_2 molecules into the Bi-N bond resulted in moderately air-stable bismuth carbamate and thiocarbamate complexes, respectively, whereas the products of phenyl isocyanate and phenyl isothiocyanate insertion reactions were found to be highly air sensitive. Subsequently, it was demonstrated that $Bi(NEt_2)_3$ is capable of activating a series of other carbonyl compounds, including benzophenone, acetophenone, and diethyl ketone.[11] However, the overall amination efficiency appeared to be lower compared to its Sb and As analogues. Despite the initial fast insertion of carbonyl groups into the Bi-N bond, decomposition of the resulting bismuth amino alkoxides was observed, attributed to the relatively low oxophilicity of bismuth. Following these reports, homoleptic $Bi(NEt_2)_3$ and $Bi(NMe_2)_3$ compounds have also been shown to readily insert ethenone, displaying faster reaction rates than their As and Sb counterparts.[12]

Examples of well-defined reactivity of heteroleptic bismuth amides with small molecules remain rare, encouraging fundamental studies in this field. Roesky and co-workers examined a bismuth amide complex supported by a 1,8-diaminonaphthalene ligand, demonstrating the facile insertion of unsaturated C-C, C-O, and C-N bonds into the Bi-N bond (**Scheme 5.1b**).[13, 14] This complex was also shown to react with S_8 to form a bimetallic species with a bridging μ^2-S unit, stabilised by inter- and intramolecular Bi-arene interactions.



Scheme 5.1 Selected examples of bismuth(III) amides utilised for small molecule activation.

Lichtenberg and co-workers reported the first example of CO insertion into the Bi-N bond by means of a dinuclear cationic bismuth amide complex (**Scheme 5.1c**).[15] The compound was also reactive towards carbodiimides, CS_2, and CO_2.[16] Upon the release of CO_2 from the metastable insertion product, the complex was shown to undergo C-H

activation.[17] In contrast, the enhanced stability of the CS_2 insertion product required photochemical conditions to promote the release of CS_2. The CE_2 (E = O, S) extrusion was proposed to proceed *via* heterolytic cleavage of the Bi-E bond, with the carbamate product favoured due to its greater stability.

5.2 Synopsis

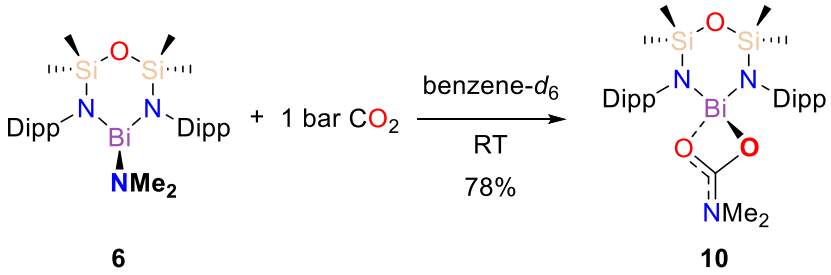
In **Chapter Five**, the reactivity studies of di(amido)siloxane bismuth amide complex (NON^{Dipp})Bi(NMe_2) (**6**) are presented. In light of the observed reactivity of the Bi-N bond towards cyclic esters described in **Chapter Four**, the capability of **6** to activate a range of unsaturated organic molecules has been explored. Four new di(amido)siloxane bismuth complexes have been synthesised and characterised.

5.3 Reactivity studies of di(amido)siloxane bismuth amide (6)

5.3.1 Reactivity with carbon dioxide

An NMR-scale reaction between compound **6** and 1 bar of CO_2 in benzene-d_6 proceeded instantly at room temperature. ^{1}H NMR analysis indicated the quantitative formation of the CO_2 insertion product (NON^{Dipp})Bi(CO_2NMe_2) (**10**), which was subsequently isolated as an off-white powder in 78% yield (**Scheme 5.2**).

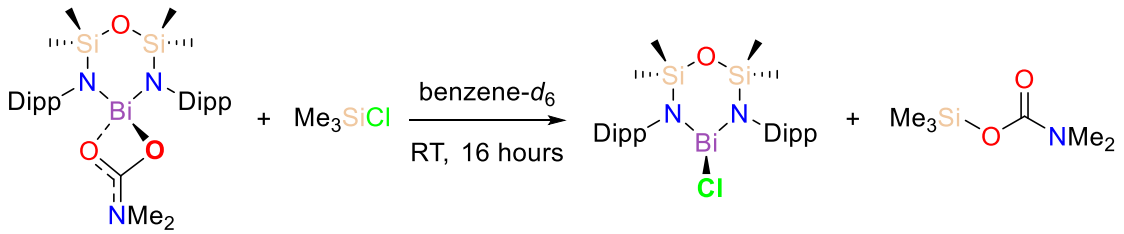
The insertion of CO_2 into **6** appears to be irreversible as CO_2 could not be released from the benzene-d_6 solution of the carbamate complex **10** under reduced pressure. Heating the corresponding solution to 50 °C for 24 hours resulted in the partial decomposition of **10** into the (NON^{Dipp})H_2 pro-ligand.



6 **10**

Scheme 5.2 Synthesis of (NON^{Dipp})Bi(CO_2NMe_2) (**10**).

Alternatively, the carbamate fragment in **10** can undergo transformation *via* a substitution reaction. The trimethylsilyl chloride (Me_3SiCl) reagent is commonly used for the abstraction of CO_2 and N_2 units in organometallic complexes.[18, 19] The addition of a stoichiometric amount of Me_3SiCl to the benzene-d_6 solution of **10** generated the bismuth chloride complex (NON^{Dipp})BiCl (see **Figure A.1.5** in **Appendix** for its ^{1}H NMR spectrum) alongside trimethylsilyl *N*,*N*-dimethylcarbamate (**Scheme 5.3**). The formation of the carbamate product was confirmed by ^{1}H NMR spectroscopy, revealing a characteristic Si*Me*$_3$ singlet at δ 0.33 ppm and two distinct signals at δ 2.59 and 2.48 ppm assigned to the N*Me*$_2$ protons.



10

Scheme 5.3 Abstraction of the carbamate group from (NON^{Dipp})Bi(CO_2NMe_2) (**10**).

When an analogous reaction with CO_2 was conducted using di(amido)siloxane bismuth aryloxide **2**, the addition product across the Bi-O bond was not formed. This can be explained by the increased strength of the Bi-O bond relative to the Bi-N bond, consistent

with the observed slow reactivity of **2** towards cyclic esters (see **Chapter Three** for detailed discussion).

5.3.1.1 NMR and IR spectroscopic analyses

The ^{1}H NMR spectrum of **10** is consistent with C_s molecular symmetry in solution (**Figure 5.1**). The presence of two Si*Me*$_2$ resonances at δ 0.57 and 0.23 ppm reflects impeded ring flipping of the BiN_2Si_2O metallacycle, leading to the formation of two inequivalent faces of the ligand. Due to the insertion of CO_2 into the Bi-N bond, the resonance for the N*Me*$_2$ protons is shifted to a lower frequency compared to that for **6** (δ 2.73 and 3.78 ppm, respectively). Two inequivalent C*H*Me$_2$ proton environments, represented by septets at δ 4.11 and 3.76 ppm, and four distinct doublets between δ 1.37–1.02 ppm corresponding to the CH*Me*$_2$ protons, indicate restricted rotation of the amido-*N*-aryl bond. The ^{13}C{^{1}H} NMR spectrum displays the carbonyl carbon as the highest frequency signal at δ 162.9 ppm, consistent with that recorded for the homoleptic bismuth carbamate $Bi(CO_2N^iPr_2)_3$ (δ 162.2 ppm).[20]

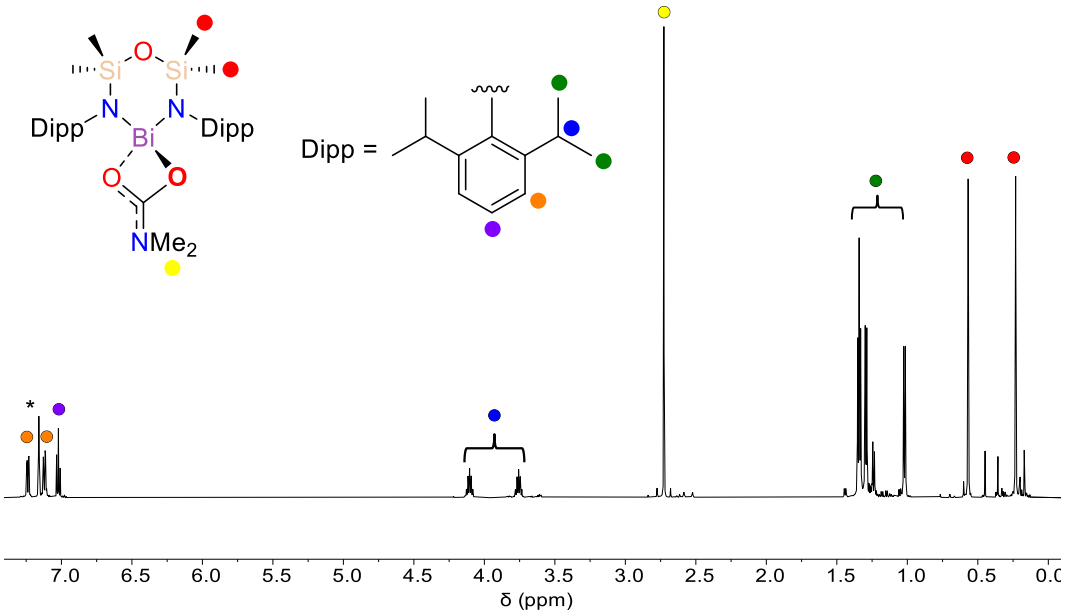


Figure 5.1 ^{1}H NMR spectrum (*benzene-d_6, 600 MHz, 298 K) of (NON^{Dipp})Bi(CO_2NMe_2) (**10**).

The IR spectrum of **10** (**Figure A.4.1** in **Appendix**) contains strong absorptions at 1594 and 1391 cm^{-1} assigned to asymmetric and symmetric C=O stretching vibrations, respectively. These values compare well with the range of the corresponding vibrations for previously reported metal carbamate complexes, such as $TlMe_2(CO_2NMe_2)$ and $AlEt_2(CO_2NEt_2)$.[21, 22]

5.3.1.2 X-ray crystallographic analysis

Single crystals of compound **10**, suitable for an X-ray diffraction study, were grown from slow evaporation of a hexane solution at 23 °C and solved in the triclinic space group, $P\overline{1}$ (**Figure 5.2**, **Table 5.1**).

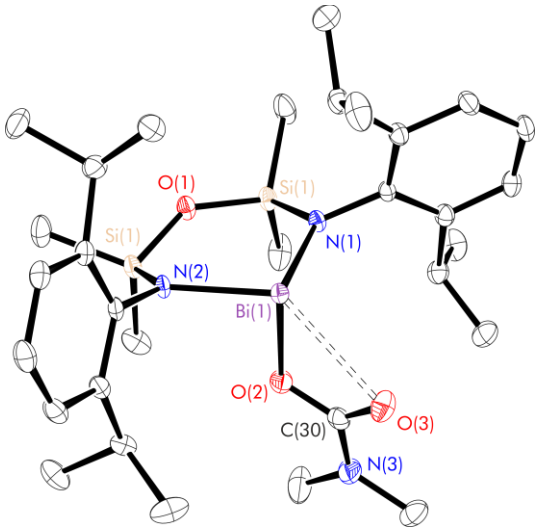


Figure 5.2 Thermal displacement ellipsoid drawing (30%) of the asymmetric unit of $(NON^{Dipp})Bi(CO_2NMe_2)$ (**10**). All hydrogen atoms have been omitted for clarity.

The solid-state structure of **10** reveals a distorted pyramidal geometry at the bismuth centre ($\Sigma(\angle Bi) = 277.9°$). The six-membered BiN_2Si_2O metallacycle adopts a chair conformation, characterised by a small torsion angle (N(1)-Si(1)-Si(2)-N(2) = 8.02(2)°) and statistically indistinguishable Bi-N bond lengths (2.163(3) and 2.166(3) Å). The carbamate group is planar ($\Sigma(\angle C(30)) = 360.1°$), consistent with the delocalisation of

π electron density over the OCN fragment. This coincides with the shortening of the C-N bond length, implying a partial double bond character.

Table 5.1 Selected experimental metrical parameters (bond lengths (Å) and angles (°)) for (NON^{Dipp})Bi(CO_2NMe_2) (**10**). Estimated standard deviations shown in brackets.

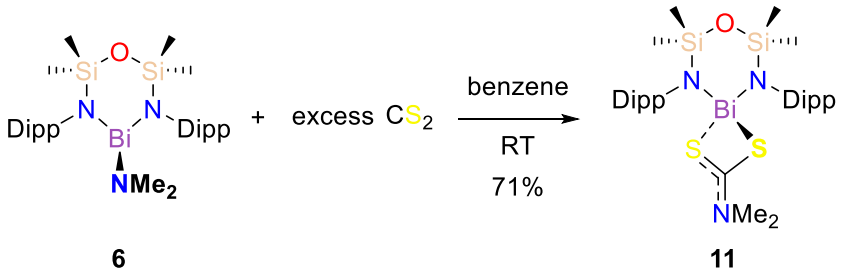
Space group	$P\bar{1}$
Bi(1)-N(1)	2.163(3)
Bi(1)-N(2)	2.166(3)
Bi(1)-O(2)	2.181(3)
Bi(1)-O(3)	2.794(3)
C(30)-O(3)	1.241(5)
C(30)-O(2)	1.293(5)
C(30)-N(3)	1.355(5)
N(1)-Bi(1)-N(2)	100.00(10)
Si(1)-O(1)-Si(2)	139.24(17)

The carbamate ligand exhibits two different Bi-O distances suggestive of κ^1 coordination. The Bi(1)-O(2) bond length corresponds to a typical covalent bond (2.181(3) *vs.* $\sum r_{cov}$(Bi,O) = 2.16 Å),[23] whereas a significantly longer Bi(1)-O(3) distance reflects only a weak non-covalent interaction (2.794(3) Å). Both values fall within a broad range of Bi-O distances reported for related bismuth carbamate compounds (2.107(4)–3.058(4) Å).[20] The coordination asymmetry is further observed in the variation in C-O bond lengths in the carbamate group, indicating the presence of a single bond (C(30)-O(2) = 1.293(5) Å) and a partial double bond (C(30)-O(3) = 1.241(5) Å).[4] Overall, this asymmetric chelation of the carbamate ligand is comparable to the bonding

environment in two previously structurally charactered bismuth carbamate compounds, $Bi(CO_2N^iPr_2)_3$ and its oxo-cluster derivative $Bi_8(O)_6(CO_2N^iPr_2)_{12}$.[20]

5.3.2 Reactivity with carbon disulfide

The reactivity of **6** was investigated using CS_2 as an isoelectronic analogue to CO_2. The addition of an excess of CS_2 to a solution of **6** in benzene resulted in the immediate formation of the thiocarbamate complex $(NON^{Dipp})Bi(CS_2NMe_2)$ (**11**), as confirmed by the *in situ* ^{1}H NMR spectrum. The compound was isolated as a yellow powder in 71% yield (**Scheme 5.4**).



6 **11**

Scheme 5.4 Synthesis of $(NON^{Dipp})Bi(CS_2NMe_2)$ (**11**).

5.3.2.1 NMR and IR spectroscopic analyses

Compound **11** forms a C_{2v}-symmetric species on the NMR timescale (**Figure 5.3**). The presence of a single resonance for both the Si*Me*$_2$ (singlet at δ 0.45 ppm) and the C*H*Me$_2$ protons (septet at δ 4.00 ppm) implies an energetically accessible dithiocarbamate ligand exchange process that occurs rapidly on the NMR timescale at room temperature. This contrasts with the restricted solution-state fluxionality seen for all the other di(amido)siloxane bismuth complexes **1**–**10**. The CH*Me*$_2$ protons in **11** are located as two doublets at δ 1.39 and 1.36 ppm, indicative of hindered amido-*N*-aryl bond rotation.

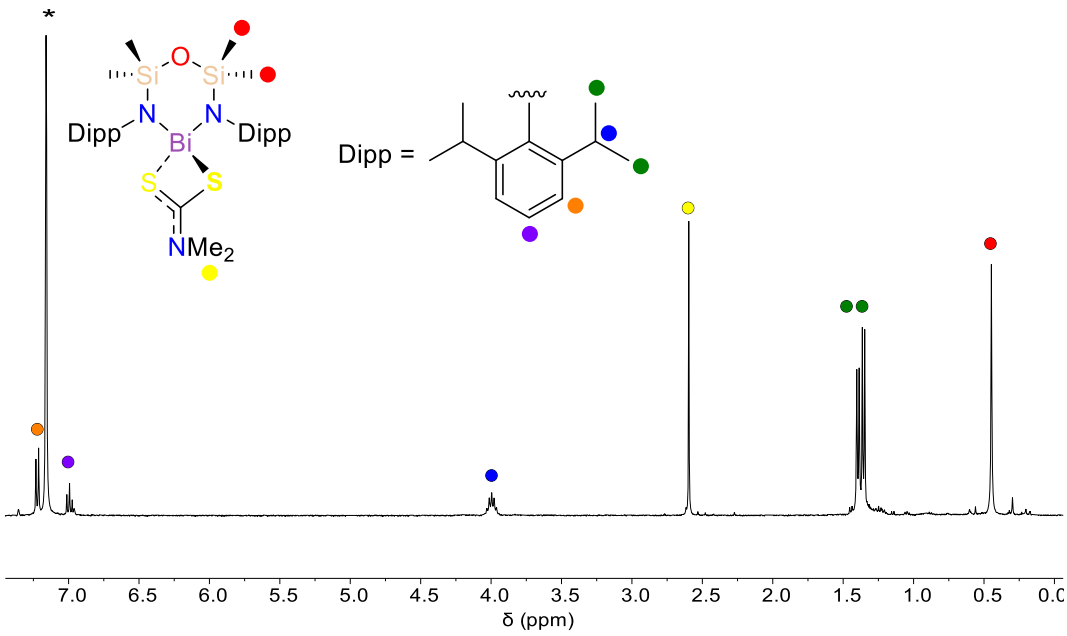
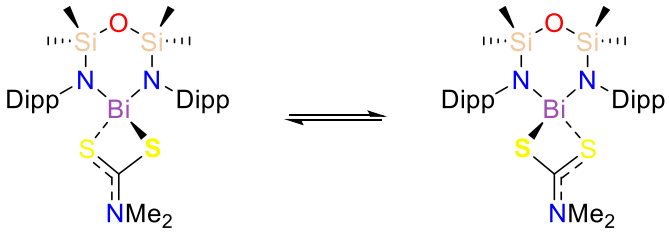


Figure 5.3 ^{1}H NMR spectrum (*benzene-d_6, 400 MHz, 298 K) of (NON^{Dipp})Bi(CS_2NMe_2) (**11**).

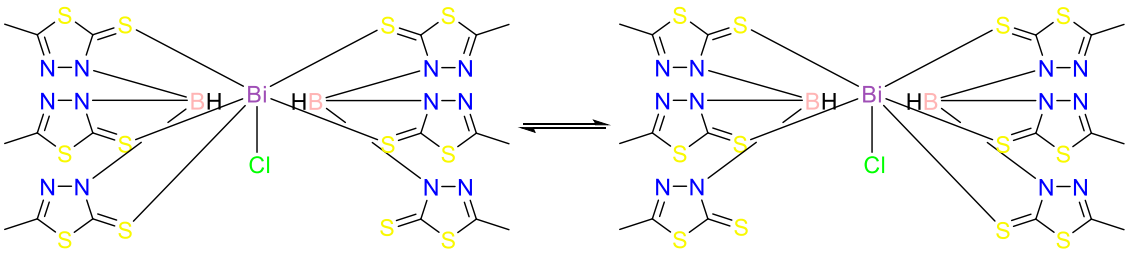
When the toluene-d_8 solution of **11** was cooled to –50 °C (223 K), a sharp Si*Me*$_2$ singlet split into two resonances, and a septet corresponding to the C*H*Me$_2$ protons was replaced by two broad signals (**Figure 5.4**). Warming up the solution resulted in the coalescence of the resonances as the ring flip, presumably *via* the Bi-S bond cleavage and recombination, became energetically accessible (**Scheme 5.5**). Further evidence for this solution-state fluxionality for **11** could be provided by DFT analysis.



Scheme 5.5 Proposed solution-state fluxionality of **11**.

Comparable fluxionality of Bi-S bonds has been discussed for a bismuth complex bearing two symmetric heterocyclic Janus scorpionato ligands, coordinated in two different, κ^3-*S*,*S*′,*S*″ and κ^2-*S*,*S*′, bonding modes (**Scheme 5.6**).[24] ^{1}H NMR spectroscopic studies

revealed rapid exchange of the coordinating units occurring above 293 K, whereas further heating above 333 K led to a complete dissociation of the ligand.



Scheme 5.6 Solution-state fluxionality of $(L)_2BiCl$.[24]

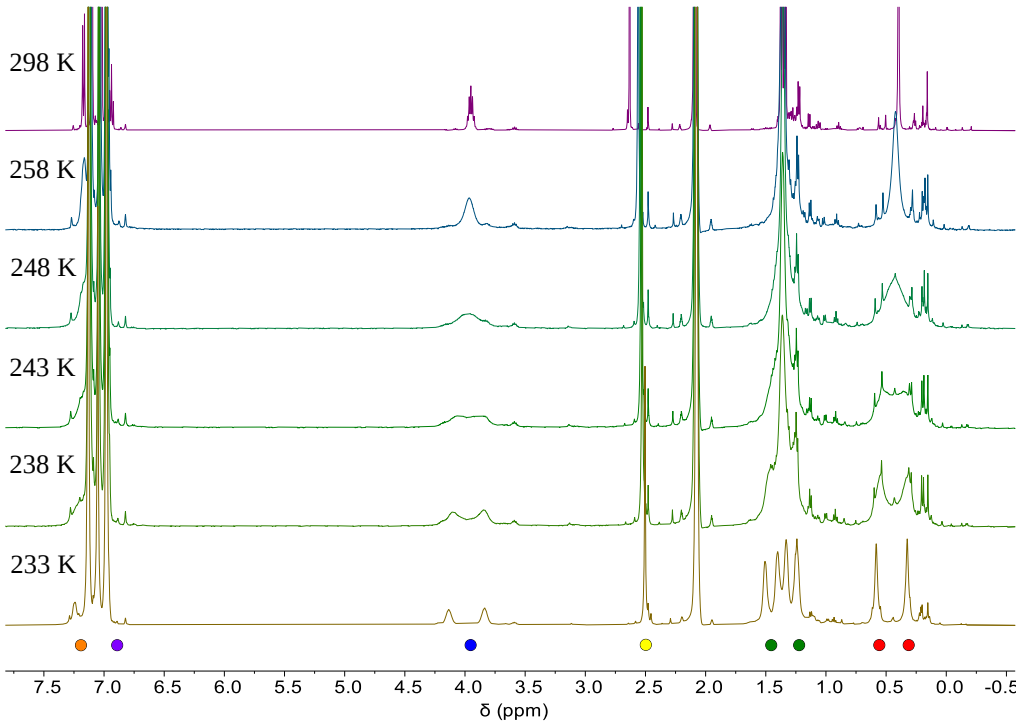


Figure 5.4 Variable temperature ^{1}H NMR spectra (toluene-d_8, 500 MHz) of $(NON^{Dipp})Bi(CS_2NMe_2)$ (**11**).

Based on the variable temperature studies using **11**, the coalescence temperature (T_c) of –30 °C (243 K) was measured as the lowest temperature limit, where two resonances for the C*H*Me$_2$ protons appear with the maximum peak separation ($\Delta\nu$) of 177.83 Hz. From these results, the Gibbs free energy barrier ($\Delta G^{\ddagger}$) for the ring flipping at the bismuth centre was determined to be 47.0 kJ mol^{-1} (**Equation 5.1**).[25]

In comparison, a slightly higher activation barrier ($\Delta G^{\ddagger}$ = 60.8–60.4 kJ mol^{-1}) has been reported for the pyramidal inversion at the bismuth centre *via* a weakened Bi-O bond in the related di(amido)siloxane bismuth TEMPO complex (NON$^{t\text{Bu}}$)Bi(OTEMP).[26] These findings support a relatively labile nature of the Bi-S bond in **11**.

$$\Delta G^{\ddagger} = RT_{\mathrm{c}}\left(23 + \ln\left(\frac{T_{\mathrm{c}}}{\Delta\nu}\right)\right)$$

$$k_{\mathrm{c}} = \frac{\pi\Delta\nu}{\sqrt{2}}$$

Equation 5.1 Definition of the activation barrier for a fluxional process, where $\Delta G^{\ddagger}$ = Gibbs free energy, T_{c} = coalescence temperature, R = gas constant, k_{c} = rate of fluxionality at T_{c}, $\Delta\nu$ = peak separation.

The IR spectrum of **11** shows absorptions at 961 and 1506 cm^{-1} corresponding to the ν(CS) and ν(CN) vibrations, respectively.[27, 28] These data imply partial double bond character, consistent with the delocalisation of π electron density within the dithiocarbamate unit.

5.3.2.2 X-ray crystallographic analysis

Single crystals of complex **11**, suitable for an X-ray diffraction study, were grown from slow evaporation of a hexane solution at 23 °C and solved in the triclinic space group, $P\overline{1}$ (**Figure 5.5**, **Table 5.2**).

The solid-state structure of **11** indicates a four-coordinate bismuth centre in a distorted disphenoidal environment. Axial sites are occupied by atoms N(2) and S(2) (N(2)-Bi(1)-S(2) = 151.57(8)°), while N(1) with S(1) sit in equatorial positions (N(1)-Bi(1)-S(1) = 101.80(8)°). In contrast to the chair conformation observed for **10**, the BiN_2Si_2O metallacycle in **11** adopts a twist-boat conformation, defined by a significantly

larger torsion angle (N(1)-Si(1)-Si(2)-N(2) = 34.6(1)°). The twist-boat conformation has also been formed in other di(amido)siloxane bismuth complexes **1**–**4**, **12**, and **13** (*vide infra*).

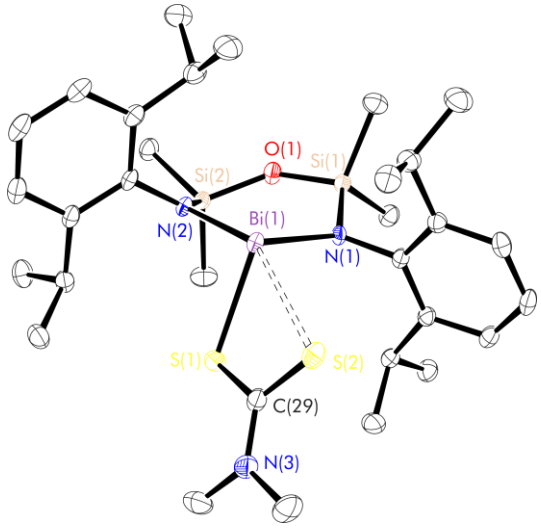


Figure 5.5 Thermal displacement ellipsoid drawing (30%) of the asymmetric unit of (NON^{Dipp})Bi(CS_2NMe_2) (**11**). All hydrogen atoms have been omitted for clarity.

The dithiocarbamate moiety coordinates to the bismuth centre in an asymmetric κ^2-bonding mode, with one Bi-S distance notably shorter than the other (Bi(1)-S(1) = 2.593(9) Å and Bi(1)-S(2) = 3.0081(10) Å). Both values are comparable to corresponding bond lengths reported for previously characterised organobismuth dithiocarbamates (Bi-S = 2.66–3.02 Å).[28-30]

There is also a clear asymmetry in the two C-S distances: the C(29)-S(1) bond length corresponds to a single covalent bond, while a shorter C(29)-S(2) distance indicates a partial double bond character (1.749(4) and 1.688(4) Å, respectively, *vs.* $\sum r_{cov}$(C,S) = 1.78 Å).[31] This, combined with the shortening of the C(29)-N(3) bond, implies that π electron density is delocalised over the planar SCN fragment (Σ(∠C(29)) = 359.9°). Similarly, the asymmetric κ^2-coordination of the dithiocarbamate

unit has been described for various other organometallic complexes.[32, 33] The lengthening of the M-S bond has been proposed to result from both the steric constraints and the electronic *trans* influence of supporting ligands.[34] By contrast, examples of a symmetric metal-dithiocarbamate bonding environment are rare.[35, 36]

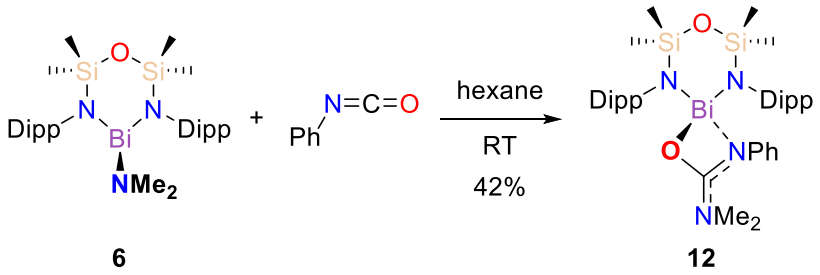
Table 5.2 Selected experimental metrical parameters (bond lengths (Å) and angles (°)) for (NON^{Dipp})Bi(CS_2NMe_2) (**11**). Estimated standard deviations shown in brackets.

Space group	$P\bar{1}$
Bi(1)-N(1)	2.170(2)
Bi(1)-N(2)	2.202(3)
Bi(1)-S(1)	2.5933(9)
Bi(1)-S(2)	3.0081(10)
Bi(1)-O(1)	3.595(2)
C(29)-S(1)	1.749(4)
C(29)-S(2)	1.688(4)
C(29)-N(3)	1.331(5)
N(1)-Bi(1)-N(2)	96.82(10)
Si(1)-O(1)-Si(2)	139.98(17)

5.3.3 Reactivity with phenyl isocyanate

When excess phenyl isocyanate (PhNCO) was added to a benzene-d_6 solution of **6**, the ^{1}H NMR spectrum revealed the immediate consumption of **6** to yield a single new product, suggesting the insertion of the ureato (RN=C=O) fragment into the Bi-N bond. The reaction was then repeated in hexane with equimolar stoichiometry, and the insertion

product (NON^{Dipp})Bi(NPhCONMe$_2$) (**12**) was isolated as colourless crystals in 42% yield (**Scheme 5.7**).



Scheme 5.7 Synthesis of (NON^{Dipp})Bi(NPhCONMe$_2$) (**12**).

5.3.3.1 NMR spectroscopic analysis

The ^{1}H NMR spectrum of **12** confirms the chelation of the [NON^{Dipp}]-ligand to the bismuth centre in a C_s-symmetric environment (**Figure 5.6**). The rotation of the amido-*N*-aryl bond and the fluxionality at the bismuth centre are both energetically inaccessible on the NMR timescale at room temperature. This is confirmed by the presence of two singlets at δ 0.59 and 0.31 ppm corresponding to the Si*Me*$_2$ protons, two septets at δ 4.26 and 3.81 ppm for the C*H*Me$_2$ protons, and four doublets between δ 1.38–1.03 ppm assigned to the CH*Me*$_2$ protons. In addition, the phenyl substituent in the ureato ligand is capable of free rotation, as the corresponding *ortho*- and *meta*-protons appear as a doublet at δ 6.14 ppm and a triplet at δ 6.99 ppm, respectively, implying that the two opposite phenyl sides are equivalent. The N*Me*$_2$ resonance at δ 2.41 ppm is at a comparable frequency relative to the corresponding signals for **10** (δ 2.73 ppm) and **11** (δ 2.60 ppm).

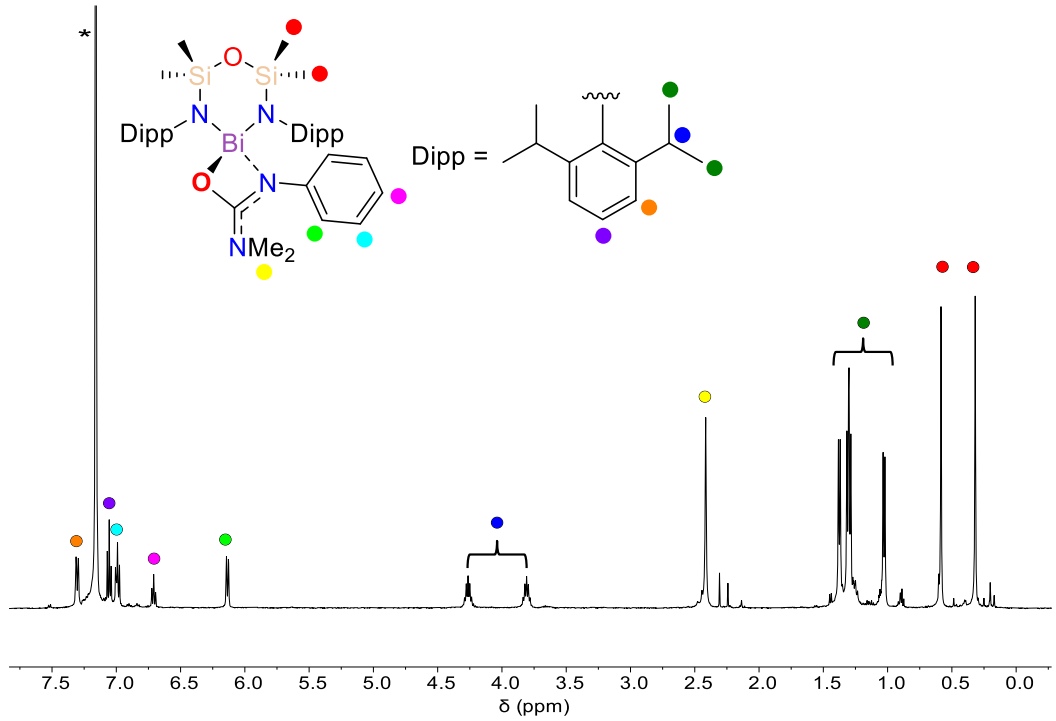


Figure 5.6 ^{1}H NMR spectrum (*benzene-d_6, 400 MHz, 298 K) of (NON^{Dipp})Bi(NPhCONMe$_2$) (**12**).

5.3.3.2 X-ray crystallographic analysis

Single crystals of **12**, suitable for an X-ray diffraction study, were grown from slow evaporation of a hexane solution at –30 °C. Compound **12** crystallised in the triclinic space group, $P\bar{1}$ (**Figure 5.7**, **Table 5.3**).

In the solid state, the bismuth centre adopts a distorted disphenoidal geometry with axial positions occupied by atoms N(1) and N(3) (N(1)-Bi(1)-N(3) = 140.14(9)°), while the remaining N(2) and O(2) atoms are located in equatorial sites (O(2)-Bi(1)-N(2) = 94.82(8)°). The ureato fragment is bound to the bismuth centre *via* a covalent Bi-O bond, which is slightly longer compared to the corresponding bond in **10** (2.210(2) *vs*. 2.181(3) Å, respectively), as well as a weaker Bi-N interaction (Bi(1)-N(3) = 2.554(2) Å), exceeding the typical covalent bond length ($\sum r_{cov}$(Bi,N) = 2.22 Å).[37] The resulting BiOCN metallacycle is planar, with a maximum displacement of 0.059 Å for C(29) relative to the BiOCN mean plane. Both C-N bond

distances (C(29)-N(3) = 1.321(4) Å and C(29)-N(4) = 1.352(4) Å) are shorter than a standard C-N single bond.[37] These results suggest the delocalisation of π electrons over the NCN fragment, consistent with previous reports of ureato complexes.[38, 39] Additionally, the C-O bond length is comparable to that of a single C-O bond formed in **10** (1.306(4) and 1.293(5) Å, respectively).

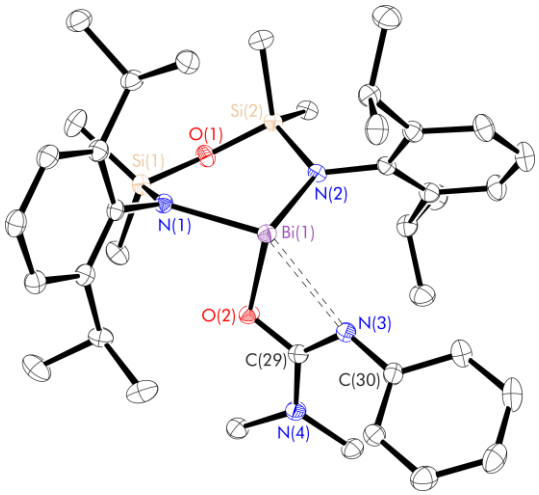


Figure 5.7 Thermal displacement ellipsoid drawing (30%) of the asymmetric unit of (NON^{Dipp})Bi(NPhCONMe$_2$) (**12**). All hydrogen atoms have been omitted for clarity.

In addition to the κ^2-*N*,*O*-bonding environment in the case of **6**, a range of possible coordination modes have been reported for single-site main group compounds supported by ureato ligands. For example, the κ^1-ureato bismuth complex, formed by treating *bis*(amino)naphthalene bismuth amide (L)Bi(NMe$_2$) previously discussed in **Section 5.1** with PhNCO, exhibited a covalent Bi-N bond and a non-covalent Bi-O interaction, concomitant with a partial double bond character of the C=O bond within the ureato ligand (**Table 5.3**).[40]

Steric effects of alkyl isocyanate reagents have been examined with regard to the reactivity of tin(II) amide [Sn(NMe$_2$)$_2$]$_2$.[41] The insertion of RNCO substrates (R = cyclohexyl and mesityl) into the Sn-N bond led to the formation of complexes

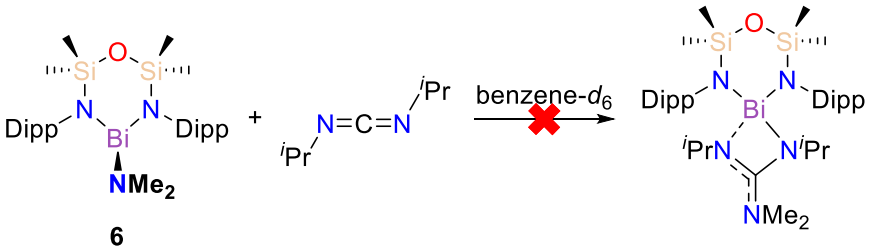
featuring two κ^2-*N*,*O*-bound ureato ligands, with the Sn-O bond elongated compared to the Sn-N bond. Conversely, the insertion products of sterically bulkier *tert*-butyl and adamantyl RNCO derivatives were found to consist of one κ^2-*N*,*O*-bound ligand and one ureato group exhibiting an unusual κ^2-*N*,*N'* coordination mode, with nitrogen donors provided by both the NR and NMe_2 groups.

Table 5.3 Selected experimental metrical parameters (bond lengths (Å) and angles (°)) for (NON^{Dipp})Bi(NPhCONMe$_2$) (**12**) and a related bismuth complex (L)Bi(NPhCONMe$_2$).[40] Estimated standard deviations shown in brackets.

	12	(L)Bi(NPhCONMe$_2$)[40] L = 1,8-(NSiMe$_3$)$_2$C$_{10}$H$_6$
Space group	$P\bar{1}$	$P\bar{1}$
Bi(1)-N(1)	2.196(2)	-
Bi(1)-N(2)	2.162(2)	-
Bi(1)-N(3)	2.554(2)	2.224(2)
Bi(1)-O(2)	2.210(2)	2.730(1)
Bi(1)-O(1)	3.443(3)	-
C(29)-O(2)	1.306(4)	1.245(2)
C(29)-N(3)	1.321(4)	1.395(2)
C(29)-N(4)	1.352(4)	1.353(2)
N(1)-Bi(1)-N(2)	99.49(9)	-
Si(1)-O(1)-Si(2)	142.25(15)	-

5.3.4 Reactivity with *N,N'*-di*iso*propylcarbodiimide

An equimolar NMR-scale reaction was carried out to probe the reactivity between **6** and *N,N'*-di*iso*propylcarbodiimide, an alternative heteroallene that is isoelectronic to CO_2 (**Scheme 5.8**). No change in the ^{1}H NMR spectrum of the reaction mixture was detected even upon heating to 50 °C for 48 hours. The observed resistance to the insertion of *N,N'*-di*iso*propylcarbodiimide is likely due to a combination of factors, including the steric constraints of the unsatured NCN fragment and the relatively low electrophilicity of carbodiimide substrates compared to the previously studied heteroallenes (CO_2, CS_2, and isocyanate).[42]



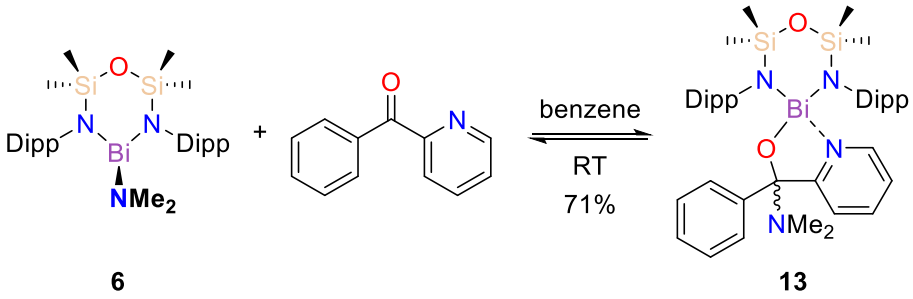
Scheme 5.8 Attempted synthesis of (NON^{Dipp})Bi(^{i}PrNCN^{i}PrNMe$_2$).

Lichtenberg and co-workers demonstrated that the insertion of *N,N'*-di*iso*propylcarbodiimide into the Bi-N bond of Bi(NMe$_2$)$_3$ was slow, proceeding over 24 hours at room temperature, whereas no reactivity was observed using sterically bulkier Bi(N^{i}Pr$_2$)$_3$.[43] In contrast, the cationic derivatives of these bismuth amide compounds were found to be significantly more reactive. A facile reaction with *N,N'*-di*iso*propylcarbodiimide has also been reported using the *bis*(amino)naphthalene bismuth amide complex (L)Bi(NMe$_2$).[40] This difference in reactivity compared to **6** may arise from the lesser steric demand of the SiMe$_3$ groups on the amido ligand compared to the Dipp substituents in **6**.

5.3.5 Reactivity with 2-benzoylpyridine

Initially, the reactivity of **6** towards ketones was tested in reactions using acetophenone and benzophenone substrates. No reaction was observed after heating the mixtures to 70 °C for 24 hours.

The insertion of the more electrophilic ketone, 2-benzoylpyridine, has been previously reported for Bi-N and Sn(II)-N bonds.[14, 44] Following these methods, treatment of **6** with 2-benzoylpyridine resulted in the formation of (NON^{Dipp})Bi(PhCONMe$_2$Py) (**13**) as a *racemic* mixture. The compound was isolated as an off-white powder in 71% yield (**Scheme 5.9**).



Scheme 5.9 Synthesis of (NON^{Dipp})Bi(PhCONMe$_2$Py) (**13**).

5.3.5.1 NMR spectroscopic analysis

The ^{1}H NMR spectrum of **13** is indicative of a C_1-symmetric species, consistent with the presence of a chiral centre in the inserted amino alkoxide moiety. This aligns with the solution-state structures of two previously reported examples for the addition of 2-benzoylpyridine across the M-NMe$_2$ bond of (L)Bi(NMe$_2$) and (L)Sn(NMe$_2$).[14, 44] A highly constrained geometry of the [NON^{Dipp}]-ligand features four Si*Me*$_2$, eight CH*Me*$_2$, and four C*H*Me$_2$ proton environments. While these signals are broad at room temperature, ^{1}H NMR spectra measured below 5 °C (278 K) reveal four sharp singlets corresponding to the Si*Me*$_2$ protons, eight resolved doublets for CH*Me*$_2$, and four septets

representing the C*H*Me$_2$ protons (**Figure 5.8**). 2D COSY, HSQC, and HMBC NMR spectral analyses were used to identify these signals; however, complete assignment of the aromatic protons (Ar) was not possible due to signal overlap. The insertion of the ketone into the Bi-N bond was also confirmed by $^{13}C\{^1H\}$ NMR spectroscopic analysis, with a significantly lower frequency signal observed for the carbonyl carbon in **13** with respect to 2-benzoylpyridine (δ 96.3 and 193.7 ppm, respectively).

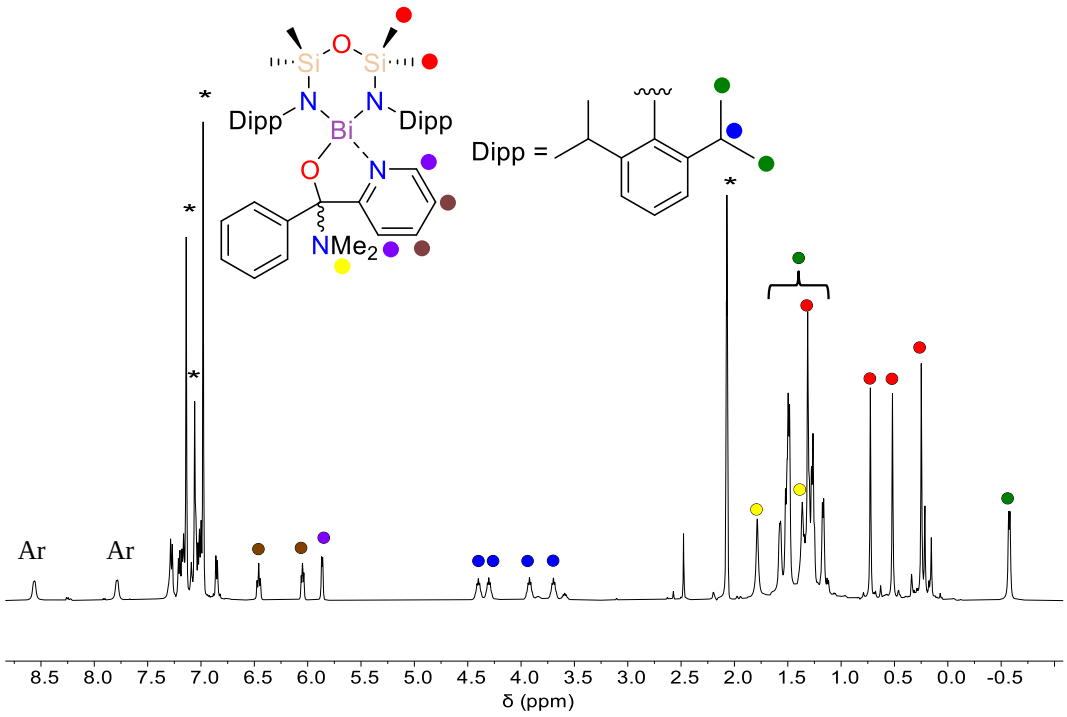


Figure 5.8 ^{1}H NMR spectrum (*toluene-d_8, 500 MHz, 213 K) of (NON^{Dipp})Bi(PhCONMe$_2$Py) (**13**).

One of the CH*Me*$_2$ proton resonances at δ –0.47 ppm is notably shifted to a lower frequency relative to the others. It can be hypothesised that the shielding effect on the corresponding methyl group is due to its close proximity to the aromatic protons of the inserted 2-benzoylpyridine moiety. 1D NOESY NMR spectroscopic analysis was attempted to investigate this hypothesis but provided no evidence of through-space interactions between these groups, presumably because of the dynamic coordination of the amino alkoxide ligand.

The observed room-temperature signal broadening is proposed to result from the hemilabile nature of the pyridine unit. Above 5 °C (278 K), the cleavage and recombination of the bonding between the inserted amino alkoxide unit and the bismuth centre become energetically accessible. The proposed lability accounts for unrestricted rotation of the NMe_2 and phenyl substituents at room temperature, both represented by broad signals at δ 1.58 and 8.06 ppm, respectively. These resonances split into two when the toluene-d_8 solution of **13** was cooled to –60 °C (213 K) (**Figure 5.9**).

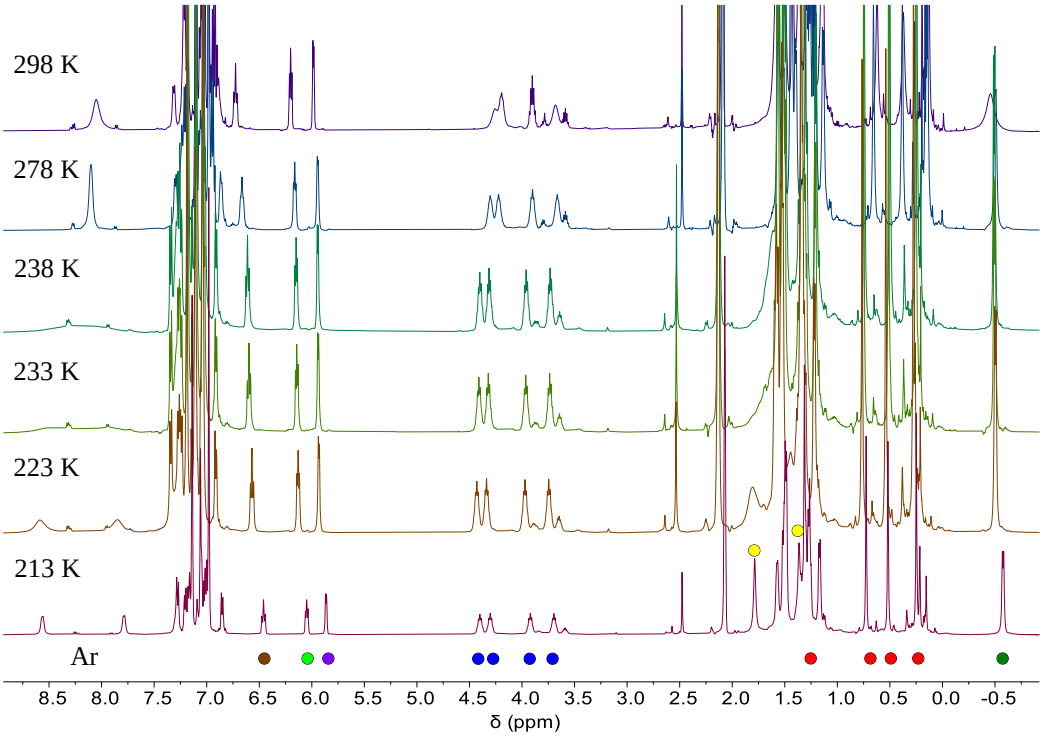


Figure 5.9 Variable temperature ^{1}H NMR spectra (toluene-d_8, 500 MHz) of (NON^{Dipp})Bi($PhCONMe_2Py$) (**13**).

Upon warming up the solution, the coalescence of the signals was observed. The T_c value was determined to be –40 °C (233 K), with $\Delta\nu$ estimated to be 380.1 Hz. According to **Equation 5.1**, the $\Delta G^{\ddagger}$ of the fluxional process was calculated to be 43.5 kJ mol^{-1}; this value is comparable to that associated with the fluxionality at the bismuth centre in **11** ($\Delta G^{\ddagger}$ = 47.0 kJ mol^{-1}).

Attempts to obtain a clean ^{1}H NMR spectrum of **13** were frustrated by the persistence of the 2-benzoylpyridine starting material in solution. These observations were ultimately rationalised by the reversible nature of the insertion reaction. ^{1}H NMR spectra recorded over the temperature range of 25–100 °C revealed the dissociation of **13**, accompanied by increasing relative amounts of **6** (e.g. singlet at δ 2.41 ppm corresponding to the N*Me*$_2$ protons) and 2-benzoylpyridine (**Figure 5.10**). The reverse reactivity was observed when the reaction mixture was cooled to 25 °C, resulting in the predominant formation of **13**.

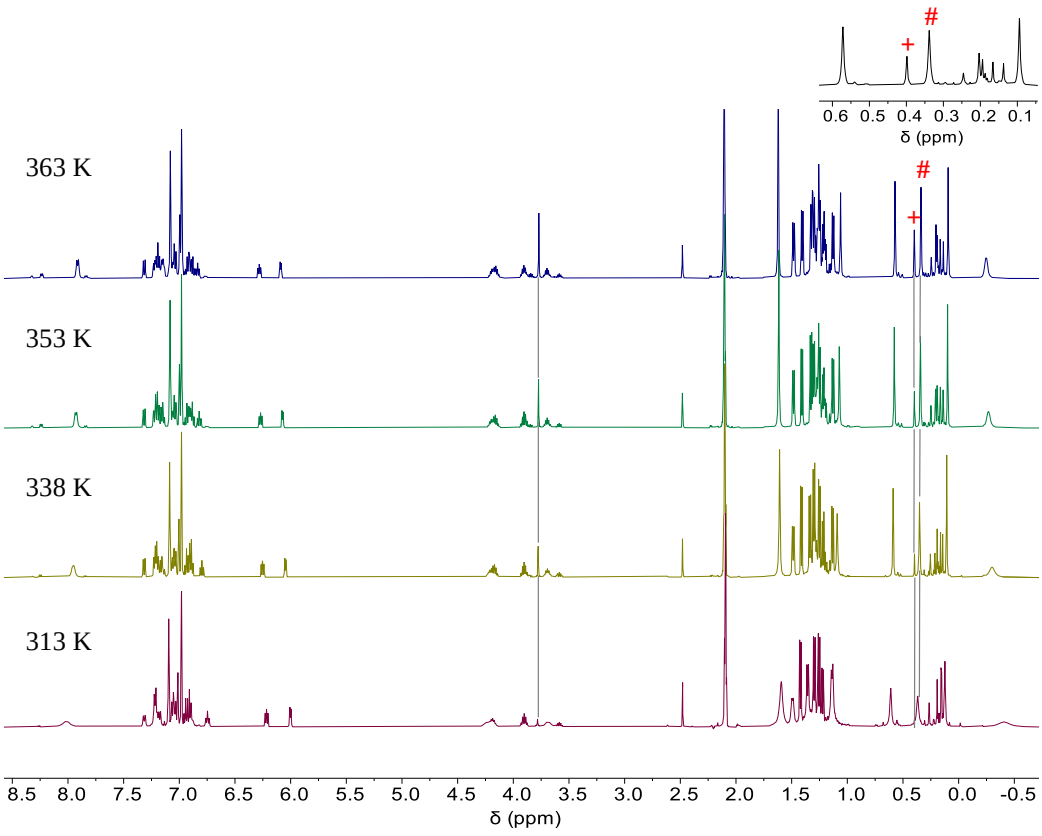


Figure 5.10 Variable temperature ^{1}H NMR spectra (toluene-d_8, 500 MHz) of (NON^{Dipp})Bi(PhCONMe$_2$Py) (**13**). + and # represent (NON^{Dipp})Bi(NMe$_2$) (**6**) and (NON^{Dipp})Bi(PhCONMe$_2$Py) (**13**), respectively.

Equilibrium constants (K_{eq}) for the insertion reaction were estimated by measuring relative integrals for characteristic resonances corresponding to **13** (Si*Me*$_2$ at δ 0.34 ppm)

and **6** (Si*Me*$_2$ at δ 0.40 ppm) (**Figure 5.10**, **Table 5.4**). The concentration of **6** was assumed to be equal to that of 2-benzoylpyridine, given that the recrystallised sample of **13** was used for the analysis. Based on the van't Hoff equation (**Equation 5.2**), a van't Hoff plot was then constructed to determine the standard reaction enthalpy ($\Delta H^{\ominus}$) and entropy ($\Delta S^{\ominus}$) (**Figure 5.11**).

$$\ln K_{\mathrm{eq}} = -\frac{\Delta H^{\ominus}}{RT} + \frac{\Delta S^{\ominus}}{R}$$

$$K_{\mathrm{eq}} = \frac{[\mathbf{13}]}{[\mathbf{6}][2-\mathrm{benzoylpyridine}]}$$

Equation 5.2 Definition of the van't Hoff equation with regard to the formation of **13**, where K_{eq} = equilibrium constant, $\Delta H^{\ominus}$ = standard reaction enthalpy, $\Delta S^{\ominus}$ = standard reaction entropy, R = gas constant, T = temperature.

Table 5.4 Equilibrium constants (K_{eq}) for the insertion of 2-benzoylpyridine into **6** measured at different temperatures.

***T* (K)**	**K_{eq}**
333	612.2
338	415.3
348	247.9
353	164.6
363	87.7

The insertion of 2-benzoylpyridine into **6** was found to be exothermic ($\Delta H^{\ominus}$ = –64.1 kJ mol^{-1}) but disfavoured entropically ($\Delta S^{\ominus}$ = –138.9 J K^{-1} mol^{-1}). Comparable thermodynamic parameters have also been reported for the reversible activation of P_4 using a related bismuth radical species ((NON^{Dipp})Bi;

ΔH^{o} = –64.8 kJ mol^{-1}, ΔS^{o} = –154.8 J K^{-1} mol^{-1}).[45] While the formation of **13** is favoured at room temperature (ΔG^{o} = –105.5 kJ mol^{-1} at 298 K), the equilibrium shifts towards the reagents when the reaction temperature is increased (ΔG^{o} = –17.8 kJ mol^{-1} at 363 K).

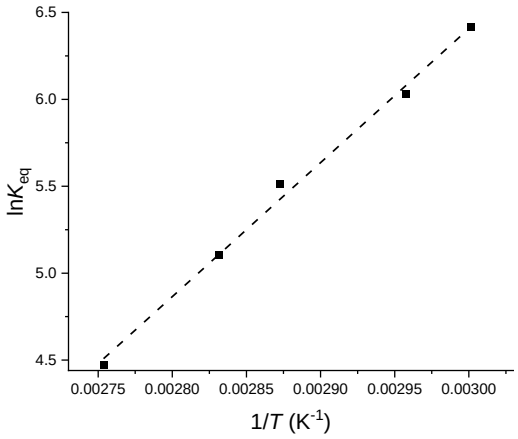


Figure 5.11 van't Hoff plot of lnK_{eq} *vs.* 1/T for the formation of (NON^{Dipp})Bi(PhCONMe$_2$Py) (**13**) (slope = 7 706 ± 317, intercept = −16.7 ± 0.9, R^2 = 0.995, ΔH^{o} = −64.1 kJ mol^{-1}, ΔS^{o} = −138.9 J K^{-1} mol^{-1}).

5.3.5.2 X-ray crystallographic analysis

Slow evaporation of a hexane solution at –30 °C afforded single crystals of complex **13**, solved in the triclinic space group, $P\bar{1}$, with both enantiomers present in the unit cell (**Figure 5.12**, **Table 5.5**).

The bismuth centre in **13** is in a four-coordinate distorted disphenoidal environment, consistent with the solid-state structures of compounds **11**–**12**. Atoms N(2) and N(4) are in axial positions (N(2)-Bi(1)-N(4) = 162.12(6)°), with atoms N(1) and O(2) occupying equatorial sites (N(1)-Bi(1)-O(2) = 93.92(6)°). Due to enhanced steric congestion, the N-Bi-N bite angle of the [NON^{Dipp}]-ligand is small compared to those in **10**–**12** (93.83(7) *vs*. 96.82(10)–100.00(10)°, respectively). In addition, an acute Si-O-Si angle is formed (133.46(10)° *vs*. 136.1(2)–142.25(15)° in **10**–**12**).

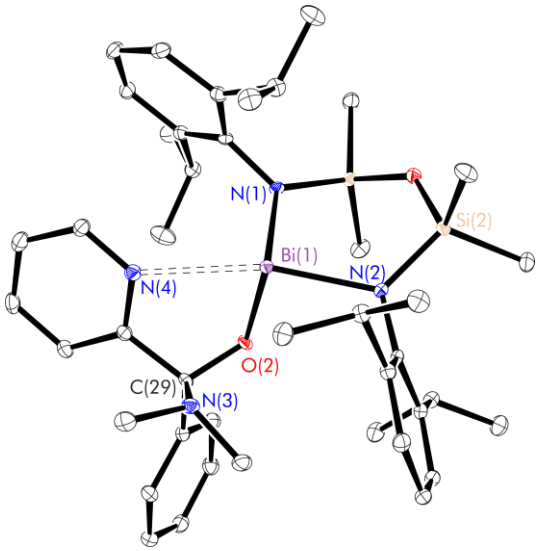


Figure 5.12 Thermal displacement ellipsoid drawing (30%) of the asymmetric unit of (NON^{Dipp})Bi($PhCONMe_2Py$) (**13**), showing a single enantiomer only. All hydrogen atoms have been omitted for clarity.

The [NON^{Dipp}]-ligand is asymmetrically bound to the bismuth centre, as indicated by a clear discrepancy in the Bi-N bond lengths (Bi(1)-N(1) = 2.1914(17) Å and Bi(1)-N(2) = 2.2539(18) Å). This bond elongation is likely attributed to the *trans* influence of the pyridine nitrogen donor. The amino alkoxide ligand is coordinated to the bismuth centre *via* a typical covalent Bi-O bond (Bi(1)-O(2) = 2.1093(15) Å) and a relatively long Bi-N bond (Bi(1)-N(4) = 2.6832(19) Å) with respect to the Bi-N distance observed in the case of the κ^2-ureato ligand in **12**. Both Bi-O and Bi-N distances are slightly longer than those reported for the 2-benzoylpyridine insertion product using the *bis*(amino)naphthalene bismuth amide complex (**Table 5.5**).[14] The C-O bond length is elongated with respect to 2-benzoylpyridine (1.424(2) *vs.* 1.213(2) Å, respectively) and can be regarded as single.[46]

Table 5.5 Selected experimental metrical parameters (bond lengths (Å) and angles (°)) for (NON^{Dipp})Bi($PhCONMe_2Py$) (**13**) and a related bismuth complex (L)Bi($PhCONMe_2Py$).[14] Estimated standard deviations shown in brackets.

	13	(L)Bi($PhCONMe_2Py$)[14] L = 1,8-$(NSiMe_3)_2C_{10}H_6$
Space group	$P\bar{1}$	$P\bar{1}$
Bi(1)-N(1)	2.1914(17)	-
Bi(1)-N(2)	2.2539(18)	-
Bi(1)-N(4)	2.6832(19)	2.615(4)
Bi(1)-O(2)	2.1093(15)	2.089(2)
C(29)-O(2)	1.424(2)	1.405(4)
C(29)-N(3)	1.485(3)	1.470(4)
N(1)-Bi(1)-N(2)	93.83(7)	-
Si(1)-O(1)-Si(2)	142.25(15)	-

5.4 Conclusions

The reactivity of di(amido)siloxane bismuth amide **6** was demonstrated towards a range of heteroallenes (CO_2, CS_2, and phenyl isocyanate) and 2-benzoylpyridine. The addition of C-O, C-S, and C-N bonds of these substrates across the Bi-N bond of **6** afforded four new complexes **10**–**13**.

Reactions with electrophilic, unhindered heteroallenes proceeded to yield insertion products, with π electron density delocalised over the ECN fragment (E = O, S, N) of carbamate, dithiocarbamate, and ureato units. These ligands were found to coordinate to

the bismuth centre in either an asymmetric κ^2-bidentate or κ^1-monodentate bonding mode, comprising a covalent and a weaker intramolecular Bi-E interaction.

The activation of less electrophilic, more sterically demanding 2-benzoylpyridine appeared to be reversible in solution, with the dissociation of the insertion product favoured with increasing temperature. This coincided with the hemilabile nature of the pyridine group. In contrast, compound **6** was unreactive towards *N,N'*-di*iso*propylcarbodiimide, attributed to its insufficient electrophilicity and large steric bulk.

The solid-state structures of all four new insertion products highlighted the conformational flexibility of the κ^2-*N,N'*-bound [NON^{Dipp}]-ligand, with variations in bond lengths and angles based on the steric profile of the inserted moiety. Upon reaction with 2-benzoylpyridine, the most sterically demanding substrate in the series, the insertion product exhibited the longest Bi-N distances, combined with an acute Si-O-Si angle.

The diverse reactivity of **6** towards small molecules, facilitated by its labile Bi-N bond, offers potential for both stoichiometric and catalytic bond activation reactions. Generally, the selective formation of C-N bonds is a crucial step in various organic transformations, including the synthesis of natural products and pharmaceuticals.[47] The insertion reactivity for CO_2 is also an important factor in the formation of polycarbonates *via* the copolymerisation of CO_2 with epoxides. To date, there are no examples of bismuth-based catalysts active in this process.[48]

5.5 References

1. M. Mato and J. Cornella, *Angew. Chem. Int. Ed.*, 2024, **63**, e202315046.

2. K. Balasubramanian, Y. S. Chung and W. S. Glaunsinger, *J. Chem. Phys.*, 1993, **98**, 8859-8869.

3. D. Dai and K. Balasubramanian, *J. Chem. Phys.*, 1990, **93**, 1837-1846.

4. I. J. Casely, J. W. Ziller, M. Fang, F. Furche and W. J. Evans, *J. Am. Chem. Soc.*, 2011, **133**, 5244-5247.

5. C. Hering-Junghans, A. Schulz, M. Thomas and A. Villinger, *Dalton Trans.*, 2016, **45**, 6053-6059.

6. C. Limberg, *Angew. Chem. Int. Ed.*, 2003, **42**, 5932-5954.

7. M. Vehkamäki, T. Hatanpää, M. Ritala and M. Leskelä, *J. Mater. Chem.*, 2004, **14**, 3191-3197.

8. M. Yarema, M. V. Kovalenko, G. Hesser, D. V. Talapin and W. Heiss, *J. Am. Chem. Soc.*, 2010, **132**, 15158-15159.

9. P. P. Power, *Nature*, 2010, **463**, 171-177.

10. F. Ando, T. Hayashi, K. Ohashi and J. Koketsu, *J. Inorg. Nucl. Chem.*, 1975, **37**, 2011-2013.

11. A. Fumio, O. Kumao and K. Jugo, *Bull. Chem. Soc. Jpn.*, 1976, **49**, 727-729.

12. F. Ando, Y. Kohmura and J. Koketsu, *Bull. Chem. Soc. Jpn.*, 2006, **60**, 1564-1566.

13. B. Nekoueishahraki, P. P. Samuel, H. W. Roesky, D. Stern, J. Matussek and D. Stalke, *Organometallics*, 2012, **31**, 6697-6703.

14. B. Nekoueishahraki, S. P. Sarish, H. W. Roesky, D. Stern, C. Schulzke and D. Stalke, *Angew. Chem. Int. Ed.*, 2009, **48**, 4517-4520.

15. J. Ramler, J. Poater, F. Hirsch, B. Ritschel, I. Fischer, F. M. Bickelhaupt and C. Lichtenberg, *Chem. Sci.*, 2019, **10**, 4169-4176.

16. K. Oberdorf, P. Pfister, P. Grenzer, J. Ramler, A. Hanft, A. Stoy, X. Xie and C. Lichtenberg, *Organometallics*, 2023, **42**, 885-895.

17. K. Oberdorf, A. Hanft, X. Xie, F. M. Bickelhaupt, J. Poater and C. Lichtenberg, *Chem. Sci.*, 2023, **14**, 5214-5219.

18. A. J. Keane, W. S. Farrell, B. L. Yonke, P. Y. Zavalij and L. R. Sita, *Angew. Chem. Int. Ed.*, 2015, **54**, 10220-10224.

19. Q. Zhuo, X. Zhou, T. Shima and Z. Hou, *Angew. Chem. Int. Ed.*, 2023, **62**, e202218606.

20. S. D. Cosham, M. S. Hill, G. A. Horley, A. L. Johnson, L. Jordan, K. C. Molloy and D. C. Stanton, *Inorg. Chem.*, 2014, **53**, 503-511.

21. S. Inoue and Y. Yokoo, *Bull. Chem. Soc. Jpn.*, 2006, **45**, 3651-3653.

22. B. Walther, R. Mahrwald, C. Jahn and W. Klar, *Z. Anorg. Allg. Chem.*, 1976, **423**, 144-154.

23. N. H.-W. Wiberg, *Lehrbuch der Anorganischen Chemie*, De Gruyter Berlin, 1985.

24. M. Imran, A. Mix, B. Neumann, H.-G. Stammler, U. Monkowius, P. Bleckenwegner and N. W. Mitzel, *Dalton Trans.*, 2014, **43**, 10956-10968.

25. J. Sandstorm, *Dynamic NMR Spectroscopy*, Academic Press, London, 1982.

26. R. J. Schwamm, M. Lein, M. P. Coles and C. M. Fitchett, *Chem. Commun.*, 2018, **54**, 916-919.

27. M. Arda, I. I. Ozturk, C. N. Banti, N. Kourkoumelis, M. Manoli, A. J. Tasiopoulos and S. K. Hadjikakou, *RSC Adv.*, 2016, **6**, 29026-29044.

28. A. Anton, A. Soran and C. Silvestru, *J. Mol. Struct.*, 2022, **1247**, 131335.

29. L. Dostál, R. Jambor, A. Růžička, R. Jirásko, E. Černošková, L. Beneš and F. d. Proft, *Organometallics*, 2010, **29**, 4486-4490.

30. P. Šimon, R. Jambor, A. Růžička and L. Dostál, *J. Organomet. Chem.*, 2013, **740**, 98-103.

31. P. Pyykkö, *J. Phys. Chem. A*, 2015, **119**, 2326-2337.

32. M. G.B. Drew, D. M. Williams and D. A. Rice, *Inorg. Chim. Acta*, 1984, **89**, L19-L20.

33. C. L. Raston, G. L. Rowbottom and A. H. White, *J. Chem. Soc., Dalton Trans.*, 1981, 1352-1359.

34. E. R. T. Tiekink, *Appl. Organomet. Chem.*, 2008, **22**, 533-550.

35. J. A. McCleverty, N. Spencer, N. A. Bailey and S. L. Shackleton, *J. Chem. Soc., Dalton Trans.*, 1980, 1939-1944.

36. S. A. A. Nami and K. S. Siddiqi, *Synth. React. Inorg. Met.-Org. Chem.*, 2004, **34**, 1581-1590.

37. P. Pyykkö and M. Atsumi, *Chem. Eur. J.*, 2009, **15**, 186-197.

38. L. Mao, Q. Shen, M. Xue and J. Sun, *Organometallics*, 1997, **16**, 3711-3714.

39. J.-W. Hsu, Y.-C. Lin, C.-S. Hsiao, A. Datta, C.-H. Lin, J.-H. Huang, J.-C. Tsai and W.-C. Hsu, *Dalton Trans.*, 2012, **41**, 7700-7707.

40. L. Nekoueishahraki, P. P. Samuel, H. W. Roesky, D. Stern, J. Matussek and D. Stalke, *Organometallics*, 2012, **31**, 6697-6703.

41. T. Wildsmith, J. D. Parish, I. Y. Ahmet, K. C. Molloy, M. S. Hill and A. L. Johnson, *Inorg. Chem.*, 2021, **60**, 17083-17093.

42. Z. Li, R. J. Mayer, A. R. Ofial and H. Mayr, *J. Am. Chem. Soc.*, 2020, **142**, 8383-8402.

43. H. Dengel and C. Lichtenberg, *Chem. Eur. J.*, 2016, **22**, 18465-18475.

44. A. Jana, I. Objartel, H. W. Roesky and D. Stalke, *Dalton Trans.*, 2010, **39**, 4647-4650.

45. R. J. Schwamm, M. Lein, M. P. Coles and C. M. Fitchett, *Angew. Chem. Int. Ed.*, 2016, **55**, 14798-14801.

46. M. Sievert, R. Dienelt and H. Bock, *Acta crystallogr., C*, 1998, **54**, 674-676.

47. S. H. Cho, J. Y. Kim, J. Kwak and S. Chang, *Chem. Soc. Rev.*, 2011, **40**, 5068-5083.

48. G. A. Bhat and D. J. Darensbourg, *Green Chem.*, 2022, **24**, 5007-5034.

Chapter 6

Synthesis, characterisation, and reactivity of di(amido)siloxane scandium complexes

6.1 Introduction

Research on the coordination chemistry of the di(amido)siloxane ligand has primarily focused on transition and main group elements. Despite the potential of the ligand to stabilise reactive, coordinatively unsaturated rare-earth species by variations in steric bulk, coordination modes, and electronic properties, only two examples of related di(amido)siloxane rare-earth complexes with an yttrium centre have been reported,[1, 2] alongside a small number of actinide compounds.

The ligand scaffold was first employed by Leznoff and co-workers to develop actinide complexes.[3] A dimeric uranium(IV) chloride complex $[(NON^{tBu})UCl_2]_2$ (**Figure 6.1a**) was prepared *via* a straightforward salt-metathesis reaction between the dilithium salt of the ligand $(NON^{tBu})Li_2$ and UCl_4.[3] In the solid state, the ligand was found to adopt a κ^3-*N,O,N'*-tridentate coordination mode, enabling electron donation from the siloxane oxygen atom to the oxophilic uranium centre. Treatment of this uranium compound with anhydrous LiI resulted in the formation of $[(NON^{tBu})UI_3][Li(THF)_2]$ as an "ate" complex,

incorporating the LiI salt into the molecular structure (**Figure 6.1b**).[4] Generally, the formation of "ate" structures is common in the synthesis of complexes comprising *f*-elements due to their preference to increase coordination numbers, thus stabilising large coordination spheres.[5] Conducting salt-metathesis reactions in donor solvents further exacerbates the solvation of alkali metal salts, favouring molecular "ate" structures.[6, 7]

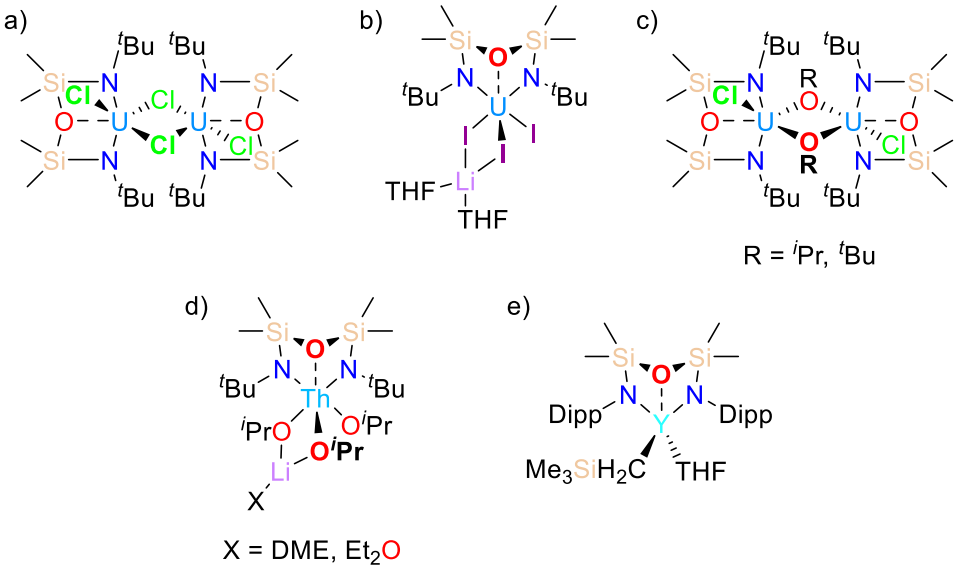


Figure 6.1 Selected examples of di(amido)siloxane actinide and rare-earth complexes.

Uranium(IV) and thorium(IV) alkoxide complexes supported by a [NON$^{t\text{Bu}}$]-ligand (**Figure 6.1c** and **d**, respectively) have been investigated as initiators for the polymerisation of *L*-lactide.[8] Polymerisation initiated by the thorium "ate" complex was significantly slower and less controlled than that using the neutral uranium *iso*propoxide initiator ($Đ_M$ = 1.63 and 1.16, respectively). When employed in the polymerisation of *rac*-lactide, this uranium complex afforded heterotactic-enriched PLA (P_r = 0.61–0.73).

Recently, Anker and co-workers described the synthesis of di(amido)siloxane yttrium alkyl (NON$^{\text{Dipp}}$)Y(CH_2SiMe_3)(THF) (**Figure 6.1e**) *via* a protonolysis reaction using the Y(CH_2SiMe_3)$_3$(THF)$_3$ precursor.[1] Upon subsequent reaction with a hydride source, the

complex was found to undergo ligand rearrangement, resulting in the formation of the dimeric hydride-bridged species $[(\mu\text{-NON}^{Dipp})Y(\mu\text{-H})(THF)]_2$, with each $[NON^{Dipp}]$-ligand bridging between the two metal centres.

Incorporation of scandium into the di(amido)siloxane ligand framework has no precedent. As the lightest rare-earth element, scandium exhibits properties that are intermediate between alkaline earth, transition, and lanthanide elements.[9] A range of well-defined scandium complexes have demonstrated activity in polymerisation processes, including the ROP of polar monomers, offering the advantage of a non-toxic initiator.[10-13]

6.2 Synopsis

Chapter Six describes the development of new scandium(III) compounds, thus expanding the scope of previously reported di(amido)siloxane rare-earth complexes. Six scandium complexes with diverse steric and electronic profiles have been prepared and characterised by NMR spectroscopy, and in most cases, IR spectroscopy, single-crystal X-ray diffraction and elemental analysis.

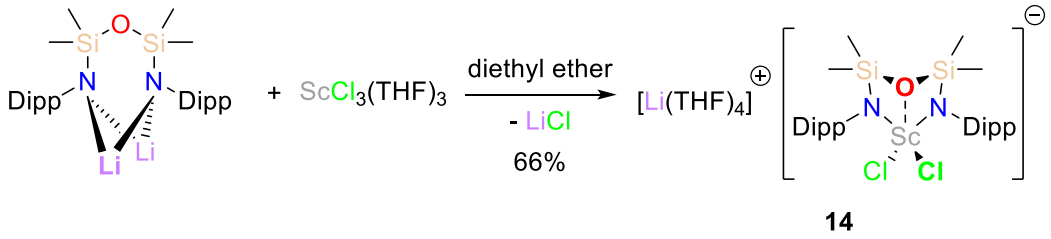
6.3 Synthesis, characterisation, and reactivity of di(amido)siloxane scandium complexes

6.3.1 Scandium chloride complexes

Di(amido)siloxane scandium chloride complexes were synthesised as precursors for further salt-metathesis reactions, with the aim of introducing various nucleophilic groups at the metal centre. Scandium complexes incorporating aryloxide, alkyl, and borohydride groups were targeted due to their potential as effective ROP initiators.[13, 14]

6.3.1.1 Synthesis of scandium chloride complexes

Salt-metathesis reactions using $(NON^{R})Li_2$ (R = Dipp, ^{t}Bu) and $ScCl_3(THF)_3$ were explored according to a modified procedure for the synthesis of $(NON^{R})BiCl$ compounds.[15] Treatment of $ScCl_3(THF)_3$ with $(NON^{Dipp})Li_2$ in diethyl ether yielded the "ate" complex $[(NON^{Dipp})ScCl_2][Li(THF)_4]$ (**14**) as an off-white powder in 66% yield (**Scheme 6.1**).



14

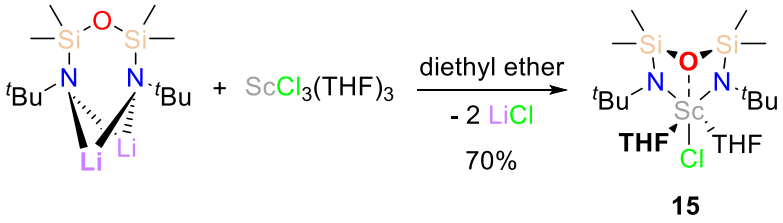
Scheme 6.1 Synthesis of $[(NON^{Dipp})ScCl_2][Li(THF)_4]$ (**14**).

The retention of alkali metal cations has been widely documented in the synthesis of scandium complexes.[16, 17] "Ate" complexation is generally undesirable as the incorporation of non-labile salt moieties results in the coordinative saturation of the metal centre, hindering onward reactivity.[16, 18] Although several rare-earth "ate" complexes have been found to be active for the polymerisation of both polar and non-polar monomers, a decrease in polymerisation rate and/or control has typically been observed compared to those using related salt-free initiators.[8, 19, 20]

To avoid salt occlusion during the preparation of **14**, an alternative synthesis using the dipotassium salt of the ligand $(NON^{Dipp})K_2$ was attempted. It was anticipated that the KCl by-product would have a lower solubility in diethyl ether compared to LiCl.[21] However, the formation of a less clean reaction product was indicated by ^{1}H NMR spectroscopic analysis. The corresponding spectroscopic shifts appeared to be comparable to those assigned to **14**, implying the retention of the "ate" structure. Alternatively, the reaction

between (NON^{Dipp})Li$_2$ and ScCl$_3$(THF)$_3$ was repeated in toluene, selected as a non-coordinating solvent to minimise the solvation of LiCl. However, despite heating the reaction mixture to 80 °C for 48 hours, no reactivity was observed.

An analogous reaction between (NON$^{t\text{Bu}}$)Li$_2$ and ScCl$_3$(THF)$_3$ produced salt-free (NON$^{t\text{Bu}}$)ScCl(THF)$_2$ (**15**) as a white powder in 70% yield (**Scheme 6.2**).



Scheme 6.2 Synthesis of (NON$^{t\text{Bu}}$)ScCl(THF)$_2$ (**15**).

The structural differences between the "ate" complex **14** and the salt-free compound **15** reflect the Lewis acidity of the scandium centre resulting from the differing amido substituents. Contrary to the relatively less Lewis acidic scandium centre in **15** bound by electron-donating *tert*-butyl amido groups, the retention of LiCl in **14** provides greater stabilisation to the more Lewis acidic scandium centre through the coordination of an additional anionic donor.

The [NON$^{t\text{Bu}}$]-ligand scaffold has been previously employed to stabilise salt-free complexes with oxophilic iron, yttrium, and uranium metal centres.[2, 4, 22] However, these syntheses proved to be sensitive to reaction conditions, with "ate" complexation possible due to variations in the steric bulk of the ligand and the polarity of the reaction solvent.

6.3.1.2 NMR spectroscopic analysis

Both **14** and **15** form C_{2v}-symmetric species in THF-d_8 (**Figures 6.2** and **6.3**). The ^{1}H NMR spectrum of **14** contains a singlet at δ 0.21 ppm corresponding to the equivalent

Si*Me*$_2$ protons, a doublet at δ 1.17 ppm assigned to the CH*Me*$_2$ protons, a septet at δ 4.05 ppm for the C*H*Me$_2$ protons, with the remaining resonances at δ 6.85 and 6.64 ppm representing the aromatic protons.

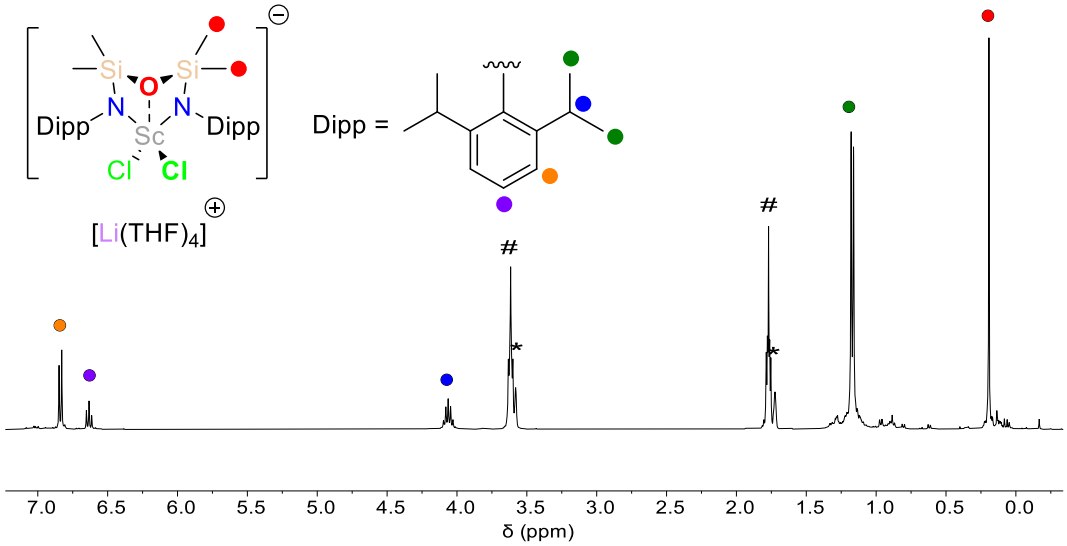


Figure 6.2 ^{1}H NMR spectrum (*THF-d_8, 400 MHz, 298 K) of [(NON^{Dipp})ScCl$_2$][Li(THF)$_4$] (**14**). # represents coordinated THF.

In addition, its ^{45}Sc NMR spectrum displays a broad signal at δ 395.7 ppm, which is at a slightly higher frequency with respect to the range of ^{45}Sc NMR spectroscopic shifts previously reported for salt-free six-coordinate scandium chloride complexes (δ 227–307 ppm).[23] Generally, chemical shifts and line widths in ^{45}Sc NMR spectra are sensitive to small changes in both the electronic and coordination environment at the scandium centre, rendering qualitative analysis challenging.[24, 25] Higher frequency signals are typically attributed to compounds having lower coordination numbers; this may explain the somewhat high-frequency resonance observed for **14**.

In contrast to the solution-state structure of **14** in THF-d_8, the ^{1}H NMR spectrum recorded in benzene-d_6 reveals the loss of C_{2v} molecular symmetry (**Figure A.5.1** in **Appendix**). The Si*Me*$_2$ protons appear as two singlets at δ 0.53 and 0.36 ppm, the C*H*Me$_2$

protons are represented by two septets at δ 4.25 and 3.79 ppm, and four doublets between δ 1.48–1.17 ppm are assigned to the CH*Me*$_2$ protons. These results indicate the formation of two inequivalent faces of the [NON^{Dipp}]-ligand along with restricted rotation of the amido-*N*-aryl bond. It can be hypothesised that **14** forms a contact ion pair in benzene-d_6, with the lithium cation coordinated to the scandium unit in an asymmetrical fashion. A previously reported uranium chloride "ate" complex bearing a related di(amido) ligand, [(NCOCN^{Dipp})UCl$_3$][Li(THF)$_2$], has been shown to adopt a comparable asymmetric structure in toluene-d_8 at room temperature.[4] Upon heating the solution to 100 °C, an increase in symmetry was observed, attributed to the loss of incorporated LiCl. In comparison, **14** retains its asymmetry in benzene-d_6 when heated to 80 °C, while the C_{2v}-symmetric species can be regenerated by redissolving the sample in THF-d_8.

In the ^{1}H NMR spectrum of **15** (**Figure 6.3**), the Si*Me*$_2$ and *tert*-butyl protons appear as singlets at δ 0.17 and 1.17 ppm, respectively. A broad resonance at δ 290.6 ppm observed in the ^{45}Sc NMR spectrum is at a slightly lower frequency than that for **14**, consistent with an increase in the coordination number at the scandium centre.

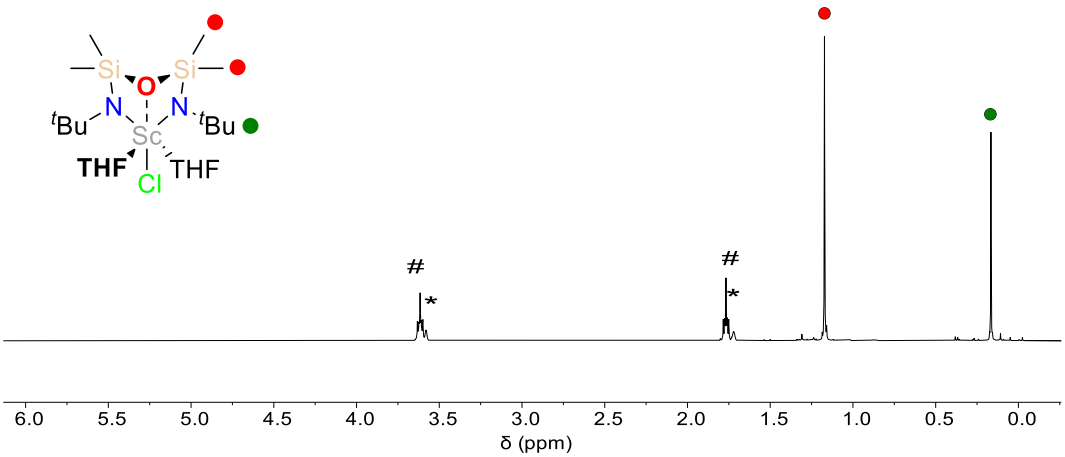


Figure 6.3 ^{1}H NMR spectrum (*THF-d_8, 400 MHz, 298 K) of (NON^{tBu})ScCl(THF)$_2$ (**15**).

represents coordinated THF.

6.3.1.3 X-ray crystallographic analysis

Single crystals of compounds **14** and **15**, suitable for X-ray diffraction studies, were grown from slow evaporation of a THF/diethyl ether mixture (1:1) (**14**) and a THF/HMDSO mixture (4:1) (**15**) at 23 °C (**Figure 6.4**, **Table 6.1**). **14** and **15** crystallised in the orthorhombic space group, $Pna2_1$, and monoclinic space group, $P2_1/c$, respectively.

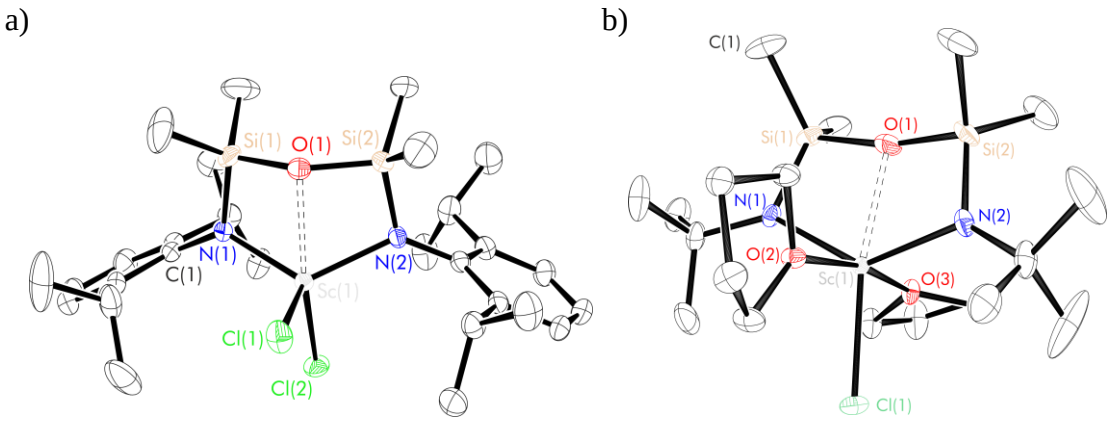


Figure 6.4 Thermal displacement ellipsoid drawings (30%) of asymmetric units of a) $[(NON^{Dipp})ScCl_2][Li(THF)_4]$ (**14**) (showing the anion only) and b) $(NON^{tBu})ScCl(THF)_2$ (**15**). All hydrogen atoms have been omitted for clarity.

The solid-state structure of **14** confirms the formation of the scandium "ate" complex, with the $[Li(THF)_4]^+$ cation well-separated from the $[(NON^{Dipp})ScCl_2]^-$ anion. The $[NON^{Dipp}]$-ligand-chelated scandium centre adopts a five-coordinate, distorted trigonal bipyramidal geometry (τ_5 = 0.64),[26] with atoms O(1) and Cl(2) occupying axial positions (O(1)-Sc(1)-Cl(2) = 159.20(10)°). Conversely, the scandium centre in **15** is bound to a terminal chloride group and two *trans*-oriented THF molecules in a *pseudo*-octahedral geometry.

In both structures, the di(amido)siloxane ligand exhibits a κ^3-*N*,*O*,*N'*-coordination mode. The siloxane O(1) atom is coordinated to the scandium centre with comparable Sc-O distances (2.392(3) Å (**14**) and 2.3240(16) Å (**15**)), both of which are only slightly outside

the sum of the corresponding covalent radii ($\sum r_{cov}$(Sc,O) = 2.11 Å).[27] Due to the relatively high oxophilicity of the scandium centre, these Sc-O distances are short with respect to the corresponding distances reported for complexes featuring a κ^3-*N*,*O*,*N'*-bound di(amido)siloxane ligand (M-O = 2.119(6)–2.726(2) Å, where M = Mg, Fe, Mn, Cr, Y, Th, U).[2, 15, 22, 28, 29] Comparatively, the bond between the scandium centre in **15** and two coordinated THF molecules is slightly stronger, with an average Sc-O bond length of 2.224 Å.

The formation of a symmetric coordination environment at the scandium centre in **14** is indicated by the essentially equivalent distances of the two Sc-N bonds (2.088(4) and 2.091(4) Å) and the two Sc-Cl bonds (2.3902(14) and 2.3869(14) Å). These distances appear to be longer in **15** (Sc(1)-N(1) = 2.1247(16) Å and Sc(1)-Cl(1) = 2.4376(6) Å), likely due to the higher coordination number and thus increased steric congestion at the scandium centre. The Sc-Cl distance in **15** is consistent with the corresponding distances reported for other neutral scandium chloride complexes supported by *N*-donor ligands ((L)$ScCl_x(THF)_y$: Sc-Cl = 2.412(3)–2.4569(11) Å).[30-33]

The six-membered ScN_2Si_2O metallacycles in **14** and **15** adopt a boat conformation defined by a small N(1)-Si(1)-Si(2)-N(2) torsion angle (4.9(2)° (**14**) and 6.4(1)° (**15**)). The formation of such butterfly-like structures has been well-documented for [NON^R]-ligand-supported complexes in the presence of κ^3-*N*,*O*,*N'*-bonding.[1, 3] Steric congestion at the metal centre reinforces the planarity of the metallacycle in **15**, as evidenced by comparison of the obtuse fold angles between the mean planes defined by atoms Sc(1)-N(1)-Si(1)-O(1) and Sc(1)-N(2)-Si(2)-O(1) (140.53° (**14**) *vs*. 167.82° (**15**)). This coincides with the formation of a larger N-Sc-N bite angle in **15** (120.89(16)° (**14**) *vs*. 134.07(8)° (**15**)).

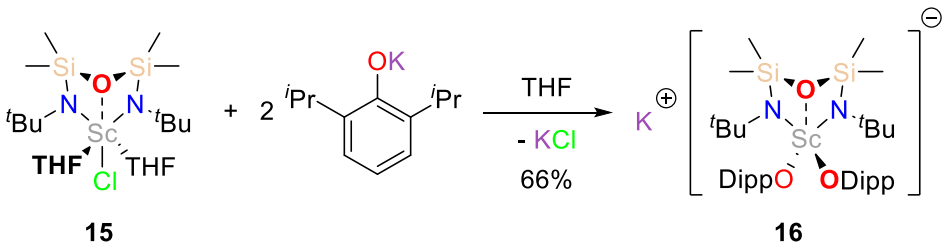
Table 6.1 Selected experimental metrical parameters (bond lengths (Å) and angles (°)) for [(NON^{Dipp})ScCl$_2$][Li(THF)$_4$] (**14**) and (NON^{tBu})ScCl(THF)$_2$ (**15**). Estimated standard deviations shown in brackets.

	14	**15**
Space group	*Pna*2$_1$	*P*2$_1$/*c*
Sc(1)-N(1)	2.088(4)	2.1247(16)
Sc(1)-N(2)	2.091(4)	2.1121(18)
Sc(1)-Cl(1)	2.3902(14)	2.4376(6)
Sc(1)-Cl(2)	2.3869(14)	-
Sc(1)-O(1)	2.392(3)	2.3240(16)
N(1)-Sc(1)-N(2)	120.89(16)	134.07(8)
N(1)-Si(1)-Si(2)-N(2)	4.9(2)	6.4(1)

6.3.2 Scandium aryloxide complexes

6.3.2.1 Synthesis of a scandium aryloxide complex

A salt-metathesis reaction using a potassium aryloxide reagent was carried out to introduce an aryloxide group at the scandium centre. The addition of one equivalent of potassium 2,6-di*iso*propylphenoxide to a THF-d_8 solution of **15** resulted in the formation of a new aryloxide complex, with half an equivalent of **15** remaining unreacted. Upon the use of two equivalents of the aryloxide precursor, the quantitative formation of K[(NON^{tBu})Sc(O-2,6-^{i}Pr-C$_6$H$_3$)$_2$] (**16**) was observed (**Scheme 6.3**). This compound was isolated as a brown powder in 66% yield.



Scheme 6.3 Synthesis of K[(NON$^{t\text{Bu}}$)Sc(O-2,6-^{i}Pr-C_6H_3)$_2$] (**16**).

An analogous reaction using **14** did not proceed cleanly. ^{1}H NMR spectroscopic analysis indicated the formation of the anticipated scandium aryloxide complex as a major product, accompanied by decomposition products, including the (NON$^{\text{Dipp}}$)H_2 pro-ligand. Attempts to carry out the substitution reaction using a less sterically bulky potassium phenoxide reagent were also unsuccessful. These findings suggest that the steric encumbrance of the [NON$^{\text{Dipp}}$]-ligand framework renders the selective formation of target aryloxide complexes unfavourable. The steric influence of aryloxide groups has recently been examined in the synthesis of cerium(IV) complexes bearing a sterically demanding tripodal *O*-donor ligand.[34] Reactions utilising aryloxide reagents with none or only one *ortho*-group afforded cerium *bis*(aryloxide) complexes. In contrast, analogous complexes proved to be unstable in the presence of *ortho*-disubstituted aryloxides, resulting in ligand exchange and/or reduction of the metal centre.

6.3.2.2 NMR spectroscopic analysis

The ^{1}H NMR spectrum of **16** confirms the retention of C_{2v} molecular symmetry in THF-d_8 (**Figure 6.5**), suggestive of the coordination of the potassium cation by THF molecules. The characteristic resonances of the chelated ligand include a singlet at δ 0.06 ppm corresponding to the Si*Me*$_2$ protons and a singlet at δ 1.18 ppm for the *tert*-butyl protons. The two aryloxide groups are chemically equivalent and their rotation around the Sc-O bond is unrestricted, as indicated by the presence of a single doublet at

δ 1.03 ppm due to the CH*Me*$_2$ protons and a single septet at δ 3.71 ppm assigned to the C*H*Me$_2$ protons.

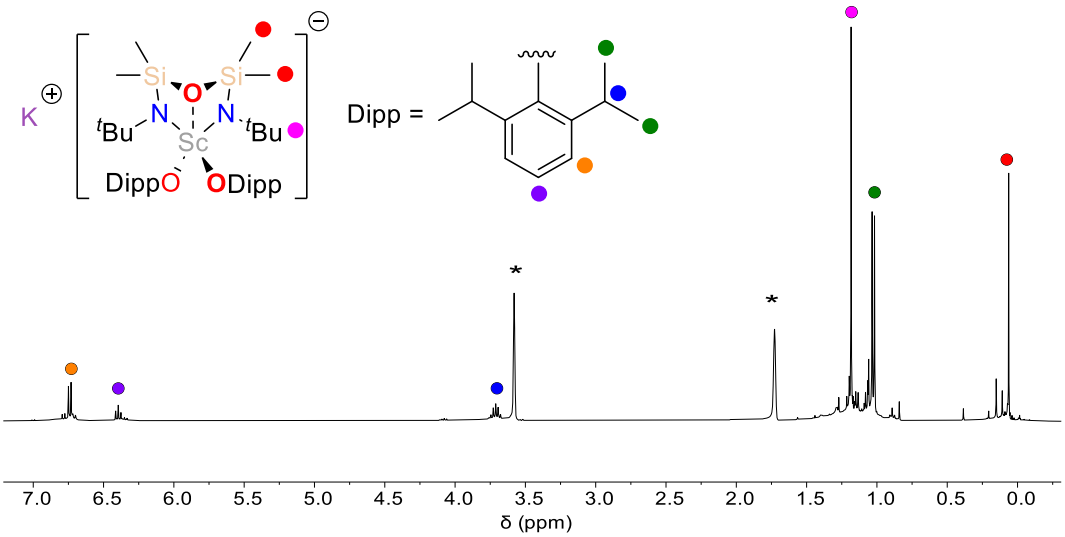


Figure 6.5 ^{1}H NMR spectrum (*****THF-d_8, 400 MHz, 298 K**)** of K[(NON$^{t\text{Bu}}$)Sc(O-2,6-^{i}Pr-C$_6$H$_3$)$_2$] (**16**).

In addition, the ^{45}Sc NMR spectroscopic resonance for **16** is found at δ 290.3 ppm, a lower frequency than that for the chloride "ate" complex **14**. A comparable trend has been reported in the study of four-coordinate scandium compounds, with the homoleptic 2,6-di*iso*propylphenoxide dimer [Sc(μ-O-2,6-^{i}Pr-C$_6$H$_3$)(O-2,6-^{i}Pr-C$_6$H$_3$)$_2$]$_2$ represented by a significantly lower frequency signal relative to those observed for alkyl or mixed alkyl/chloride derivatives [{Sc(CH(SiMe$_3$)$_2$}$_x$(μ-R)$_y$Li(THF)$_z$]$_{z'}$ (δ 118.1 *vs.* 876.9–705.3 ppm, respectively).[35]

6.3.2.3 X-ray crystallographic analysis

Single crystals of **16** suitable for an X-ray diffraction study were grown from slow evaporation of a THF/HMDSO mixture (4:1) at 23 °C and were solved in the triclinic space group, $P\bar{1}$ (**Figure 6.6**, **Table 6.2**).

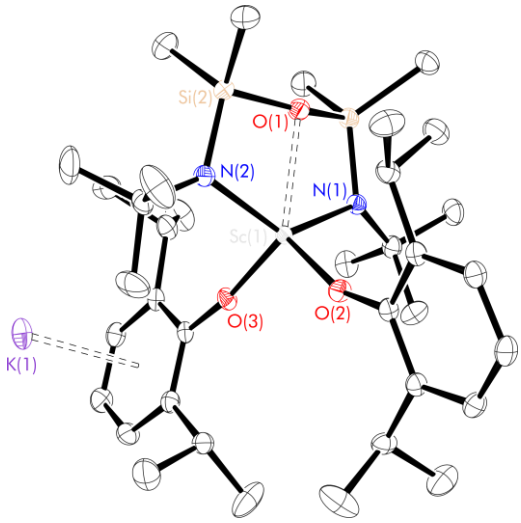


Figure 6.6 Thermal displacement ellipsoid drawing (30%) of the asymmetric unit of K[(NON$^{t\text{Bu}}$)Sc(O-2,6-^{i}Pr-C$_6$H$_3$)$_2$] (**16**). All hydrogen atoms have been omitted for clarity.

In the solid state, **16** forms a one-dimensional coordination polymer, where the monomeric units are linked by non-covalent interactions between the potassium cation and the aryloxide groups. Such interactions are commonly observed in metal aryloxide "ate" structures, including complexes of rare-earth metals.[6, 36-38] The K-C(aryl) distances in **16**, with an average of 3.138 Å, are consistent with a η^6-aryl bonding mode and appear to be short relative to those defined for other relevant K-η^6-aryl interactions (average K-C(aryl) = 3.15–3.30 Å).[36, 39-41] The formation of a solid-state polymeric structure has also been observed in the case of the di(amido)siloxane indium "ate" complex K[(NON$^{\text{Dipp}}$)InCl$_2$], stabilised by η^6-interactions between the potassium cation and the Dipp groups on the ligand backbone, with an average K-C(aryl) distance of 3.25 Å.[42]

As expected, the scandium centre of **16** is chelated by the [NON$^{t\text{Bu}}$]-ligand in a κ^3-*N*,*O*,*N'*-tridentate bonding mode. This results in a distorted square-base pyramidal geometry (τ_5 = 0.017), with the O(2) atom located 2.681 Å from the equatorial plane defined by the N(1)-O(1)-N(2)-O(3) atoms. The ScN$_2$Si$_2$O metallacycle adopts a boat

conformation, with the Sc-O distance (2.3936(13) Å) and the N-Sc-N bite angle (131.96(6)°) comparable to those observed for the parent **15**. The aryloxide substituents are positioned *trans* and twisted away from each other by 29.95° to minimise steric clash between the *iso*propyl groups. The Sc-O distances display a narrow distribution (1.9876(12) and 1.9744(12) Å) and are slightly longer than the corresponding distances in previously characterised scandium 2,6-di*iso*propylphenoxide compounds (1.8950(8)–1.9450(9) Å).[11, 14, 35, 43]

Table 6.2 Selected experimental metrical parameters (bond lengths (Å) and angles (°)) for K[(NON$^{t\text{Bu}}$)Sc(O-2,6-^{i}Pr-C_6H_3)$_2$] (**16**). Estimated standard deviations shown in brackets.

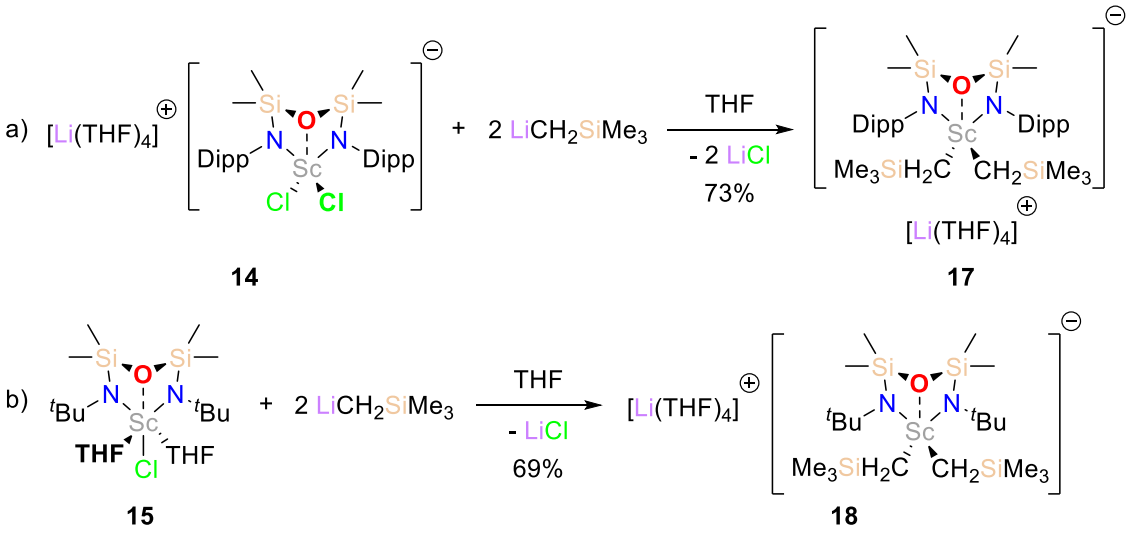
Space group	$P\bar{1}$
Sc(1)-N(1)	2.1305(15)
Sc(1)-N(2)	1.9876(12)
Sc(1)-O(1)	2.3936(13)
Sc(1)-O(2)	1.9876(12)
Sc(1)-O(3)	1.9744(12)
K(1)-C(aryl)	3.0683(19)–3.2262(18)
N(1)-Sc(1)-N(2)	131.96(6)
N(1)-Si(1)-Si(2)-N(2)	2.13(9)

6.3.3 Scandium alkyl complexes

6.3.3.1 Synthesis of scandium alkyl complexes

In light of the observed reactivity with potassium 2,6-di*iso*propylphenoxide, scandium chloride complexes **14** and **15** were treated with (trimethylsilyl)methyllithium

($LiCH_2SiMe_3$) in THF to prepare their scandium alkyl derivatives. In both cases, two equivalents of the alkyl reagent were used to drive the reactions to completion due to the selective formation of "ate" complexes (**Scheme 6.4**). The formation of compounds $[(NON^{Dipp})Sc(CH_2SiMe_3)_2][Li(THF)_4]$ (**17**) and $[(NON^{tBu})Sc(CH_2SiMe_3)_2][Li(THF)_4]$ (**18**) was confirmed by ^1H NMR spectroscopy, and they were subsequently isolated as pink powders in 73% (**17**) and 69% (**18**) yields. Due to their high solubility in common solvents, attempts to crystallise these species were unsuccessful.



Scheme 6.4 Synthesis of a) $[(NON^{Dipp})Sc(CH_2SiMe_3)_2][Li(THF)_4]$ (**17**) and b) $[(NON^{tBu})Sc(CH_2SiMe_3)_2][Li(THF)_4]$ (**18**).

Although a clean chloride/aryloxide substitution for **14** was not achieved using potassium 2,6-di*iso*propylphenoxide (*vide supra*, **Section 6.3.2.1**), a less sterically demanding and more nucleophilic reagent, (trimethylsilyl)methyllithium, proved to be a suitable choice to promote the reactivity of the chloride complex.

Generally, the reactivity of scandium *mono*(alkyl) and *bis*(alkyl) complexes has been widely investigated for small molecule insertion, ligand substitution reactions, and the polymerisation of various monomers, including cyclic esters, styrene and

2-vinylpyridine.[13, 44-46] To prevent the formation of "ate" complexes and therefore facilitate the development of more reactive di(amido)siloxane scandium alkyls, a $[CH(SiMe_3)_2]^-$ ligand could be investigated as a sterically demanding neosilyl alternative, providing enhanced saturation of the scandium coordination sphere.[47]

6.3.3.2 NMR spectroscopic analysis

The ^{1}H NMR spectra of **17** and **18** are indicative of C_{2v} molecular symmetry, with two CH_2SiMe_3 groups bound by the scandium centre (**Figures 6.7** and **6.8**, respectively).

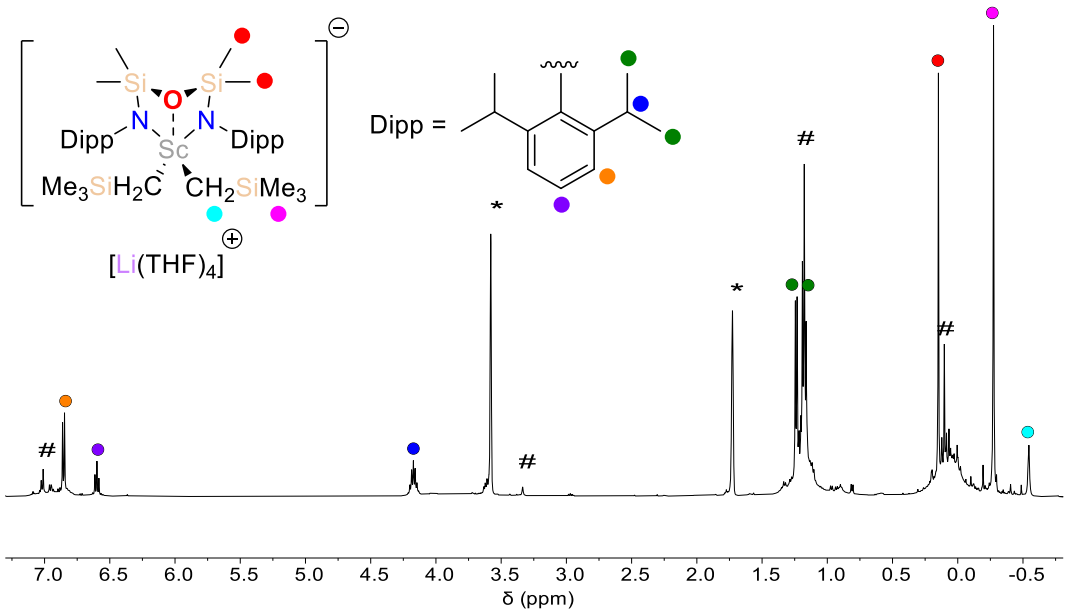


Figure 6.7 ^{1}H NMR spectrum (*THF-d_8, 500 MHz, 298 K) of $[(NON^{Dipp})Sc(CH_2SiMe_3)_2][Li(THF)_4]$ (**17**). # represents pro-ligand.

The singlets corresponding to the CH_2 protons (δ –0.55 (**17**) and –0.45 ppm (**18**)) are each shifted to a higher frequency than the corresponding signal for the $LiCH_2SiMe_3$ precursor (δ –2.22 ppm), consistent with their transfer to the more Lewis acidic scandium centre.[48] The steric profile of the supporting ligand is known to have an influence on the solution-state fluxionality of CH_2SiMe_3 groups, as evidenced by instances of both

restricted and unrestricted rotation of these moieties in previously reported NNN-pincer scandium *bis*(alkyl) complexes.[13, 49]

In contrast to the solution-state structure of chloride "ate" **14**, an increased steric constraint imparted by the CH_2SiMe_3 substituents in **17** results in restricted rotation around the amido-*N*-aryl bond. The $CHMe_2$ protons therefore appear as two doublets at δ 1.24 and 1.18 ppm. Conversely, the *tert*-butyl groups on the [NON$^{t\text{Bu}}$]-ligand in **18** are located as a singlet δ 1.29 ppm, implying their unhindered rotation in solution.

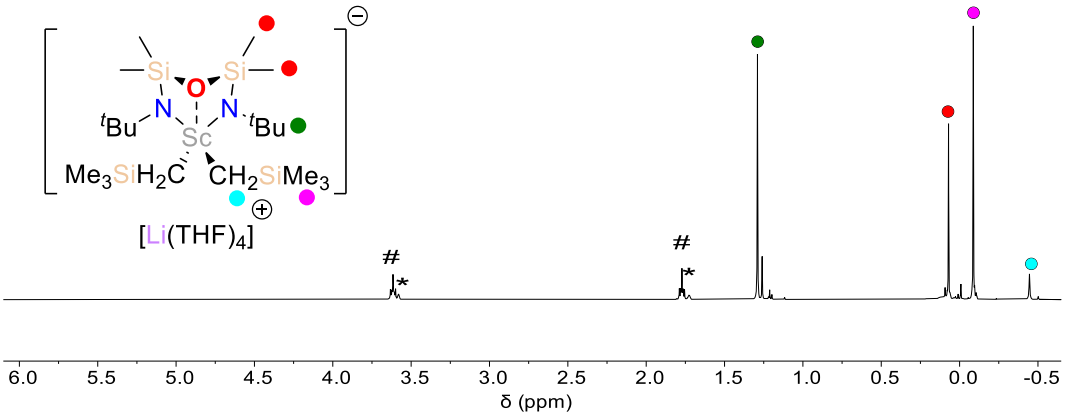


Figure 6.8 ^{1}H NMR spectrum (*****THF-d_8**,** 500 MHz, 298 K) of [(NON$^{t\text{Bu}}$)Sc(CH_2SiMe_3)$_2$][Li(THF)$_4$] (**18**). # represents coordinated THF.

The ^{45}Sc NMR spectrum of **18** displays a resonance at δ 589.5 ppm, which is at a considerably higher frequency than those observed for [NON$^{t\text{Bu}}$]-supported **15** (δ 290.6 ppm) and **16** (δ 290.3 ppm). A similar trend is also seen in the [NON$^{\text{Dipp}}$]-ligand system as **17** is assigned a higher frequency signal (δ 578.8 ppm) than **14** (δ 395.7 ppm).

The apparent deshielding effect of alkyl ligands has been studied in several other scandium compounds. For example, treating a scandium chloride complex supported by a *N*,*N*,*S*-donor ligand with MeLi as an alkylating reagent resulted in a significant ^{45}Sc NMR spectroscopic shift from δ 261 to 560 ppm.[23] Notably, the scandium alkyl

"ate" complex $[Sc(CH_2SiMe_3)_4][Li(THF)_4]$ has been assigned the highest frequency ^{45}Sc NMR spectroscopic shift yet recorded (δ 929.3 ppm).[35] A comparison of the ^{45}Sc NMR spectroscopic data for **14**–**18** and relevant scandium literature compounds is summarised in **Table 6.3**.

Table 6.3 ^{45}Sc NMR (THF-d_8) spectroscopic data for compounds **14–18** and relevant literature scandium complexes.[23, 35, 50]

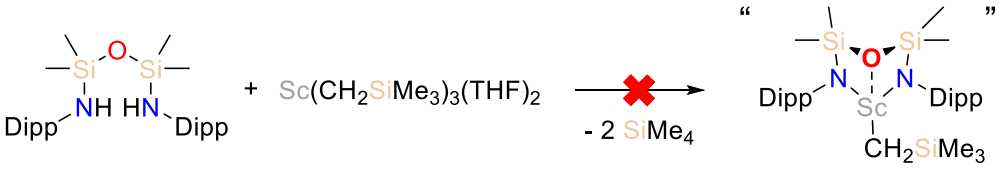
Compound	CN	δ (^{45}Sc) (ppm)
$[(NON^{Dipp})ScCl_2][Li(THF)_4]$ (**14**)	5	395.7
$(NON^{tBu})ScCl(THF)_2$ (**15**)	6	290.6
$(L)_3ScCl_3$[23]	6	228–306
$K[(NON^{tBu})Sc(O\text{-}2,6\text{-}^{i}Pr\text{-}C_6H_3)_2]$ (**16**)	5	290.3
$[Sc(\mu\text{-}ODipp)(ODipp)_2]_2$[35]	4	118.1
$[(NON^{Dipp})Sc(CH_2SiMe_3)_2][Li(THF)_4]$ (**17**)	5	578.8
$[(NON^{tBu})Sc(CH_2SiMe_3)_2][Li(THF)_4]$ (**18**)	5	589.5
$ScMe_3(THF)_x$[50]	6–7	601.7
$[Sc(CH(SiMe_3)_2)_3(\mu\text{-}Me)_xLi(THF)_y]_z$[35]	4	876.9–928.5
$[Sc(CH_2SiMe_3)_4][Li(THF)_4]$[35]	4	929.3

6.3.3.3 Alternative synthesis of a scandium alkyl complex

Neosilyl rare-earth compounds $M(CH_2SiMe_3)_3(THF)_n$ are commonly used as alkyl precursors in protonolysis reactions, enabling the facile elimination of a tetramethylsilane by-product. This approach has found broad applications in the synthesis of scandium alkyl complexes, employing a variety of ligand structures, including phenolate, BDI, (pyrazolyl)borate, and cyclopentadienyl derivatives.[44, 51-53] The use of $Sc(CH_2SiMe_3)_3(THF)_2$ has also been shown to prevent alkali metal ion retention in scandium complexes. For example, a neutral scandium *bis*(alkyl) complex

$(L)Sc(CH_2SiMe_3)_2$ was prepared by the protonolysis reaction between the neosilyl precursor and a disilazide pro-ligand, whereas an alternative salt-metathesis route using a chloride derivative of this complex and $LiCH_2SiMe_3$ resulted in "ate" complexation.[54]

A protonolysis reaction between the $(NON^{Dipp})H_2$ pro-ligand and $Sc(CH_2SiMe_3)_3(THF)_2$ was explored as an alternative route to incorporate an alkyl group into the scandium complex, with the goal of preventing the formation of an "ate" complex. (**Scheme 6.5**).



Scheme 6.5 Attempted synthesis of $(NON^{Dipp})Sc(CH_2SiMe_3)$.

No reactivity was observed by ^1H NMR spectroscopy after 24 hours at room temperature, whereas heating the reaction mixture to 60 °C (in THF-d_8) or 70 °C (in benzene-d_6) resulted in the decomposition of $Sc(CH_2SiMe_3)_3(THF)_2$. This reaction pathway was therefore deemed unsuitable, despite an analogous procedure recently employed to prepare a neutral yttrium alkyl complex $(NON^{Dipp})Y(CH_2SiMe_3)(THF)$.[1] The difference in reactivities may arise from disparities in the size and electrophilic properties of the scandium and yttrium metal centres, alongside the comparatively lower stability of the $Sc(CH_2SiMe_3)_3(THF)_2$ precursor.[48, 55]

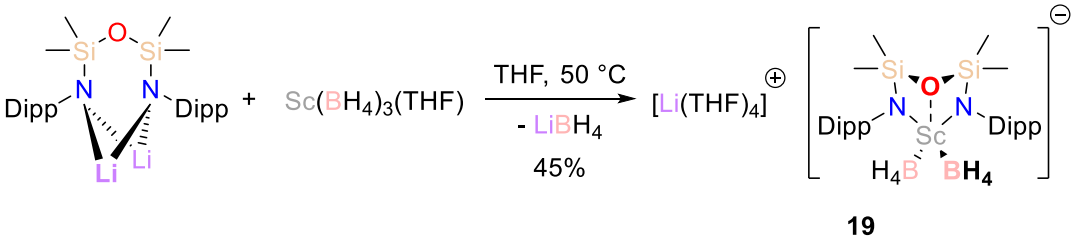
6.3.4 Scandium borohydride complex

Rare-earth borohydride compounds can be prepared using $M(BH_4)_3(THF)_n$ as starting materials in salt-metathesis reactions with alkali metal salts.[56] Due to their electron-donating properties, borohydride groups often provide greater stability to reactive metal centres, allowing for the formation of monomeric complexes as opposed to halide derivatives.[56, 57] Coordination of a borohydride group to the metal centre occurs

through μ_2-hydride linkages, adopting either a bidentate or tridentate coordination mode.[58] Generally, metal borohydride compounds are attractive synthetic targets as hydride surrogates, as evidenced by their application in hydrogenation reactions.[59, 60] In addition, a variety of borohydride compounds have been used as efficient initiators for the polymerisation of both polar and non-polar monomers.[61-65] However, examples of well-defined scandium borohydride complexes are rare due to challenges in their synthesis, including ligand scrambling and the ring-opening of THF, a commonly used reaction solvent.[14, 56, 57, 65-68]

6.3.4.1 Synthesis of a scandium borohydride complex

Using a salt-metathesis reaction between (NON^{Dipp})Li$_2$ and freshly prepared Sc(BH$_4$)$_3$(THF) heated to 50 °C for 72 hours, the *bis*(borohydride) complex [(NON^{Dipp})Sc(BH$_4$)$_2$][Li(THF)$_4$)] (**19**) was synthesised (**Scheme 6.6**). The compound was obtained as a pale brown powder in 45% yield.



Scheme 6.6 Synthesis of [(NON^{Dipp})Sc(BH$_4$)$_2$][Li(THF)$_4$)] (**19**).

Contrary to the majority of previously reported scandium borohydride compounds that exist as neutral species, **19** represents a rare example of a structurally characterised scandium borohydride "ate" complex (*vide infra*).[69]

6.3.4.2 NMR and IR spectroscopic analyses

The ^{1}H NMR spectrum of **19** displays resonances characteristic of a C_{2v}-symmetric compound (**Figure 6.9**), consistent with the solution-state structures of the other two [NON^{Dipp}]-chelated scandium complexes **14** and **17**.

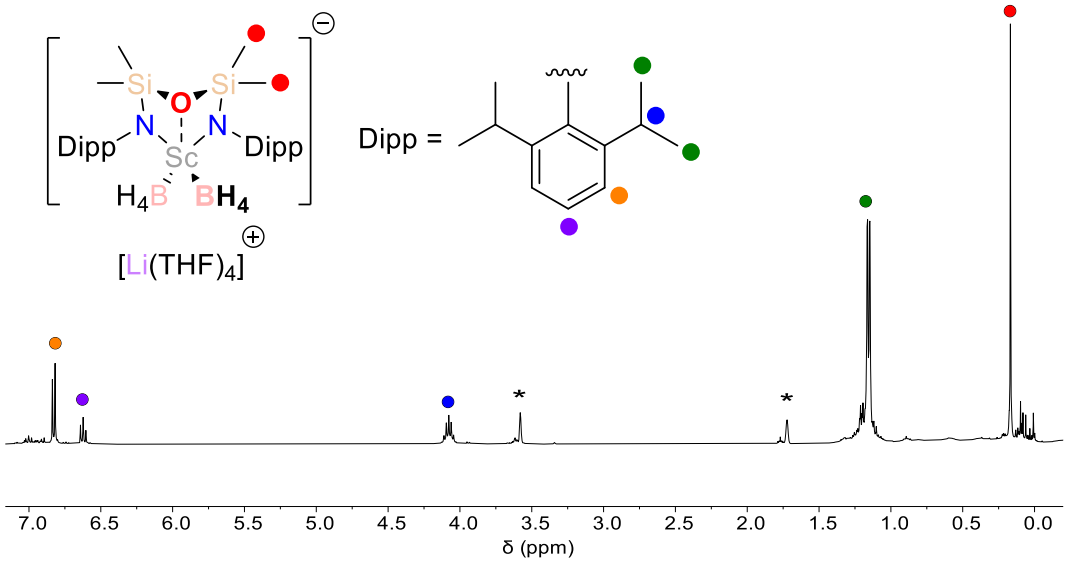


Figure 6.9 ^{1}H NMR spectrum (*THF-d_8, 400 MHz, 298 K**)** of [(NON^{Dipp})Sc(BH$_4$)$_2$][Li(THF)$_4$)] (**19**).

The Si*Me*$_2$ protons are represented by a singlet at δ 0.17 ppm, the CH*Me*$_2$ protons are located as a doublet at δ 1.16 ppm, and a septet at δ 4.08 ppm is assigned to the C*H*Me$_2$ protons. The absence of the B*H*$_4$ proton resonance is likely due to signal broadening caused by proton coupling to two quadrupolar nuclei: ^{45}Sc (I = 7/2, 100% natural abundance) and ^{11}B (I = 3/2, 80% natural abundance). Alternatively, the B*H*$_4$ protons were located by ^{1}H{^{11}B} NMR spectroscopic analysis, revealing their characteristic broad signal at δ 0.50 ppm (**Figure A.5.2** in **Appendix**).[14] In the ^{11}B NMR spectrum, a well-resolved pentet (δ –25.7 ppm, $^{1}J_{B–H}$ = 76 Hz) is indicative of coupling to four hydrogen atoms (**Figure A.5.3** in **Appendix**). This signal is shifted to a higher frequency than that of the Sc(BH$_4$)$_3$(THF) precursor (δ –41.8 ppm). This compares well with

^{11}B NMR spectroscopic shifts reported for homoleptic M[Sc(BH$_4$)$_4$] compounds (δ −22.2 (M = K), −23.0 (M = Li), −21.6 (M = Na) ppm).[70-72]

The IR spectrum of **19** (**Figure A.5.4** in **Appendix**) shows two broad absorption regions centred around 2225 and 2291 cm^{-1}, assigned to B-H vibrations. Both of these values fall within the range of those reported for terminal Sc(κ^3-BH$_4$) units.[56, 67]

6.3.4.3 X-ray crystallographic analysis

Single crystals of **19**, suitable for an X-ray diffraction study, were grown from slow evaporation of a THF/HMDSO mixture (4:1) at 23 °C and solved in the orthorhombic space group, *Pna*2$_1$ (**Figure 6.10**, **Table 6.4**).

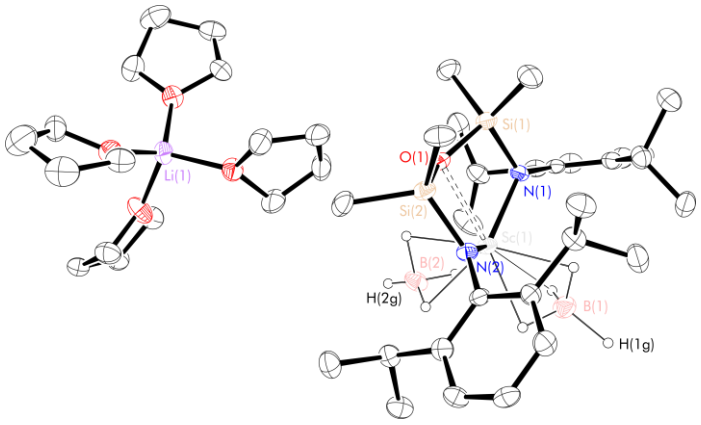


Figure 6.10. Thermal displacement ellipsoid drawing (30%) of the asymmetric unit of [(NON^{Dipp})Sc(BH$_4$)$_2$][Li(THF)$_4$)] (**19**). All hydrogen atoms apart from BH$_4$ groups have been omitted for clarity.

The solid-state structure of **19** confirms the formation of an "ate" complex as a solvent-separated ion pair, consisting of the [(NON^{Dipp})Sc(BH$_4$)$_2$]$^-$ anion and the solvated [Li(THF)$_4$]$^+$ cation. The scandium centre is coordinated by two terminal [BH$_4$]$^-$ units and the κ^3-*N*,*O*,*N'*-bound [NON^{Dipp}]-ligand in a distorted square-base pyramidal environment (τ_5 = 0.17). The axial B(2) atom is located 3.063 Å above of the equatorial plane defined by the B(1)-N(2)-O(1)-N(1) atoms. The Sc-O distance is longer than that

of the [NON^{Dipp}]-chelated scandium chloride complex **14** (2.412(6) Å (**19**) *vs*. 2.392(3) Å (**14**)). This can be ascribed to an increase in electron donation from the borohydride groups, reducing the electrophilicity of the scandium centre.[56] The *trans*-influence of the borohydride groups is evident in the elongation of the Sc-N bonds in **19** relative to those in **14** (average Sc-N = 2.109 Å (**19**) *vs*. 2.0945 Å (**14**)).

Table 6.4 Selected experimental metrical parameters (bond lengths (Å) and angles (°)) for [(NON^{Dipp})Sc(BH$_4$)$_2$][Li(THF)$_4$)] (**19**). Estimated standard deviations shown in brackets.

Space group	*Pna*2$_1$
Sc(1)-N(1)	2.119(7)
Sc(1)-N(2)	2.100(7)
Sc(1)-O(1)	2.412(6)
Sc(1)-B(2)	2.383(13)
Sc(1)-B(1)	2.35(1)
N(1)-Sc(1)-N(2)	121.4(3)
N(1)-Si(1)-Si(2)-N(2)	16.8(4)

As expected, the ScN$_2$Si$_2$O metallacycle adopts a boat conformation, featuring a comparable N-Sc-N bite angle to that observed for **14** (121.4(3)° (**19**) and 120.89(16)° (**14**)). Both borohydride groups are bound to the scandium centre in a κ^3-tridentate manner *via* their hydrogen atoms, which were located in the difference map and freely refined. This is confirmed by short Sc-B distances (2.35(1) and 2.383(13) Å), consistent with the corresponding bond lengths reported for terminal Sc(κ^3-BH$_4$) groups (2.310(5)–2.475 Å).[14, 56, 57, 65-68] An alternative κ^2-coodination mode has been shown to result in longer Sc-B bond distances (e.g. 2.526(5)–2.557(3) Å).[56, 73-75]

6.4 Conclusions

Two different [NON^{R}]-ligand frameworks (R = Dipp, ^{t}Bu) were employed to prepare a new family of di(amido)siloxane scandium complexes, incorporating a range of nucleophilic substituents at the metal centre. The modulation of the steric and electronic properties of the ligand scaffold was found to result in the formation of both "ate" and neutral compounds.

A salt-metathesis route afforded two distinct scandium chloride compounds: the [NON^{Dipp}]-chelated "ate" complex and its salt-free counterpart bearing a [NON^{tBu}]-ligand. These chloride compounds proved to be useful precursors for the synthesis of scandium *bis*(aryloxide) and *bis*(alkyl) "ate" complexes. While the relatively large steric bulk of the [NON^{Dipp}]-ligand impeded reactivity with sterically demanding aryloxide substrates, successful substitution of the chloride group was observed in the presence of the [NON^{tBu}]-ligand scaffold. Additionally, a scandium *bis*(borohydride) "ate" complex was synthesised *via* a salt-metathesis reaction between the dilithium salt of the [NON^{Dipp}]-ligand and the Sc(BH$_4$)$_3$(THF) precursor.

In the solid state, all di(amido)siloxane scandium compounds **14**–**19** formed a boat conformation, with the scandium centre coordinated by the ancillary ligand in a κ^3-*N*,*O*,*N'*-tridentate manner. The intrinsic conformational flexibility of the ScN$_2$Si$_2$O metallacycle allowed for variations in bond lengths and angles, thereby accommodating varying degrees of steric demand. For the chloride complexes, the increased steric encumbrance of the [NON^{Dipp}]-ligand led to the formation of a more acute N-Sc-N bite angle, coupled with a longer Sc-O distance to the siloxane backbone, compared to the [NON^{tBu}]-ligand-supported complex. This coincided with varying coordination

geometries at the five-coordinate scandium centre across the series, ranging from trigonal bipyramidal (**14**) to square-base pyramidal (**16** and **19**). Furthermore, the incorporation of borohydride groups, with similar steric characteristics but enhanced electron-donating properties relative to chloride substituents, resulted in the elongation of Sc-O and Sc-N distances in the supporting [NON^{Dipp}]-ligand.

Further exploration of the reactivity of these systems could involve tuning the steric and electronic profile of the ligand framework as well as selecting appropriate synthetic procedures to minimise both aggregation and alkali metal ion retention. The observed conformational flexibility of these di(amido)siloxane scandium compounds offers a promising pathway to develop next generation ROP initiators.

6.5 References

1. M. D. Anker, M. J. Evans, S. A. Cameron and G. Laufersky, *Polyhedron*, 2024, **247**, 116741.
2. E. W. Y. Wong, A. K. Das, M. J. Katz, Y. Nishimura, R. J. Batchelor, M. Onishi and D. B. Leznoff, *Inorg. Chim. Acta*, 2006, **359**, 2826-2834.
3. K. C. Jantunen, R. J. Batchelor and D. B. Leznoff, *Organometallics*, 2004, **23**, 2186-2193.
4. K. C. Jantunen, F. Haftbaradaran, M. J. Katz, R. J. Batchelor, G. Schatte and D. B. Leznoff, *Dalton Trans.*, 2005, 3083-3091.
5. M. Zimmermann and R. Anwander, *Chem. Rev.*, 2010, **110**, 6194-6259.
6. D. L. Clark, J. G. Watkin and J. C. Huffman, *Inorg. Chem.*, 1992, **31**, 1554-1556.
7. O. Just and W. S. Rees, *Inorg. Chem.*, 2001, **40**, 1751-1755.
8. C. E. Hayes, Y. Sarazin, M. J. Katz, J.-F. Carpentier and D. B. Leznoff, *Organometallics*, 2013, **32**, 1183-1192.
9. H. Herath, L. D. Silvio and J. Evans, *J. Mater. Sci.: Mater. Med.*, 2005, **16**, 1061-1065.
10. H. Ma, T. P. Spaniol and J. Okuda, *Angew. Chem. Int. Ed.*, 2006, **45**, 7818-7821.
11. N. Diteepeng, I. A. P. Wilson, J.-C. Buffet, Z. R. Turner and D. O'Hare, *Polym. Chem.*, 2020, **11**, 6308-6318.
12. A. F. A. Alshamrani, O. Santoro, T. J. Prior, M. A. Alamri, G. J. Stasiuk, M. R. J. Elsegood and C. Redshaw, *Dalton Trans.*, 2021, **50**, 8302-8306.

13. G. Du, Y. Wei, W. Zhang, Y. Dong, Z. Lin, H. He, S. Zhang and X. Li, *Dalton Trans.*, 2013, **42**, 1278-1286.

14. N. Diteepeng, J.-C. Buffet, Z. R. Turner and D. O'Hare, *Dalton Trans.*, 2019, **48**, 16099-16107.

15. R. J. Schwamm, J. R. Harmer, M. Lein, C. M. Fitchett, S. Granville and M. P. Coles, *Angew. Chem. Int. Ed.*, 2015, **54**, 10630-10633.

16. F.-G. Fontaine, K. A. Tupper and T. D. Tilley, *J. Organomet. Chem.*, 2006, **691**, 4595-4600.

17. K. R. D. Johnson and P. G. Hayes, *Polyhedron*, 2016, **108**, 43-49.

18. W. E. Piers and D. J. H. Emslie, *Coord. Chem. Rev.*, 2002, **233-234**, 131-155.

19. M. Visseaux, M. Terrier, A. Mortreux and P. Roussel, *Eur. J. Inorg. Chem.*, 2010, 2867-2876.

20. Y. Luo, W. Li, D. Lin, Y. Yao, Y. Zhang and Q. Shen, *Organometallics*, 2010, **29**, 3507-3514.

21. M. Veith, S. Mathur and C. Mathur, *Polyhedron*, 1998, **17**, 1005-1034.

22. G. Mund, R. J. Batchelor, R. D. Sharma, C. H. W. Jones and D. B. Leznoff, *J. Chem. Soc., Dalton Trans.*, 2002, 136-137.

23. S. A. Bartlett, G. Cibin, A. J. Dent, J. Evans, M. J. Hanton, G. Reid, R. P. Tooze and M. Tromp, *Dalton Trans.*, 2013, **42**, 2213-2223.

24. G. A. Melson, D. J. Olszanski and A. K. Rahimi, *Spectrochim. Acta A*, 1977, **33**, 301-309.

25. G. A. Kirakosyan, V. P. Tarasov and Y. A. Buslaev, *Magn. Reson. Chem.*, 1989, **27**, 103-111.

26. A. W. Addison, T. N. Rao, J. Reedijk, J. van Rijn and G. C. Verschoor, *J. Chem. Soc., Dalton Trans.*, 1984, 1349-1356.

27. N. H.-W. Wiberg, *Lehrbuch der Anorganischen Chemie*, De Gruyter Berlin, 1985.

28. F. Haftbaradaran, G. Mund, R. J. Batchelor, J. F. Britten and D. B. Leznoff, *Dalton Trans.*, 2005, 2343-2345.

29. A. J. Elias, H. W. Roesky, W. T. Robinson and G. M. Sheldrick, *J. Chem. Soc., Dalton Trans.*, 1993, 495-500.

30. T. K. Panda, H. Kaneko, K. Pal, H. Tsurugi and K. Mashima, *Organometallics*, 2010, **29**, 2610-2615.

31. J. Hong, L. Zhang, K. Wang, Z. Chen, L. Wu and X. Zhou, *Organometallics*, 2013, **32**, 7312-7322.

32. T. Jia, S.-y. Xu, L.-c. Huang and W. Gao, *Polyhedron*, 2018, **145**, 182-190.

33. B. D. Ward, S. R. Dubberley, A. Maisse-François, L. H. Gade and P. Mountford, *J. Chem. Soc., Dalton Trans.*, 2002, 4649-4657.

34. H.-L. Pham, T. Rajeshkumar, L. U.-h. Wang, Y. H. Ng, K.-H. Wong, Y.-M. So, H. H. Y. Sung, R. Lortz, I. D. Williams, L. Maron and W.-H. Leung, *Organometallics*, 2023, **42**, 1094-1105.

35. A. Mortis, D. Barisic, K. Eichele, C. Maichle-Mössmer and R. Anwander, *Dalton Trans.*, 2020, **49**, 7829-7841.

36. G. B. Deacon, A. Gitlits, P. C. Junk, B. W. Skelton and A. H. White, *Z. Anorg. Allg. Chem.*, 2005, **631**, 861-865.
37. M. L. Cole, P. C. Junk, K. M. Proctor, J. L. Scott and C. R. Strauss, *Dalton Trans.*, 2006, 3338-3349.
38. D. L. Clark, R. V. Hollis, B. L. Scott and J. G. Watkin, *Inorg. Chem.*, 1996, **35**, 667-674.
39. S. D. McKee, C. J. Burns and L. R. Avens, *Inorg. Chem.*, 1998, **37**, 4040-4045.
40. K. Hoffmann and E. Weiss, *J. Organomet. Chem.*, 1974, **67**, 221-228.
41. L. N. Saunders, L. N. Dawe and C. M. Kozak, *J. Organomet. Chem.*, 2014, **749**, 34-40.
42. M. D. Anker, M. Lein and M. P. Coles, *Chem. Sci.*, 2019, **10**, 1212-1218.
43. L. N. Grant, B. Pinter, B. C. Manor, H. Grützmacher and D. J. Mindiola, *Angew. Chem. Int. Ed.*, 2018, **57**, 1049-1052.
44. F. Lin, Z. Liu, M. Wang, B. Liu, S. Li and D. Cui, *Angew. Chem. Int. Ed.*, 2020, **59**, 4324-4328.
45. X. Zhang, S. Zhou, D. Wang, L. Zhang, Y. Wei, X. Zhu, P. Cui, G. Luo and S. Wang, *Organometallics*, 2021, **40**, 3462-3471.
46. J. Arnold, C. G. Hoffman, D. Y. Dawson and F. J. Hollander, *Organometallics*, 1993, **12**, 3645-3654.
47. H. Yan, J. Wei and W.-X. Zhang, *Organometallics*, 2021, **40**, 3245-3252.
48. A. L. Allred and E. G. Rochow, *J. Inorg. Nucl. Chem.*, 1958, **5**, 264-268.
49. W. Rong, D. Liu, H. Zuo, Y. Pan, Z. Jian, S. Li and D. Cui, *Organometallics*, 2013, **32**, 1166-1175.
50. D. Barisic, D. Diether, C. Maichle-Mössmer and R. Anwander, *J. Am. Chem. Soc.*, 2019, **141**, 13931-13940.
51. J. Blackwell, C. Lehr, Y. Sun, W. E. Piers, S. D. Pearce-Batchilder, M. J. Zaworotko and V. G. Y. Jr., *Can. J. Chem.*, 1997, **75**, 702-711.
52. J. Hitzbleck and J. Okuda, *Z. Anorg. Allg. Chem.*, 2006, **632**, 1947-1949.
53. G. A. Gurina, A. V. Markin, A. V. Cherkasov, I. A. Godovikov, A. M. Ob'edkov and A. A. Trifonov, *Eur. J. Inorg. Chem.*, 2023, **26**, e202300392.
54. L. T. J. Evans, M. P. Coles, F. G. N. Cloke and P. B. Hitchcock, *Inorg. Chim. Acta*, 2010, **363**, 1114-1125.
55. R. D. Shannon, *Acta Crystallogr. A*, 1976, **32**, 751-767.
56. J. Jenter, G. Eickerling and P. W. Roesky, *J. Organomet. Chem.*, 2010, **695**, 2756-2760.
57. T. P. Seifert, T. S. Brunner, T. S. Fischer, C. Barner-Kowollik and P. W. Roesky, *Organometallics*, 2018, **37**, 4481-4487.
58. T. J. Marks and J. R. Kolb, *Chem. Rev.*, 1977, **77**, 263-293.
59. S. Murugesan, B. Stöger, M. Weil, L. F. Veiros and K. Kirchner, *Organometallics*, 2015, **34**, 1364-1372.
60. A. G. Kalola, P. Prasad, J. A. Mokariya and M. P. Patel, *Synth. Commun.*, 2021, **51**, 3565-3589.
61. M. Visseaux, M. Mainil, M. Terrier, A. Mortreux, P. Roussel, T. Mathivet and M. Destarac, *Dalton Trans.*, 2008, 4558-4561.

62. F. Bonnet, A. R. Cowley and P. Mountford, *Inorg. Chem.*, 2005, **44**, 9046-9055.

63. J. Thuilliez, R. Spitz and C. Boisson, *Macromol. Chem. Phys.*, 2006, **207**, 1727-1731.

64. J. Jenter, P. W. Roesky, N. Ajellal, S. M. Guillaume, N. Susperregui and L. Maron, *Chem. Eur. J.*, 2010, **16**, 4629-4638.

65. Z. Jian, W. Zhao, X. Liu, X. Chen, T. Tang and D. Cui, *Dalton Trans.*, 2010, **39**, 6871-6876.

66. S. Fadlallah, J. Jothieswaran, F. Capet, F. Bonnet and M. Visseaux, *Chem. Eur. J.*, 2017, **23**, 15644-15654.

67. J. Jenter, N. Meyer, P. W. Roesky, S. K.-H. Thiele, G. Eickerling and W. Scherer, *Chem. Eur. J.*, 2010, **16**, 5472-5480.

68. F. Bonnet, C. Da Costa Violante, P. Roussel, A. Mortreux and M. Visseaux, *Chem. Commun.*, 2009, 3380-3382.

69. A. Starobrat, T. Jaroń and W. Grochala, *Inorg. Chim. Acta*, 2015, **437**, 70-73.

70. R. Černý, D. B. Ravnsbæk, G. Severa, Y. Filinchuk, V. D' Anna, H. Hagemann, D. Haase, J. Skibsted, C. M. Jensen and T. R. Jensen, *J. Phys. Chem. C*, 2010, **114**, 19540-19549.

71. H. Hagemann, M. Longhini, J. W. Kaminski, T. A. Wesolowski, R. Černý, N. Penin, M. H. Sørby, B. C. Hauback, G. Severa and C. M. Jensen, *J. Phys. Chem. A*, 2008, **112**, 7551-7555.

72. R. Černý, G. Severa, D. B. Ravnsbæk, Y. Filinchuk, V. D'Anna, H. Hagemann, D. Haase, C. M. Jensen and T. R. Jensen, *J. Phys. Chem. C*, 2010, **114**, 1357-1364.

73. B. G. Segal and S. J. Lippard, *Inorg. Chem.*, 1978, **17**, 844-850.

74. M. F. Lappert, A. Singh, J. L. Atwood and W. E. Hunter, *J. Chem. Soc., Chem. Commun.*, 1983, 206-207.

75. S. Demir, N. A. Siladke, J. W. Ziller and W. J. Evans, *Dalton Trans.*, 2012, **41**, 9659-9666.

Chapter 7

Experimental details

7.1 Materials and methods

7.1.1 General procedures

Air- and moisture-sensitive manipulations were conducted under an inert atmosphere of nitrogen, employing standard Schlenk line techniques and an MBraun Unilab glove box. All syntheses involving compounds **1–13** were carried out under conditions that excluded light (in the dark and/or by coating surfaces with an aluminium foil).

7.1.2 Commercially supplied materials

^{n}BuLi (1.6 M and 2.5 M solution in hexanes; Sigma Aldrich), anhydrous $BiCl_3$ (Sigma Aldrich), 1,3-dichloro-1,1,3,3-tetramethyldisiloxane (Sigma Aldrich), potassium *tert*-butoxide (Sigma Aldrich), $LiNMe_2$ (Sigma Aldrich), CO_2 (N4.5 grade; BUSE Scientific), *D*-Lactide (Purac) were used as received. *L*-, *rac*-Lactide (Corbion Biomaterials), and *meso*-lactide (Uhde Inventa-Fischer) were recrystallised repeatedly from dry toluene and dried under vacuum. 2,6-dimethyl phenol (Sigma Aldrich), phenol (Sigma Aldrich), 2-benzoylpyridine (Sigma Aldrich), and $LiCH_2SiMe_3$ (Sigma Aldrich) were sublimed before use. 2,6-di*iso*propylaniline (Apollo Scientific) was dried over calcium hydride, freeze-pump-thaw degassed three times before use stored over

pre-activated 3 Å molecular sieves. *β*-Butyrolactone and *tert*-butylamine were dried over calcium hydride and distilled. Me_3SiCl was distilled before use. Phenyl isocyanate and *N,N'*-di*iso*propylcarbodiimide were provided by Dr Eric Yang (University of Oxford). Carbon disulfide, dried over calcium hydride, distilled, and stored over pre-activated 3 Å molecular sieves, was provided by Dr Nichabhat Blake (University of Oxford). ε-Caprolactone, dried over calcium hydride and distilled, was provided by Mr Justin Hayden (University of Oxford). Molecular sieves (Sigma Aldrich) were dried under vacuum at 140 °C for 48 hours before use.

7.1.3 Solvent preparation

Solvents (pentane, *n*-hexane, toluene, benzene) were dried using an MBraun SPS-800 solvent purification system, stored over a potassium mirror, and degassed under partial pressure prior to use. Tetrahydrofuran was distilled from sodium/benzophenone, stored over pre-activated 3 Å molecular sieves, and degassed under partial pressure prior to use. Diethyl ether was distilled from sodium/benzophenone, stored over a potassium mirror, and degassed under partial pressure prior to use. Hexamethyldisiloxane (HMDSO, Sigma Aldrich) was dried over calcium hydride, distilled, and stored over pre-activated 3 Å molecular sieves.

Deuterated solvents were refluxed under partial pressure over potassium (benzene-d_6, toluene-d_8) or dried over calcium hydride (tetrahydrofuran-d_8, chloroform-d_1), distilled, freeze-pump-thaw degassed three times, and stored over pre-activated 3 or 4 Å molecular sieves.

7.1.4 Published procedures

$Bi(NMe_2)_3$, $Sc(BH_4)_3(THF)$, KOC_6H_5, KO-2,6-Me-C_6H_3, $Sc(CH_2SiMe_3)_3(THF)_2$, and $(NON^{Dipp})K_2$ were prepared according to the literature procedures.[1-5] KO-2,6-^{i}Pr-C_6H_3 was synthesised by Dr Rebecca Jones (University of Oxford) according to a literature procedure.[6] $ScCl_3(THF)_3$ was synthesised by Mr Justin Hayden (University of Oxford) according to a literature procedure.[7]

7.1.5 Solution phase NMR spectroscopy

NMR spectra were recorded on a Bruker Avance III HD NanoBay NMR (9.4 T, 400.2 MHz), a Bruker Avance III NMR (11.75 T, 499.9 MHz), a Bruker Avance NMR fitted with a ^{13}C cryoprobe (11.75 T, 500.3 MHz) or a Bruker NEO 600 (14.1 T, 600.4 MHz) spectrometers. Spectra were recorded at 298 K, unless otherwise stated, and internally referenced to residual protio solvent ^{1}H or ^{13}C resonances. MestreNova software was used to process and analyse spectra. Chemical shifts were quoted in δ (ppm) with respect to tetramethylsilane (δ = 0 ppm), and coupling constants were reported in Hertz. Air-sensitive samples were prepared in a glove box under a nitrogen atmosphere using dried deuterated solvents in 5 mm J. Young's tap NMR spectroscopy tubes.

7.1.6 Fourier-transform infrared (FTIR) spectroscopy

Samples were prepared in a glove box under a nitrogen atmosphere as pellets pressed with anhydrous potassium bromide, which was dried above 150 °C at 10^{-6} mbar for 24 hours prior to use. FTIR spectra were measured using a Nicolet iS5 ThermoScientific spectrometer, with a background spectrum run prior to the sample and subtracted from the sample spectra.

7.1.7 Elemental analysis

Samples were prepared in a glove box under a nitrogen atmosphere and sealed in glass vials. CHN analyses were conducted in duplicate by Ms Orla McCullough (London Metropolitan University). Multiple runs did not provide satisfactory data for compounds **3**, **12**, **14**, **16**, **17**, **18**, and **19**; this was attributed to sample degradation caused by sensitivity to air, moisture, and/or light.

7.1.8 Single crystal X-ray crystallography

Single crystal X-ray diffraction data collection and structure determination were performed by Dr Zoë Turner, Dr Louis Morris, and Dr Clement Collins-Rice (University of Oxford). Crystals were mounted on MiTeGen MicroMounts using perfluoropolyether oil and rapidly transferred to a goniometer head on a diffractometer fitted with an Oxford Cryostream open-flow nitrogen cooling device.[8] Data collections were conducted at 150 K using an Oxford Diffraction Supernova diffractometer with mirror-monochromated Cu Kα radiation (λ = 1.54178 Å), and the data were processed using CrysAlisPro.[9] The structures were solved using direct methods (SIR-92),[10] a charge flipping algorithm (SUPERFLIP),[11] or intrinsic phasing (SHELXT)[12] and refined by full matrix least squares procedures using the WinGX,[13] CRYSTALS software suite,[14] or SHELXL20 refinement package.[12] Molecular bond distances and angles were calculated using PLATON, if necessary.[15] ORTEP was utilised to generate images of solid-state molecular structures, with thermal ellipsoids depicted at 30% probability.[16]

7.1.9 Matrix-assisted laser desorption/ionisation time of flight (MALDI-ToF) mass spectrometry

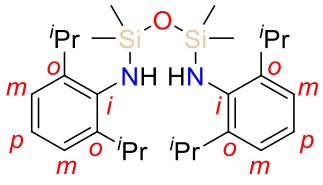
MALDI-ToF MS analysis was performed by Dr Victor Mikhailov or Mr Justin Hayden (University of Oxford) using a Bruker MALDI Autoflex ToF MS. Polymer samples were prepared in chloroform at a concentration of 1.0 mg mL^{-1} and filtered through a 0.2 μm PTFE filter membrane before analysis. The DHB matrix was prepared by mixing the sample with DHB (10 mg mL^{-1} in 70:30 H_2O:CH_3CN) in a 1:1 volume ratio. The DCTB matrix was prepared by mixing 10 μL of a sample with 10 μL DCTB (40 mg mL^{-1} in THF) and 2.5 μL KTFA (5 mg mL^{-1} in THF). 1.5 μL of the mixed solutions were spotted on the MALDI plate and dried.

7.1.10 Gel permeation chromatography (GPC)

Polymer molecular weights and molecular weight distributions were recorded on a Polymer Laboratories PLGPC50 Plus instrument equipped with a Polymer Laboratories PLgel Mixed-D column (300 mm length, 7.5 mm diameter) and a refractive index (RI) detector. THF (Sigma Aldrich, HPLC grade) was used as the eluent flowing at 1.0 mL min^{-1} at 30 °C. Polymer samples were prepared in THF at a concentration of 1.0 mg mL^{-1} and filtered through a 0.2 μm PTFE filter membrane before analysis. Experimental molecular weights were recorded as linear polystyrene equivalents and corrected by Mark-Houwink correction factors for PLA (0.58) and PCL (0.56).[17, 18]

7.2 Experimental details for Chapter Two

7.2.1 Dipp-substituted di(amido)siloxane ligand numbering scheme



7.2.2 Synthesis of $(NON^{Dipp})H_2$[19]

A solution of ^{n}BuLi in hexane (13.3 mL of a 1.6 M solution, 21.3 mmol) was added dropwise to a stirring solution of 2,6-di*iso*propylaniline (4.02 mL, 21.3 mmol) in hexane (20 mL) at –30 °C. The reaction mixture was allowed to warm to room temperature and stirred for 3 hours, resulting in a white suspension. Subsequently, 1,3-dichloro-1,1,3,3-tetramethyldisiloxane (2.09 mL, 10.7 mmol) in hexane (15 mL) was added dropwise, followed by stirring for a further 16 hours. The solution was filtered, and the volatiles were removed under vacuum to afford $(NON^{Dipp})H_2$ as a colourless oil. Yield: 3.89 g (75%).

^{1}H NMR (benzene-d_6, 298 K, 600 MHz): δ 7.22–7.10 (overlapped with benzene-d_6, 6H, *m*-, *p*-C_6H_3), 3.64 (sept, $^{3}J_{H–H}$ = 6.8 Hz, 4H, C*H*Me$_2$), 2.67 (s (br), 2H, N*H*), 1.27 (d, $^{3}J_{H–H}$ = 6.9 Hz, 24H, CH*Me*$_2$), 0.20 (s, 12H, Si*Me*$_2$) ppm.

7.2.3 Synthesis of $(NON^{tBu})H_2$[20]

tert-Butylamine (4.38 mL, 41.7 mmol) was added dropwise to a solution of 1,3-dichloro-1,1,3,3-tetramethyldisiloxane (1.99 mL, 10.2 mmol) in hexane (20 mL) at 0 °C. The mixture was stirred for 16 hours, filtered, and the volatiles were removed under vacuum. $(NON^{tBu})H_2$ was isolated as a colourless oil. Yield: 2.09 g (74%).

^{1}H NMR (benzene-d_6, 298 K, 400 MHz): δ 1.20 (s, 18H, C*Me*$_3$), 0.88 (s (br), 2H, N*H*), 0.20 (s, 12H, Si*Me*$_2$) ppm.

7.2.4 General synthesis of (NON^R)Li$_2$ (R = Dipp, ^{t}Bu)[21]

A solution of ^{n}BuLi in hexane (2.50 mL of a 1.6 M solution, 4.00 mmol) was added dropwise to a stirring solution of (NON^R)H$_2$ (2.00 mmol) in hexane (15 mL) at –30 °C. The reaction mixture was allowed to warm to room temperature and stirred for 4 hours. After removing the volatiles under vacuum, (NON^R)Li$_2$ compounds were isolated as off-white solids.

(NON^{Dipp})Li$_2$ (0.904 g (91%)): **^{1}H NMR** (THF-d_8, 298 K, 400 MHz): δ 6.64 (d, $^3J_{H–H}$ = 7.7 Hz, 4H, *m*-C$_6$*H*$_3$), 6.18 (t, $^3J_{H–H}$ = 7.4 Hz, 2H, *p*-C$_6$*H*$_3$), 4.18 (sept, $^3J_{H–H}$ = 7.0 Hz, 4H, C*H*Me$_2$), 1.05 (d, $^3J_{H–H}$ = 6.9 Hz, 24H, CH*Me*$_2$), –0.07 (s, 12H, Si*Me*$_2$) ppm.

(NON^{tBu})Li$_2$ (0.542 g (94%)): (THF-d_8, 298 K, 400 MHz): δ 1.12 (s, 18H, C*Me*$_3$), –0.04 (s, 12H, Si*Me*$_2$) ppm.

7.2.5 General synthesis of (NON^R)BiCl (R = Dipp, ^{t}Bu)[21]

A solution of (NON^R)Li$_2$ (1.40 mmol) in diethyl ether (10 mL) was added dropwise to a stirring suspension of anhydrous BiCl$_3$ (0.441 g, 1.40 mmol) in diethyl ether (10 mL) at –30 °C. After stirring the reaction mixture for 16 hours, the volatiles were removed under vacuum, and the product was extracted in hexane (3 × 10 mL). The resulting solution was dried under vacuum to yield (NON^R)BiCl compounds as orange solids.

(NON^{Dipp})BiCl (0.560 g (55%)): **^{1}H NMR** (THF-d_8, 298 K, 400 MHz): δ 7.23 (d, $^3J_{H–H}$ = 7.6 Hz, $^4J_{H–H}$ = 1.7 Hz, 2H, *m*-C$_6$*H*$_3$), 7.19 (d, $^3J_{H–H}$ = 7.7 Hz, $^4J_{H–H}$ = 1.7 Hz,

2H, *m*-C_6H_3), 6.98 (t, $^3J_{H–H}$ = 7.7 Hz, 2H, *p*-C_6H_3), 4.03 (sept, $^3J_{H–H}$ = 6.8 Hz, 2H, C*H*Me$_2$), 3.74 (sept, $^3J_{H–H}$ = 6.8 Hz, 2H, C*H*Me$_2$), 1.30 (d, $^3J_{H–H}$ = 6.8 Hz, 6H, CH*Me*$_2$), 1.24 (d, $^3J_{H–H}$ = 6.7 Hz, 6H, CH*Me*$_2$), 1.21 (d, $^3J_{H–H}$ = 6.7 Hz, 6H, CH*Me*$_2$), 1.18 (d, $^3J_{H–H}$ = 6.7 Hz, 6H, CH*Me*$_2$), 0.36 (s, 6H, Si*Me*$_2$), 0.11 (s, 6H, Si*Me*$_2$) ppm.

(NON$^{t\text{Bu}}$)BiCl (0.443 g (61%)): **^{1}H NMR** (benzene-d_6, 298 K, 400 MHz): δ 1.19 (s, 18H, C*Me*$_3$), 0.56 (s, 6H, Si*Me*$_2$), 0.33 (s, 6H, Si*Me*$_2$) ppm.

7.2.6 Synthesis of (NON^{Dipp})Bi(OC$_6$H$_5$) (1)

Potassium phenoxide (0.0181 g, 0.137 mmol) in benzene (1 mL) was added to a solution of (NON^{Dipp})BiCl (0.100 g, 0.137 mmol) in benzene (1 mL). The resulting yellow reaction mixture was sonicated for 30 minutes and allowed to stir overnight. The solution was then filtered through a 0.2 μm PTFE filter membrane and freeze-dried to produce (NON^{Dipp})Bi(OC$_6$H$_5$) (**1**) as a pale yellow solid. Yield: 0.0526 g (49%). Colourless crystals, suitable for single-crystal X-ray diffraction, were grown from slow evaporation of a hexane solution at 23 °C.

^{1}H NMR (benzene-d_6, 298 K, 600 MHz): δ 7.18 (dd, $^3J_{H–H}$ = 7.6 Hz, $^4J_{H–H}$ = 1.8 Hz, 2H, *m*-C_6H_3), 7.12 (dd, $^3J_{H–H}$ = 7.7 Hz, $^4J_{H–H}$ = 1.8 Hz, 2H, *m*-C_6H_3), 7.06–6.99 (m, 4H, *p*-C_6H_3 and O-*m*-C_6H_5 overlapping), 6.69 (t, $^3J_{H–H}$ = 7.3 Hz, 1H, O-*p*-C_6H_5), 6.17–6.12 (m, 2H, O-*o*-C_6H_5), 4.10 (sept, $^3J_{H–H}$ = 6.8 Hz, 2H, C*H*Me$_2$), 3.77 (sept, $^3J_{H–H}$ = 7.0 Hz, 2H, C*H*Me$_2$), 1.28 (d, $^3J_{H–H}$ = 6.7 Hz, 6H, CH*Me*$_2$), 1.23 (d, $^3J_{H–H}$ = 6.8 Hz, 6H, CH*Me*$_2$), 1.19 (d, $^3J_{H–H}$ = 6.7 Hz, 6H, CH*Me*$_2$), 1.13 (d, $^3J_{H–H}$ = 7.0 Hz, 6H, CH*Me*$_2$), 0.66 (s, 6H, Si*Me*$_2$), 0.26 (s, 6H, Si*Me*$_2$) ppm. **^{13}C{^{1}H} NMR** (benzene-d_6, 298 K, 151 MHz): δ 157.2 (O-*i*-C_6H_5), 150.6 (*i*-C_6H_3), 146.8 (*o*-C_6H_3), 139.3 (*o*-C_6H_3), 129.5 (O-*m*-C_6H_5), 126.4 (*p*-C_6H_3), 125.1 (*m*-C_6H_3), 123.8 (*m*-C_6H_3), 120.7 (O-*o*-C_6H_5), 120.0 (O-*p*-C_6H_5), 27.9

(CH*Me*$_2$), 27.7 (*C*HMe$_2$), 27.6 (*C*HMe$_2$), 26.5 (CH*Me*$_2$), 25.5 (CH*Me*$_2$), 25.1 (CH*Me*$_2$), 4.3 (Si*Me*$_2$), 3.1 (Si*Me*$_2$) ppm. **CHN analysis** (%): Calculated for $C_{34}H_{51}BiN_2O_2Si_2$: C, 52.03; H, 6.55; N, 3.57. Found: C, 54.41; H, 7.19; N, 3.67.

7.2.7 Synthesis of (NON^{Dipp})Bi(O-2,6-Me-C$_6$H$_3$) (2)

Potassium 2,6-dimethylphenoxide (0.0240 g, 0.150 mmol) in benzene (1 mL) was added to a solution of (NON^{Dipp})BiCl (0.109 g, 0.150 mmol) in benzene (1 mL). The resulting yellow reaction mixture was sonicated for 30 minutes and allowed to stir overnight. The solution was then filtered through a 0.2 μm PTFE filter membrane and freeze-dried to produce (NON^{Dipp})Bi(O-2,6-Me-C$_6$H$_3$) (**2**) as a pale yellow solid. Yield: 0.0915 g (75%). Orange crystals, suitable for single-crystal X-ray diffraction, were grown from slow evaporation of a diethyl ether solution at –30 °C.

^{1}H NMR (benzene-d_6, 298 K, 600 MHz): δ 7.15–7.12 (m, 2H, *m*-C$_6$*H*$_3$), 7.08 (dd, $^3J_{H–H}$ = 7.7 Hz, $^4J_{H–H}$ = 1.7 Hz, 2H, *m*-C$_6$*H*$_3$), 6.98 (t, $^3J_{H–H}$ = 7.7 Hz, 2H, *p*-C$_6$*H*$_3$), 6.91 (d, $^3J_{H–H}$ = 7.4 Hz, 2H, O-*m*-2,6-Me-C$_6$*H*$_3$), 6.61 (t, $^3J_{H–H}$ = 7.4 Hz, 1H, O-*p*-2,6-Me-C$_6$*H*$_3$), 4.06 (sept, $^3J_{H–H}$ = 6.8 Hz, 2H, C*H*Me$_2$), 3.77 (sept, $^3J_{H–H}$ = 6.9 Hz, 2H, C*H*Me$_2$), 1.97 (s, 6H, *Me*), 1.32–1.21 (m, 12H, CH*Me*$_2$), 1.11 (d, $^3J_{H–H}$ = 7.0 Hz, 6H, CH*Me*$_2$), 1.03 (d, $^3J_{H–H}$ = 6.7 Hz, 6H, CH*Me*$_2$), 0.71 (s, 6H, Si*Me*$_2$), 0.24 (s, 6H, Si*Me*$_2$) ppm. **^{13}C{^{1}H} NMR** (benzene-d_6, 298 K, 151 MHz): δ 157.2 (O-*i*-2,6-Me-*C*$_6$H$_3$), 150.6 (*o*-*C*$_6$H$_3$), 146.8 (*o*-*C*$_6$H$_3$), 139.3 (*i*-*C*$_6$H$_3$), 129.1 (O-*m*-2,6-Me-*C*$_6$H$_3$), 126.2 (*p*-*C*$_6$H$_3$), 124.9 (*m*-*C*$_6$H$_3$), 123.8 (*m*-*C*$_6$H$_3$), 119.4 (O-*p*-2,6-Me-*C*$_6$H$_3$), 27.9 (CH*Me*$_2$), 27.7 (*C*HMe$_2$), 27.5 (*C*HMe$_2$), 25.9 (CH*Me*$_2$), 25.4 (CH*Me*$_2$), 25.2 (CH*Me*$_2$), 18.7 (*Me*), 4.8 (Si*Me*$_2$), 2.4 (Si*Me*$_2$) ppm. δ (O-*o*-2,6-Me-*C*$_6$H$_3$) was not observed. **CHN analysis** (%): Calculated for $C_{36}H_{56}BiN_2O_2Si_2$: C, 53.19; H, 6.82; N, 3.45. Found: C, 54.22; H, 7.21; N, 3.06.

7.2.8 Synthesis of (NON^{Dipp})Bi(O-2,6-^{i}Pr-C$_6$H$_3$) (3)

Potassium 2,6-di*iso*propylphenoxide (0.0327 g, 0.151 mmol) and (NON^{Dipp})BiCl (0.106 g, 0.151 mmol) were mixed in benzene (2 mL). The resulting yellow reaction mixture was sonicated for 30 minutes and allowed to stir overnight. The solution was then filtered through a 0.2 μm PTFE filter membrane and freeze-dried to produce (NON^{Dipp})Bi(O-2,6-^{i}Pr-C$_6$H$_3$) (**3**) as a pale yellow solid. Yield: 0.0892 g (68%). Yellow crystals, suitable for single-crystal X-ray diffraction, were grown from slow evaporation of a hexane solution at 23 °C.

^{1}H NMR (benzene-d_6, 298 K, 600 MHz): δ 7.13 (dd, $^{3}J_{H–H}$ = 7.7 Hz, $^{4}J_{H–H}$ = 1.7 Hz, 2H, *m*-C$_6$*H*$_3$), 7.08 (dd, $^{3}J_{H–H}$ = 7.7 Hz, $^{4}J_{H–H}$ = 1.7 Hz, 2H, *m*-C$_6$*H*$_3$), 7.06 (d, $^{3}J_{H–H}$ = 7.6 Hz, 2H, O-*m*-2,6-^{i}Pr-C$_6$*H*$_3$), 6.95 (t, $^{3}J_{H–H}$ = 7.7 Hz, 2H, *p*-C$_6$*H*$_3$), 6.80 (t, $^{3}J_{H–H}$ = 7.6 Hz, 1H, O-*p*-2,6-^{i}Pr-C$_6$*H*$_3$), 4.03 (sept, $^{3}J_{H–H}$ = 6.8 Hz, 2H, C*H*Me$_2$), 3.81 (sept, $^{3}J_{H–H}$ = 6.8 Hz, 2H, C*H*Me$_2$), 3.05 (br, 2H, O-2,6-C*H*Me$_2$-C$_6$H$_3$), 1.30 (d, $^{3}J_{H–H}$ = 6.7 Hz, 6H, CH*Me*$_2$), 1.26 (d, $^{3}J_{H–H}$ = 6.7 Hz, 6H, CH*Me*$_2$), 1.19 (d, $^{3}J_{H–H}$ = 6.9 Hz, 6H, CH*Me*$_2$), 1.10 (d, $^{3}J_{H–H}$ = 6.7 Hz, 12H, O-2,6-CH*Me*$_2$-C$_6$H$_3$), 0.96 (d, $^{3}J_{H–H}$ = 6.7 Hz, 6H, CH*Me*$_2$), 0.70 (s, 6H, Si*Me*$_2$), 0.22 (s, 6H, Si*Me*$_2$) ppm. **^{13}C{^{1}H} NMR** (benzene-d_6, 298 K, 151 MHz): δ 154.2 (O-*i*-2,6-^{i}Pr-*C*$_6$H$_3$), 150.7 (*o*-*C*$_6$H$_3$), 147.4 (*o*-*C*$_6$H$_3$), 139.0 (O-*o*-2,6-^{i}Pr-*C*$_6$H$_3$), 138.8 (*i*-*C*$_6$H$_3$), 126.6 (*p*-*C*$_6$H$_3$), 125.1 (*m*-*C*$_6$H$_3$), 124.1 (*m*-*C*$_6$H$_3$), 123.7 (O-*m*-2,6-^{i}Pr-*C*$_6$H$_3$), 120.5 (O-*p*-2,6-^{i}Pr-*C*$_6$H$_3$), 28.8 (CH*Me*$_2$), 27.8 (*C*HMe$_2$), 27.7 (*C*HMe$_2$), 27.1 (O-2,6-*C*HMe$_2$-C$_6$H$_3$), 26.8 (CH*Me*$_2$), 25.6 (CH*Me*$_2$), 25.1 (CH*Me*$_2$), 24.8 (O-2,6-CH*Me*$_2$-C$_6$H$_3$), 2.3 (Si*Me*$_2$), 1.4 (Si*Me*$_2$) ppm.

7.2.9 Synthesis of (NON^{Dipp})Bi(O^{t}Bu) (4)

Potassium *tert*-butoxide (0.0122 g, 0.109 mmol) and (NON^{Dipp})BiCl (0.0793 g, 0.109 mmol) were mixed in in benzene (2 mL). The resulting yellow reaction mixture

was sonicated for 30 minutes and allowed to stir overnight. The solution was then filtered through a 0.2 μm PTFE filter membrane and freeze-dried to produce (NON^{Dipp})Bi(O^{t}Bu) (**4**) as a pale yellow solid. Yield: 0.0509 g (61%). Pale yellow crystals, suitable for single-crystal X-ray diffraction, were grown from slow evaporation of a hexane solution at 23 °C.

^{1}H NMR (benzene-d_6, 298 K, 600 MHz): δ 7.25 (dd, $^{3}J_{H–H}$ = 7.6 Hz, $^{4}J_{H–H}$ = 1.8 Hz, 2H, *m*-C$_6$*H*$_3$), 7.07 (dd, $^{3}J_{H–H}$ = 7.7 Hz, $^{4}J_{H–H}$ = 1.8 Hz, 2H, *m*-C$_6$*H*$_3$), 7.01 (t, $^{3}J_{H–H}$ = 7.6 Hz, 2H, *p*-C$_6$*H*$_3$), 4.13 (sept, $^{3}J_{H–H}$ = 6.8 Hz, 2H, C*H*Me$_2$), 3.82 (sept, $^{3}J_{H–H}$ = 6.9 Hz, 2H, C*H*Me$_2$), 1.58 (d, $^{3}J_{H–H}$ = 6.8 Hz, 6H, CH*Me*$_2$), 1.30 (d, $^{3}J_{H–H}$ = 6.8 Hz, 6H, CH*Me*$_2$), 1.28–1.21 (m, 12H, CH*Me*$_2$), 0.72 (s, 9H, C*Me*$_3$), 0.62 (s, 6H, Si*Me*$_2$), 0.33 (s, 6H, Si*Me*$_2$) ppm. **^{13}C{^{1}H} NMR** (benzene-d_6, 298 K, 151 MHz): δ 150.5 (*o*-*C*$_6$H$_3$), 146.3 (*o*-*C*$_6$H$_3$), 140.6 (*i*-*C*$_6$H$_3$), 125.5 (*p*-*C*$_6$H$_3$), 124.6 (*m*-*C*$_6$H$_3$), 123.8 (*m*-*C*$_6$H$_3$), 71.8 (*C*Me$_3$), 34.9 (C*Me*$_3$), 27.9 (CH*Me*$_2$), 27.5 (*C*HMe$_2$), 26.8 (*C*HMe$_2$), 26.3 (CH*Me*$_2$), 26.0 (CH*Me*$_2$), 25.9 (CH*Me*$_2$), 3.7 (Si*Me*$_2$), 3.3 (Si*Me*$_2$) ppm. **CHN analysis** (%): Calculated for C$_{32}$H$_{55}$BiN$_2$O$_2$Si$_2$: C, 50.25; H, 7.25; N, 3.66. Found: C, 50.29; H, 7.09; N, 3.38.

7.2.10 Synthesis of (NON^{tBu})Bi(O-2,6-Me-C$_6$H$_3$) (5)

Potassium 2,6-dimethylphenoxide (0.0293 g, 0.183 mmol) in benzene (1 mL) was added to a solution of (NON^{tBu})BiCl (0.0950 g, 0.183 mmol) in benzene (1 mL). The resulting yellow reaction mixture was sonicated for 30 minutes and allowed to stir overnight. The solution was then filtered through a 0.2 μm PTFE filter membrane and freeze-dried to produce (NON^{tBu})Bi(O-2,6-Me-C$_6$H$_3$) (**5**) as an orange solid. Yield: 0.0631 g (57%).

^{1}H NMR (benzene-d_6, 298 K, 400 MHz): δ 7.12 (d, $^{3}J_{H–H}$ = 7.4 Hz, 2H, O-*m*-2,6-Me-C$_6$*H*$_3$) 6.78 (t, $^{3}J_{H–H}$ = 7.4 Hz, 1H, O-*p*-2,6-Me-C$_6$*H*$_3$), 2.55 (s, 6H, *Me*),

1.15 (s, 18H, C*Me*$_3$), 0.54 (s, 6H, Si*Me*$_2$), 0.38 (s, 6H, Si*Me*$_2$) ppm. **^{13}C{^{1}H} NMR** (benzene-d_6, 298 K, 126 MHz): 158.8 (O-*i*-2,6-Me-*C*$_6$H$_3$), 129.8 (O-*o*-2,6-Me-*C*$_6$H$_3$), 128.5 (O-*m*-2,6-Me-*C*$_6$H$_3$), 119.9 (O-*p*-2,6-Me-*C*$_6$H$_3$), 53.3 (*C*Me$_3$) 37.5 (C*Me*$_3$), 18.9 (*Me*), 8.0 (Si*Me*$_2$), 6.7 (Si*Me*$_2$) ppm. **CHN analysis** (%): Calculated for $C_{20}H_{39}BiN_2O_2Si_2$: C, 39.73; H, 6.50; N, 4.63. Found: C, 39.44; H, 6.37; N, 4.85.

7.2.11 Synthesis of (NON^{Dipp})Bi(NMe$_2$) (6)

(NON^{Dipp})H$_2$ (0.112 g, 0.231 mmol) in benzene (1 mL) was added dropwise to a solution of freshly sublimed Bi(NMe$_2$)$_3$ (0.0788 g, 0.231 mmol) in benzene (1 mL). The resulting yellow mixture was allowed to react overnight and freeze-dried to produce (NON^{Dipp})Bi(NMe$_2$) (**6**) as a pale yellow solid. Yield: 0.127 g (75%). Colourless crystals, suitable for single-crystal X-ray diffraction, were grown from slow evaporation of a hexane solution at 23 °C.

^{1}H NMR (benzene-d_6, 298 K, 400 MHz): δ 7.19 (dd, $^3J_{H–H}$ = 7.6 Hz, $^4J_{H–H}$ = 1.8 Hz, 2H, *m*-C$_6$*H*$_3$), 7.13 (dd, $^3J_{H–H}$ = 7.7 Hz, $^4J_{H–H}$ = 1.8 Hz, 2H, *m*-C$_6$*H*$_3$), 7.04 (t, $^3J_{H–H}$ = 7.6 Hz, 2H, *p*-C$_6$*H*$_3$), 3.89 (sept, $^3J_{H–H}$ = 6.8 Hz, 4H, C*H*Me$_2$), 3.78 (s, 6H, N*Me*$_2$), 1.35 (d, $^3J_{H–H}$ = 7.1 Hz, 6H, CH*Me*$_2$), 1.33 (d, $^3J_{H–H}$ = 7.1 Hz, 6H, CH*Me*$_2$), 1.22 (d, $^3J_{H–H}$ = 6.8 Hz, 6H, CH*Me*$_2$), 1.19 (d, $^3J_{H–H}$ = 6.9 Hz, 6H, CH*Me*$_2$), 0.44 (s, 6H, Si*Me*$_2$), 0.27 (s, 6H, Si*Me*$_2$) ppm. **^{13}C{^{1}H} NMR** (benzene-d_6, 298 K, 101 MHz): δ 150.6 (*o*-*C*$_6$H$_3$), 148.3 (*o*-*C*$_6$H$_3$), 140.1 (*i*-*C*$_6$H$_3$), 125.8 (*p*-*C*$_6$H$_3$), 124.6 (*m*-*C*$_6$H$_3$), 124.2 (*m*-*C*$_6$*H*$_3$), 45.7 (N*Me*$_2$), 28.7 (CH*Me*$_2$), 27.7 (*C*HMe$_2$), 27.5 (*C*HMe$_2$), 27.4 (CH*Me*$_2$), 25.3 (CH*Me*$_2$), 24.8 (CH*Me*$_2$), 3.9 (Si*Me*$_2$), 3.1 (Si*Me*$_2$) ppm. **IR** (KBr): 2963, 1462, 1440, 1257, 1061, 910, 793 cm^{-1}. **CHN analysis** (%): Calculated: C, 48.96; H, 7.12; N, 5.71. Found: C, 48.61; H, 7.00; N, 5.10.

7.3 Experimental details for Chapters Three and Four

7.3.1 General polymerisation procedure

In a glove box, a J. Young's tap NMR tube was loaded with a monomer: either *L*-, *D*-, *rac*- or *meso*-lactide (0.0430 g, 0.298 mmol), or ε-caprolactone (33.3 µL, 0.298 mmol), or γ-butyrolactone (22.7 µL, 0.298 mmol). A required amount of the initiator in a deuterated polymerisation solvent (0.6 mL) was then added so that the initial monomer concentration was 0.5 M. Polymerisations were carried out at stated temperatures and quenched with wet pentane. The solvent was allowed to evaporate from the isolated polymer samples before characterisation.

^{1}H NMR spectroscopy was utilised to determine the monomer conversion based on the integrated area ratios for *methine* proton resonances (lactide polymerisation) and *methylene* C*H*$_2$O resonances (ε-caprolactone polymerisation), unless otherwise stated. The isolated samples were analysed by GPC and MALDI-ToF analyses. PLA tacticity was determined by the integrations of the tetrad levels in the ^{1}H{^{1}H} NMR spectrum according to Bernoullian statistics.[22]

7.3.2 Synthesis of (NON^{Dipp})Bi(OCH(Me)C(O)NMe$_2$) (7)

L-Lactide (0.00699 g, 0.0485 mmol) was added to a solution of (NON^{Dipp})Bi(NMe$_2$) (0.0718 g, 0.0970 mmol) in benzene (1 mL), resulting in a pale yellow reaction mixture. The solution was freeze-dried to afford (NON^{Dipp})Bi(OCH(Me)C(O)NMe$_2$) (**7**) as a white solid. Yield: 0.0321 g (82%). Colourless crystals, suitable for single-crystal X-ray diffraction, were grown from slow evaporation of a hexane solution at 23 °C.

^{1}H NMR (benzene-d_6, 298 K, 600 MHz): δ 7.34 (dd, $^{3}J_{H–H}$ = 7.6 Hz, $^{4}J_{H–H}$ = 1.8 Hz, 1H, *m*-C$_6$*H*$_3$), 7.20 (dd, $^{3}J_{H–H}$ = 7.6 Hz, $^{4}J_{H–H}$ = 1.8 Hz, 1H, *m*-C$_6$*H*$_3$), 7.18 (overlapped with

benzene-d_6, 1H, *m*-C_6H_3), 7.11 (dd, $^3J_{H–H}$ = 7.6 Hz, $^4J_{H–H}$ = 1.7 Hz, 1H, *m*-C_6H_3), 7.06 (t, $^3J_{H–H}$ = 7.6 Hz, 1H, *p*-C_6H_3), 6.94 (t, $^3J_{H–H}$ = 7.6 Hz, 1H, *p*-C_6H_3), 6.22 (q, $^3J_{H–H}$ = 6.6 Hz, 1H, OC*H*Me) 4.33 (sept, $^3J_{H–H}$ = 6.9 Hz, 1H, C*H*Me$_2$), 4.22 (sept, $^3J_{H–H}$ = 6.8 Hz, 1H, C*H*Me$_2$), 4.03 (sept, $^3J_{H–H}$ = 6.9 Hz, 1H, C*H*Me$_2$), 3.97 (sept, $^3J_{H–H}$ = 6.8 Hz, 1H, C*H*Me$_2$), 2.04 (s, 3H, N*Me*$_2$), 1.83 (s, 3H, N*Me*$_2$), 1.53 (d, $^3J_{H–H}$ = 6.7 Hz, 3H, CH*Me*$_2$, 1.42–1.37 (m, 9H, CH*Me*$_2$), 1.36–1.28 (m, 12H, CH*Me*$_2$), 0.78 (s, 3H, Si*Me*$_2$), 0.71 (d, $^3J_{H–H}$ = 6.6 Hz, 3H, OCH*Me*), 0.62 (s, 3H, Si*Me*$_2$), 0.44 (s, 3H, Si*Me*$_2$), 0.36 (s, 3H, Si*Me*$_2$) ppm. **^{13}C{^{1}H} NMR** (benzene-d_6, 298 K, 151 MHz): δ 182.6 (*C*O), 150.4 (*o*-C_6H_3), 145.0 (*o*-C_6H_3), 147.3 (*o*-C_6H_3), 146.7 (*o*-C_6H_3), 142.3 (*i*-C_6H_3), 142.1 (*i*-C_6H_3), 124.6 (*p*-C_6H_3), 124.5 (*p*-C_6H_3), 124.2 (*m*-C_6H_3), 123.7 (*m*-C_6H_3), 123.6 (*m*-C_6H_3), 123.5 (*m*-C_6H_3), 67.1 (O*C*HMe), 35.7 (N*Me*$_2$), 35.4 (N*Me*$_2$), 27.9 (*C*HMe$_2$), 27.8 (*C*HMe$_2$), 27.6 (*C*HMe$_2$), 27.4 (*C*HMe$_2$), 27.3 (CH*Me*$_2$), 26.9 (CH*Me*$_2$), 26.3 (CH*Me*$_2$), 26.2 (CH*Me*$_2$), 26.1 (CH*Me*$_2$), 26.0 (CH*Me*$_2$), 26.0 (CH*Me*$_2$), 25.5 (CH*Me*$_2$), 23.5 (OCH*Me*), 4.4 (Si*Me*$_2$), 4.28 (Si*Me*$_2$), 3.7 (Si*Me*$_2$), 3.4 (Si*Me*$_2$) ppm. **IR** (KBr): 2963, 1613, 1250, 1188, 936, 827 cm^{-1}. **CHN analysis** (%): Calculated for $C_{33}H_{56}BiN_3O_3Si_2$: C, 49.06; H, 6.99; N, 5.20. Found: C, 49.82; H, 6.88; N, 4.81.

7.3.3 Synthesis of (NON^{Dipp})Bi(OC$_5$H$_{10}$C(O)NMe$_2$) (8)

ε-Caprolactone (0.00576 mL, 0.052 mmol) was added to a solution of (NON^{Dipp})Bi(NMe$_2$) (0.038 g, 0.052 mmol) in benzene (1 mL). The resulting pale yellow solution was freeze-dried to afford (NON^{Dipp})Bi(OC$_5$H$_{10}$C(O)NMe$_2$) (**8**) as a yellow oil. Yield: 0.045 g (91%).

^{1}H NMR (benzene-d_6, 298 K, 500 MHz): δ 7.24 (dd, $^3J_{H–H}$ = 7.6 Hz, $^4J_{H–H}$ = 1.8 Hz, 2H, *m*-C_6H_3), 7.11 (dd, $^3J_{H–H}$ = 7.7 Hz, $^4J_{H–H}$ = 1.8 Hz, 2H, *m*-C_6H_3), 7.04 (t, $^3J_{H–H}$ = 7.6 Hz, 2H, *p*-C_6H_3), 4.15 (sept, $^3J_{H–H}$ = 6.8 Hz, 2H, C*H*Me$_2$), 4.08 (t, $^3J_{H–H}$ = 7.0 Hz, 2H,

C*H*$_2$-O), 3.81 (sept, $^3J_{H–H}$ = 6.8 Hz, 2H, C*H*Me$_2$), 2.65 (s, 3H, N*Me*$_2$), 2.24 (s, 3H, N*Me*$_2$), 1.91 (t, $^3J_{H–H}$ = 7.4 Hz, 2H, C*H*$_2$-CO), 1.61 (p, $^3J_{H–H}$ = 7.4 Hz, 2H, C*H*$_2$-CH$_2$-CO), 1.46 (d, $^3J_{H–H}$ = 6.8 Hz, 6H, CH*Me*$_2$), 1.32 (d, $^3J_{H–H}$ = 6.8 Hz, 6H, CH*Me*$_2$), 1.29 (d, $^3J_{H–H}$ = 6.8 Hz, 6H, CH*Me*$_2$), 1.28–1.22 (overlapped with CH*Me*$_2$, 2H, C*H*$_2$-CH$_2$-O), 1.21 (d, $^3J_{H–H}$ = 7.0 Hz, 6H, CH*Me*$_2$), 1.17–1.07 (m, 2H, CH$_2$-C*H*$_2$-CH$_2$), 0.60 (s, 6H, Si*Me*$_2$), 0.28 (s, 6H, Si*Me*$_2$) ppm. **^{13}C{^{1}H} NMR** (benzene-d_6, 298 K, 126 MHz): δ 171.8 (*C*O), 150.5 (*o*-*C*$_6$H$_3$), 147.1 (*o*-*C*$_6$H$_3$), 140.4 (*i*-*C*$_6$H$_3$), 125.0 (*p*-*C*$_6$H$_3$), 123.9 (*m*-*C*$_6$H$_3$), 124.0 (*m*-*C*$_6$H$_3$), 66.4 (*C*H$_2$-O), 36.5 (N*Me*$_2$), 36.1 (*C*H$_2$-CH$_2$-O), 35.1 (N*Me*$_2$), 33.4 (*C*H$_2$-CO), 28.0 (CH*Me*$_2$), 27.7 (*C*HMe$_2$), 27.7 (*C*HMe$_2$), 27.0 (CH*Me*$_2$), 25.7 (CH*Me*$_2$), 26.1 (CH$_2$-*C*H$_2$-CH$_2$), 25.6 (*C*H$_2$-CH$_2$-CO), 25.4 (CH*Me*$_2$), 4.1 (Si*Me*$_2$), 3.3 (Si*Me*$_2$) ppm. **IR** (KBr): 2360, 2340, 1650, 1464, 1431, 1397, 1253, 1185, 1043 cm^{-1}. Satisfactory CHN analysis could not be achieved due to the persistence of the starting materials in the reaction mixture.

7.3.4 Synthesis of (NON^{Dipp})Bi(OC$_3$H$_6$C(O)NMe$_2$) (9)

γ-Butyrolactone (5.75 µL, 0.0670 mmol) was added to a solution of (NON^{Dipp})Bi(NMe$_2$) (0.0493 g, 0.0670 mmol) in benzene (1 mL). The solution was heated to 50 °C for 16 hours and freeze-dried to afford (NON^{Dipp})Bi(OC$_3$H$_6$C(O)NMe$_2$) (**9**) as a pale yellow solid. Yield: 0.048 g (87%).

^{1}H NMR (benzene-d_6, 298 K, 400 MHz): δ 7.24 (dd, $^3J_{H–H}$ = 7.6 Hz, $^4J_{H–H}$ = 1.8 Hz, 2H, *m*-C$_6$*H*$_3$), 7.11 (dd, $^3J_{H–H}$ = 7.7 Hz, $^4J_{H–H}$ = 1.8 Hz, 2H, *m*-C$_6$*H*$_3$), 7.01 (t, $^3J_{H–H}$ = 7.6 Hz, 2H, *p*-C$_6$*H*$_3$), 4.30 (t, $^3J_{H–H}$ = 6.2 Hz, 2H, C*H*$_2$-O), 4.19 (sept, $^3J_{H–H}$ = 6.9 Hz, 2H, C*H*Me$_2$), 3.86 (sept, $^3J_{H–H}$ = 6.9 Hz, 2H, C*H*Me$_2$), 2.47 (s, 3H, N*Me*$_2$), 2.15 (s, 3H, N*Me*$_2$), 1.82 (t, $^3J_{H–H}$ = 6.7 Hz, 2H, C*H*$_2$-CO), 1.62 (pent, $^3J_{H–H}$ = 6.4 Hz, 2H, CH$_2$-C*H*$_2$-CH$_2$), 1.45 (d, $^3J_{H–H}$ = 6.7 Hz, 6H, CH*Me*$_2$), 1.35 (d, $^3J_{H–H}$ = 6.8 Hz, 6H,

CH*Me*$_2$), 1.30 (d, $^3J_{H–H}$ = 6.7 Hz, 6H, CH*Me*$_2$), 1.26 (d, $^3J_{H–H}$ = 6.9 Hz, 6H, CH*Me*$_2$), 0.62 (s, 6H, Si*Me*$_2$), 0.29 (s, 6H, Si*Me*$_2$) ppm. **^{13}C{^{1}H} NMR** (benzene-d_6, 298 K, 101 MHz): δ 171.6 (*C*O), 149.9 (*o*-*C*$_6$H$_3$), 146.8 (*o*-*C*$_6$H$_3$), 140.2 (*i*-*C*$_6$H$_3$), 125.3 (*p*-*C*$_6$H$_3$), 124.2 (*m*-*C*$_6$H$_3$), 123.6 (*m*-*C*$_6$H$_3$), 64.99 (*C*H$_2$-O), 36.0 (N*Me*$_2$), 34.6 (N*Me*$_2$), 30.6 (*C*H$_2$), 29.4 (*C*H$_2$-CO), 27.6 (*C*HMe$_2$), 27.2 (*C*HMe$_2$), 27.2 (CH*Me*$_2$), 26.6 (CH*Me*$_2$), 25.3 (CH*Me*$_2$), 25.2 (CH*Me*$_2$), 3.8 (Si*Me*$_2$), 2.9 (Si*Me*$_2$) ppm. **IR** (KBr): 2959, 2868, 1630, 1464, 1441, 1259, 1059, 940 cm^{-1}. Satisfactory CHN analysis could not be achieved due to the persistence of the starting materials in the reaction mixture.

7.4 Experimental details for Chapter Five

7.4.1 Synthesis of (NON^{Dipp})Bi(CO$_2$NMe$_2$) (10)

(NON^{Dipp})Bi(NMe$_2$) (0.0800 g, 0.109 mmol) was dissolved in benzene-d_6 (0.5 mL) in a J. Young's tap NMR tube. The solution was freeze-pump-thaw degassed and CO_2 (1 bar) was added. The reaction mixture was agitated for 30 seconds and subsequently freeze-dried to afford (NON^{Dipp})Bi(CO$_2$NMe$_2$) (**10**) as a white solid. Yield: 0.0664 g (78%). Colourless crystals, suitable for single-crystal X-ray diffraction, were grown from slow evaporation of a hexane solution at 23 °C.

^{1}H NMR (benzene-d_6, 298 K, 600 MHz): δ 7.24 (dd, $^3J_{H–H}$ = 7.6 Hz, $^4J_{H–H}$ = 1.7 Hz, 2H, *m*-C$_6$*H*$_3$), 7.12 (dd, $^3J_{H–H}$ = 7.7 Hz, $^4J_{H–H}$ = 1.7 Hz, 2H, *m*-C$_6$*H*$_3$), 7.02 (t, $^3J_{H–H}$ = 7.6 Hz, 2H, *p*-C$_6$*H*$_3$), 4.10 (sept, $^3J_{H–H}$ = 6.9 Hz, 2H, C*H*Me$_2$), 3.77 (sept, $^3J_{H–H}$ = 6.8 Hz, 2H, C*H*Me$_2$), 2.73 (s, 6H, N*Me*$_2$), 1.37–1.32 (m, 12H, CH*Me*$_2$), 1.31–1.28 (m, 6H, CH*Me*$_2$), 1.02 (d, $^3J_{H–H}$ = 6.9 Hz, 6H, CH*Me*$_2$), 0.56 (s, 6H, Si*Me*$_2$), 0.23 (s, 6H, Si*Me*$_2$) ppm. **^{13}C{^{1}H} NMR** (benzene-d_6, 298 K, 126 MHz): δ 162.9 (*C*O), 150.3 (*o*-*C*$_6$H$_3$), 147.9 (*o*-*C*$_6$H$_3$), 139.1 (*i*-*C*$_6$H$_3$), 126.3 (*p*-*C*$_6$H$_3$), 124.5 (*m*-*C*$_6$H$_3$), 123.9 (*m*-*C*$_6$*H*$_3$), 36.6 (N*Me*$_2$),

28.8 (CH*Me*$_2$), 27.6 (*C*HMe$_2$), 27.5 (*C*HMe$_2$), 27.1 (CH*Me*$_2$), 25.46 (CH*Me*$_2$), 24.5 (CH*Me*$_2$), 4.3 (Si*Me*$_2$), 2.9 (Si*Me*$_2$) ppm. **IR** (KBr): 2963, 1594, 1465, 1432, 1391, 1291, 1251, 1226, 1043, 935 cm^{-1}. **CHN analysis** (%): Calculated for $C_{31}H_{52}BiN_3O_3Si_2$: C, 47.74; H, 6.72; N, 5.39. Found: C, 49.76; H, 6.76; N, 5.17.

7.4.2 Synthesis of (NON^{Dipp})Bi(CS$_2$NMe$_2$) (11)

Excess CS_2 (0.1 mL, 1.655 mmol) was added to a solution of (NON^{Dipp})Bi(NMe$_2$) (0.048 g, 0.065 mmol) in benzene (1 mL). The solution was agitated and freeze-dried to afford (NON^{Dipp})Bi(CS$_2$NMe$_2$) (**11**) as a yellow solid. Yield: 0.0375 g (71%). Pale yellow crystals, suitable for single-crystal X-ray diffraction, were grown from slow evaporation of a hexane solution at 23 °C.

^{1}H NMR (benzene-d_6, 298 K, 400 MHz): δ 7.22 (d, $^3J_{H–H}$ = 7.7 Hz, 4H, *m*-C$_6$*H*$_3$), 6.99 (t, $^3J_{H–H}$ = 7.6 Hz, 2H, *p*-C$_6$*H*$_3$), 4.00 (sept, $^3J_{H–H}$ = 6.7 Hz, 4H, C*H*Me$_2$), 2.60 (s, 6H, N*Me*$_2$), 1.39 (d, $^3J_{H–H}$ = 6.8 Hz, 12H, CH*Me*$_2$), 1.36 (d, $^3J_{H–H}$ = 6.7 Hz, 12H, CH*Me*$_2$), 0.45 (s, 12H, Si*Me*$_2$) ppm. **^{13}C{^{1}H} NMR** (benzene-d_6, 298 K, 101 MHz): δ 125.7 (*p*-*C*$_6$H$_3$), 124.0 (*m*-*C*$_6$H$_3$), 43.6 (N*Me*$_2$), 27.6 (*C*HMe$_2$), 27.7 (CH*Me*$_2$), 25.8 (CH*Me*$_2$), 3.7 (Si*Me*$_2$) ppm. δ (*i*-*C*$_6$H$_3$), (*o*-*C*$_6$H$_3$), and (*C*S) were not observed. **IR** (KBr): 2958, 2359, 1506, 1099, 1079, 961, 887 cm^{-1}. **CHN analysis** (%): Calculated for $C_{31}H_{52}BiN_3O_3S_2Si_2$: C, 45.85; H, 6.45; N, 5.17. Found: C, 46.54; H, 6.41; N, 5.08.

7.4.3 Attempted synthesis of (NON^{Dipp})Bi(^{i}PrNCN^{i}PrNMe$_2$)

(NON^{Dipp})Bi(NMe$_2$) (0.030 g, 0.0408 mmol) was dissolved in benzene-d_6 (0.5 mL) in a J. Young's tap NMR tube, and *N,N'*-di*iso*propylcarbodiimide (6.28 µL, 0.0408 mmol) was added. After heating the solution at 50 °C for 48 hours, ^{1}H NMR spectroscopy indicated that no reaction had taken place.

7.4.4 Synthesis of (NON^{Dipp})Bi(NPhCONMe$_2$) (12)

Phenyl isocyanate (7.43 µL, 0.0680 mmol) was added dropwise to a solution of (NON^{Dipp})Bi(NMe$_2$) (0.0504 g, 0.0680 mmol) in hexane (1 mL). After filtering the solution, its slow evaporation at –30 °C yielded colourless crystals of (NON^{Dipp})Bi(NPhCONMe$_2$) (**12**) suitable for single-crystal X-ray diffraction. Yield: 0.0244 g (42%).

^{1}H NMR (benzene-d_6, 298 K, 400 MHz): δ 7.30 (d, $^3J_{H–H}$ = 7.6 Hz, 4H, *m*-C$_6$*H*$_3$), 7.06 (t, $^3J_{H–H}$ = 7.6 Hz, 2H, *p*-C$_6$*H*$_3$), 6.99 (t, $^3J_{H–H}$ = 7.5 Hz, 2H, *o*-C$_6$*H*$_5$), 6.71 (t, $^3J_{H–H}$ = 7.3 Hz, 1H, *p*-C$_6$*H*$_5$), 6.14 (d, $^3J_{H–H}$ = 7.9 Hz, 2H, *m*-C$_6$*H*$_5$), 4.26 (sept, $^3J_{H–H}$ = 6.9 Hz, 2H, C*H*Me$_2$), 3.81 (sept, $^3J_{H–H}$ = 7.0 Hz, 2H, C*H*Me$_2$), 2.41 (s, 6H, N*Me*$_2$), 1.38 (d, $^3J_{H–H}$ = 6.5 Hz, 6H, CH*Me*$_2$, 1.31 (d, $^3J_{H–H}$ = 6.8 Hz, 6H, CH*Me*$_2$), 1.29 (d, $^3J_{H–H}$ = 6.8 Hz, 6H, CH*Me*$_2$), 1.03 (d, $^3J_{H–H}$ = 7.0 Hz, 6H, CH*Me*$_2$), 0.59 (s, 6H, Si*Me*$_2$), 0.31 (s, 6H, Si*Me*$_2$) ppm. **^{13}C{^{1}H} NMR** (benzene-d_6, 298 K, 151 MHz): δ 160.2 (O*C*N), 150.0 (*o*-*C*$_6$H$_3$), 147.4 (*o*-*C*$_6$H$_3$), 146.0 (*i*-*C*$_6$H$_5$), 141.1 (*i*-*C*$_6$H$_3$), 128.5 (*o*-*C*$_6$H$_5$), 125.5 (*p*-*C*$_6$H$_3$), 124.8 (*m*-*C*$_6$H$_3$), 124.4 (*m*-*C*$_6$H$_3$), 123.9 (*m*-*C*$_6$H$_5$), 121.63 (*p*-*C*$_6$H$_5$), 38.6 (N*Me*$_2$), 28.4 (CH*Me*$_2$), 27.5 (*C*HMe$_2$), 27.1 (*C*HMe$_2$), 26.8 (CH*Me*$_2$), 25.4 (CH*Me*$_2$), 24.8 (CH*Me*$_2$), 4.3 (Si*Me*$_2$), 3.3 (Si*Me*$_2$) ppm.

7.4.5 Synthesis of (NON^{Dipp})Bi(PhCONMe$_2$Py) (13)

Freshly sublimed 2-benzoylpyridine (0.0132 g, 0.0720 mmol) in benzene (0.5 mL) was added dropwise to the solution of (NON^{Dipp})Bi(NMe$_2$) (0.0530 g, 0.0720 mmol) in benzene (0.5 mL). The mixture was left to react for 1 hour and freeze-dried to afford (NON^{Dipp})Bi(PhCONMe$_2$Py) (**13**) as an off-white solid. Yield: 0.0523 g (79%). Colourless crystals, suitable for single-crystal X-ray diffraction, were grown from slow evaporation of a hexane solution at –30 °C.

^{1}H NMR (toluene-d_8, 213 K, 500 MHz): δ 8.57 (s, 1H, *o*-C_6H_5), 7.81 (s, 1H, *o*-C_6H_5), 7.33–7.21 (m, overlapped with toluene-d_8, Ar-*H*), 7.21–7.17 (m, 2H, C_6H_3), 7.13–7.06 (m, overlapped with toluene-d_8, Ar-*H*), 7.05–7.01 (m, 3H, C_6H_3), 6.89–6.85 (m, 1H, C_6H_3), 6.48 (t, $^{3}J_{H–H}$ = 7.7 Hz, 1H, *m*/*p*-Py-*H*), 6.07 (t, $^{3}J_{H–H}$ = 6.3 Hz, 1H, *m*/*p*-Py-*H*), 5.88 (d, $^{3}J_{H–H}$ = 5.0 Hz, 1H, *o*/*m*-Py-*H*), 4.42 (sept, $^{3}J_{H–H}$ = 6.7 Hz, 1H, C*H*Me$_2$), 4.32 (sept, $^{3}J_{H–H}$ = 6.7 Hz, 1H, C*H*Me$_2$), 3.94 (sept, $^{3}J_{H–H}$ = 6.9 Hz, 1H, C*H*Me$_2$), 3.72 (sept, $^{3}J_{H–H}$ = 6.9 Hz, 1H, C*H*Me$_2$), 1.81 (s, 3H, N*Me*$_2$), 1.59 (d, $^{3}J_{H–H}$ = 6.4 Hz, 3H, CH*Me*$_2$), 1.56–1.48 (m, 12H, CH*Me*$_2$), 1.38 (s, 3H, N*Me*$_2$), 1.36–1.25 (m, overlapped with Si*Me*$_2$, 3H, CH*Me*$_2$), 1.33 (s, 3H, Si*Me*$_2$), 1.19 (d, $^{3}J_{H–H}$ = 6.6 Hz, 3H, CH*Me*$_2$), 0.74 (s, 3H, Si*Me*$_2$), 0.54 (s, 3H, Si*Me*$_2$), 0.27 (s, 3H, Si*Me*$_2$), –0.56 (d, $^{3}J_{H–H}$ = 6.5 Hz, 3H, CH*Me*$_2$) ppm. **^{13}C{^{1}H} NMR** (toluene-d_8, 213 K, 126 MHz): δ 166.6 (*C*N), 149.9 (Ar-*C*), 149.2 (Ar-*C*), 149.0 (Ar-*C*), 146.0 (Ar-*C*), 144.1 (Ar-*C*), 144.0 (*o*/*m*-Py-*C*), 142.5 (Ar-*C*), 137.1 (*m*/*p*-Py-*C*), 125.0 (overlapped with toluene-d_8, *o*/*m*-Py-*C*), 129.1 (*o*-C_6H_5), 128.2 (overlapped with toluene-d_8, *o*-C_6H_5), 122.0 (*m*/*p*-Py-*C*), 38.7 (N*Me*$_2$), 38.3 (N*Me*$_2$), 28.1 (CH*Me*$_2$), 28.1 (CH*Me*$_2$), 27.9 (*C*HMe$_2$), 27.8 (*C*HMe$_2$), 27.7 (*C*HMe$_2$), 26.9 (*C*HMe$_2$), 26.3 (CH*Me*$_2$), 26.0 (CH*Me*$_2$), 25.5 (CH*Me*$_2$), 25.0 (CH*Me*$_2$), 23.8 (CH*Me*$_2$), 22.1 (CH*Me*$_2$), 5.1 (Si*Me*$_2$), 4.3 (Si*Me*$_2$), 3.2 (Si*Me*$_2$), 2.4 (Si*Me*$_2$) ppm. Satisfactory CHN analysis could not be achieved due to the persistence of the starting materials in the reaction mixture.

7.5 Experimental details for Chapter Six

7.5.1 Synthesis of [(NON^{Dipp})ScCl$_2$][Li(THF)$_4$] (14)

A solution of (NON^{Dipp})Li$_2$ (0.265 g, 0.533 mmol) in diethyl ether (10 mL) was added dropwise to a stirring suspension of $ScCl_3(THF)_3$ (0.196 g, 0.533 mmol) in diethyl ether

(10 mL). The reaction mixture was stirred overnight to yield a pale brown solution with a white precipitate. The solution was filtered, and the volatiles were removed under vacuum. The product was then further extracted in benzene (3 × 10 mL) and dried under vacuum to afford [(NON^{Dipp})ScCl$_2$][Li(THF)$_4$] (**14**) as an off-white solid. Yield: 0.315 g (66%). Colourless crystals, suitable for single-crystal X-ray diffraction, were grown from slow evaporation of a THF/diethyl ether mixture (1:1) at 23 °C.

^{1}H NMR (THF-d_8, 298 K, 400 MHz): δ 6.85 (d, $^3J_{H–H}$ = 7.5 Hz, 4H, *m*-C$_6$*H*$_3$), 6.64 (t, $^3J_{H–H}$ = 7.5 Hz, 2H, *p*-C$_6$*H*$_3$), 4.05 (sept, $^3J_{H–H}$ = 6.9 Hz, 4H, C*H*Me$_2$), 3.67–3.60 (m, 16H, THF-OC*H*$_2$), 1.81–1.74 (m, 16H, THF-C*H*$_2$), 1.17 (d, $^3J_{H–H}$ = 6.8 Hz, 24H, CH*Me*$_2$), 0.21 (s, 12H, Si*Me*$_2$) ppm. **^{1}H NMR** (benzene-d_6, 298 K, 400 MHz): δ 7.13–7.07 (d, 4H, *m*-C$_6$*H*$_3$), 7.00 (t, $^3J_{H–H}$ = 7.6 Hz, 2H, *p*-C$_6$*H*$_3$), 4.25 (sept, $^3J_{H–H}$ = 6.8 Hz, 2H, C*H*Me$_2$), 3.79 (sept, $^3J_{H–H}$ = 6.8 Hz, 2H, C*H*Me$_2$), 3.66–3.52 (m (br), 8H, THF-OC*H*$_2$), 1.48 (d, $^3J_{H–H}$ = 6.8 Hz, 6H, CH*Me*$_2$), 1.46–1.36 (m, overlapped with CH*Me*$_2$, 8H, THF-C*H*$_2$), 1.33 (d, $^3J_{H–H}$ = 6.7 Hz, 6H, CH*Me*$_2$), 1.24 (d, $^3J_{H–H}$ = 6.9 Hz, 6H, CH*Me*$_2$), 1.18 (d, $^3J_{H–H}$ = 6.9 Hz, 6H, CH*Me*$_2$), 0.53 (s, 6H, Si*Me*$_2$), 0.37 (s, 6H, Si*Me*$_2$) ppm. **^{13}C{^{1}H} NMR** (THF-d_8, 298 K, 126 MHz): δ 147.9 (*i*-*C*$_6$H$_3$), 143.7 (*o*-*C*$_6$H$_3$), 123.2 (*m*-*C*$_6$H$_3$), 120.8 (*p*-*C*$_6$H$_3$), 68.4 (THF-O*C*H$_2$), 27.9 (CH*Me*$_2$), 27.9 (*C*HMe$_2$), 26.6 (THF-O*C*H$_2$), 24.7 (CH*Me*$_2$), 3.2 (Si*Me*$_2$) ppm. **^{45}Sc NMR** (THF-d_8, 298 K, 121 MHz): δ 395.7 ppm.

7.5.2 Synthesis of (NON^{tBu})ScCl(THF)$_2$ (15)

A solution of (NON^{tBu})Li$_2$ (0.419 g, 1.45 mmol) in diethyl ether (10 mL) was added dropwise to a stirring suspension of ScCl$_3$(THF)$_3$ (0.533 g, 1.45 mmol) in diethyl ether (10 mL). The reaction mixture was stirred overnight, resulting in a clear solution with a white precipitate. After removing the volatiles under vacuum, the product was extracted

in benzene (3 × 10 mL), and dried under vacuum to afford (NON$^{t\text{Bu}}$)ScCl(THF)$_2$ (**15**) as a white solid. Yield: 0.507 g (70%). Colourless crystals, suitable for single-crystal X-ray diffraction, were grown from slow evaporation of a THF/HMDSO mixture (4:1) at 23 °C.

^{1}H NMR (THF-d_8, 298 K, 400 MHz): δ 3.65–3.59 (m, 8H, THF-OCH_2), 1.78–1.74 (m, 8H, THF-CH_2), 1.17 (s, 18H, CMe_3), 0.17 (s, 12H, SiMe_2) ppm. **^{13}C{^{1}H} NMR** (THF-d_8, 298 K, 151 MHz): δ 68.4 (THF-*C*H$_2$), 52.4 (*C*Me$_3$), 36.4 (CMe_3), 26.5 (THF-*C*H$_2$), 6.2 (SiMe_2) ppm. **^{45}Sc NMR** (THF-d_8, 298 K, 121 MHz): δ 290.6 ppm. **CHN analysis** (%): Calculated for $C_{20}H_{46}ClN_2O_3ScSi_2$: C, 48.12; H, 9.29; N, 5.61. Found: C, 44.17; H, 9.09; N, 4.84.

7.5.3 Synthesis of K[(NON$^{t\text{Bu}}$)Sc(O-2,6-^{i}Pr-C$_6$H$_3$)$_2$] (16)

Potassium 2,6-di*iso*propylphenoxide (0.0433 g, 0.200 mmol) was added to a solution of (NON$^{t\text{Bu}}$)ScCl(THF)$_2$ (0.0499 g, 0.100 mmol) in THF (1 mL). The reaction mixture was sonicated for 15 minutes and allowed to react overnight. The supernatant was decanted, and the volatiles were removed under vacuum. The resulting brown solid was extracted in benzene (1 mL) and freeze-dried to afford K[(NON$^{t\text{Bu}}$)Sc(O-2,6-^{i}Pr-C$_6$H$_3$)$_2$] (**16**) as a pale brown solid. Yield: 0.0471 g (66%). Colourless crystals, suitable for single-crystal X-ray diffraction, were grown from slow evaporation of a THF/HMDSO mixture (4:1) at 23 °C.

^{1}H NMR (THF-d_8, 298 K, 600 MHz): δ 6.74 (d, $^3J_{H–H}$ = 7.5 Hz, 4H, *m*-C$_6H_3$), 6.40 (t, $^3J_{H–H}$ = 7.5 Hz, 2H, *p*-C$_6H_3$), 3.71 (sept, $^3J_{H–H}$ = 6.7 Hz, 4H, C*H*Me$_2$), 1.18 (s, 18H, CMe_3), 1.03 (d, $^3J_{H–H}$ = 6.9 Hz, 24H, CHMe_2), 0.06 (s, 12H, SiMe_2) ppm. **^{13}C{^{1}H} NMR** (THF-d_8, 298 K, 151 MHz): δ 160.2 (*i*-*C*$_6$H$_3$), 137.4 (*o*-*C*$_6$H$_3$), 122.4 (*m*-*C*$_6$H$_3$), 116.3

(*p*-C_6H_3), 49.9 (CMe$_3$), 34.2 (CMe_3), 27.5 (CHMe$_2$), 24.4 (CHMe_2), 2.8 (SiMe_2) ppm. **^{45}Sc NMR** (THF-d_8, 298 K, 121 MHz): δ 290.3 ppm.

7.5.4 Synthesis of [(NON^{Dipp})Sc(CH$_2$SiMe$_3$)$_2$][Li(THF)$_4$] (17)

A solution of LiCH$_2$SiMe$_3$ (0.0630 g, 0.669 mmol) in THF-d_8 (0.5 mL) was added to a solution of [(NON^{Dipp})ScCl$_2$][Li(THF)$_4$] (0.300 g, 0.335 mmol) in THF-d_8 (0.5 mL), and the reaction mixture was left to react overnight. After removing the volatiles under vacuum, the light pink solid was extracted in benzene (0.5 mL) and freeze-dried to afford [(NON^{Dipp})Sc(CH$_2$SiMe$_3$)$_2$][Li(THF)$_4$] (**17**) as a pink solid. Yield: 0.243 g (73%).

^{1}H NMR (THF-d_8, 298 K, 500 MHz): δ 6.85 (d, $^3J_{H–H}$ = 7.5 Hz, 4H, *m*-C$_6H_3$), 6.60 (t, $^3J_{H–H}$ = 7.6 Hz, 2H, *p*-C$_6H_3$), 4.17 (sept, $^3J_{H–H}$ = 6.7 Hz, 4H, CHMe$_2$), 1.24 (d, $^3J_{H–H}$ = 6.7 Hz, 12H, CHMe_2), 1.18 (d, $^3J_{H–H}$ = 6.8 Hz, 12H, CHMe_2), 0.15 (s, 12H, SiMe_2), –0.27 (s, 18H, SiMe_3), –0.55 (s (br), 4H, CH_2) ppm. **^{13}C{^{1}H} NMR** (THF-d_8, 298 K, 101 MHz): δ 149.2 (*i*-C_6H_3), 143.8 (*o*-C_6H_3), 123.4 (*m*-C_6H_3), 119.7 (*p*-C_6H_3), 27.7 (CHMe_2), 27.6 (CHMe$_2$), 26.0 (CHMe_2), 5.0 (SiMe_2), 4.4 (SiMe_3) ppm. δ (CH$_2$) was not observed. **^{45}Sc NMR** (THF-d_8, 298 K, 121 MHz): δ 578.8 ppm.

7.5.5 Synthesis of [(NON^{tBu})Sc(CH$_2$SiMe$_3$)$_2$][Li(THF)$_4$] (18)

A solution of LiCH$_2$SiMe$_3$ (0.0200 g, 0.212 mmol) in THF-d_8 (0.5 mL) was added to a solution of (NON^{tBu})ScCl(THF)$_2$ (0.0530 g, 0.106 mmol) in THF-d_8 (0.5 mL), and the reaction mixture was left to react overnight. After removing the volatiles under vacuum, the light pink solid was extracted in benzene (0.5 mL) and freeze-dried to afford [(NON^{tBu})Sc(CH$_2$SiMe$_3$)$_2$][Li(THF)$_4$] (**18**) as a pink solid. Yield: 0.0551 g (69%).

^{1}H NMR (THF-d_8, 298 K, 400 MHz): δ 3.66–3.59 (m, 16H, THF-OCH_2), 1.79–1.75 (m, 16H, THF-CH_2), 1.29 (s, 18H, CMe_3), 0.07 (s, 12H, SiMe_2), –0.09 (s, 18H, SiMe_3), –0.45 (s, 4H, CH_2) ppm. **^{45}Sc NMR** (THF-d_8, 298 K, 121 MHz): δ 589.5 ppm.

7.5.6 Attempted synthesis of (NON^{Dipp})Sc(CH$_2$SiMe$_3$)

$Sc(CH_2SiMe_3)_3(THF)_2$ (0.0198 g, 0.0440 mmol) was dissolved in either benzene-d_6 or THF-d_8 (0.5 mL) in a J. Young's tap NMR tube, and (NON^{Dipp})H_2 (0.0213 g, 0.0440 mmol) was added. ^{1}H NMR spectroscopy indicated that no reaction had taken place after 24 hours at room temperature, whereas heating the sample to 60 °C (in THF-d_8) or 70 °C (in benzene-d_6) resulted in the decomposition of $Sc(CH_2SiMe_3)_3(THF)_2$.

7.5.7 Synthesis of [(NON^{Dipp})Sc(BH$_4$)$_2$][Li(THF)$_4$)] (19)

(NON^{Dipp})Li_2 (0.0492 g, 0.0990 mmol) and freshly sublimed $Sc(BH_4)_3(THF)$ (0.0160 g, 0.0990 mmol) were each dissolved in THF-d_8 (0.5 mL) and combined in a J. Young NMR tube. The reaction mixture was heated at 50 °C for 72 hours to yield a brown solution with a grey precipitate. The supernatant was decanted, and the volatiles were removed under vacuum. The resulting brown solid was extracted in benzene (0.5 mL) and freeze-dried to afford [(NON^{Dipp})$Sc(BH_4)_2$][Li(THF)$_4$)] (**19**) as a pale brown solid. Yield: 0.0378 g (45%). Colourless crystals, suitable for single-crystal X-ray diffraction, were grown from slow evaporation of a THF/HMDSO mixture (4:1) at 23 °C.

^{1}H NMR (THF-d_8, 298 K, 400 MHz): δ 6.83 (d, $^{3}J_{H–H}$ = 7.5 Hz, 4H, *m*-C_6H_3), 6.62 (t, $^{3}J_{H–H}$ = 7.5 Hz, 2H, *p*-C_6H_3), 4.08 (sept, $^{3}J_{H–H}$ = 6.7 Hz, 4H, C*H*Me$_2$), 1.16 (d, $^{3}J_{H–H}$ = 6.7 Hz, 24H, CHMe_2), 0.17 (s, 12H, SiMe_2) ppm. **^{13}C{^{1}H} NMR** (THF-d_8, 298 K, 101 MHz): δ 149.4 (*i*-C_6H_3), 143.9 (*o*-C_6H_3), 123.4 (*m*-C_6H_3), 120.5 (*p*-C_6H_3),

27.5 (*C*HMe$_2$), 25.5 (CH*Me*$_2$), 3.5 (Si*Me*$_2$) ppm. **^{11}B NMR** (THF-d_8, 298 K, 160 MHz): δ –25.7 (pent, $^1J_{B–H}$ = 76.0 Hz) ppm. **^{1}H{^{11}B} NMR** (THF-d_8, 298 K, 500 MHz): δ 6.83 (d, $^3J_{H–H}$ = 7.5 Hz, 4H, *m*-C$_6$*H*$_3$), 6.63 (t, $^3J_{H–H}$ = 7.5 Hz, 2H, *p*-C$_6$*H*$_3$), 4.08 (sept, $^3J_{H–H}$ = 6.7 Hz, 4H, C*H*Me$_2$), 1.16 (d, $^3J_{H–H}$ = 6.7 Hz, 24H, CH*Me*$_2$), 0.50 (s (br), 8H, B*H*$_4$), 0.18 (s, 12H, Si*Me*$_2$) ppm. **IR** (KBr): 2963, 2925, 2869, 2291, 2225, 1465, 1431, 1315, 1253, 945, 920, 404 cm^{-1}.

7.6 References

1. W. Clegg, N. A. Compton, R. J. Errington, G. A. Fisher, M. E. Green, D. C. R. Hockless and N. C. Norman, *Inorg. Chem.*, 1991, **30**, 4680-4682.
2. H. Peng, J. Ling, Y. Zhu, L. You and Z. Shen, *J. Polym. Sci., Part A: Polym. Chem.*, 2012, **50**, 3016-3029.
3. N. Ibrahim, M. H. Vilhelmsen, M. Pernpointner, F. Rominger and A. S. K. Hashmi, *Organometallics*, 2013, **32**, 2576-2583.
4. M. F. Lappert and R. Pearce, *J. Chem. Soc., Chem. Commun.*, 1973, 126-126.
5. M. D. Anker, M. Lein and M. P. Coles, *Chem. Sci.*, 2019, **10**, 1212-1218.
6. M. J. Monreal, R. K. Thomson, T. Cantat, N. E. Travia, B. L. Scott and J. L. Kiplinger, *Organometallics*, 2011, **30**, 2031-2038.
7. V. Ripert, L. G. Hubert-Pfalzgraf and J. Vaissermann, *Polyhedron*, 1999, **18**, 1845-1851.
8. J. T. Cosier and A. Glazer, *J. Appl. Crystallogr.*, 1986, **19**, 105-107.
9. *CrysAlisPRO*, Oxford Diffraction / Agilent Technologies UK Ltd, 2013.
10. A. Altomare, G. Cascarano, C. Giacovazzo and A. Guagliardi, *J. Appl. Crystallogr.*, 1993, **26**, 343-350.
11. L. Palatinus and G. Chapuis, *J. Appl. Crystallogr.*, 2007, **40**, 786-790.
12. G. M. Sheldrick, *Acta Crystallogr., Sect. C: Struct. Chem.*, 2015, **71**, 3-8.
13. L. J. Farrugia, *J. Appl. Crystallogr.*, 2012, **45**, 849-854.
14. P. W. Betteridge, J. R. Carruthers, R. I. Cooper, K. Prout and D. J. Watkin, *J. Appl. Crystallogr.*, 2003, **36**, 1487-1487.
15. A. Spek, *J. Appl. Crystallogr.*, 2003, **36**, 7-13.
16. L. J. Farrugia, *J. Appl. Crystallogr.*, 1997, **30**, 565-565.
17. J. R. Dorgan, J. Janzen, D. M. Knauss, S. B. Hait, B. R. Limoges and M. H. Hutchinson, *J. Polym. Sci., Part B: Polym. Phys.*, 2005, **43**, 3100-3111.
18. M. Haddad, M. Laghzaoui, R. Welter and S. Dagorne, *Organometallics*, 2009, **28**, 4584-4592.

19. D. B. Leznoff, G. Mund, K. C. Jantunen, P. H. Bhatia, A. J. Gabert and R. J. Batchelor, *J. Nucl. Sci. Technol.*, 2002, **39**, 406-409.

20. N. A. H. Male, M. Thornton-Pett and M. Bochmann, *J. Chem. Soc., Dalton Trans.*, 1997, 2487-2494.

21. R. J. Schwamm, J. R. Harmer, M. Lein, C. M. Fitchett, S. Granville and M. P. Coles, *Angew. Chem. Int. Ed.*, 2015, **54**, 10630-10633.

22. J. Coudane, C. Ustariz-Peyret, G. Schwach and M. Vert, *J. Polym. Sci., Part A: Polym. Chem.*, 1997, **35**, 1651-1658.

Chapter 8

Conclusions

The research discussed in this Thesis has covered two main topics: firstly, the development of new di(amido)siloxane complexes containing relatively non-toxic bismuth and scandium metal centres, and secondly, the investigation of the reactivity of the bismuth complexes in the ROP of cyclic esters and in small molecule activation reactions.

i) Novel di(amido)siloxane bismuth complexes

A new family of di(amido)siloxane bismuth complexes has been developed, incorporating a variety of substitution patterns of the initiating group and the supporting ligand structure. Di(amido)siloxane bismuth aryloxide and alkoxide compounds were prepared by salt-metathesis reactions using the related bismuth chloride complexes as precursors. Alternatively, a straightforward protonolysis route was employed for the synthesis of di(amido)siloxane bismuth amide. All six new complexes were characterised by multinuclear NMR spectroscopy, and in most cases, IR spectroscopy, single-crystal X-ray diffraction, and elemental analysis.

ii) Di(amido)siloxane bismuth aryloxide and alkoxide complexes as active ROP initiators

Di(amido)siloxane bismuth aryloxide and alkoxide complexes (NON^{R})Bi(OR') (R = Dipp, R' = OC_6H_5 (**1**), O-2,6-Me-C_6H_3 (**2**), O-2,6-^{i}Pr-C_6H_3 (**3**), ^{t}Bu (**4**); R = ^{t}Bu, R' = O-2,6-Me-C_6H_3 (**5**)) were found to be active for the ROP of lactide and ε-caprolactone monomers. Variations in both the steric profile of the supporting ligand and the initiating group, as well as the Lewis acidity of the active site, had a significant impact on polymerisation rates and control.

The polymerisation of lactide displayed notable induction periods, most pronounced using bismuth complexes with sterically bulky initiating groups. This induction period was attributed to the rate-limiting step of the first monomer insertion, followed by faster subsequent insertion steps. While the nature of the initiating group did not significantly influence propagation activity, an enhanced rate was achieved by introducing a less sterically demanding and more electron-donating substituent on the ligand backbone.

The ROP of cyclic ester monomers was proposed to follow a typical coordination-insertion mechanism with a first-order dependency with respect to both monomer and initiator concentrations. All initiators demonstrated moderate polymerisation control ($Đ_M$ = 1.33–1.85), coupled with limited stereocontrol in the case of *rac*- and *meso*-lactide polymerisation. Although these observations are common for large ionic radii metal initiators, further optimisation of initiator performance could be achieved through fine-tuning of the ligand backbone. Possible modifications of the amido substituents include the use of groups with varying steric demands, such as phenyl, 2,6-dimethylphenyl, and 2,6-di-*tert*-butylphenyl, or electronic properties, including

2,6-difluorophenyl and 2,6-dichlorophenyl groups. In addition, a larger steric bulk could be achieved by introducing phenyl groups on the siloxane backbone. Based on previously reported ROP studies, increasing the steric bulk of the ancillary ligand may enhance stereocontrol; however, this could potentially compromise polymerisation kinetics. A systematic analysis of di(amido)siloxane bismuth complexes with varying steric and electronic properties for further polymerisation studies of lactide and lactone monomers would contribute to elucidating the structure-activity relationships in the relatively underexplored bismuth ROP initiators.

iii) Di(amido)siloxane bismuth amide as an active ROP initiator

Di(amido)siloxane bismuth amide (NON^{Dipp})Bi(NMe_2) (**6**) proved to be a more active initiator than its aryloxide and alkoxide counterparts. When used in the ROP of *L*-lactide, it led to an approximately four-fold increase in the observed rate compared to the aryloxide initiator **2** under the same reaction conditions, while maintaining relatively good polymerisation control ($Đ_M$ = 1.36). The proposed lability of the Bi-N bond facilitated a rapid insertion of the first lactide monomer unit, thereby resulting in the absence of an induction period. Analogous to the aryloxide and alkoxide initiators, polymerisation occurred *via* a coordination-insertion mechanism, leading to the formation of $-NMe_2$ terminated PLA.

The ROP of *meso*-lactide afforded heterotactic-enriched PLA (P_m = 0.86), likely formed *via* a chain-end controlled mechanism. In contrast, atactic PLA was produced in the ROP of *rac*-lactide, consistent with significantly lower levels of polymerisation control ($Đ_M$ = 2.07). In a broader context, the relatively moderate activity of **6** compared to other main group and rare-earth amide initiators can be attributed to a combination of factors,

including the modest Lewis acidity of bismuth, steric constraints, and possible aggregation of the system.

The di(amido)siloxane bismuth lactate compound **7** was prepared in an equimolar reaction between **6** and *L*-lactide. Kinetic and mechanistic studies suggested that **7** is formed as an active propagating species in the polymerisation of lactide in the presence of **6** as the initiator. The insertion activity of **6** was also investigated for ε-caprolactone and γ-butyrolactone monomers, resulting in the formation of stable and isolable bismuth compounds featuring ring-opened chelating lactone ligands.

The polymerisation of ε-caprolactone exhibited an induction period and proceeded three times slower with respect to *L*-lactide. In contrast, initiator **6** was completely inactive towards the ROP for γ-butyrolactone. These results imply that several factors, such as the thermodynamic stability of the monomer, the lability of the initiating group, and the chelate effect of the cyclic ester insertion product, are crucial in determining the ROP capability of the initiator.

The reactivity of **6** towards the ring-opening of these lactide and lactone substrates offers the potential for insertion reactions using a wider range of polar monomers, including *rac*-β-butyrolactone and δ-valerolactone. Studying the resulting compounds as model catalytic intermediates could provide new mechanistic insights into ROP processes. Furthermore, structural modifications of the di(amido)siloxane ligand backbone could be used to optimise the ROP activity of bismuth chelate compounds. For example, reducing the steric bulk of the amido groups may decrease chelate stability, potentially leading to faster propagation. Finally, the differing reactivities of the cyclic ester insertion products could be explored in copolymerisation reactions for block polyester formation.

iv) Small molecule activation using a di(amido)siloxane bismuth amide complex

In addition to the insertion reactivity with lactide and lactone compounds, bismuth amide **6** demonstrated activity towards a variety of unsaturated electrophilic substrates. Its reactions with electrophilic and relatively unhindered heteroallenes: carbon dioxide, carbon disulfide, and phenyl isocyanate, proceeded rapidly at room temperature, yielding three new insertion products **10**–**12**. Consistent with related literature examples, their molecular structures indicated the presence of delocalised π electron density within carbamate, dithiocarbamate, and ureato ligands, bound to the bismuth centre in an asymmetric κ^2-bidentate or κ^1-monodentate bonding mode.

Using 2-benzoylpyridine, a less electrophilic and more sterically bulky ketone, the addition across the Bi-N was found to be reversible. ^{1}H NMR spectroscopic studies of the reaction product **13** indicated the occurrence of energetically accessible room-temperature fluxionality, proposed to involve the cleavage and recombination of the bonding between the inserted amino alkoxide unit and the bismuth centre. In the solid state, the structures of all four new insertion products displayed variations in bond lengths and angles based on the steric profile of the inserted unit, hence highlighting the conformational flexibility of the di(amido)siloxane ligand.

v) Novel di(amido)siloxane scandium complexes

The di(amido)siloxane ligand was successfully employed as a platform for the development of new scandium complexes. Using a salt-metathesis route, two different di(amido)siloxane scandium chloride compounds were prepared: “ate” complex **14** and neutral compound **15**, both serving as precursors for further ligand substitution reactions.

Subsequent salt-metathesis reactions using these compounds afforded scandium *bis*(aryloxide) (**16**) and *bis*(alkyl) (**17**) "ate" derivatives. In addition, a scandium *bis*(borohydride) complex (**18**) was prepared, representing a rare example of a structurally characterised "ate" borohydride compound.

In light of the structural diversity observed in the new bismuth complexes described in this Thesis, the incorporation of a smaller and more electrophilic scandium metal centre further highlighted the versatility of the di(amido)siloxane ligand. While the solid-state structures of these bismuth complexes revealed a κ^2-*N*,*N'*-bound di(amido)siloxane ligand in conformations ranging from chair to twist-boat, the scandium counterparts adopted a boat conformation, with the ligand coordinated to the more oxophilic scandium metal in a κ^3-*N*,*O*,*N'*-tridentate bonding mode. Variation of the steric and electronic profile of these di(amido)siloxane scandium systems could be pursued to target the formation of salt-free structures, with the goal of developing efficient ROP initiators.

Appendix

Supplementary Data for Chapters 2–6

A.1 Appendix for Chapter Two

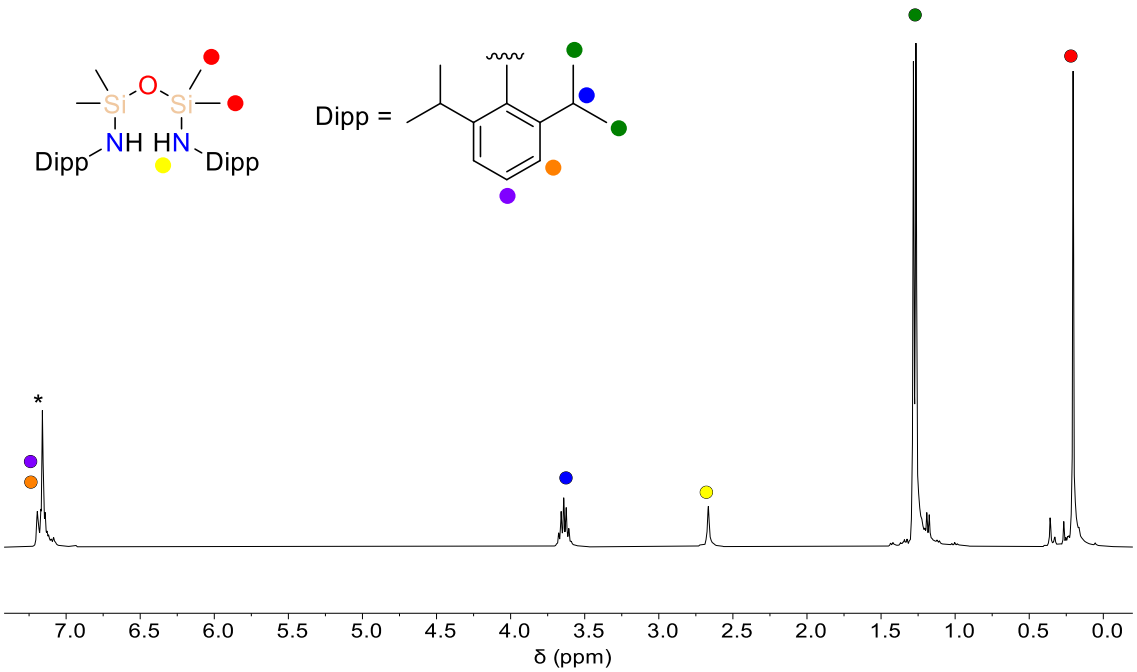


Figure A.1.1 ^{1}H NMR spectrum (*benzene-d_6, 600 MHz, 298 K) of $(NON^{Dipp})H_2$.

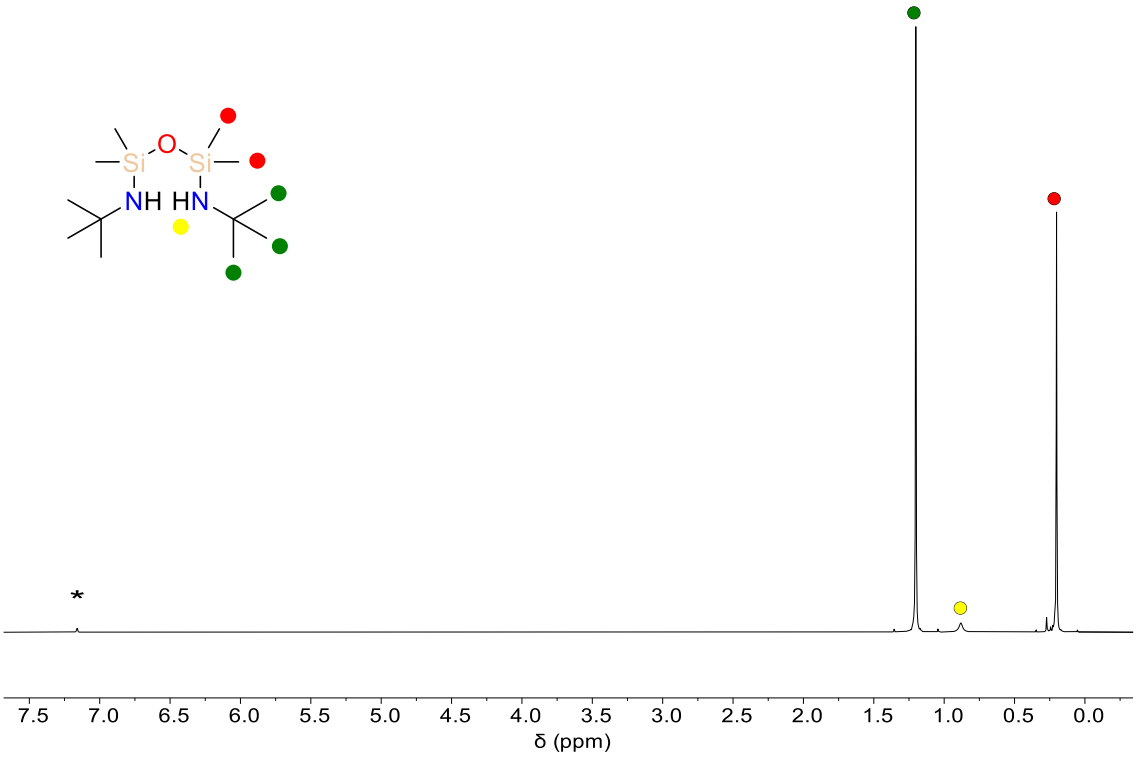


Figure A.1.2 ^{1}H NMR spectrum (*benzene-d_6, 400 MHz, 298 K) of (NON$^{t\text{Bu}}$)H$_2$.

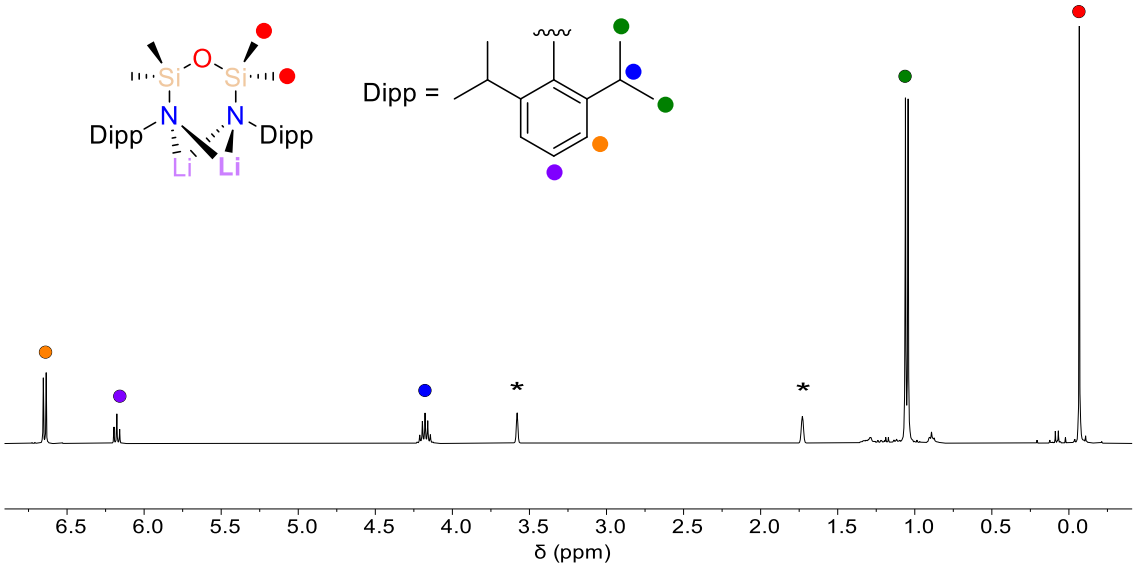


Figure A.1.3 ^{1}H NMR spectrum (*THF-d_8, 400 MHz, 298 K) of (NON^{Dipp})Li$_2$.

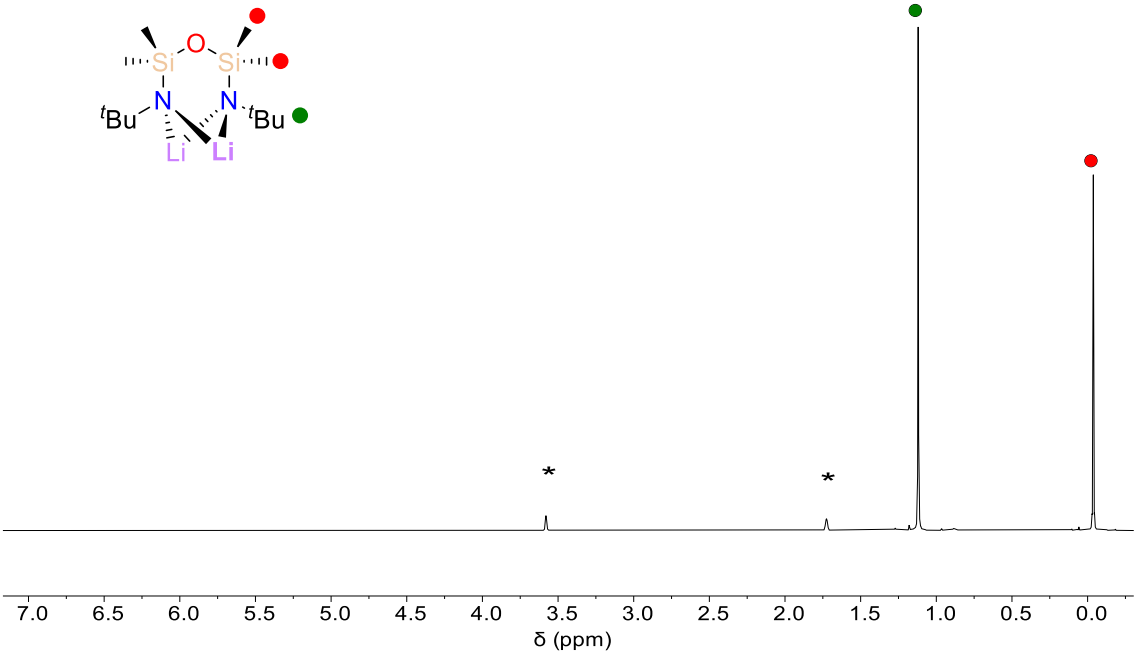


Figure A.1.4 ^{1}H NMR spectrum (*THF-d_8, 400 MHz, 298 K) of (NON^{tBu})Li$_2$.

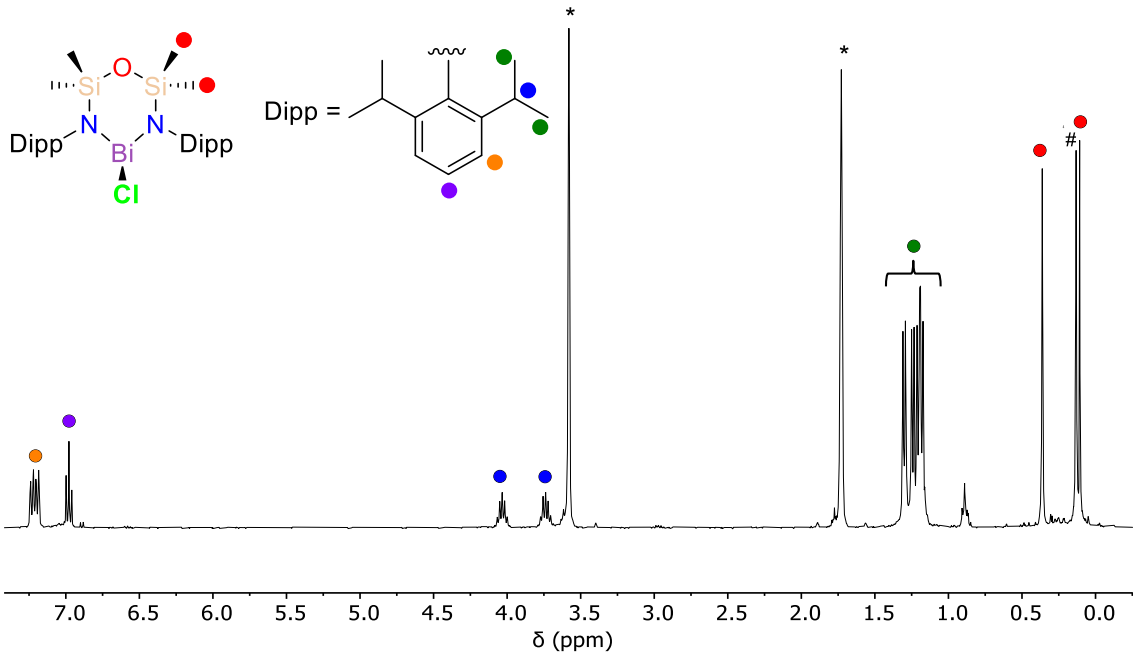


Figure A.1.5 ^{1}H NMR spectrum (*THF-d_8, 400 MHz, 298 K) of (NON^{Dipp})BiCl. # represents grease.

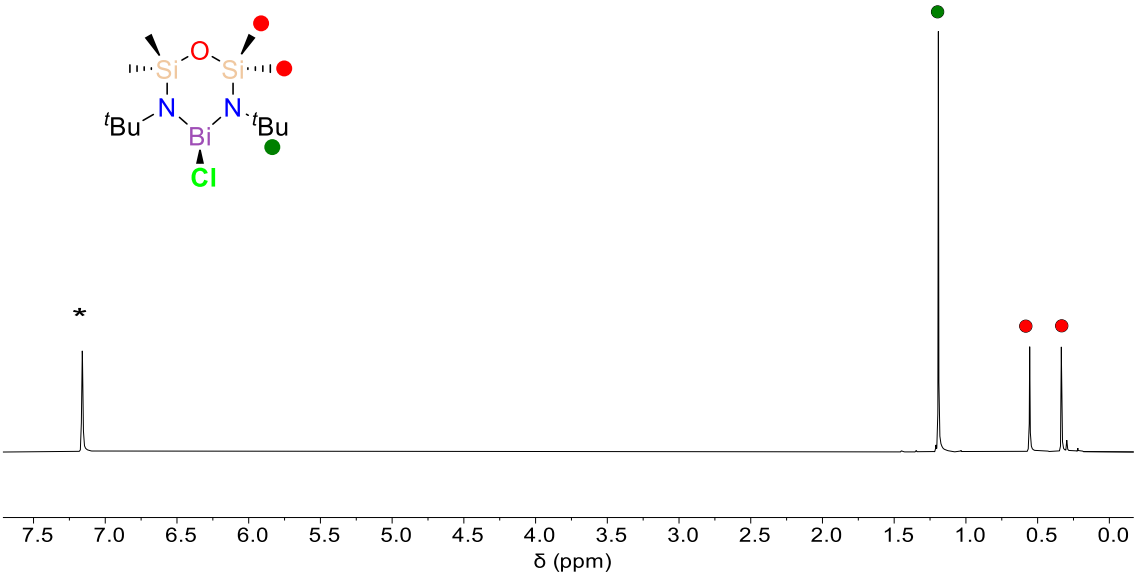


Figure A.1.6 ^{1}H NMR spectrum (*benzene-d_6, 400 MHz, 298 K) of (NON$^{t\text{Bu}}$)BiCl.

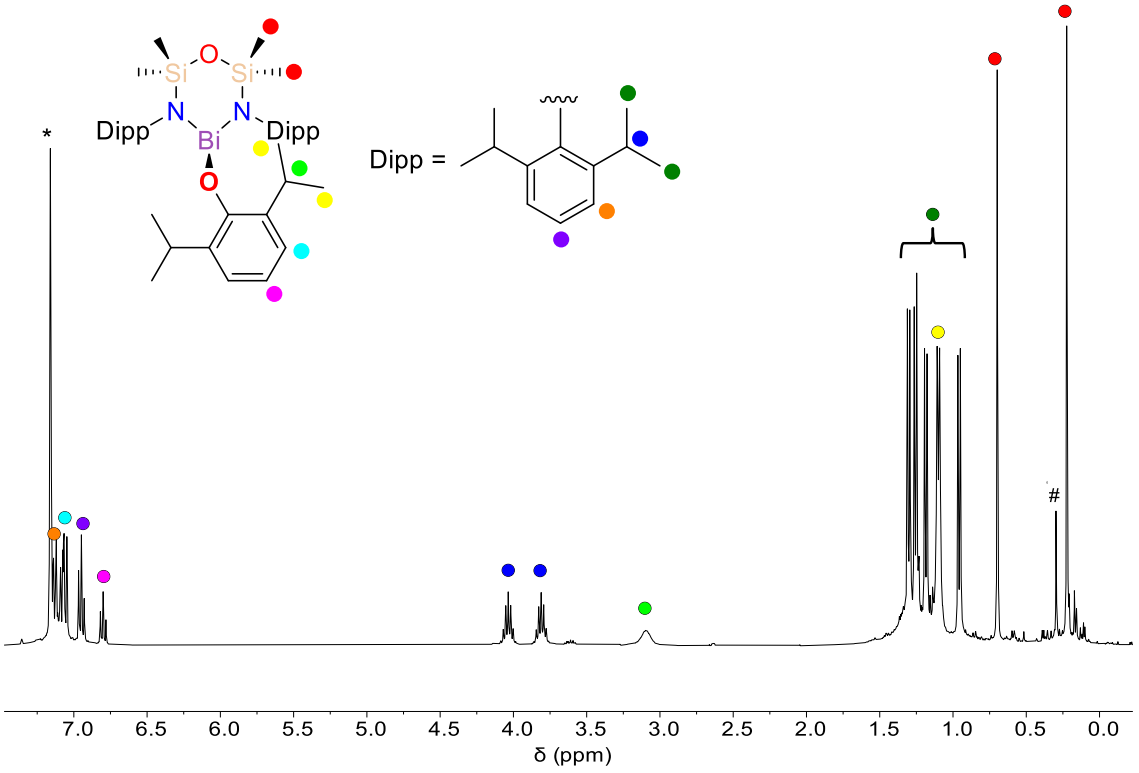


Figure A.1.7 ^{1}H NMR spectrum (*benzene-d_6, 600 MHz, 298 K) of (NON$^{\text{Dipp}}$)Bi(O-2,6-^{i}Pr-C_6H_3) (**3**). # represents grease.

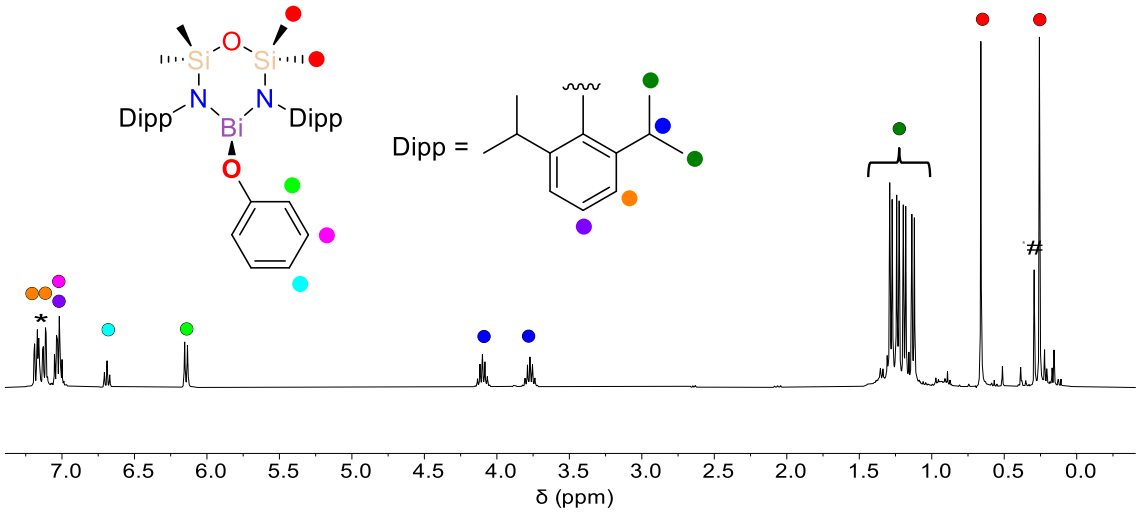


Figure A.1.8 ^{1}H NMR spectrum (*benzene-d_6, 400 MHz, 298 K) of (NON^{Dipp})Bi(OC_6H_5) (**1**).

represents grease.

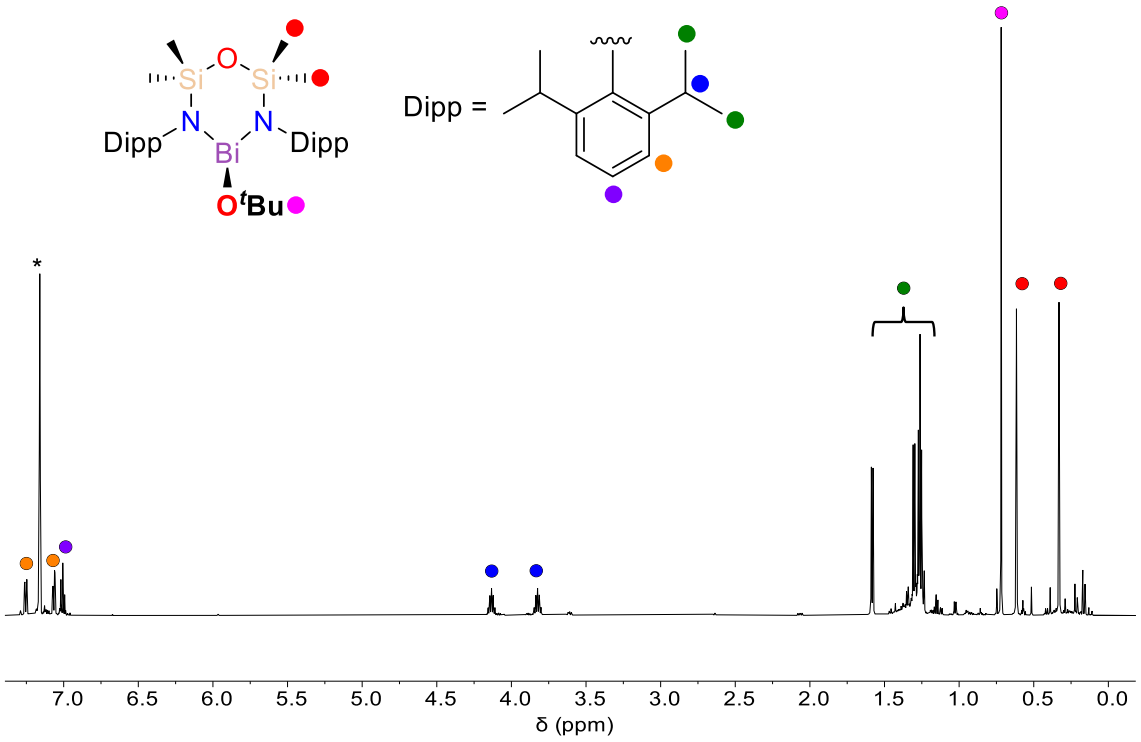


Figure A.1.9 ^{1}H NMR spectrum (*benzene-d_6, 600 MHz, 298 K) of (NON^{Dipp})Bi(O^{t}Bu) (**4**).

A.2 Appendix for Chapter Three

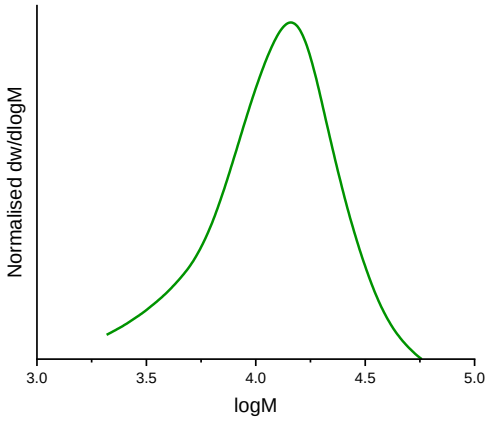


Figure A.2.1 GPC plot of the PLA produced using **5** (M_n = 5 424 g mol^{-1}, $Đ_M$ = 1.56). Polymerisation conditions: benzene-d_6, 70 °C, [*L*-LA]$_0$/[Bi]$_0$ = 50:1, and [*L*-LA]$_0$ = 0.5 M.

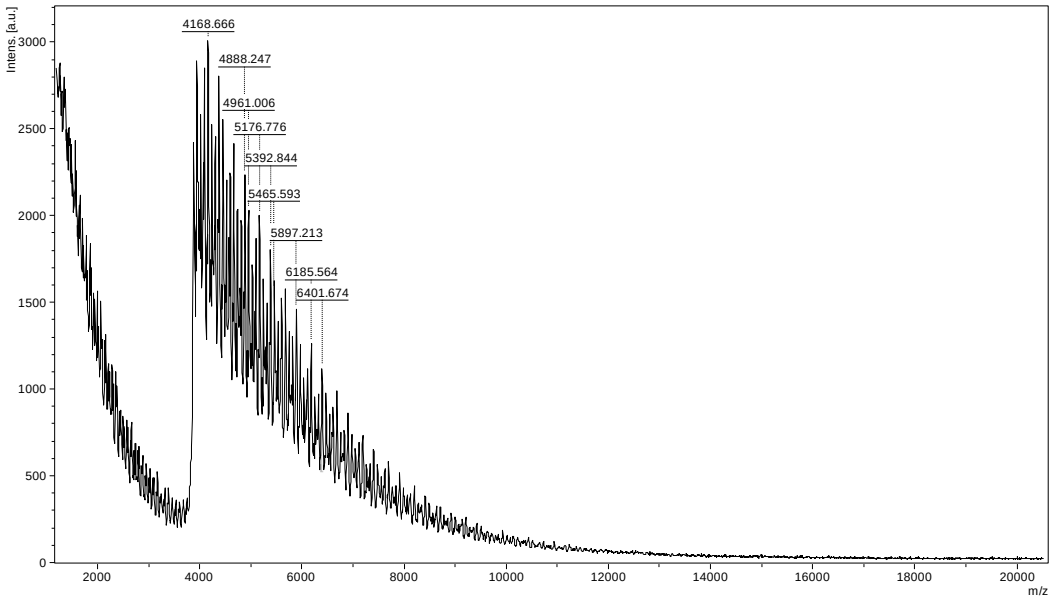


Figure A.2.2 MALDI-ToF mass spectrum of the PLLA produced using **1**. Polymerisation conditions: benzene-d_6, 70 °C, [*L*-LA]$_0$/[Bi]$_0$ = 50:1, [*L*-LA]$_0$ = 0.5 M.

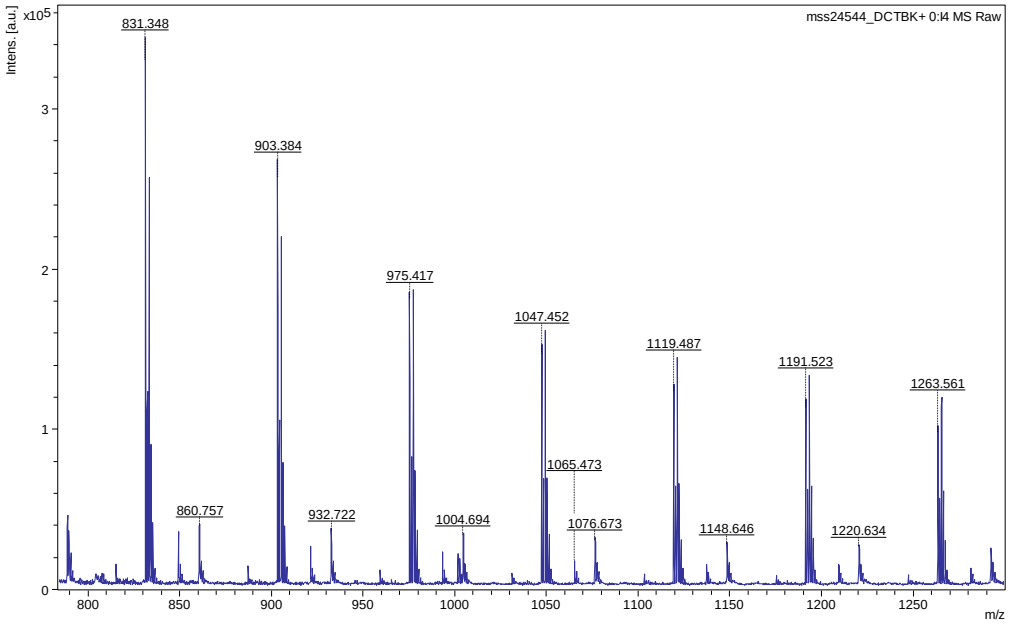


Figure A.2.3 MALDI-ToF mass spectrum of the PLLA produced using **4**. Polymerisation conditions: benzene-d_6, 70 °C, $[L\text{-LA}]_0/[\text{Bi}]_0$ = 25:1, $[L\text{-LA}]_0$ = 0.5 M.

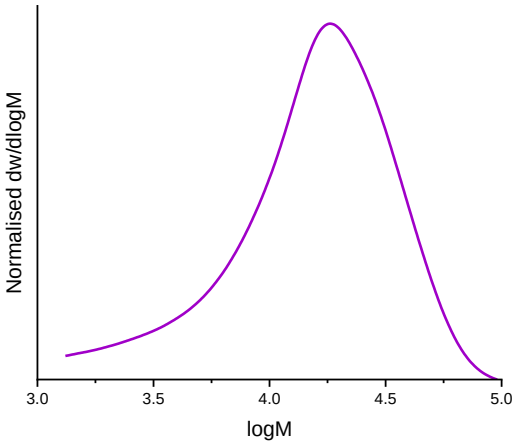


Figure A.2.4 GPC plot of the PCL produced using **2** (M_n = 5 874 g mol^{-1}, $Đ_M$ = 1.89). Polymerisation conditions: benzene-d_6, 70 °C, $[\varepsilon\text{-CL}]_0/[\text{Bi}]_0$ = 50:1, and $[\varepsilon\text{-CL}]_0$ = 0.5 M.

A.3 Appendix for Chapter Four

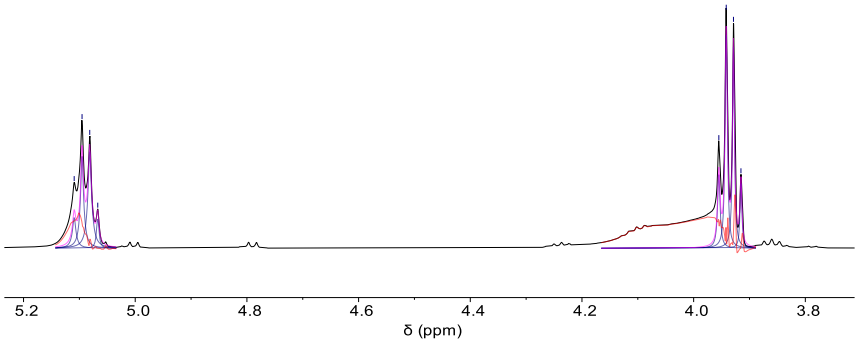


Figure A.3.1 ^{1}H NMR spectrum (*benzene-d_6, 600 MHz, 298 K) for the polymerisation of *L*-lactide using **6**, demonstrating the deconvoluted *methine* proton regions. Polymerisation conditions: benzene-d_6, 50 °C, $[L\text{-LA}]_0/[\text{Bi}]_0$ = 50:1, $[L\text{-LA}]_0$ = 0.5 M.

The deconvolution of ^{1}H NMR spectra was carried out using MestReNova software. Manual line fitting was performed on monomer and polymer *methine* proton regions. Monomer percentage conversion was calculated as a relative ratio of the area under the fitted lines corresponding to monomer and polymer *methine* resonances.

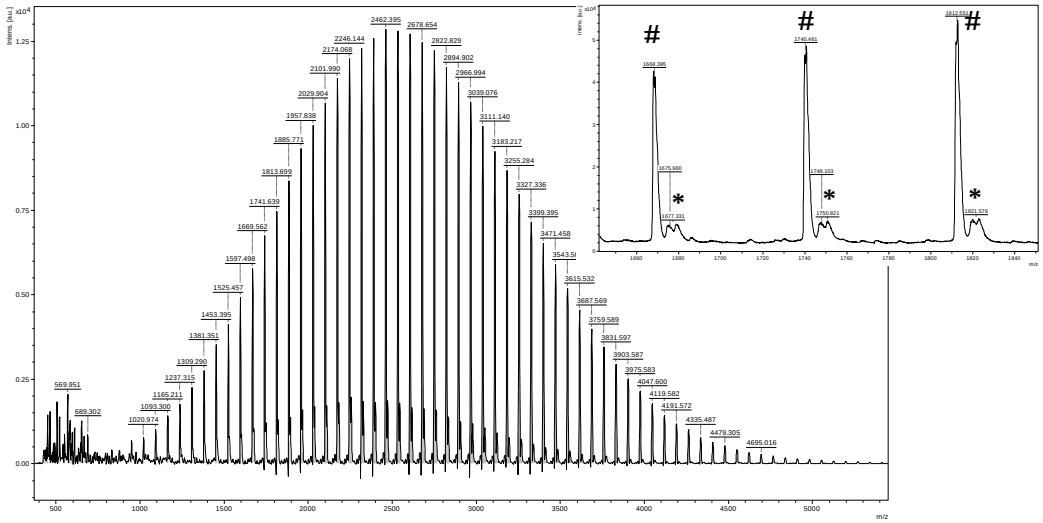


Figure A.3.2 MALDI-ToF mass spectrum of the PLA produced from the ROP of *rac*-LA using **6**. Polymerisation conditions: benzene-d_6, 50 °C, $[rac\text{-LA}]_0/[\text{Bi}]_0$ = 50:1, $[rac\text{-LA}]_0$ = 0.5 M. # represents α–NMe_2/ω–OH terminated PLLA. * represents unknown species.

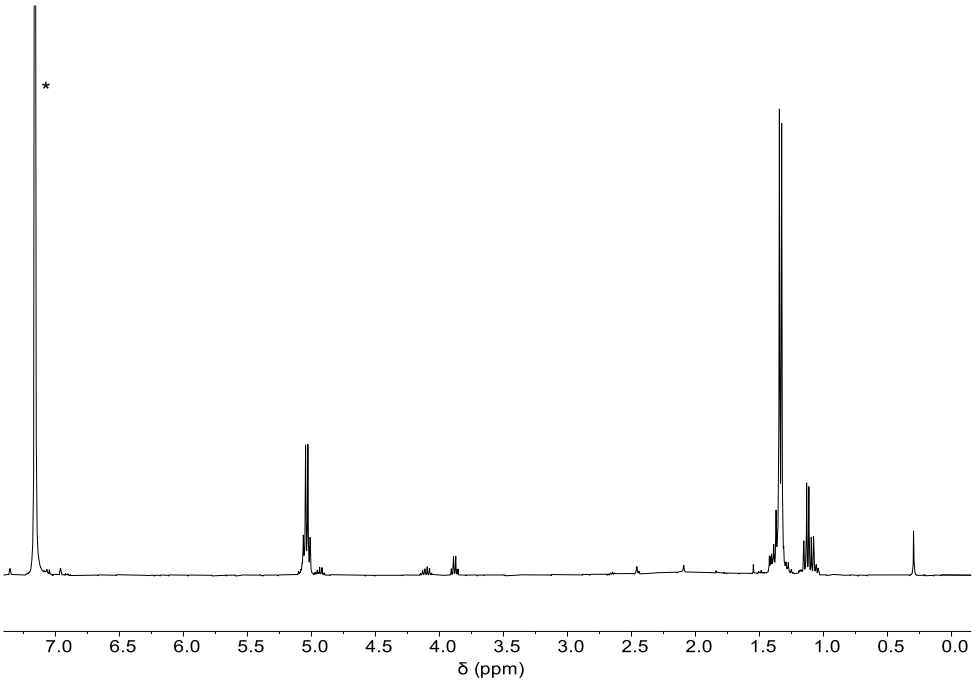


Figure A.3.3 ^{1}H NMR spectrum (*benzene-d_6, 600 MHz, 298 K) of the PLLA produced using **6**. Polymerisation conditions: benzene-d_6, 50 °C, $[L\text{-LA}]_0/[\text{Bi}]_0$ = 50:1, $[L\text{-LA}]_0$ = 0.5 M.

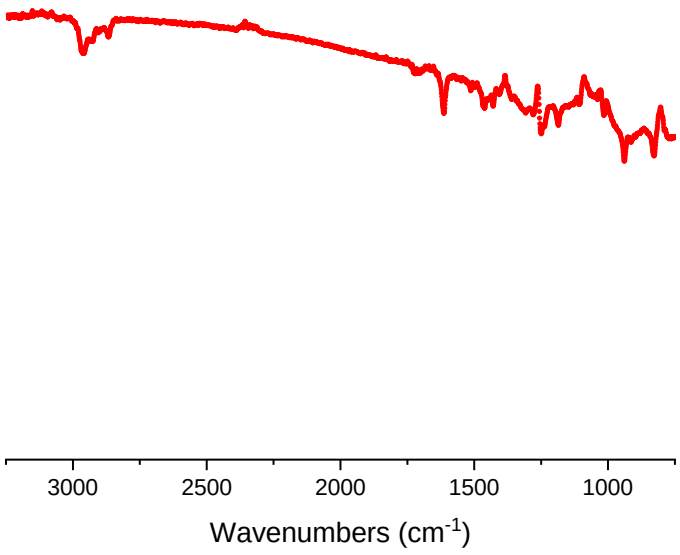


Figure A.3.4 IR (KBr) spectrum of (NON^{Dipp})Bi(OCH(Me)C(O)NMe_2) (**7**).

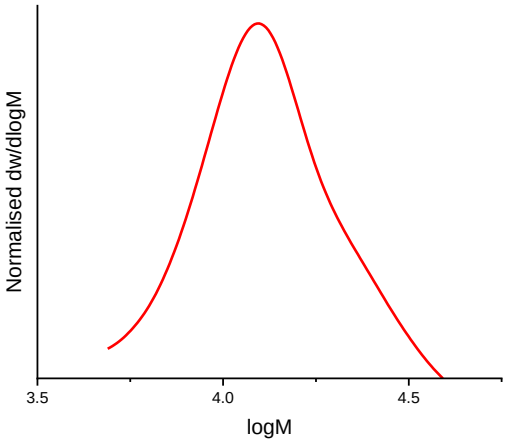


Figure A.3.5 GPC plot of the PLA produced using **7** (M_n = 6 914 g mol^{-1}, $Đ_M$ = 1.20). Polymerisation conditions: benzene-d_6, 50 °C, [*L*-LA]$_0$/[Bi]$_0$ = 50:1, and [*L*-LA]$_0$ = 0.5 M.

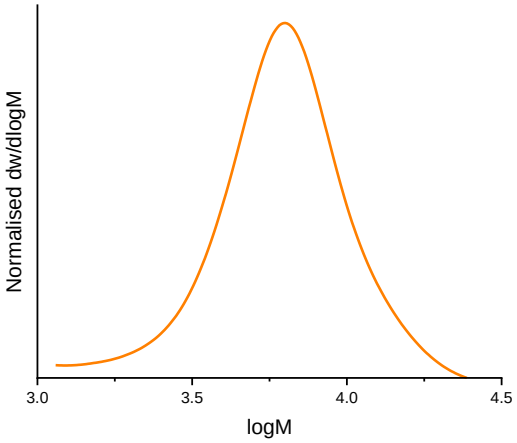


Figure A.3.6 GPC plot of the PCL produced using **6** (M_n = 2 928 g mol^{-1}, $Đ_M$ = 1.32). Polymerisation conditions: benzene-d_6, 50 °C, [ε-CL]$_0$/[Bi]$_0$ = 50:1, and [ε-CL]$_0$ = 0.5 M.

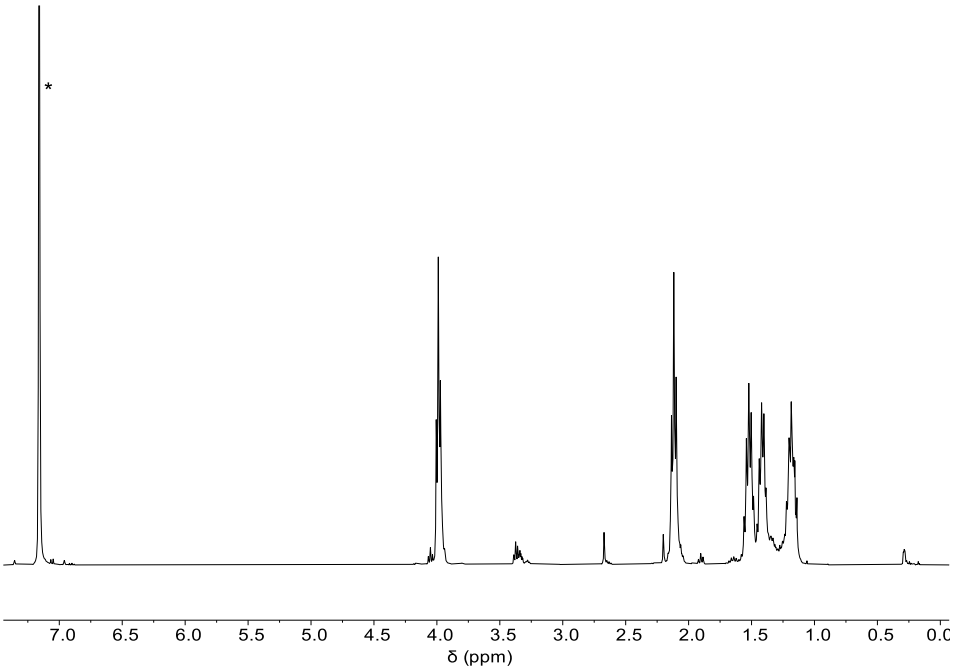


Figure A.3.7 ^{1}H NMR spectrum (*benzene-d_6, 600 MHz, 298 K) of the PCL produced using **6**. Polymerisation conditions: benzene-d_6, 50 °C, $[\varepsilon\text{-CL}]_0/[\text{Bi}]_0 = 50{:}1$, $[\varepsilon\text{-CL}]_0 = 0.5$ M.

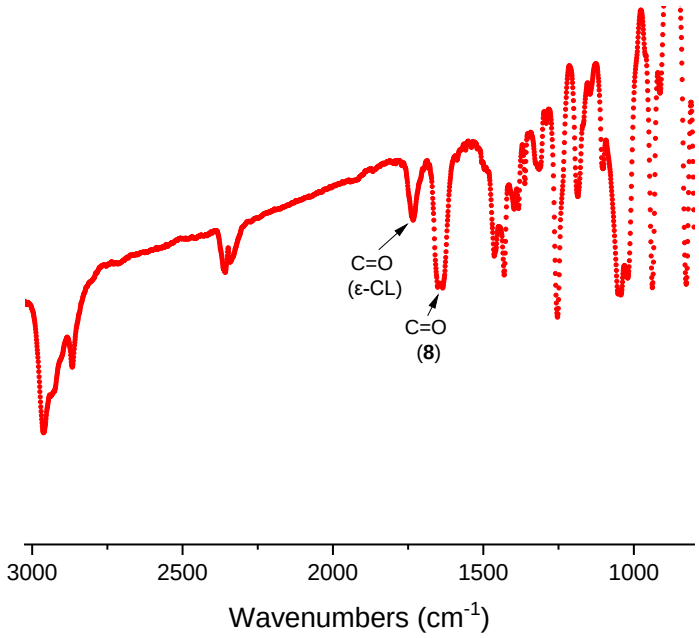


Figure A.3.8 IR (KBr) spectrum of (NON^{Dipp})Bi($OC_5H_{10}C(O)NMe_2$) (**8**).

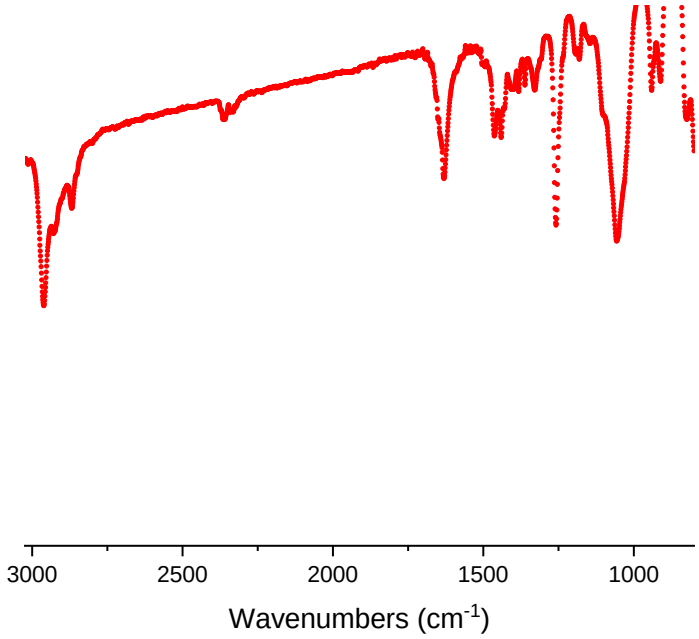


Figure A.3.9 IR (KBr) spectrum of (NON^{Dipp})Bi($OC_3H_6C(O)NMe_2$) (**9**).

A.4 Appendix for Chapter Five

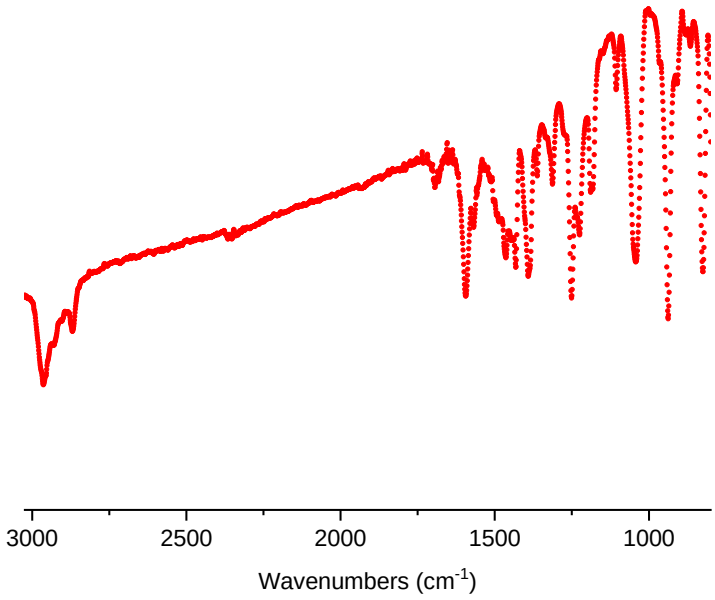


Figure A.4.1 IR (KBr) spectrum of (NON^{Dipp})Bi(CO_2NMe_2) (**10**).

A.5 Appendix for Chapter Six

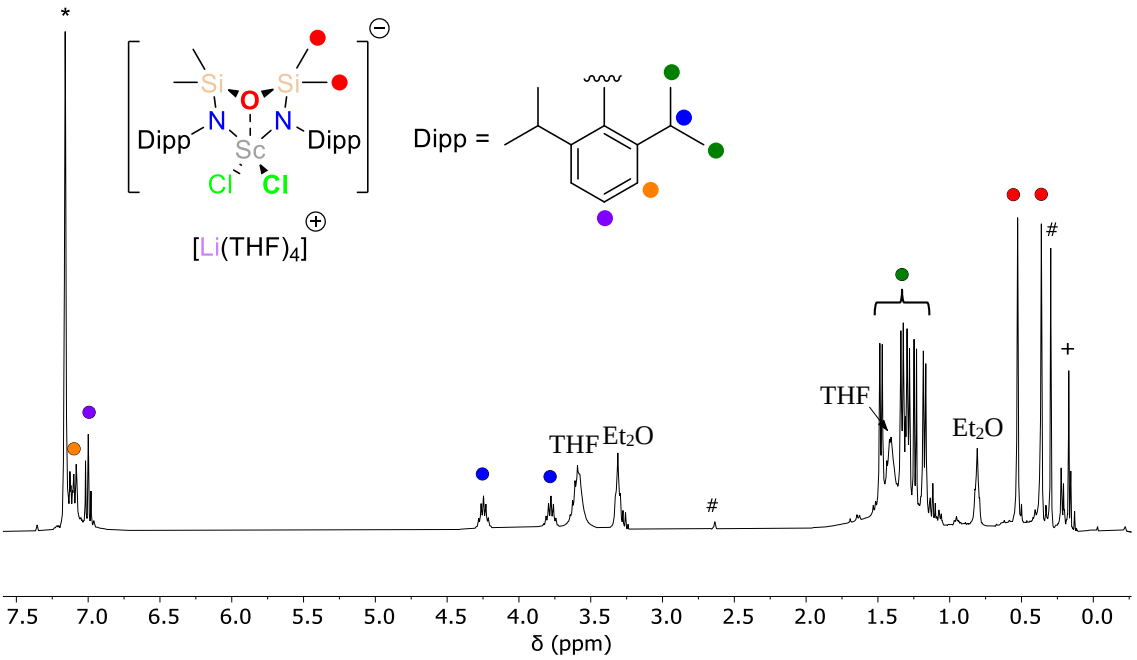


Figure A.5.1 ^{1}H NMR spectrum (*benzene-d_6, 400 MHz, 298 K) of $[(NON^{Dipp})ScCl_2][Li(THF)_4]$ (**14**). # and + represent grease and pro-ligand, respectively.

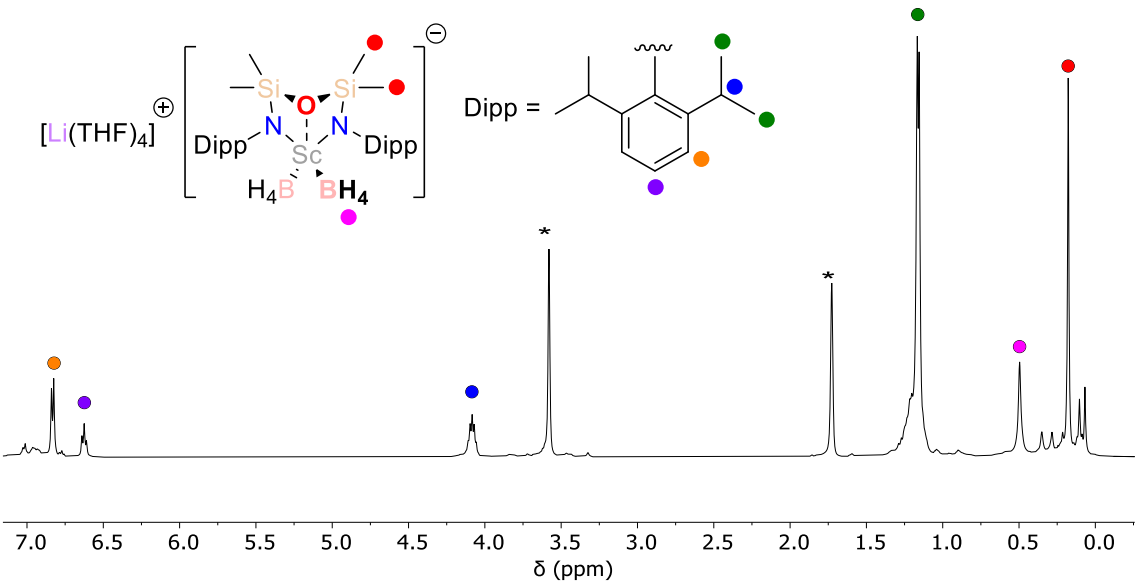


Figure A.5.2 ^{1}H{^{11}B} NMR spectrum (*THF-d_8, 500 MHz, 298 K) of $[(NON^{Dipp})Sc(BH_4)_2][Li(THF)_4)]$ (**19**).

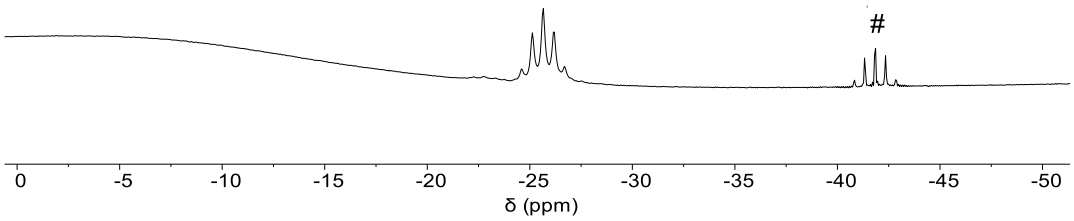


Figure A.5.3 ^{11}B NMR spectrum (*THF-d_8, 160 MHz, 298 K) of [(NON^{Dipp})Sc(BH$_4$)$_2$][Li(THF)$_4$)] (**19**). # represents residual Sc(BH$_4$)$_3$(THF).

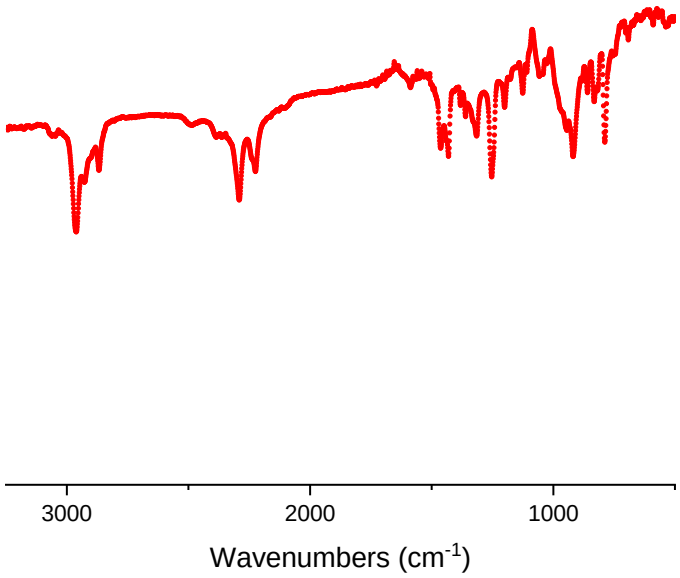


Figure A.5.4 IR (KBr) spectrum of [(NON^{Dipp})Sc(BH$_4$)$_2$][Li(THF)$_4$)] (**19**).

Crystallographic data

A.6 Appendix for crystallographic data

Table A.6.1 Selected experimental crystallographic data.

Complex	**1**	**2**	**3**
Crystal data			
cif file	006ljm23	001ZRT22	046ljm23
Chemical formula	$C_{34}H_{51}BiN_2O_2Si_2$	$C_{36}H_{55}BiN_2O_2Si_2$	$C_{40}H_{63}BiN_2O_2Si_2$
M_r	784.92	812.98	869.08
Crystal system, space group	Triclinic, $P\overline{1}$	Monoclinic, $P2_1/n$	Triclinic, $P\overline{1}$
Temperature (K)	150	150	150
a, *b*, *c* (Å)	9.9336 (2), 16.2405 (3), 23.7245 (4)	17.1656 (1), 10.7027 (1), 21.3975 (2)	12.1626 (2), 13.2032 (3), 15.7301 (4)
α, β, γ (°)	70.353 (2), 89.354 (1), 82.604 (2)	90, 105.125 (1), 90	69.373 (2), 71.699 (2), 63.409 (2)
V (Å^3)	3572.48 (12)	3794.93 (6)	2076.82 (9)
Z	4	4	2
Radiation type	Cu $K\alpha$	Cu $K\alpha$	Cu $K\alpha$
μ (mm^{-1})	10.56	9.96	9.13
Crystal size (mm)	0.21 × 0.14 × 0.08	0.30 × 0.22 × 0.14	0.22 × 0.16 × 0.13
Data collection			

Diffractometer	SuperNova, Dual, Cu at home/near, Atlas	SuperNova, Dual, Cu at home/near, Atlas	SuperNova, Dual, Cu at home/near, Atlas
Absorption correction	Gaussian *CrysAlis PRO* 1.171.42.49 (Rigaku Oxford Diffraction, 2022) Numerical absorption correction based on gaussian integration over a multifaceted crystal model Empirical absorption correction using spherical harmonics, implemented in SCALE3 ABSPACK scaling algorithm.	Gaussian *CrysAlis PRO* 1.171.41.93a (Rigaku Oxford Diffraction, 2020) Numerical absorption correction based on gaussian integration over a multifaceted crystal model Empirical absorption correction using spherical harmonics, implemented in SCALE3 ABSPACK scaling algorithm.	Gaussian *CrysAlis PRO* 1.171.42.72a (Rigaku Oxford Diffraction, 2022) Numerical absorption correction based on gaussian integration over a multifaceted crystal model Empirical absorption correction using spherical harmonics, implemented in SCALE3 ABSPACK scaling algorithm.
T_{min}, T_{max}	0.250, 0.629	0.380, 1.000	0.256, 0.734
No. of measured, independent and observed [$I > 2\sigma(I)$] reflections	92078, 14893, 13750	45397, 7763, 7369	23743, 8572, 8105
R_{int}	0.032	0.033	0.026
$(\sin \theta/\lambda)_{max}$ ($Å^{-1}$)	0.631	0.625	0.629
Refinement			
$R[F^2 > 2\sigma(F^2)]$, $wR(F^2)$, S	0.016, 0.039, 1.02	0.023, 0.060, 1.09	0.018, 0.044, 1.04
No. of reflections	14893	7763	8572
No. of parameters	763	402	440

H-atom treatment	H-atom parameters constrained	H-atom parameters constrained	H-atom parameters constrained
$\Delta\rho_{max}$, $\Delta\rho_{min}$ (e Å^{-3})	0.50, −0.84	0.93, −1.62	0.68, −0.72

Table A.6.2 Selected experimental crystallographic data.

Complex	**4**	**6**
Crystal data		
cif file	009ccr23	010ljm23
Chemical formula	$C_{32}H_{55}BiN_2O_2Si_2$	$C_{30}H_{52}BiN_3OSi_2$
M_r	764.95	735.90
Crystal system, space group	Monoclinic, $P2_1/c$	Monoclinic, $P2_1/c$
Temperature (K)	100	150
a, *b*, *c* (Å)	15.5086 (3), 11.9606 (2), 18.8342 (2)	12.3266 (1), 19.4479 (2), 14.5432 (2)
α, β, γ (°)	90, 97.8165 (14), 90	90, 108.878 (1), 90
V (Å^3)	3461.14 (10)	3298.86 (7)
Z	4	4
Radiation type	Mo *K*α	Cu *K*α
μ (mm^{-1})	5.19	11.37
Crystal size (mm)	0.10 × 0.05 × 0.02	0.41 × 0.09 × 0.05
Data collection		
Diffractometer	Oxford Diffraction SuperNova	SuperNova, Dual, Cu at home/near, Atlas

Absorption correction	Multi-scan *CrysAlis PRO* (Rigaku Oxford Diffraction, 2017)	Gaussian *CrysAlis PRO* 1.171.42.49 (Rigaku Oxford Diffraction, 2022) Numerical absorption correction based on gaussian integration over a multifaceted crystal model Empirical absorption correction using spherical harmonics, implemented in SCALE3 ABSPACK scaling algorithm.
T_{min}, T_{max}	0.60, 0.90	0.142, 0.857
No. of measured, independent and observed [$I > 2\sigma(I)$] reflections	111555, 7932, 6612	27385, 6840, 5877
R_{int}	0.084	0.044
$(\sin \theta/\lambda)_{max}$ (Å^{-1})	0.649	0.630
Refinement		
$R[F^2 > 2\sigma(F^2)]$, $wR(F^2)$, S	0.077, 0.206, 0.98	0.031, 0.081, 1.04
No. of reflections	7932	6840
No. of parameters	352	348
H-atom treatment	H-atom parameters constrained	H-atom parameters constrained
$\Delta\rho_{max}$, $\Delta\rho_{min}$ (e Å^{-3})	15.83, −2.66	4.20, −1.24

Table A.6.3 Selected experimental crystallographic data.

Complex	**7**	**10**	**11**
Crystal data			
cif file	029ljm23	021ljm23	040ljm23
Chemical formula	$C_{33}H_{56}BiN_3O_3Si_2$	$C_{31}H_{52}BiN_3O_3Si_2$	$C_{31}H_{52}BiN_3OS_2Si_2$
M_r	807.96	779.91	812.03
Crystal system, space group	Orthorhombic, $P2_12_12_1$	Triclinic, $P\overline{1}$	Triclinic, $P\overline{1}$
Temperature (K)	150	150	100
a, *b*, *c* (Å)	9.7945 (1), 15.4970 (1), 24.3631 (2)	11.3089 (3), 11.7228 (4), 15.7044 (5)	9.8249 (1), 12.3132 (2), 16.1328 (2)
α, β, γ (°)	-	96.229 (3), 110.167 (3), 111.120 (3)	73.776 (1), 76.347 (1), 88.517 (1)
V (Å^3)	3697.96 (5)	1757.48 (11)	1819.33 (4)
Z	4	2	2
Radiation type	Cu *K*α	Cu *K*α	Cu *K*α
μ (mm^{-1})	10.24	10.75	11.41
Crystal size (mm)	0.54 × 0.07 × 0.06	0.27 × 0.14 × 0.09	0.18 × 0.09 × 0.08
Data collection			
Diffractometer	SuperNova, Dual, Cu at home/near, Atlas	SuperNova, Dual, Cu at home/near, Atlas	XtaLAB Synergy R, DW system, HyPix-Arc 150
Absorption correction	Gaussian *CrysAlis PRO* 1.171.42.72a (Rigaku Oxford	Gaussian *CrysAlis PRO* 1.171.42.72a (Rigaku Oxford	Gaussian *CrysAlis PRO* 1.171.42.83a (Rigaku Oxford

	Diffraction, 2022) Numerical absorption correction based on gaussian integration over a multifaceted crystal model Empirical absorption correction using spherical harmonics, implemented in SCALE3 ABSPACK scaling algorithm.	Diffraction, 2022) Numerical absorption correction based on gaussian integration over a multifaceted crystal model Empirical absorption correction using spherical harmonics, implemented in SCALE3 ABSPACK scaling algorithm.	Diffraction, 2023) Numerical absorption correction based on gaussian integration over a multifaceted crystal model Empirical absorption correction using spherical harmonics, implemented in SCALE3 ABSPACK scaling algorithm.
T_{min}, T_{max}	0.111, 0.953	0.074, 0.625	0.476, 1.000
No. of measured, independent and observed [$I > 2\sigma(I)$] reflections	55520, 7704, 7312	17184, 7233, 6746	35305, 7416, 7152
R_{int}	0.052	0.040	0.029
$(\sin \theta/\lambda)_{max}$ (Å^{-1})	0.630	0.630	0.625
Refinement			
$R[F^2 > 2\sigma(F^2)]$, $wR(F^2)$, S	0.021, 0.048, 1.06	0.027, 0.064, 1.07	0.026, 0.065, 1.10
No. of reflections	7704	7233	7416
No. of parameters	394	375	376
H-atom treatment	H-atom parameters constrained	H-atom parameters constrained	H-atom parameters constrained
$\Delta\rho_{max}$, $\Delta\rho_{min}$ (e Å^{-3})	0.90, −0.82	1.00, −2.16	1.21, −1.60
Flack parameter	−0.043 (4)	-	-

Table A.6.4 Selected experimental crystallographic data.

Complex	**12**	**13**	**14**
Crystal data			
cif file	047ljm23	052ljm23	010ZRT22
Chemical formula	$C_{37}H_{57}BiN_4O_2Si_2$	$C_{42}H_{61}BiN_4O_2Si_2$	$C_{44}H_{72}Cl_2LiN_2O_5ScSi_2$
M_r	855.02	919.10	888.01
Crystal system, space group	Triclinic, $P\overline{1}$	Triclinic, $P\overline{1}$	Orthorhombic, $Pna2_1$
Temperature (K)	150	100	150
a, *b*, *c* (Å)	10.6866 (3), 12.7677 (2), 15.6587 (4)	11.49163 (5), 12.03889 (6), 18.44706 (7)	17.9947 (5), 19.4693 (4), 14.6719 (4)
α, β, γ (°)	75.027 (2), 77.365 (2), 73.135 (2)	92.4526 (4), 107.0458 (4), 117.8366 (5)	-
V (Å^3)	1951.18 (9)	2108.34 (2)	5140.2 (2)
Z	2	2	4
Radiation type	Cu *K*α	Cu *K*α	Cu *K*α
μ (mm^{-1})	9.73	9.05	2.94
Crystal size (mm)	0.16 × 0.14 × 0.09	0.16 × 0.11 × 0.09	0.22 × 0.12 × 0.02
Data collection			
Diffractometer	SuperNova, Dual, Cu at home/near, Atlas	XtaLAB Synergy R, DW system, HyPix-Arc 150	SuperNova, Dual, Cu at home/near, Atlas
Absorption correction	Gaussian *CrysAlis PRO* 1.171.42.72a (Rigaku Oxford	Gaussian *CrysAlis PRO* 1.171.42.83a (Rigaku Oxford	Gaussian *CrysAlis PRO* 1.171.41.93a (Rigaku Oxford

	Diffraction, 2022) Numerical absorption correction based on gaussian integration over a multifaceted crystal model Empirical absorption correction using spherical harmonics, implemented in SCALE3 ABSPACK scaling algorithm.	Diffraction, 2023) Numerical absorption correction based on gaussian integration over a multifaceted crystal model Empirical absorption correction using spherical harmonics, implemented in SCALE3 ABSPACK scaling algorithm.	Diffraction, 2020) Numerical absorption correction based on gaussian integration over a multifaceted crystal model Empirical absorption correction using spherical harmonics, implemented in SCALE3 ABSPACK scaling algorithm.
T_{min}, T_{max}	0.117, 0.435	0.432, 0.685	0.385, 1.000
No. of measured, independent and observed [$I > 2\sigma(I)$] reflections	25081, 8054, 7512	88793, 8649, 8597	24904, 9704, 7492
R_{int}	0.032	0.030	0.063
$(\sin \theta/\lambda)_{max}$ (Å^{-1})	0.629	0.629	0.630
Refinement			
$R[F^2 > 2\sigma(F^2)]$, $wR(F^2)$, S	0.024, 0.061, 1.04	0.018, 0.042, 1.10	0.051, 0.136, 1.03
No. of reflections	8054	8649	9704
No. of parameters	429	474	576
H-atom treatment	H-atom parameters constrained	H-atom parameters constrained	H-atom parameters constrained
$\Delta\rho_{max}$, $\Delta\rho_{min}$ (e Å^{-3})	1.61, −1.13	0.50, −0.95	0.40, −0.30

Table A.6.5 Selected experimental crystallographic data.

Complex	**15**	**16**	**19**
Crystal data			
cif file	016ljm23	042ljm23	044ljm23
Chemical formula	$C_{20}H_{46}ClN_2O_3ScSi_2$	$C_{36}H_{64}KN_2O_3ScSi_2$	$C_{28}H_{51}B_2N_2OScSi_2 \cdot C_{16}H_{32}LiO_4$
M_r	499.18	713.13	849.82
Crystal system, space group	Monoclinic, $P2_1/c$	Triclinic, $P\overline{1}$	Orthorhombic, $Pna2_1$
Temperature (K)	150	150	100
a, *b*, *c* (Å)	12.5507 (2), 9.7079 (2), 22.9167 (3)	10.4504 (4), 12.7427 (5), 17.1274 (7)	17.9714 (6), 19.7590 (5), 14.4502 (4)
α, β, γ (°)	91.951 (1)	86.448 (3), 76.416 (4), 66.807 (4)	-
V (Å^3)	2790.57 (8)	2036.63 (15)	5131.2 (3)
Z	4	2	4
Radiation type	Cu *K*α	Cu *K*α	Cu *K*α
μ (mm^{-1})	4.12	3.28	1.98
Crystal size (mm)	0.27 × 0.24 × 0.15	0.11 × 0.11 × 0.08	0.2 × 0.12 × 0.02
Data collection			
Diffractometer	SuperNova, Dual, Cu at home/near, Atlas	SuperNova, Dual, Cu at home/near, Atlas	XtaLAB Synergy R, DW system, HyPix-Arc 150
Absorption correction	Gaussian *CrysAlis PRO* 1.171.42.72a	Multi-scan *CrysAlis PRO* 1.171.42.72a	Multi-scan *CrysAlis PRO* 1.171.42.83a

	(Rigaku Oxford Diffraction, 2022) Numerical absorption correction based on gaussian integration over a multifaceted crystal model Empirical absorption correction using spherical harmonics, implemented in SCALE3 ABSPACK scaling algorithm.	(Rigaku Oxford Diffraction, 2022) Empirical absorption correction using spherical harmonics, implemented in SCALE3 ABSPACK scaling algorithm.	(Rigaku Oxford Diffraction, 2023) Empirical absorption correction using spherical harmonics, implemented in SCALE3 ABSPACK scaling algorithm.
T_{min}, T_{max}	0.472, 1.000	0.923, 1.000	0.718, 1.000
No. of measured, independent and observed [$I > 2\sigma(I)$] reflections	26454, 5806, 5339	30414, 8415, 6697	45488, 9434, 7076
R_{int}	0.031	0.047	0.141
$(\sin \theta/\lambda)_{max}$ (Å^{-1})	0.630	0.630	0.610
Refinement			
$R[F^2 > 2\sigma(F^2)]$, $wR(F^2)$, S	0.043, 0.111, 1.07	0.036, 0.096, 1.01	0.110, 0.300, 1.13
No. of reflections	5806	8415	9434
No. of parameters	272	464	546
H-atom treatment	H-atom parameters constrained	H-atom parameters constrained	H atoms treated by a mixture of independent and constrained refinement
$\Delta\rho_{max}$, $\Delta\rho_{min}$ (e Å^{-3})	0.68, −0.72	0.29, −0.34	1.25, −0.79